The influence of off-diagonal disorder on resonant transmission and emergent phenomena in nanostructured carbon thin films

A Dissertation submitted to the Faculty of Science, University of the Witwatersrand, Johannesburg, in fulfilment of the requirements for the degree of PhD.

Ross William McIntosh
School of Physics
University of the Witwatersrand

Supervisor:
Professor Somnath Bhattacharyya
University of the Witwatersrand

University of the Witwatersrand

August 9, 2017

Declaration

I declare that this thesis is my own, unaided work. It is being submitted for the Degree of PhD at the University of the Witwatersrand, Johannesburg. It has not been submitted before for any degree or examination at any other University.

10^{th} February 2017

Abstract

Nano-structured carbon films, long studied due to the promise of exceptional quantum transport properties, present a significant problem in condensed matter due to the disorder which inherently forms in these materials. This work addresses the role of structural disorder in low dimensional carbon systems. The influence of structural disorder on resonant transmission is studied in diamond-like carbon superlattices. Having established a model for disorder, this model for the structural changes is then applied to interpret experimental measurements of diamond-like carbon superlattices. The role of phonons on resonant transmission under a high frequency gate potential was also studied. This model for structural disorder in heterogeneous carbon films was then applied to disordered superconductors close to the Anderson-Mott transition using the inhomogeneous Bogoliubov-de Gennes theory. This analysis is then used in support of experimental work to understand the superconductor-insulator transition in boron doped nano-crystalline diamond films.

Coherent quantum transport effects were demonstrated in structurally-disordered diamond-like carbon (DLC) superlattices through distinct current modulation (step-like features) with negative differential resistance in the current-voltage (I-V) measurements. A model for these structurally disordered superlattices was developed using tight-binding calculations within the Landauer-Büttiker formalism assuming a random variation of the hopping integral following a Gaussian distribution. Calculations of the I-V characteristics for different configurations of superlattices compliment the interpretation of the measured I-V characteristics and illustrate that while these DLC superlattice structures do not behave like conventional superlattices, the present model can be used to tailor the properties of future devices. Furthermore this tandem theoretical and experimental analysis establishes the validity of the model for structural disorder.

The same model for the variation of disorder was then applied to interpret the electronic transport properties of disordered graphene-like carbon thin films. The influence of disorder on the activation energy in few layer graphitic films was modelled and compared with experimental observations through collaboration. The films, grown by laser ablation, allowed the specific effects of structural disorder in the $sp^2 - C$ phase to be probed. Defects acted as effective barriers resulting in localization of charge carriers. Electron transmission spectra, calculated with a tight-binding model, accounted for the change of localization length as a result of disorder in the $sp^2 - C$ phase. This theoretical study showed that the localization

length of the thin graphitic films can be tuned with the level of disorder and was shown to be consistent with experimental studies.

The influence of nitrogen incorporation on resonant transmission in DLC superlattices was then studied theoretically. This study illuminated the specific role of the nitrogen potential in relation to the Fermi level (E_F) in nitrogen incorporated amorphous carbon (a-CN) superlattice structures. In a-CN systems, the variation of conductivity with nitrogen percentage has been found to be strongly non-linear due to the change of disorder level. The effect of correlated carbon and nitrogen disorder was investigated in conjunction with the nitrogen potential through analysis of transmission spectra, calculated using a tight binding model, which showed two broad peaks related to these species. It was shown that the characteristic transmission time through nitrogen centres can be controlled through a combination of the nitrogen potential and correlated disorder. In particular, by controlling the arrangement of the nitrogen sites within the $sp^2 - C$ clusters as well as their energetic position relative to E_F, a crossover of the pronounced transmission peaks of nitrogen and carbon sites can be achieved. Furthermore, it was shown that nitrogen incorporated as a potential barrier can also enhance the transmission in the a-CN superlattice structures. The strong non-linear variation of resistance and the characteristic time of the structures can explain the transport features observed experimentally in a-CN films.

This analysis was then partnered with measurements performed on nitrogen-incorporated carbon superlattices (N-DLC QSL) by Neeraj Dwivedi (National University of Singapore). The electrical characteristics of these nitrogen incorporated superlattice devices revealed prominent negative differential resistance (NDR) behavior. The interpretation of these measurements was supported by $1D$ tight binding calculations of disordered superlattice structures (chains), which included significant bond alternation in sp^3-hybridized regions. This analysis showed improved resonant transmission, which can be ascribed to nitrogen-driven structural modification of the N-DLC QSL structures, especially the increased sp^2-C clustering that provides additional conduction paths throughout the network.

In order to determine the influence of additional factors on coherent quantum states in molecular systems as an extension to the analysis on superlattices, a theoretical study of the electron-phonon interaction in double barrier structures under the influence of a time-dependent gate potential was undertaken. The Floquet theory was employed along with expansion in a polaron eigenbasis to render a multi-dimensional single body problem. An essentially exact solution was found using the Riccati matrix technique. It was demonstrated that optimal transmission can be achieved by varying the frequency of the gate potential. In addition, it was shown that the gate potential can be used to control the energy of the resonant states very precisely while maintaining optimal transmission.

Having gained a deep understanding of the structural changes induced in carbon systems through the incorporation of nitrogen, a similar structural model was then applied to study the changes induced in diamond and nanocrystalline films by boron incorpora-

tion. Boron doped diamond provides an interesting superconductor with ongoing debate surrounding the nature of the impurity band and the effect on the superconducting phase transition of structural changes induced by boron incorporation. The influence of disorder, both structural (non-diagonal) and on-site (diagonal), was studied through the inhomogeneous Bogoliubov-de Gennes (BdG) theory in narrow-band disordered superconductors with a view towards understanding superconductivity in boron doped diamond (BDD) and boron-doped nanocrystalline diamond (B-NCD) films. We employed the attractive Hubbard model within the mean field approximation, including a short range Coulomb interaction between holes in the narrow acceptor band. We studied substitutional boron incorporation in a triangular lattice, with disorder in the form of random potential fluctuations at the boron sites. The role of structural disorder was investigated through non-uniform variation of the tight-binding coupling parameter where, following experimental findings in BDD and B-NCD films, we incorporated the concurrent increase in structural disorder with increasing boron concentration.

Stark differences between the effects of structural and on-site disorder were demonstrated and showed that structural disorder has a much greater effect on the density of states, mean pairing amplitude and superfluid density than on-site potential disorder. We showed that structural disorder can increase the mean pairing amplitude while the spectral gap in the density of states decreases, with states eventually appearing within the spectral gap for high levels of disorder. This study illustrated how the effects of structural disorder can explain some of the features found in superconducting BDD and B-NCD films, such as a tendency towards saturation of the critical temperature (T_c) with boron doping and deviations from the expected Bardeen-Cooper-Shrieffer (BCS) theory in the temperature dependence of the pairing amplitude and spectral gap. The variation of the superfluid density considering only structural disorder was markedly different from the variation with on-site disorder only and revealed that structural disorder is far more detrimental to superconductivity and accounts for the relatively low T_c of BDD and B-NCD in comparison to the T_c predicted using the conventional BCS theory.

This theoretical work was then used to interpret features in the measured transport properties of B-NCD films with different doping concentrations and microstructures. The temperature dependence of a distinct local maximum in field dependent magnetoresistance measurements showed suppression of the density of states as the system breaks up into superconducting regions separated by grain boundaries. Differential resistance measurements at different temperatures and magnetic fields showed a transition from a local minimum at zero applied current, indicative of persisting superconducting regions, to a local maximum. A power law dependence over a certain current range in the measured I-V characteristics at different magnetic fields suggests a Berezinski-Kosterlitz-Thouless (BKT) transition. In addition, features in the magnetoresistance clearly indicate additional phases. Together with features in current-voltage measurements, these signatures show the coexistence of superconductivity and additional competing phases close to the Anderson-Mott transition.

Finally, measurements on superconducting spin valves towards the study of triplet superconductivity are presented in the appendix.

Dedicated to Jess, who showed me what courage and determination are.

Acknowledgements

This work would not have been possible but for the generous efforts of many people. I thank my supervisor Prof. Somnath Bhattacharyya. I am deeply grateful to Prof. Arghya Taraphder for his constant support, many discussions and wise words. Many thanks also to Dr. Narayan Mohanta for introducing me to the Bogoliubov de Gennes theory and for a great deal of support along the way. Without the contributions from Prof. Taraphder and Dr. Mohanta, this work would not have been possible. I also thank the Centre for Theoretical Studies, Indian Institute of Technology Kharagpur for supporting a research visit.

I thank Prof. Bryan Hickey, Dr. Oscar Cespedes and the Condensed Matter group at the University of Leeds for going out of their way to support a research visit and for many useful discussions. In particular I would like to thank Dr. Mannan Ali for teaching me a great deal about sputtering and many other aspects of experimental physics. Thanks also to Dr. Fatma Al Ma'Mari, Dr. May Wheeler and Dr. Tim Moorsom for teaching me about organic spintronics and for helping out with sputtering and measurements. Thanks also to Dr. Nathan Satchell, Dr. Joseph Bately and Dr. Georgios Stefanou for help with work on superconducting spin valves and low temperature measurements. Thanks also to Dr. Gavin Burnell. I also thank Mr. John Turton and Mr. Brian Gibbs for keeping the cryostats at Leeds running like clockwork.

I thank the members of the Nano-scale Transport Physics Lab (past and present), Dr. Dmitry Churochkin, Dr. George Chimowa, Ms. Kirsty Sanders, Ms. Siphephile Ncube, Mr. Christopher Coleman, Mr. Tahir Aslan and Dr. Davie Mtsuko. I thank Prof. Michael Katkov for teaching me the tight-binding method and for help with theoretical work on phonons. Once again I thank Dr. Zivayi Chiguvare for teaching me many different aspects of experimental physics and for help with calculations. I also thank Dr. Sergio Coelho for help in experimental aspects. I would like to thank Mr. John Augustine, Mr. Lundersteady Mafemba, Mr. Don Mckenna, Mr. Gerrard Peters, Mr. Jeffrey Nyandeni and Mr. Vincent Govender for a great deal of technical support over the years. Thanks also to Mr. Charles Sandrock for much support with many issues over many years. I thank Mr. Daniel Jautse for support with many computer and network issues and for always managing to find an extra mouse, keyboard or hard drive. I thank Mrs. Thembisile Nkabinde and Mrs. Ragnie Leahy for a great deal of administrative support. Thanks also to Mr. Shanmuga Pillay for

support in running the Mathematical Sciences cluster at Wits and Mr. Brian Maistry for sorting out Mathematica licenses.

I thank Prof. Alex Quandt for many useful discussions and for his insights and support over many years. I thank Dr. Daniel Wamwangi for a great deal of help on many issues and for sharing so freely of his time and knowledge in many, many interesting discussions. I thank Prof. Deena Naidoo for looking out for me and Prof. Jonathan Keartland for much help over the years. Thanks also to Dr. Robert Warmbier. I thank my unfortunate office mates, particularly Dr. William Wright for many discussions and for putting up with my madness. Many thanks to Mr. Warren Carlson for many useful discussions on a range of topics in physics, mathematics and computational aspects. I also thank Dr. Vincent Marcicano for many discussions. I thank Mr. Dario Fanucchi for many stimulating discussions over the years and for support recently.

I thank Prof. David Tománek for many, many useful discussions and for giving so freely of his time. I also thank Prof. S. R. P. Silva and Prof. Gehan Amaratunga for useful discussions. I thank Prof. Milos Nesladek (for providing samples and useful discussions), Prof. Thomas Ihn, Prof. Emmanuel Flahaut, Prof. Ping Sheng, Prof. Klaus Ensslin, Prof. Andrea Ferarri and others who attended the annual Nano-carbon conferences - I learnt a great deal from them. I also thank Prof. Luis Foa Torres and Prof. Holger Fehske for useful discussions on phonons. I thank Dr. Neeraj Dwivedi for a fruitful collaboration and for many illuminating discussions.

Once again, I sincerely thank Prof. Alex Quandt, Dr. Shane Durbach and Prof. Ted Lowther for helping to source funding. I thank the Centre of Excellence in Strong Materials for funding and I thank Mrs. Casey Sparks and Mrs. Marina Labuschagne for help over the years. I also thank the NRF for funding.

I sincerely thank my parents, my sister and the dogs for putting up with this insanity - I would have moved out of the house at some stage, I feel that fleeing the continent was maybe a bit extreme. I also thank Ann Marie Wood and Keith Wood for a great deal of support. Thanks also to Keegan Ward for always keeping me in the loop and Reynhardt Van As for getting me into trouble. I sincerely thank my fantastic girlfriend for always being there for me and somehow keeping the wheels on when everything seemed to go pear shaped - it goes without saying that I couldn't have done it without you.

Contents

1 Introduction **21**

1.1 Introduction . . . 21

1.2 Outline . . . 34

2 Experimental Procedures **36**

2.1 Sample Preparation . . . 36

2.1.1 DLC Superlattices . . . 36

2.1.2 Boron-doped Nano-crystalline Diamond . . . 36

2.2 Transport Measurements . . . 37

3 Resonant Transmission in Diamond-like Carbon Superlattices **41**

3.1 Introduction . . . 41

3.1.1 DLC Superlattices . . . 41

3.2 Model . . . 43

3.2.1 The incorporation of disorder . . . 44

3.3 Diamond-like Carbon Superlattices . . . 45

3.3.1 Measured Transport Properties . . . 45

3.3.2 Calculated Current-Voltage characteristics . . . 49

3.4 Effect of disorder in thin graphitic films . . . 54

3.5 Nitrogen Incorporation in a-C Superlattices . . . 56

3.6 Comparison with experiment for nitrogen incorporated a-C superlattices . . . 63

3.7 Summary . . . 70

4 Phonons in 1D Chains **71**

4.1 Introduction . . . 71

4.2 Model . . . 72

4.3 Frequency-Independent Results . . . 75

4.4 Time Dependent Electron-phonon Interactions . . . 76

4.5 Results using the Ricatti Matrix Method . . . 77

4.6 Results from the Double Barrier Case . . . 78

4.7 Summary . . . 85

5 Inhomogeneous BdG Theory Applied to B-NCD **89**

5.1 Introduction . . . 89
5.2 Model . . . 91
5.2.1 The incorporation of disorder . . . 95
5.2.2 Lattice size . . . 96
5.3 Results . . . 97
5.3.1 On-site potential disorder . . . 97
5.3.2 Correlated Structural disorder . . . 104
5.3.3 Combined Structural and On-site Disorder . . . 106
5.3.4 Finite Temperature Analysis . . . 110
5.3.5 Superfluid phase stiffness . . . 116
5.4 Discussion . . . 118

6 Measured Transport Properties of B-NCD **124**
6.1 Introduction . . . 124
6.2 Results . . . 125
6.2.1 B-NCD device grown with 1 % CH_4 in the chamber . . . 125
6.2.2 B-NCD device grown with 5 % CH_4 in the chamber . . . 138
6.3 Discussion . . . 144

7 Conclusion **149**

8 Publications **152**

9 Appendix **154**
9.1 Triplet Superconductivity in Superconducting spin valves . . . 154
9.1.1 Experimental Methods . . . 155
9.1.2 Magnetic Properties . . . 155
9.1.3 Transport Measurements . . . 158
9.2 Superconducting Spin Valve Without Large Exchange Bias . . . 164
9.2.1 Magnetic Measurements . . . 164
9.2.2 Transport Measurements . . . 166

References **169**

List of Figures

1.1 Calculated real part of the AC conductivity (conductance) for a resonant device up to 200 GHz. 23
1.2 Calculated imaginary part of the AC conductivity for a resonant device up to 100 GHz. 24
1.3 Bright field images of a-C superlattices courtesy of S.R.P Silva and V. Stolojan. 26

2.1 Janis micromanipulated probe station. Upper left inset: Viewed from above. Upper right inset: Agilent B1500A Semiconductor Device Analyser. 38
2.2 Cryogenic free measurement system. 40

3.1 An atomic scale schematic diagram of the quantum well formed by a predominantly $sp^2 - C$ well (maroon atoms) embedded within two predominantly $sp^3 - C$ barriers (blue atoms). The potential is overlain in yellow. 44
3.2 An atomic scale schematic diagram of the quantum superlattice formed by alternating layers of predominantly $sp^2 - C$ well (maroon atoms) embedded within two predominantly $sp^3 - C$ barriers (blue atoms). The potential is overlain in yellow. 46
3.3 An atomic scale schematic diagram of the quantum superlattice formed by alternating layers of predominantly $sp^2 - C$ well (maroon atoms) embedded within two predominantly $sp^3 - C$ barriers (blue atoms). The chemical potential across the device is shown in green. 47
3.4 Current-voltage characteristics of a DLC superlattice with 4 barriers of 7 nm and 3 wells of 7 nm. Inset is the hopping term at each lattice site. 47
3.5 Current-voltage characteristics of a DLC superlattice with 4 barriers of 7 nm and 3 wells of 4 nm. Inset is the hopping term at each lattice site. 48
3.6 Current-voltage characteristics of a DLC superlattice with 4 barriers of 8 nm and 3 wells of width 2 nm. Inset is the hopping term at each lattice site. . . 49
3.7 Calculated current-voltage characteristics of a DLC superlattice with 4 barriers of 7 nm and 3 well of 7 nm. 50
3.8 Calculated current-voltage characteristics of a DLC superlattice with 4 barriers of 7 nm and 3 wells of 4 nm. 51

3.9 Calculated current-voltage characteristics of a DLC superlattice with 4 barriers of 7 nm and 3 wells of 1 nm assuming a Gaussian distribution of around a mean hopping parameter in the $sp^3 - C$ regions and the inclusion of impurity states. 51
3.10 Calculated current-voltage characteristics of a DLC superlattice with 4 barriers of 7 nm and 3 wells of 7 nm considering significant bond alternation in the sp^3 hybridized regions. 52
3.11 Current-voltage characteristics of a DLC superlattice with 4 barriers of 8 nm and 3 wells of width 2 nm as a function of voltage squared to examine Poole-Frenkel and Schottky emission. 53
3.12 (a) Calculated normalized localization length as a function of the disorder parameter δ_π (mean of the Gaussian distribution of π phase hopping terms). (b) to (d) The first transmission peak of the calculated transmission coefficient as a function of energy for different values of δ_π. (e) Schematic diagram of the microstructure of two overlapping disordered graphene layers as a representation of thin graphitic films. The diagram includes bond-length distortions as well as in plane and out of plane bond-angle distortions and vacancies. . . 55
3.13 (a) The full width at half maximum of the Raman G peak (ΔG) as a function of the activation energy. (b) Activation energy determined through application of Eq. (1) as a function of the I_D/I_G ratio. 57
3.14 Schematic diagram of a range of possible nitrogen induced impurity levels in carbon systems [1]. 58
3.15 Transmission coefficient as a function of incident electron energy as the N potential is varied from N_{up} to N_{down}. 58
3.16 Full width at half maximum of the carbon and nitrogen transmission peaks as a function of t_N (the N hopping parameter). 59
3.17 The corresponding $T(E)$ peak height as a function of energy. 60
3.18 The corresponding peak position as a function of t_N. 60
3.19 a) Schematic diagram of nitrogen incorporated DLC superlattice with nitrogen incorporated in the sp^3 hybridized layers. b) Calculated current-voltage characteristics of a DLC superlattice with 4 barriers of 7 nm and 3 well of 7 nm with nitrogen incorporated in the sp^3 hybridized regions. 62
3.20 Measured I-V characteristics, with first and second derivatives, of DLC superlattices with different amounts of nitrogen incorporation: a) 0 %, b) 48.3 %, c) 65.2 %. Measurements performed by N. Dwivedi [2]. 64
3.21 An atomic scale schematic diagram of the quantum superlattice formed by alternating layers of predominantly $sp^2 - C$ well (maroon atoms) embedded within two predominantly $sp^3 - C$ barriers (blue atoms) considering significant bond alternation in the $sp^3 - C$ regions. The potential is overlain in yellow. . 66

3.22 a) Calculated current-voltage characteristics of a DLC superlattice with 7 barriers of 3.5 nm and 6 wells of 2.5 nm with no nitrogen incorporated in the sp^2 hybridized regions. b) Schematic diagram of DLC superlattice. c) Calculated current-voltage characteristics of a DLC superlattice with 7 barriers of 3.5 nm and 6 wells of 2.5 nm with nitrogen incorporated in the sp^2 hybridized regions. d) Schematic diagram of nitrogen incorporated DLC superlattice with nitrogen incorporated in the sp^2 hybridized layers. 67

3.23 a) Calculated current-voltage characteristics of a DLC superlattice with 7 barriers of 3.5 nm and 6 wells of 2.5 nm with nitrogen incorporated in the sp^2 hybridized regions. b) Schematic diagram of nitrogen incorporated DLC superlattice with nitrogen incorporated in the sp^2 hybridized layers. c) Calculated current-voltage characteristics of a DLC superlattice with 7 barriers of 3.5 nm and 6 wells of 2.5 nm with nitrogen incorporated in the sp^2 hybridized regions. d) Schematic diagram of nitrogen incorporated DLC superlattice with nitrogen incorporated in the sp^2 hybridized layers. 69

4.1 Representation of the many-body Hilbert space with each site representing a basis state, sites in the horizontal direction and phonon quanta in the vertical direction. 74

4.2 Intensity map of the transmission through a single molecular site as a function of the electron energy and the electron-phonon coupling strength. 74

4.3 Intensity map of the transmission through a single molecular site as a function of the electron energy and the phonon frequency. 75

4.4 Mapping the many-body Hilbert space onto a multi-dimensional single-body problem within the tight-binding scheme using the Floquet theory. 77

4.5 Transmission coefficient as a function of energy for a single barrier in the presence of the electron-phonon interaction. The electron-phonon coupling parameter λ is changed from 0 to 0.3 in steps of 0.1 from top to bottom. . . 79

4.6 Transmission coefficient as a function of energy for a single barrier in the presence of the electron-phonon interaction under the influence of a time-periodic potential. The phonon frequency Ω is changed from 0.1 to 0.4 in steps of 0.1 from top to bottom. 80

4.7 Transmission coefficient as a function of energy for a single barrier in the presence of the electron-phonon interaction under the influence of a time-periodic potential. The frequency of the gate potential ω is changed from 0.1 to 0.4 in steps of 0.1 from top to bottom. 81

4.8 Intensity map of the transmission through a double barrier structure in the presence of the electron-phonon interaction and a time-dependent external potential as a function of the electron energy and the electron-phonon coupling parameter with the phonon frequency $\Omega = 0.2$ and $\omega = 0.2$. 82

4.9 Transmission coefficient as a function of energy for a double barrier in the presence of the electron-phonon interaction under the influence of a time-periodic potential. The electron-phonon coupling strength λ is changed from 0.1 to 0.4 in steps of 0.1 from the top figure to the bottom figure. 83
4.10 Intensity map of the transmission through a double barrier structure in the presence of the electron-phonon interaction and a time-dependent external potential as a function of the electron energy and the phonon frequency with $\lambda = 0.3$ and $\omega = 0.3$. 84
4.11 Transmission coefficient as a function of energy for a double barrier in the presence of the electron-phonon interaction under the influence of a time-periodic potential. The frequency of the gate potential ω is changed from 0.2 to 0.5 in steps of 0.1 from the top figure to the bottom figure, with $\lambda = 0.3$ and $\omega = 0.3$. 86
4.12 Intensity map of the transmission through a double barrier structure in the presence of the electron-phonon interaction and a time-dependent external potential as a function of the electron energy and the frequency of the gate potential with $\lambda = 0.2$ and $\Omega = 0.5$. 87
4.13 Intensity map of the transmission through a double barrier structure in the presence of the electron-phonon interaction and a time-dependent external potential as a function of the electron energy and the frequency of the gate potential with $\lambda = 0.5$ and $\Omega = 0.2$. 88

5.1 Schematic diagram of the structural model we employ. 96
5.2 Spectral gap as a function of the structural disorder parameter expressed in units of the hopping parameter, t, (in the absence of on-site disorder with W = 0 i.e. no Coulomb interaction) for different lattice sizes. 96
5.3 Mean pairing amplitude as a function of the boron concentration considering only on-site disorder where the disorder parameter is varied from 0.5 to 1.5. Inset is the local pairing amplitude considering a small on-site disorder parameter $\sigma = 0.05$ 97
5.4 a) Mean pairing amplitude as a fucntion of the on-site disorder paramater (considering only on-site potential disorder at the boron sites only) where the atomic boron concentration is held fixed at 15 %. Inset is the local pairing amplitude at each lattice site with a relatively large on-site disorder parameter of $\sigma = 1.5$. b) The corresponding spectral gap as a function of the on-site disorder paramater. Inset is the density of the states in the vicinity of the gap. 98
5.5 a) Density of states where the boron concentration is held fixed and the on-site disorder parameter is varied. b) Corresponding local density of states 99

5.6 Distribution of the local pairing amplitude for different realizations of the on-site disorder parameter considering only on-site disorder at the boron sites. Inset is the pairing amplitude correlation function considering only on-site disorder with a disorder parameter of $\sigma = 0.02$ (blue) and $\sigma = 1.5$ (red). . . . 101
5.7 a) Mean pairing amplitude as a function of the on-site disorder parameter considering on-site disorder at all sites in the lattice at a constant atomic boron concentration of 15 %. Inset is the local pairing amplitude considering an on-site disorder parameter of $\sigma = 1.5$. b) The corresponding spectral gap. Inset is the density of states around the gap region. 102
5.8 Distribution of the local pairing amplitude as a function of the boron concentration for different realizations of the on-site disorder parameter considering on-site disorder at all sites. Inset is the pairing amplitude correlation function considering a small on-site disorder parameter (blue dots) and a larger diosrder parameter (red dashed line). 103
5.9 a) Variation of the structural disorder parameter as a function of the atomic boron concentration for three different cases. b) The mean pairing amplitude as a function of the atomic boron concentration for three different cases. The case of linear correlated disorder corresponds to the blue dashed line while the exponential variation of disorder corresponds to the red diamonds and inverse exponential variation corresponds to the green dots. 105
5.10 a) Mean pairing amplitude at a constant boron concentration of 15.4 % while the structural disorder parameter varies from 0 to 0.5 in the absence of on-site disorder. Inset is the local pairing amplitude where the structural disorder patameter is 0.5. b) The corresponding spectral gap as a function of the disorder paramater. Inset is the density of states in the region around the gap. 107
5.11 a) The density of states considering different structural disorder parameters. b) The corresponding local density of states. 108
5.12 a) The density of states considering different structural disorder parameters with a large Coulomb interaction ($W = 3t$). b) The corresponding local density of states. 109
5.13 Distribution of the local pairing amplitude as a function of the boron concentration for different realizations of structural disorder in the absence of on-site disorder. Inset is the pairing amplitude correlation function for a relatively low disorder parameter (0.025, blue dots) and a higher disorder parameter (0.5, red dashed line). 110

5.14 Mean pairing amplitude as a function of the atomic boron concentration where the on-site disorder parameter is 0.8, the Coulomb interaction parameter is turned on (W = 3) and the structural disorder parameter varies with the atomic boron concentration. The case of linear correlated disorder corresponds to the dashed blue line while exponentially varying disorder corresponds to the red diamonds and inverse exponentially varying disorder corresponds to the green dots. 111
5.15 Comparison between measured T_c as a function of the boron concentration (open symbols) from various references and the calculated variation of the mean pairing amplitude as a function of the atomic boron concentration (filled green circles). 112
5.16 The mean pairing amplitude (a) and the spectral gap (b) as a function of temperature for different realizations of disorder. The black open circles represent a high boron atomic concentration (15%) considering only on-site disorder at the boron sites with a disorder parameter of 1.5 while the green squares represent on-site disorder at all lattice sites with a disorder parameter of 0.5. The red diamonds represent structural disorder with a relatively low boron concentration (5%) while the blue dots represent structural disorder with a high boron concentration (15%) while the structural disorder parameter is 0.5. 113
5.17 Density of states for different temperatures considering only structural disorder (a) and only on-site disorder at all lattice sites (b). The blue curve represents $T = 0$, the green curve $T = 0.5t$, the orange curve $T = 0.75t$ and the maroon curve $T = 1.0t$. 114
5.18 a) Local kinetic energy where the on-site disorder parameter is 0.05 considering on-site disorder at the boron sites only. b) Corresponding figure considering on-site disorder at all lattice sites when the disorder parameter is 0.5. c) Local kinetic energy considering only structural disorder where the disorder parameter is 0.5. d) Local paramagnetic response where the on-site disorder parameter is 0.05 considering on-site disorder at the boron sites only. e) Corresponding figure considering on-site disorder at all lattice sites when the disorder parameter is 0.5. f) Local kinetic energy considering only structural disorder where the disorder parameter is 0.5. 115
5.19 a) Total superfluid density as a function of the on-site disorder parameter (at a fixed boron concentration). b) Corresponding figure considering structural disorder only. c) Corresponding figure considering structural disorder only with the Coulomb interaction turned on. 117
5.20 a) Kinetic energy with changing on-site disorder (in the absence of structural disorder). b) Paramagnetic response with changing on-site disorder (in the absence of structural disorder). 118

5.21 a) Kinetic energy with changing structural disorder (in the absence of on-site disorder). b) Paramagnetic response with changing structural disorder (in the absence of on-site disorder). 119
5.22 a) (Top left)Local kinetic energy where the on-site disorder parameter is 0.05 considering on-site disorder at the boron sites only *with a large Coulomb interaction parameter* $W = 3t$. b) (Middle left) Corresponding figure considering on-site disorder at all lattice sites when the disorder parameter is 0.5. c) (Lower left) Local kinetic energy considering only structural disorder where the disorder parameter is 0.5. d) (Top right)Local paramagnetic response where the on-site disorder parameter is 0.05 considering on-site disorder at the boron sites only. e (Middle right)) Corresponding figure considering on-site disorder at all lattice sites when the disorder parameter is 0.5. f) (Bottom right) Local kinetic energy considering only structural disorder where the disorder parameter is 0.5. 120

6.1 Resistivity as a function of temperature for a B-NCD device grown with 1% CH_4 in the chamber. 126
6.2 Semi-logarithmic plot of the resistivity as a function of temperature for a B-NCD sample grown with 1% CH_4 in the chamber. The red line is a straight line showing the logarithmic trend. 126
6.3 Resistivity as a function of temperature at different magnetic fields for a B-NCD device grown with 1% CH_4 in the chamber. 127
6.4 Magnetoresistivity for a B-NCD device grown with 1% CH_4 in the chamber at different temperatures, from 0.3 K to 0.67 K. 127
6.5 Magnetoresistivity of a B-NCD device grown with 1 % CH_4 at 1.4 K. 128
6.6 Low field magnetoresistivity of a B-NCD device grown with 1 % CH_4 at 1.4 K. 128
6.7 Magnetoresistivity of a B-NCD device grown with 1 % CH_4 at 1.8 K. 129
6.8 Magnetoresistivity for B-NCD sample grown with 1% CH_4 in the chamber at 2.1 K. 130
6.9 Magnified magnetoresistivity for B-NCD sample grown with 1% CH_4 in the chamber at 2.1 K. 130
6.10 Magnetoresistivity for B-NCD sample grown with 1% CH_4 in the chamber at 2.8 K. 131
6.11 Magnetoresistivity of a B-NCD device grown with 1 % CH_4 at 3.4 K. 131
6.12 Magnetoresistivity of a B-NCD device grown with 1 % CH_4 at 10.1 K. . . . 132
6.13 Magnetoresistivity of a B-NCD device grown with 1 % CH_4 at 14.9 K. . . . 132
6.14 Voltage-current characteristics of a B-NCD device grown with 1% CH_4 at different temperatures. 133
6.15 Voltage-current characteristics plotted logarithmically at different temperatures for a B-NCD device grown with 1% CH_4 in the chamber at different temperatures. 133

6.16 Differential resistivity as a function of current for a B-NCD device grown with 1% CH_4 in the chamber at different temperatures. 134
6.17 Voltage-current characteristics for a B-NCD sample grown with 1% CH_4 in the chamber at 0.3 K at different magnetic fields. 135
6.18 Voltage-current characteristics on a logarithmic scale for a B-NCD sample grown with 1% CH_4 in the chamber at 0.3 K at different magnetic fields. . . 136
6.19 Differential resistance as a function of current for a B-NCD sample grown with 1% CH_4 in the chamber at 0.3 K at different magnetic fields. 137
6.20 Differential resistance plotted logarithmically as a function of current for a B-NCD sample grown with 1% CH_4 in the chamber at 0.3 K at different magnetic fields. 137
6.21 Resistance as a function of temperature for B-NCD device grown with 5 % CH_4. 138
6.22 Resistivity as a function of $T^{-1/2}$ for a B-NCD device grown with 5% CH_4 in the chamber. 139
6.23 Resistivity as a function of temperature plotted logarithmically for a B-NCD device grown with 5% CH_4 in the chamber. The red line shows the fit to a logarithmic dependence in the high temperature regime, the green line shows a significant change in gradient in the low temperature regime 139
6.24 Magnetoresistivity at 1.4 K for a B-NCD device grown with 5% CH_4 in the chamber. The red line is a fit to the data based on the model discussed in the text. 140
6.25 Magnetoresistivity of a B-NCD device grown with 5 % CH_4 at 1.6 K. 141
6.26 Magnetoresistivity of a B-NCD device grown with 5 % CH_4 at 1.8 K. 141
6.27 Magnetoresistivity of a B-NCD device grown with 5 % CH_4 at 2.0 K. 142
6.28 Magnetoresistivity of a B-NCD device grown with 5 % CH_4 at 2.4 K. 142
6.29 Magnetoresistivity of a B-NCD device grown with 5 % CH_4 at 3.0 K. 143
6.30 Magnetoresistivity of a B-NCD device grown with 5 % CH_4 at 5.1 K. 143

9.1 Hysteresis of a Pb superconducting spin valve above the T_c. 156
9.2 Hysteresis of a Pb superconducting spin valve at 5.6 K, in the region of the T_c. 157
9.3 Hysteresis of a Pb superconducting spin valve at 5.5 K, just below the T_c. . 157
9.4 Hysteresis of a Pb superconducting spin valve at 6 K with the device rotated at 90 degrees (in the plane of the substrate) to the previous measurements. . 158
9.5 Magnetization as a function of temperature for a Pb superconducting spin valve. The transition begins at 5.6 K. 159
9.6 Magnetoresistance of a Pb superconducting spin valve at 7 K. Magnetization measurements show a transition at 5.6 K. 159
9.7 Magnetoresistance of a Pb superconducting spin valve at 5.69 K. Magnetization measurements show a transition at 5.6 K. 160

9.8 Magnetoresistance of a Pb superconducting spin valve at 5.6 K. Magnetization measurements show a transition at 5.6 K. 161
9.9 Magnetoresistance of a Pb superconducting spin valve at 5.55 K. Magnetization measurements show a transition at 5.6 K. 161
9.10 Magnetoresistance of a Pb superconducting spin valve at 5.53 K. Magnetization measurements show a transition at 5.6 K. 162
9.11 Magnetoresistance of a Pb superconducting spin valve at 5.50 K. Magnetization measurements show a transition at 5.6 K. 163
9.12 Resistance as a function of temperature for a Pb superconducting spin valve saturated under a magnetic field of 0.01 T at different orientations. Magnetization measurements show a transition at 5.6 K. 163
9.13 Hysteresis of a Pb superconducting spin valve at 5.7 K (above the T_c). . . . 164
9.14 Hysteresis of a Pb superconducting spin valve at 5.2 K. 165
9.15 Hysteresis of a Pb superconducting spin valve at 4.5 K. 165
9.16 Magnetoresistance of a Pb superconducting spin valve at 5.8 K. 166
9.17 Magnetoresistance of a Pb superconducting spin valve at 5.2 K. 167
9.18 Magnetoresistance of a Pb superconducting spin valve at 5.0 K. 167
9.19 Resistance as a function of temperature for a superconducting spin valve where the field was saturated at 100 Oe in different orientations. 168

Chapter 1

Introduction

1.1 Introduction

With advent of synthetic superlattices, the ability to control coherent quantum states in synthetic nanostructures was realized for the first time and controllable quantum devices became a reality. Five decades on, quantum devices have achieved widespread application with ever more fundamental research being driven by the proven track record of these devices and the promise of unlocking new innovations to unleash cutting edge technologies based on high frequency oscillators, amplifiers, emitters and detectors for nano-electronic and opto-electronic applications. Superlattices are composed of alternating layers of material, generally in the region of a few nanometers thick, which allow confinement of quantum states through bandgap modulation.

The recent surge of technological development is underpinned by the use of solid state devices. Conventional solid state devices can act as oscillators in the range of up to tens of GHz [3, 4, 5]. Replacing robust yet high power consumption valve oscillators, these devices have enabled portable technologies. With increasing frequency though, the power output of current solid state devices decreases drastically, prohibiting the fabrication of devices operating at higher frequencies. There is therefore a gap, known as the THz gap, in the region in which useful devices can be manufactured.

There is a great need though to develop devices which can oscillate, amplify, emit and receive at higher frequencies, well into the THz regime [6]. Such devices would facilitate ever faster information transfer. The need for THz emitters and receivers is also essential for a host biomedical and environmental sensing applications as many biological molecules are active in this region. The promise of such devices has given research into developing quantum devices great impetus. Research into the properties quantum superlattices is at the forefront of this significant effort.

Resonant tunneling diodes have shown the highest fundamental frequency of any fundamental oscillators and are widely used [7]. They are however limited by low power output

at higher frequencies. Similarly, silicon impact ionization transit time diodes have suffered from low power outputs although oscillation frequencies up to 300 GHz have been demonstrated at low temperatures [7]. A further constraint is imposed by their narrow operational bandwidth [3]. While Gunn transferred electron devices can operate in the THz regime, they also suffer from low power output at high frequencies and they are not conducive to the fabrication of high density, nanoscale devices [3, 7].

These devices are also limited in terms of tuning device characteristics as they rely on doping, hence the impurity levels are fixed. Superlattices, on the other hand, present a different paradigm where quantum states can be manipulated by tailoring the quantum well widths and barrier heights. Superlattice THz devices have therefore been widely studied. The predicted operational frequency range of superlattices is higher than any other solid state device [7]. They are also low power consumption, low noise devices.

Superlattices have long been studied towards the development of THz oscillators, amplifiers and receivers. During the initial phase of work on superlattices, Esaki immediately pointed out the possibility of observing Bloch oscillations [8, 9]. Not only would this have been of fundamental interest, it was also predicted that Bloch oscillations could be exploited to produce ultra-high frequency oscillators, detectors and amplifiers. In crystalline materials, the inelastic electronic relaxation time is less than the Bloch oscillation period (even at extremely low temperatures) so Bloch oscillations are suppressed, even at high fields. In superlattices though, the lattice constant is greater than in homogeneous crystals. The Bloch oscillation frequency is given by

$$T = \frac{2\pi\hbar}{deE} \tag{1.1}$$

where d is the lattice constant of the superlattice, e is the electron charge and E is the external electric field strength. The Brillouin zone period is reduced from π/a (where a is the inter-atomic spacing) to π/d. The drift velocity of electrons in the superlattice is given by

$$v_d = eE\hbar^2 \int \frac{\partial^2 E_x}{\partial k_x^2} e^{\frac{t}{\tau}} dt \tag{1.2}$$

where E (E_x) is an applied electric field (in the x direction), t is time, τ is the inelastic relaxation time and k_x is the wavevector in the x direction. Electrons can be excited by an applied bias beyond inflection points in the band structure. This results in Bragg reflection between the Brillouin zone boundaries which in turn causes oscillations in the real-space motion of electrons. The field dependence in Eq. 1.1 shows the period of Bloch oscillations can be controlled by the external field. Theoretically, the drift velocity initially increases with the field, before reaching a maximum as Bloch oscillations begin to set in before finally reaching zero as Bloch oscillations suppress translational motion. In practice, this is

suppressed by inelastic scattering of charge carriers [10, 11] although the long sought after Bloch gain has been demonstrated [7].

The conductance of a resonant tunnelling diode at high frequencies can be determined from the Landauer-Buttiker formula which can be derived from the linear response theory [12]. Figure 1.1 shows the real part of the AC conductance of a double barrier resonant tunneling diode up to 200 GHz with $\xi = 2(E_0 - \mu)/\gamma$ where μ is the chemical potential, E_0 is the energy of the resonance and γ is the inverse of the quasi-bound state lifetime (width of the resonance) [12]. Figure 1.2 shows the corresponding imaginary part of the conductance. These figures show that the admittance changes non-monotonically with frequency for a given resonant energy. The imaginary part of the admittance shows inductive behaviour (positive admittance) for smaller resonant energies while at higher resonant energies it shows capacitive behaviour.

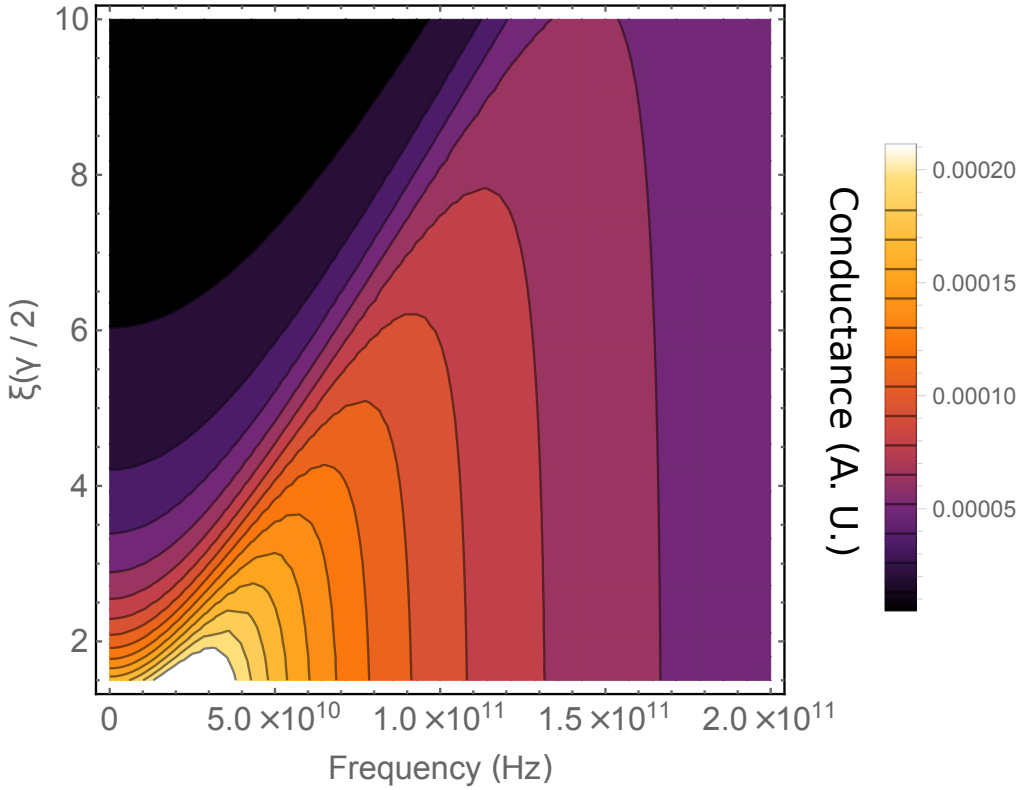


Figure 1.1: Calculated real part of the AC conductivity (conductance) for a resonant device up to 200 GHz.

Exploiting resonant transmission in superlattices allows quantum cascade lasers to operate in the THz region where current state of the art semiconductor lasers cannot. Current bipolar hetrojunction lasers function by electron-hole recombination across the heterostructure [13]. The emission wavelength is therefore limited by the available bandgaps of semiconductors. The relatively low frequency of THz radiation requires low bandgap semiconductors however these require high doping levels which result in increased defect density. This in turn is detrimental to the performance of the laser. Operating on a different paradigm, the quantum superlattice structures which are the central component of quantum cascade

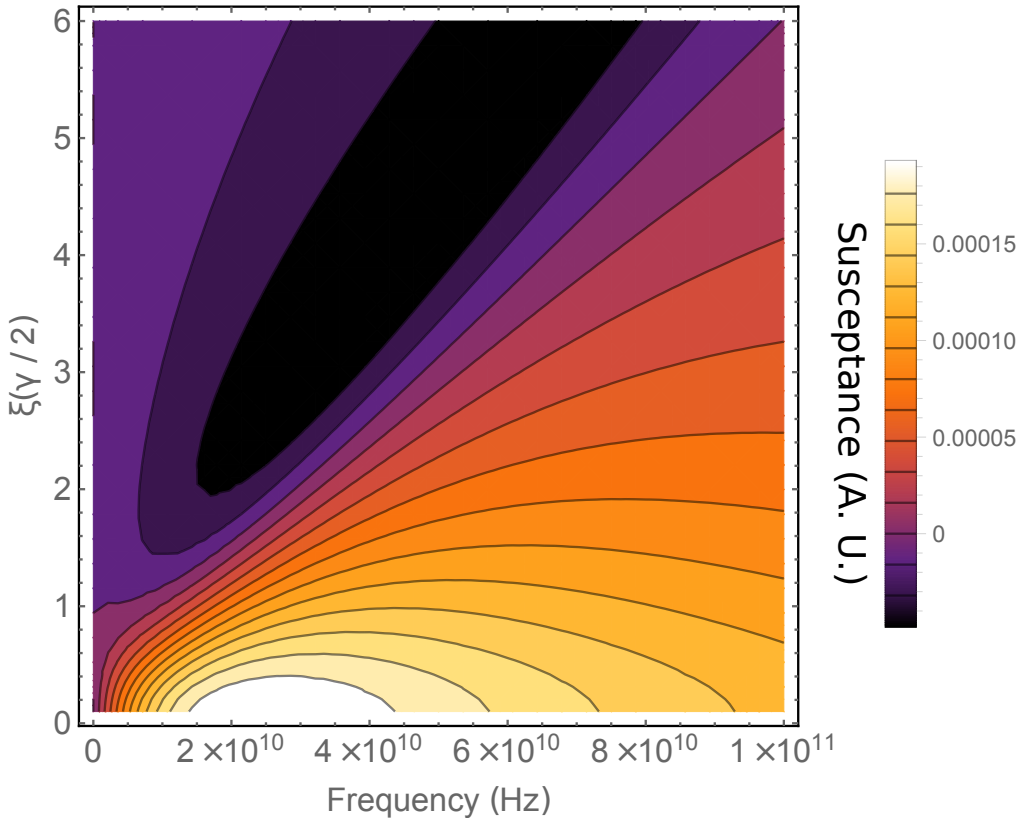


Figure 1.2: Calculated imaginary part of the AC conductivity for a resonant device up to 100 GHz.

lasers, afford the ability to control device properties, such as the frequency of emission, by controlling the device configuration i.e. the well width, barrier width, difference in potential in different regions and the type of transition between resonant states (intraband or interband when the valence band of one layer overlap with the conduction band of the other layer).

The high fidelity of eigenstates in quanutm wells make quantum cascade lasers highly coherent sources in the medium to long infrared wavelength region. Well characterized superlattices such as InGaAs/InAlAs were initially used [13]. Subsequently GaAs/AlGaAs was used. Working quantum cascade lasers have only recently been developed using Si based heterostructures [14]. Quantum cascade lasers rely on alignment of the eigenenergies of quantum wells induced by an external potential. This results in resonant transmission from a low energy state into a higher energy state in the adjacent quantum well. By applying the correct potential difference to achieve resonance, this process can carry on throughout the superlattice (cascade effect). This mechanism vastly reduces Auger recombination in comparison to conventional lasers resulting in greater spectral resolution and sensitivity in spectroscopy with quantum cascade lasers [13].

Quantum cascade lasers have a wide berth of important applications. They fill the current gap in the electromagnetic spectrum in the THz region. Of particular importance, most biological molecules exhibit absorption in the mid-infra red range [13]. Conventional Fourier

transform infrared spectroscopy, currently widely used as a diagnostic tool, has shortcomings due to low throughput and low spectral resolution. Exploiting the enhanced spectral resolution and reduced diagnosis times afforded by quantum cascade lasers, emerging technologies have recently been demonstrated for the diagnosis of various forms of cancer [15, 16]. This technology is also driving research into new cancer treatments not only through identifying diseased regions but also in determining the response to treatment [17].

Exploiting the wide tunability of quantum cascade lasers, the biomarkers of specific diseases can be detected, for example respiratory diseases can be detected just by breathing into a detection system based on quantum cascade lasers [18]. FTIR microscopy of cells in water and other aqueous media has not been possible with traditional lasers so researchers have been forced to use synchrotron radiation as a source, however the enhanced signal afforded by quantum cascade lasers has recently made high throughput studies possible [19]. The same technology can be applied to study diabetes [20] and determine blood sugar levels [21] and $in-vivo$ demonstrations have recently been carried out [22].

Quantum cascade lasers have also found extensive use in environmental monitoring as wavelengths of 3 - 12 μm can be studied [23, 24, 25]. Gasses such as NO, CO_2 and CH_4 can be detected rapidly and with high sensitivity. Another application is in-situ monitoring of plasma chemistry [26] which could be used to improve deposition of many materials including superlattices.

The efficiency of quantum cascade lasers relies on the resonant transmission of charge carriers across the superlattice. As such, a detailed understanding of the influence of disorder at the interfaces and within the quantum wells/barriers is essential in improving performance. In addition, crystalline superlattices suffer from the stringent lattice matching conditions (the scattering effects induced by a lattice mismatch cause interfacial scattering which is detrimental to resonant transmission). Amorphous superlattices have therefore been studied widely however the inherent disorder imposes limitations although the lattice matching is improved [7]. To open up THz technology, still greater control of device parameters is required, therefore different superlattice materials, including amorphous materials, must be studied. In addition, current state of the art molecular beam epitaxial synthesis of superlattices is prohibitively expensive and more cost effective alternative methods, such as RF/DC sputtering or pulsed laser ablation would be very beneficial. Robust devices which can operate in non-ideal environments are also required.

A principle step in the development of new optoelectronic devices such as quantum cascade lasers is detailed studies of the transport properties. When considering quantum transport in disordered systems, the validity of fundamental concepts such as band structure needs to be addressed. Extensive research into the microstructure of widely used amorphous materials (such as a-Si:H) has shown that these materials retain their bonding structure over small distances (greater than nearest neighbour distances), forming clusters [3]. Bond length and bond angle distortion is therefore assumed to be minimal and is often neglected.

Nearest-neighbour tight-binding schemes therefore have a great advantage in dealing with such systems as the concept of a "band" will extend across the nearest neighbour domains.

In conventional band engineered superlattices, the crystal symmetry results in sharp band edges with abrupt changes in the density of states. In amorphous materials, these band edges are smeared out by the disorder, concurrently the density of states also broadens out over a range of energies. Considering amorphous semiconductors, localized states may form within the gap. The exponentially decaying tail edges of the band become very important [27].

Amorphous heterostructures have been used successfully in certain applications. Amorphous hydrogen passivated Si and Ge superlattices have been used in the manufacture of solar cells where the hydrogen termination reduces dangling bonds [28]. Coupled with the amorphous nature of both layers, this results in the required smoothness of the interface. Amorphous non-magnetic spacer layers in spin valves enhance tunnel magnetoresistance as interfacial defects are reduced, finding application in magnetic random access memory devices [29].

Motivated by these factors, a-C superlattices were synthesized and the transport properties were studied in this work. These were grown by a variety of different techniques. Bright field transmission electron microscopy was used to determine the spatial extent of the band-gap modulated layers as well as corroborating the bandgap of the different layers. Figure 1.3 (a) shows a bright field TEM image of a double barrier quantum well made from layers of predominantly sp^2 hybridized carbon (quantum well, lighter region) sandwiched between two layers of predominantly sp^3 hybridized carbon (barriers, darker layers) while Figure 1.3 (b) shows a false colour bright field TEM image of a DLC superlattice. A model was developed to incorporate the effects of structural disorder in support of experimental work.

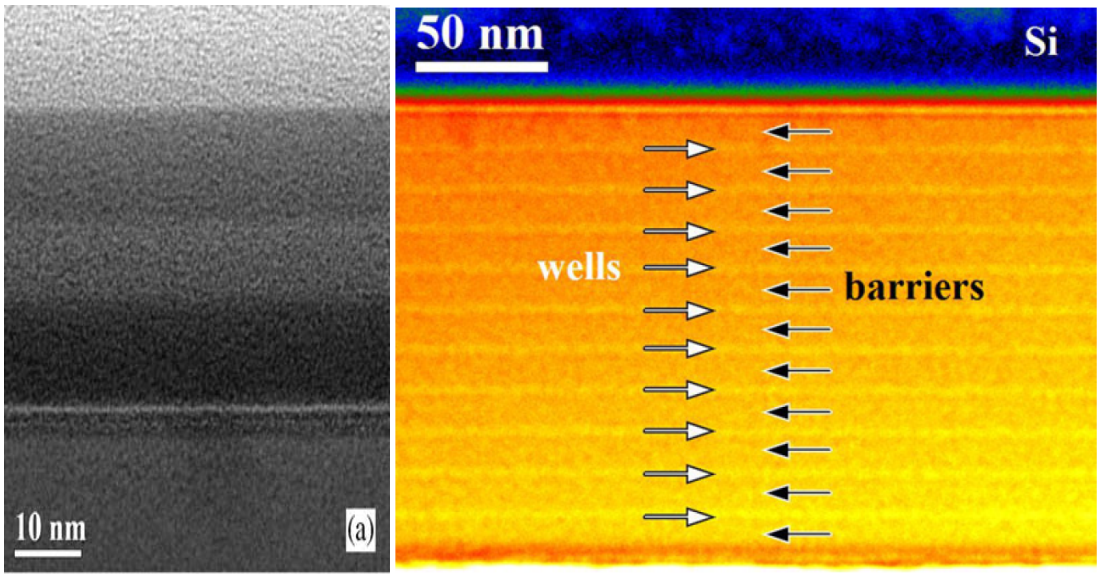


Figure 1.3: Bright field images of a-C superlattices courtesy of S.R.P Silva and V. Stolojan.

This model for resonant transmission in disordered a-C superlattices was also modified and applied to understand the transport properties of graphene-like carbon thin films. Comprehensive studies of the controlled variation of disorder in graphene are a prerequisite towards understanding and interpreting the effects of various forms of disorder in graphene and graphitic carbon thin films [30, 31, 32, 33, 34, 35, 36, 37, 38, 39]. The role of disorder in low dimensional diamond-like and graphitic carbon films should be revisited in light of the need for a new understanding of structural disorder in sp^2 hybridized carbon systems [38]. While disorder can modify the transport properties of graphene by inducing a mobility gap, it must be understood and controlled to optimize device performance [30]. Research into bilayer and multi-layer graphene is also growing rapidly under the realization of a tuneable bandgap, while control of the number of layers is of principal significance. For nano-electronic applications, it is particularly important to understand how to control structural disorder and maintain a low defect concentration in these low dimensional carbon layers [40, 41].

Disorder in sp^2 hybridized carbon systems can be estimated through Raman spectroscopy however direct transport measurements are essential to determine the influence of disorder on device performance [40]. Theoretical studies have illustrated that a disorder-induced bandgap can form in graphene [42]. In parallel, experimental studies have shown a small activation energy in graphene based weakly disordered films however a systematic study on controlling disorder in these materials deposited over a large area is yet to be reported. The application of large area graphene, whether synthesized through chemical vapour deposition (CVD) or chemical exfoliation, has so far been limited by disorder [39, 40]. The nucleation process of CVD graphene inhibits the formation of large area single crystal graphene with carrier scattering prominent at grain boundaries, limiting mobility. Chemically reduced graphene oxide films have shown semi-metallic features however residual free radicals and defects induced in the reduction process also result in carrier scattering [43].

Methods for the laser ablation of graphene were therefore developed in an attempt to overcome the inherent disorder of CVD grown and chemically exfoliated graphene. These studies showed that the number of layers could to some extent be controlled through the laser fluence however the defect concentration increases while the number of layers decreases [40]. It has been shown that the growth mechanism relies on the formation of carbon bonds to form graphene layers rather than the photo-thermal exfoliation of graphene layers. In a recent report, a progression from graphene to amorphous carbon with laser fluence was demonstrated which can be useful for probing disorder-related electronic transport in graphene as presently studied [39, 40].

Prior to graphene, the effect of disorder in diamond-like amorphous carbon and highly graphitic carbon films has been studied through combined optical and Raman studies. In hydrogenated amorphous carbon, it was shown that disorder always induces bond angle distortions which spectrally broaden the Raman G peak full width at half maximum (FWHM)

[27]. The progression with disorder from pure graphite to nanocrystalline graphite has also been studied [44]. A shift of the average G peak position to higher wavenumbers with the level of disorder was found [44]. Studies in nanocrystalline graphite also showed that the D peak intensity is related directly to the number of defects (inversely related to the inter-defect distance) [44]. These studies also showed a Gaussian distribution of the density of states around the π bonding and anti-bonding states [27]. Motivated by these dual optical and Raman studies, we have employed a tightbinding model to study the quantum transport properties of disordered superlattices formed by alternating regions of sp^2 and sp^3 hybridized carbon. In graphitic regions, the bond-length disorder reported in optical studies was incorporated through a Gaussian distribution of the hopping term. In saturated regions, we have incorporated bond-alternation which results in the formation of distinct energy bands observed in the transmission coefficient [45]. It was shown that structural disorder broadens resonant transmission peaks while reducing the transmission overall [45, 1].

In carbon materials, the effects of disorder are particularly prominent when considering the incorporation of impurities as "doping" is accompanied by structural changes [1]. Nitrogen incorporation in diamond-like carbon (DLC) films has long been studied in order to achieve shallow doping as opposed to creating the usual deep donor levels by controlling the energy levels of nitrogen centres [44, 46, 47, 48, 49, 50, 51, 52, 53, 54, 55, 56]. In contrast to conventional semiconductors, the variation of conductivity of nitrogen doped carbon with nitrogen concentration and disorder was found to be strongly non-linear [48, 49, 51]. In DLC films nitrogen incorporation initially reduces the conductivity followed by an increase, which finally saturates at high nitrogen concentrations [53, 44, 55]. The incorporation of nitrogen in confined amorphous carbon (a-C) structures was found to be limited beyond a certain concentration even if the nitrogen gas concentration during the synthesis process increases [56]. Rearrangement of carbon and nitrogen atoms is considered to be the primary cause for the increase of conductivity in these systems [44, 55, 56, 57]. However, a micro-structural transport model capable of explaining these unusual features is yet to be proposed. To interpret the level of disorder in a-CN films Raman spectroscopy was found to be useful however it requires further investigation to compare with transport properties [44].

In order to estimate the effect of the level of disorder on the electronic properties of carbon films, optical absorption and photoelectron spectroscopy has been studied extensively [53, 44, 55, 56, 57, 58, 59, 60]. Valence band photoelectron spectroscopy provides insufficient information for the development of a nitrogen-induced disorder model for a-CN films since nitrogen related peaks cannot be detected easily [58, 59, 60]. However, conduction band spectroscopy, such as near edge x-ray photoelectron spectroscopy can show the effect of disorder of nitrogen atoms which can be distinguished from the carbon peak [61, 62].

Although attempts have been made to develop devices composed of multi-layers of disordered carbon for technological applications, such as hard coatings [63] and resonant tunnel diodes [31, 62, 64, 65] there has not yet been a major theoretical study showing the en-

hanced tunnelling properties by impurity doping. Here we show how disorder at different levels can affect the transport properties of a-CN structures through a comparative analysis of the resonant transmission peaks associated with carbon and nitrogen sites. While previous studies have indicated that nitrogen can occupy a wide range of energetic positions [58, 59, 60, 63, 66], in this study we investigated the effects of the nitrogen on-site energy in relation to E_F on the transport properties in order to determine how to control device parameters.

In view of the above, investigating and understanding the tunnel transport properties of nitrogen doped DLC (N-DLC) superlattice structures is important both as a fundamental study of amorphous superlattices and towards realizing the potential of carbon superlattice devices. Thus, probing the role of nitrogen inclusion on the structural and hence the transport properties of N-DLC superlattice structures lies at the core of this study. In the present work, we have been able to illustrate enhanced resonant transmission in such structures by introducing nitrogen and controlling the microstructure. On the basis of this work, a fundamental understanding of the influence of nitrogen incorporation on the microstructure and by proxy the resonant levels, is developed and can be applied in the design of future N-DLC devices.

The influence of electron-phonon interactions, particularly coherent interactions, in molecular systems cannot be neglected [67]. Theoretical studies are forced to employ an appropriate method to treat the many-body problem. The technique of mapping the many-body variational space to a single-body multidimensional Fock space developed by Bonca and Trugman has been widely applied to study the effect on quantum transport of electron-phonon interactions [68]. Being non-perturbative, this approach can be used to study strong electron phonon coupling. The resulting Hamiltonian can then be solved using Green's functions within the Keldysh formalism [69]. This has been applied to study phonon assisted tunnelling in double barrier resonant tunnelling diodes [69] where prominent negative differential resistance was demonstrated due to the formation of resonant states in the Fock space. It was found that the transmission maximum corresponding to inelastic scattering was maximized when the incoming and outgoing scattering rates were equal [70].

Decoherence in molecular devices has been studied in detail [67]. In ideal systems, where the voltage drop might be greater than the full-width at half max of the resonance, decoherence would not significantly affect the current [67]. There is however a broadening of the transmission maxima [69] as well as additional transmission maxima when decoherence is significant. The transmission can be broken up into elastic and inelastic contributions [68]. The electron-phonon interaction modifies the transmission with satellite peaks due to inelastic scattering appearing at quantized energies corresponding to phonon eigenenergies while in elastic transmission no phonons are emitted or absorbed. If the eigenenergy of an electron in the well *after* the absorption of a phonon is the same as the incident electron energy, this results in a resonant state. Similarly if the eigenenergy in the well proceeding the

emission of an electron matches the incident electron energy this also results in a resonant state. Processes where electrons emit and then reabsorb phonons enhance the transmission as the possibility of the additional channels influences the transmission [67]. There is also a difference in the phase shift for elastic (π) and inelastic processes ($\frac{\pi}{2}$).

The role of electron-phonon interactions in metallic carbon nanotubes has been addressed [71, 72]. Transmission gaps above (below) the charge neutrality point were demonstrated for phonon emission (absorption) with significant implications for device applications [72]. A similar formalism has been applied to study the magnetoresistance and current-voltage characteristics of C_{60} molecules with ferromagnetic contacts, including the effects of the electron-phonon interaction and showed a reduction in the conductance gap [73].

The effect of time dependent gate voltages and AC fields on molecular systems and quantum dots has been widely studied [74, 75, 76]. The Floquet theory can be used to generate Hamiltonians which utilize the periodicity of the time dependence and present a more direct solution [75]. Hamiltonians of this nature can be readily combined with tight-binding Hamiltonians. This approach has been applied to carbon nanotubes, where it was demonstrated that the frequency of the AC gating can be used to tune Fabry-Pèrot interference [77], and to graphene nanoribbons where the edge effects were found to have a strong influence on interference [76]. While time dependent photon-assisted tunnelling has been widely studied [75], time dependent phonon-assisted tunnelling has received less attention and is addressed in this work.

We now discuss localization in disordered thin films and the superconductor-insulator transition. The scaling theory of localization led to the long-held belief that disorder would invariably result in localization in electronic systems confined to 2 dimensions. When silicon MOSFET devices showed a distinct metal-insulator transition, thus showing that the scaling theory of localization does not always hold true, extensive theoretical investigations followed and the interesting physics of disordered electronic systems once again drew significant attention [78]. The Hubbard model provides the necessities for such studies close to the Mott transition and the calculated temperature dependence was shown to undergo a metal-insulator transition. Many numerical studies were carried out, at first using relatively small lattices (8×8) sites due to computational restrictions [78]. With improved processing power, larger lattices have been studied.

Parallel studies of the metal-insulator transition considering Anderson disorder employed a very different approach, considering the Anderson transition as a quantum critical phenomenon [79]. This is analogous to the canonical treatment of many different inhomogeneous systems where fractal analysis has been widely used to classify the system. The central parameter in this analysis is the fractal dimension [80]. Superficially, the notion of this fractal dimension can be understood as follows. Consider an inhomogeneous, entirely random distribution of particles in a square or cube. This cube can be subdivided into smaller squares/cubes, with length l_i. The mass density is then the mean of the mass of the

particles in each region, $\langle m_i(l)\rangle$ divided by l^d where d is the dimensionality of the system.

Now assume that distribution is no longer random, rather that there are correlations between the particles which result in very large differences between the average mass in each region. In this case, the average mass density in each region is then longer proportional to l^d, it is proportional to l^{D_f-d} where D_f is defined as the fractal dimension. A system is defined as multi fractal if the fractal dimension is itself a function of some quantity.

To make progress in understanding the quantum phase transition, concepts from the Landau theory were invoked [79]. A suitable order parameter was found in the form of the density of states. The density of states vanishes in the localized phase while the order parameter becomes finite in the localized phase. In addition, the density of states exhibits power law behaviour with a critical exponent close to the transition.

Studies of the fractal dimension of the square of the amplitude of the wavefunction in 2D systems with Anderson disorder were carried out [80]. It was demonstrated that the square of the amplitude is non-homogeneous in these systems and is multifractal. There is therefore a relatively wide distribution of wavefunction amplitudes across the system. Multifractality is a signature of criticality brought about by the Anderson localization and implies anomalous scaling of moments and correlation functions of the wavefunction amplitudes. The spectra of multifractal exponents allows two universality classes to be distinguished.

A more extensively used approach is to employ the mean field theory. While the mean field theory can be applied to calculate local quantities such as the local superconducting pairing amplitude, local occupation number and the local density of states, the extension of the mean field theory to an inhomogeneous system with quantum phase fluctuations was long a subject of debate. The determination of whether a system is insulating, metallic or semiconducting was studied by Scalapino *et al.* [81]. They considered the kinetic energy term of a tight binding Hamiltonian within the Hubbard model. A superfluid weight D_s (defined as the ratio of the superfluid density to the mass) was defined in analogy to the Drude weight D which is determined by the current response of the kinetic energy term of the tight-binding Hamiltonian to a transverse external potential $A_x(\mathbf{q},\omega)$ applied for example in the x direction. It was shown that the infinite wavelength, zero frequency limit of the linear response (Kubo) function [82]

$$\langle j_x(\mathbf{q},\omega) = -e^2(\langle -k_x\rangle - \Lambda_{xx}(\mathbf{q},\omega))A_x(\mathbf{q},\omega) \tag{1.3}$$

determines whether a system is insulating, metallic or superconducting. The local kinetic energy density, $k_x(\mathbf{r}_i)$ considering a vector potential applied in the x direction is given by

$$k_x(\mathbf{r}_i) = -\sum_{\sigma}(t_{i,i+x}c^{\dagger}_{i,\sigma}c_{i+x,\sigma} + H.c) \tag{1.4}$$

while the paramagnetic component of the current density is

$$j_x^p(\mathbf{r}_i) = i\sum_{\sigma}(t_{i,i+x}c_{i,\sigma}^{\dagger}c_{i+x,\sigma} - H.c) \ . \tag{1.5}$$

The paramagnetic component of the superfluid density is given by the current-current correlation function

$$\Lambda_{xx}(\mathbf{q}, i\omega_n) = 1/N\int_0^{\beta} d\tau e^{i\omega_n\tau}\langle j_x^p(\mathbf{q},\tau)j_x^p(-\mathbf{q},0)\rangle \tag{1.6}$$

In the zero temperature, low disorder limit the ground state is expected to be a superconductor if the bulk behaviour of both D and D_s are finite, an insulator if D_s and D are both finite and a metal if D_s is zero and D is finite [81]. The ground state of the half-filled repulsive Hubbard model was found to be insulating, crossing over to a metal at higher filling. On the other hand, the ground state of the attractive Hubbard model was found to be superconducting [82]. Expanding this analysis, the influence of disorder was subsequently studied.

Widespread theoretical work within the inhomogeneous Bogoluibov-de Gennes (BdG) theory has focused on the effect of disorder in the transition out of the superconducting phase [83, 84, 85, 86, 78, 87, 88]. The bulk of the initial work was concerned with spacial inhomogeneities in the superconducting phase across disordered regions. The primary question was whether or not superconductivity persisted across the transition. Ghosal *et al.* allowed non-uniform spacial variation of the pairing amplitude and found that the spectral gap remains finite even when large Anderson disorder is considered [83]. Locally, the BdG analysis showed that disorder resulted in a non-uniform distribution of the local pairing amplitude [83]. With increasing disorder, it was shown that these regions agglomerate into smaller and smaller superconducitng droplets [83, 84].

It was illustrated that the disordered system breaks up into superconducting islands, separated by non-superconducting regions which may even be insulating. The formation of short-range Cooper pairs was shown to remain favourable in some regions while Cooper pairs could not form in others [83, 84]. Studies were also spurned by short pairing correlations of high T_c superconductors. The attractive Hubbard model was implemented in a number of studies with disorder primarily in the form of local fluctuations in the on-site energy term. With the realization that superconductivity persisted in some regions, the transition from BCS superconductor to local regions of Bose-Einstein Condensate (BEC) was studied in some detail. Recent experimental work has shown that fermionic transitions in some superconductors may also occur.

In subsequent work, the inhomogeneous BdG theory has shown significant overlap with experimental measurements [89]. This illustrates that while the interaction is treated within the mean field, mean field calculations still give local information which is qualitatively

accurate. The rigidity of the superconducting phase in regions of a material is characterised not only by the local pairing amplitude but also by the phase coherence across connected regions. It is therefore imperative to study the superfluid density which is a measure of the phase rigidity of the superconducting state. While diagonalization within the inhomogeneous BdG theory is sufficient to study the transition, Monte Carlo simulations have been studied in conjunction and have shown significant overlap [89].

The specific role of structural disorder has been studied in less detail. The influence of structural disorder in generating a BCS-BEC crossover was studied by Dey and Basu [90]. In the case of structural disorder, the transition out of the superconducting phase was claimed to be of a fermionic nature rather than a bosonic transition. The reason cited was increased delocalization due to modification of the hopping parameter as the disorder level increases. In particular, the carrier density was found to be significant in the crossover from BCS to BEC. The distinction between the BEC and the local pair phase was studied in detail.

The multi-faceted physics of the superconductor-insulator phase transition has also spurned many experimental studies due to the stark contrast between these opposing states [91, 92, 93, 94, 95, 96]. The superconductor-insulator transition in disordered and granular superconductors is strongly influenced by quantum fluctuations [91]. Strong Coulomb interactions are often found in such systems, leading to the Anderson-Mott transition [95]. The prediction that the pairing amplitude and spectral gap would only slightly decrease in the presence of moderate disorder (usually referred to as the Anderson theorem for dirty superconductors) was widely studied both theoretically and experimentally [97] however it was found that Coulomb interactions strongly suppress Cooper pairing.

In granular superconductors, unexpected local maxima in magnetoresistance measurements were found in granular Al-Ge films (which are more homogeneous than many other granular superconductors) as well as enhancements of the resistance in the insulating state due to localized superconducting regions [98]. Detailed theoretical work confirmed that this is due to a suppression of the tunnelling current which arises when superconductivity across the grain boundaries breaks down while the grains remain superconducting [99, 100]. The interplay between Josephson coupling and the charging energy of the grains plays a crucial role in the transport properties. The fluctuation of Cooper pairs introduces a new charge channel which also contributes significantly (the Aslamazov-Larkin contribution). In addition the Maki-Thompson contribution, which has localization-like characteristics, arises due to the scattering of Cooper pairs from electrons in the normal phase [99].

A long-standing puzzle was whether or not Cooper pairs would be localized during the superconductor-insulator transition or whether superconductivity would break down first, leaving behind localized electrons. The bulk of the theoretical work, using the inhomogeneous Bogoliubov-de Gennes theory and eigenfunction multi-fractal analysis, suggested that Cooper pairs would become isolated within superconducting regions. Indirect evidence was well established in the form of a sharp local maximum in magnetoresistance which was found

in many granular superconductors, arising due to suppression of tunnel arising as a result of remnant superconductivity within grains despite the breakdown of global superconductivity. However direct experimental evidence in disordered (but not granular) superconductors remained elusive until scanning transmission spectroscopy of disorder InO films clearly showed a loss of coherence peaks while a gap persisted, confirming the persistence of Cooper pairs [93].

The role of vortices is also of great interest in these systems [91, 101]. In $2D$ superconductors, the phase transition out of the superconducting phase occurs through a Berezinskii-Kosterlitz-Thouless (BKT) transition [102]. The superconducting BKT transition is an analogy to the 2D X-Y model [103]. In $2D$ superconductors, vortices are bound to anti-vortices. The free energy diverges logarithmically with the distance between these vortex anti-vortex pairs. At the BKT transition temperature, the entropy is the same as the free energy. Above the BKT transition temperature, this binding breaks down and vortex-anti-vortex pairs begin to drift through the superconductor, creating dissipation. This transition is particularly interesting in granular superconductors and 2D arrays of Josephson junctions [101].

1.2 Outline

In Chapter 2 the experimental techniques used in this work are presented. The growth conditions of DLC superlattices and B-NCD devices used in this study, which were provided by the University of Surrey and the University of Hasselt respectively, are outlined.

In Chapter 3, resonant transmission in DLC superlattices is studied. The effect of nitrogen incorporation on the transmission coefficient of DLC superlattices is then investigated. The influence of disorder in thin graphitic films is studied theoretically and compared with measurements on graphitic films with different levels of disorder. Finally, the I-V characteristics of nitrogen incorporated disordered DLC superlattices are calculated and compared with measurements.

Chapter 4 presents analysis of the influence of the electron-phonon interaction in molecular chains. The transmission coefficient of single quantum wells is studied. The influence of the electron-phonon interaction on the transmission coefficient of molecular devices under a time-dependent gate potential is then studied. The influence of different parameters such as the strength of the electron-phonon coupling, the frequency of the external gate potential and different phonon modes are studied.

In Chapter 5, the influence of disorder on superconductivity is studied through the Bogoliubov de Gennes theory and applied to boron doped diamond. We focus primarily on structural disorder, comparing and contrasting the effects of structural and on-site disorder. The local and mean pairing amplitudes are studied as well as the density of states, corre-

lation functions and superfluid density. The effects of structural disorder are isolated and comparisons are made with measured characteristics.

In Chapter 6, measurements on superconducting B-NCD samples with different microstructures are studied in the region of the transition temperature to reveal the rich physics at play in the region of the superconductor-insulator transition.

Finally, in the appendix measurements of two different configurations of superconducting spin valves are presented.

Chapter 2

Experimental Procedures

2.1 Sample Preparation

2.1.1 DLC Superlattices

DLC superlattice structures were provided by S. J. Henley, S. Bhattacharyya and S. R. P. Silva, University of Surrey. They were grown on a highly doped Si substrate by ablation of a graphite target using a 248 nm pulsed ultraviolet excimer laser (Lambda Physik LPX 210i) at a chamber pressure of 10^7 mbar. Alternating layers of predominantly sp^3 hybridized carbon and layers with a smaller $sp^3 - C$ percentage were achieved by varying the laser fluence. Alternating layers show significantly different bandgaps (85 % sp^3, 2.8 eV (barrier layer of DLC) and 50 % sp^3, 1.5 eV (well layer)). Gold contacts were evaporated onto the surface of the superlattice devices (providing one point of contact) while silver paste was used to contact the bottom of the superlattice devices. Details of the growth and characterization of the devices is given in references [104, 105, 51].

2.1.2 Boron-doped Nano-crystalline Diamond

B-NCD samples were provided by Dr. Vaklav Petrak and Prof. Milos Nesaldek, University of Hasselt. Samples were grown using microwave plasma enhanced Chemical Vapour Deposition (MPE-CVD). Boron was incorporated using trimethyl boron ($B(CH_3)_3$) in the chamber with CH_4/H_2 plasma. The B/C ratio of the trimethyl boron was kept constant while the concentration of the CH_4 in the plasma was varied to change the grain sizes of the grains in the B-NCD samples. The methane ratio also changes the concentration of boron incorporated into the diamond grains. Details of the growth and characterization of the samples studied here can be found in reference [106, 107, 108].

Samples with two different concentrations of methane in the CH_4/H_2 plasma were studied. The first set of samples was grown with a CH_4 concentration of 1% (the plasma

consisted of 99% H_2). These samples had average grain sizes of around 70 nm and the total concentration of boron incorporated into the films was found to be 3.3×10^{21} cm^{-3} by Hall measurements [106].

The second set of samples was grown with a CH_4 concentration of 5% (the plasma consisted of 95% H_2). These samples had average grain sizes of around 45-50 nm and the total concentration of boron incorporated into the films was found to be 5.3×10^{21} cm^{-3} by Hall measurements [106].

Electrical transport measurements were performed using a Cryogenic Free Measurement system at temperatures ranging from 0.3 K to 150 K and magnetic fields between 0 and 12 T. Magnetoresistance and voltage-current (V-I) measurements were performed in the van der Pauw configuration and taken at 0.3 K from -200 uA to 200 uA at field intervals of 0.25 T.

2.2 Transport Measurements

Two terminal current-voltage ($I - V$) measurements were performed on the DLC superlattices under high vacuum in a Janis free flow cryogenic micro-manipulated probe station. The system was evacuated using an Edwards turbo-molecular pump down to approximately 10^{-6} *torr* at room temperature overnight. The sample heater was then set to room temperature while cryogen was circulated through coils (isolated from the vacuum) surrounding the sample stage. This promotes the removal of atmospheric adsorbate surface and ensures that any condensation from residual moisture within the chamber does not condense on the sample surface. The reduction in temperature as the cryogen circulated through coils within the chamber facilitated cryo-pumping down to a base pressure of approximately 10^{-8} *torr* which was maintained throughout the experiment. The sample mount inside the cryostat is also shielded from radiation with a platinum radiation shield. A thin layer of thermally conductive grease was used to ensure sufficiently rapid transfer of thermal energy applied to the sample mount (chuck). The sample temperature was controlled with a Lakeshore 336 Temperature Controller, with a cernox sensor located directly below the sample on the sample chuck. The micro-manipulated probes are manufactured from tungsten due to its high electrical conductivity and the probe assembly is engineered for high accuracy low noise measurements. The entire assembly rests on a passive pneumatic vibration isolation table which protects devices and probe tips as the probes are manoeuvred into position to make contact with the micro-structure.

The electrical properties were analysed using an Agilent Semiconductor Device Analyser. The analyser combines source monitor units and allows for the application and measurement of bias and current. The system is designed for low current measurements with a resolution of approximated 1 pA in the two-probe configuration. Current voltage sweeps

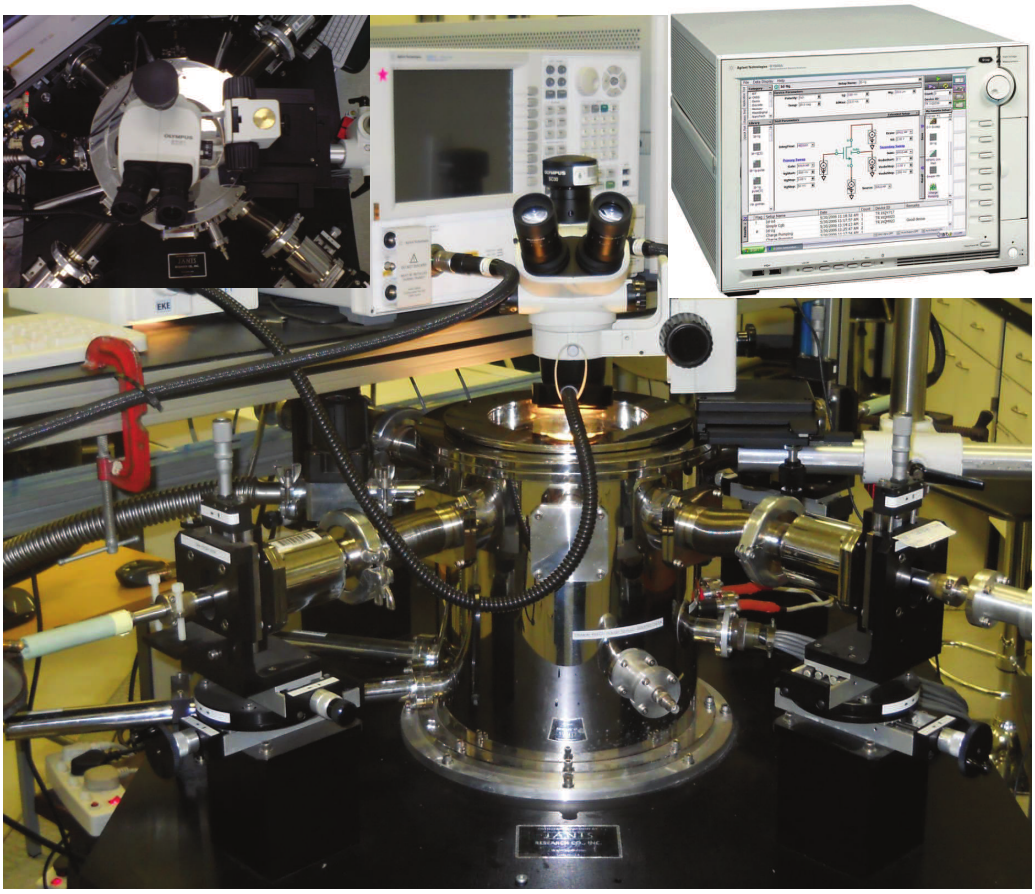


Figure 2.1: Janis micromanipulated probe station. Upper left inset: Viewed from above. Upper right inset: Agilent B1500A Semiconductor Device Analyser.

were programmed within Agilent's custom software. The potential was varied from -2 V to 2 V while the current was recorded. The semiconductor device analyser has been interfaced with the temperature controller via GPIB so that the temperature can be controlled and recorded while simultaneously recording $I-V$ measurements. A number of sequences were programmed by the author to automate the reading of $I-V$ measurements with temperature. The resistance is then available over a wide range of potentials which aids in interpretation of the transport properties. Concurrently, the flow of cryogen was carefully controlled by adjusting the pressure of the dewar and the flow valve of the transfer line. Although the temperature controller was programmed for maximum stability within the Agilent software, the temperature stability was constantly monitored and the cryogen flow adjusted accordingly to ensure accuracy during the duration of each $I-V$ measurement. Measurements on DLC superlattices were performed in the two-probe configuration.

Four probe transport measurements were performed on the B-NCD samples. Contacts were made using a combination of silver paste and wire bonding. Measurements were performed in the van der Pauw configuration using a cryogenic free measurement system of Cryogenic Ltd. design. The system relies on two closed-cycle refrigeration stages. A compressor (cooled by an external chiller) cools helium gas to 40 K in the first stage relying on the rapid expansion of helium gas to reduce thermal energy. In the second stage, helium gas

at 40 K is injected into an evacuated cryostat and driven by an external oil-free pump. The helium gas is further cooled to 4 K where it condenses to the liquid phase. In the second stage, excess thermal energy is dissipated in an external helium dump. Inside the cryostat, liquid helium is collected and further cooled to approximately 2 K by decreasing the vapour pressure using an oil free pump while the flow is controlled using a needle valve. This cooled helium is then circulated around the sample chamber, which is referred to as the variable temperature insert (VTI). The VTI is in thermal contact with the circulating cryogen while it is otherwise isolated. A vacuum is therefore created inside the VTI before the sample is lowered into the VTI. Using a closed cycle 3^He probe, 3^He can be liquefied. A sorption pumb decreases the vapour pressure until the sample reaches 300 mk. Controlling the temperature between 300 mK and 1.8 K is very difficult. For the experiments performed in this work, the PID settings had to be manually configured however excellent thermal stability was achieved with variations of around than 10 mK over the range of magnetoresistance and $I-V$measurements .

Samples were mounted on probes which were lowered into the VTI. At the top of the VTI, a series of O-rings allows a vacuum to be maintained within the VTI while the probe is lowered into the VTI. The upper section of the VTI (isolated using a gate valve) was flushed with helium gas, then evacuated with a rotary pump and the process was repeated for at least 5 minutes to ensure that any residual gas in the VTI would be a small amount of helium. After the final flush with helium gas, the VTI was evacuated, the gate valve was opened and the probe was lowered while the rotary pump maintained the vacuum.

Transport measurements were performed using a Keithly 2400 to source current and a Keithly 2182A nano-voltmeter to measure voltage in the four probe configuration. The K2400 and K2182A were connected to a breakout box which was connected to the probe via a 16-pin connector.

The sample temperature was controlled using a Lakeshore 340 temperature controller. The cryogenic system is controlled using Labview software which controls the temperature and Hall measurement systems (K2400 and K2182A) simultaneously and measurements were automated by programming sequences to control the virtual instruments within the Labview software. Resistance versus temperature measurements were recorded from 2 K to room temperature while magneto-resistance measurements were performed up to 12 T using a superconducting magnet (power supply also provided by Lakeshore). Carlibated cernox temperature sensors were used.

Some measurements on B-NCD samples were also performed in am Oxford free flow helium cryostat. Electrical measurements were carried out using a Keithly 2600 source meter and a Keithely 2182 voltmeter while electrical noise was reduced by using noise filters. The temperature was controlled using a Lakeshore 340 temperature controller.

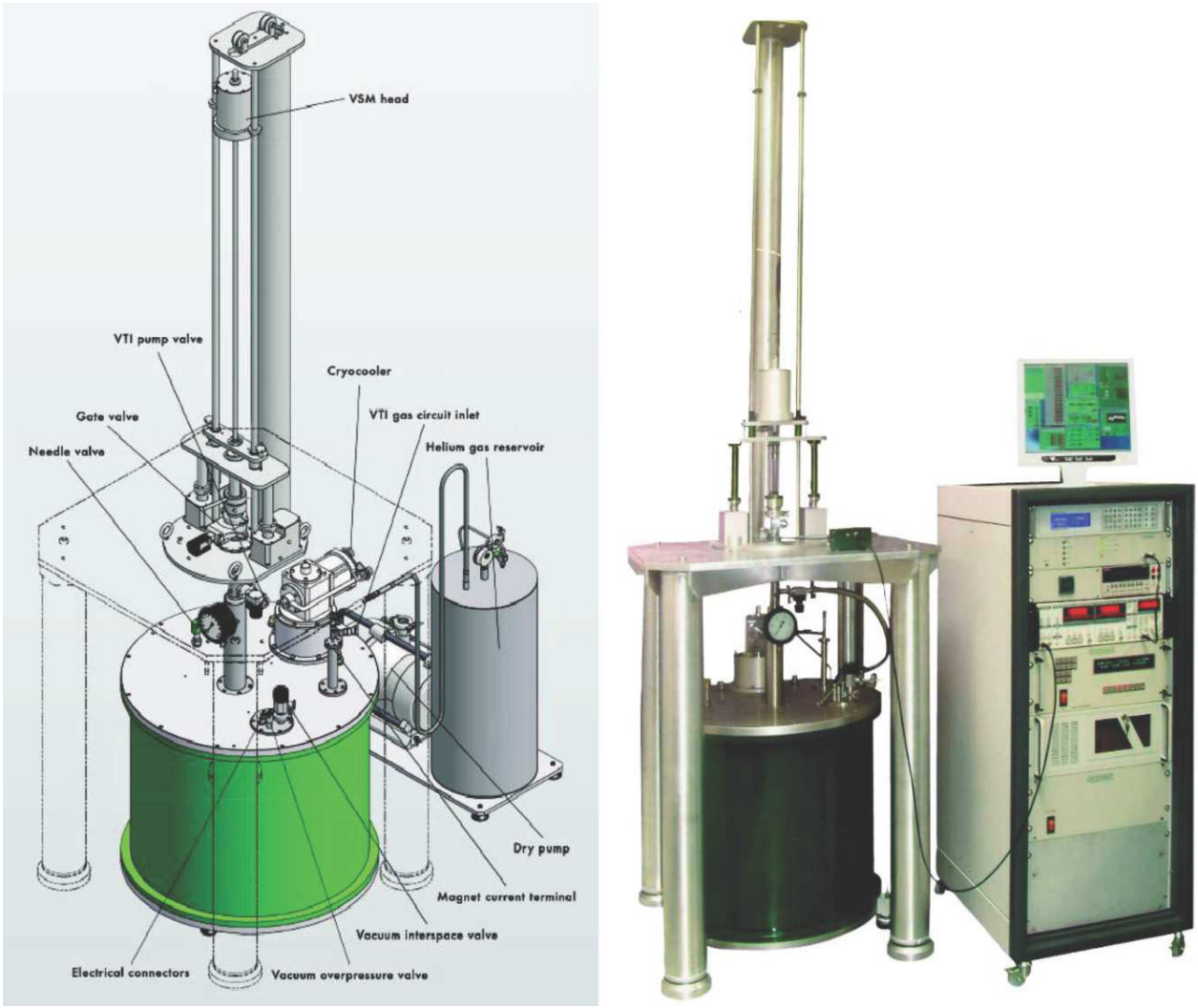


Figure 2.2: Cryogenic free measurement system.

Chapter 3

Resonant Transmission in Diamond-like Carbon Superlattices

Negative differential resistance was demonstrated in disordered diamond-like carbon (DLC) superlattices at low temperatures. These measurements were supported with calculated current-voltage (I-V) characteristics based on a model tailored for disordered carbon superlattices. This tandem approach explained why the properties of DLC superlattices cannot be tuned in the same way as conventional superlattices and provides a guide for growing structures with specific characteristics. This model was then extended to understand the transport properties of disordered thin graphitic carbon films where the degree of disorder was correlated with changes in the localization length. Enhanced transport properties and confinement was then demonstrated through nitrogen incorporation in DLC superlattices and calculated I-V characteristics were compared to measurements on nitrogen incorporated a-C superlattices.

3.1 Introduction

3.1.1 DLC Superlattices

Amorphous superlattices, known to be advantageous in overcoming the lattice mismatch problems of crystalline semiconductors, have long been studied towards developing high-speed oscillators and detectors [109]. However while resonant transmission is well understood for crystalline materials, disorder complicates the conventional concept of resonance in amorphous superlattices as the eigenenergies are no longer well defined. Pushing the limits of device miniaturization, molecular electronic devices have generated significant interest [110, 111]. Of particular interest is the origin of the negative differential resistance found in these systems which is still under debate [110, 112, 113] due to the inherent uncertainty in isolating the effects of Coulomb interactions between charge carriers, the electron-phonon interaction and quantum interference effects.

Bridging these fields are amorphous carbon (a-C) superlattices which are formed through alternating regions of diamond like carbon (predominantly $sp^3 - C$) and more graphitic carbon (with a much lower percentage of $sp^3 - C$). This is unlike conventional band-gap engineered superlattices which rely on dopants to modulate the band structure. In a-C superlattices, molecular chains and aromatic ring clusters often form within the superlattice structure [51, 114]. With a wide range of attractive properties, such as high mechanical strength and wear resistance, high breakdown voltage [105, 2], excellent thermal conductivity and fast-switching capabilities [104] along with bio-compatibility, amorphous carbon superlattice devices would facilitate a new class of robust devices. Quantum confinement has been firmly established in these disordered superlattice structures [115] which showed evidence of negative differential resistance (NDR) [116, 117, 118]. a-C double barrier structures showed a greater peak to valley ratio as well as demonstrating high frequency performance capabilities up to 110 GHz and bias-related hysteresis in the current-voltage characteristics [104]. In addition, quantized conductance features were demonstrated which is strongly suggestive of filamentary channels through the superlattice [104].

The role of bond aspect ratio and disorder on the transmission coefficient of disordered carbon superlattices has been addressed using a tight binding model for disordered superlattices [45, 1]. This model was extended to relate the changes in localization length with disorder in thin graphitic films grown by laser ablation [119], successfully relating structural changes due to disorder to transport properties. Recently, this model was applied to interpret measurements of nitrogen incorporated a-C superlattices. This work illustrated the effects of carbon networks (chains) forming within the superlattice which results in bond-alternation in the $sp^3 - C$ regions which was included in the calculations [2].

Here we study the I-V characteristics of a-C superlattices at different temperatures. Negative differential resistance is demonstrated in a-C superlattices with different microstructures. We interpret these effects using a $1D$ tight-binding model for structurally disordered superlattices with structural disorder included through a Gaussian distribution of the hopping integral about some mean value. By modelling different configurations, we illustrate that the barrier potential dominates over other factors (such as the barrier or well width) and can be used in tailoring the properties of future devices.

We then apply this disorder model to thin graphitic films to interpret the role of disorder on the activation energy of thin graphitic layers grown through laser ablation and interpret the mechanism of disorder induced localization. We illustrate a correlation between the disorder level and activation energy in these films which would be useful for electronic device applications. This study is related to our previous theoretical studies as the chemical vapor deposition (CVD) laser assisted technique employed here allows the role of structural disorder, principally in the form of bond-angle and bond-length distortions in the graphitic phase, to be studied while defects act as potential barriers.

Nitrogen inclusion has been shown to enhance the conductivity of carbon thin films

[120, 121, 122]. This makes it an attractive "dopant" to enhance the transport properties of DLC superlattices. However nitrogen inclusion does not simply have the same effect as increasing the concentration of donor atoms, as is the case in conventional semiconductors. Nitrogen inclusion modifies the microstructure of carbon films significantly [52, 122, 123, 124]. Resonant transmission is most influenced by the microstructure of the superlattice so it is essential to include the concurrent change in microstructure when considering nitrogen inclusion in DLC superlattices. Hence we study the effects of nitrogen incorporation in DLC superlattices

3.2 Model

Due to the high affinity of carbon structures to form bonds with different configurations, a-C superlattices are inherently structurally disordered in the form of non-uniform bond lengths within the superlattice structure. The bond length can be directly related to the hopping integral through a bond-length deformation potential [125, 1]. We therefore model the effects of structural disorder through a Gaussian distribution of the hopping integral about some mean value. We consider a tight-binding model of a quasi 1-D disordered carbon superlattice given by

$$\mathcal{H} = \sum_n \epsilon_n c_n^\dagger c_n - \sum_{\langle n,m \rangle} t_{n,m} c_{n,m}^\dagger c_{m,n} + H.c. \tag{3.1}$$

where ϵ_n is the on-site energy, $c_n^\dagger$ (c_n) is the fermion creation (annihilation) operator, $t_{n,m}$ is the hopping integral taken over nearest neighbours. We then solve the discretized Schrödinger equation at each site given by

$$E\psi_n = \epsilon_n \psi_n - t_{n+1,n}\psi_{n+1} - t_{n-1,n}\psi_{n-1} \ . \tag{3.2}$$

To determine the transmission coefficient we determine the incoming wave amplitude A and define the transmission coefficients as $T(E) = \frac{1}{|A|^2}\frac{\sin k_l}{\sin k_r}$, where k_r is an outgoing wave vector at the right lead (which is assumed to be an outgoing plane wave) and k_r is the incoming wave incident on the left lead. The transmission coefficient is then integrated using the Landauer-Büttiker formula to calculate the current-voltage (I-V) characteristics

$$I(V) = 2e/h \int_{-\infty}^{\infty} T(E,V)(f_L(E,V) - f_R(E,V))dE \tag{3.3}$$

where $f_{L(R)}$ is the Fermi function of the left (right) lead.

In the $sp^3 - C$ regions, we also consider the possibility of bond alternation. This is a common feature in conjugated polymers and carbon networks [2] and results in significant

variation of the hopping integral between adjacent lattice sites [125] due to significant bond angle distortions.

Transmission coefficients were calculated in Mathematica and were numerically integrated in MATLAB to get I-V characteristics.

3.2.1 The incorporation of disorder

To identify the predominant form of disorder of the layers which make up the DLC superlattice, we rely on the large body of work on individual a-C layers and thin films. Structural disorder, predominantly in the form of bond-length and bond-angle disorder, is inherent to a-C films as carbon can readily form a number of different structures [52, 27, 126]. This results in a wide berth of bond length and bond angle distortions. These distortions result in changes of the hopping integral between nearest neighbours in the lattice. Extensive experimentation has shown that this is particularly prevalent in the $sp^2 - C$ regions in DLC superlattices [126, 48].

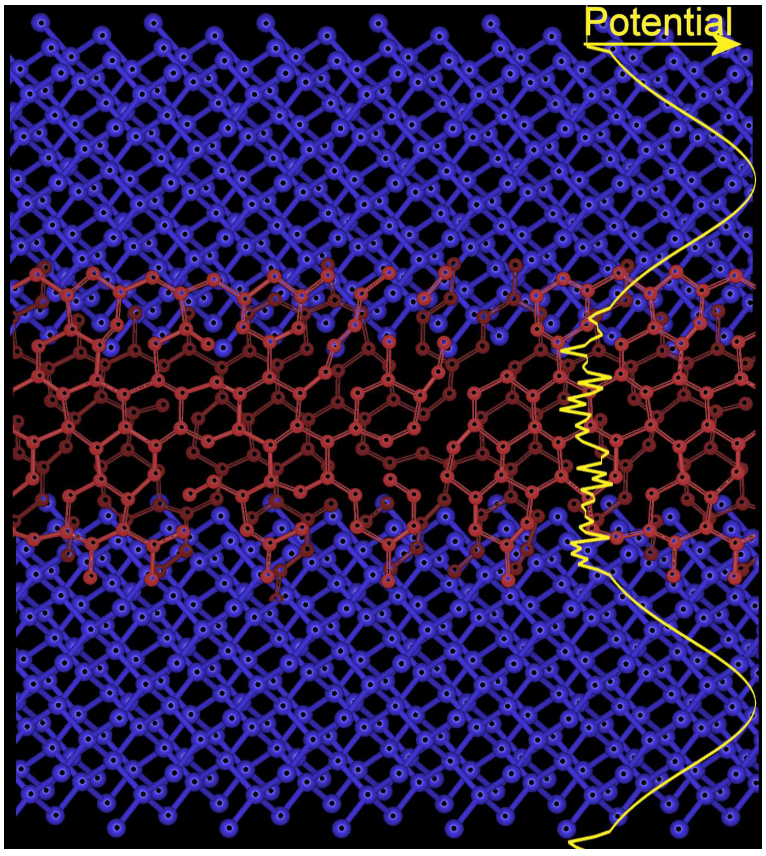


Figure 3.1: An atomic scale schematic diagram of the quantum well formed by a predominantly $sp^2 - C$ well (maroon atoms) embedded within two predominantly $sp^3 - C$ barriers (blue atoms). The potential is overlain in yellow.

The degree of structural disorder is characterized by the ratio of the intensity of the D and G peaks of Raman spectra (I_D/I_G ratio) and the G peak position. Many studies have

characterized the level of disorder in a-C carbon thin films using this ratio and correlated it with the optical bandgap and the transport gap. From these studies, the level of structural (bond length) variation can be related to the average variation of the hopping parameter in the $sp^2 - C$ regions through a deformation potential which relates changes in distance between the individual atoms to changes in the tight-binding hopping integral. Experimentally it is well established that the variation of bond lengths follows a Gaussian distribution about some mean bond length. The hopping integral in the sp^2 hybridized regions therefore follows a Gaussian distribution about the mean value for sp^2 hybridized carbon. The full width at half maximum (FWHM) of the Gaussian distribution of bond lengths can be approximately extracted from the experimentally determined distribution of bond lengths and related to the hopping integral via the deformation potential.

Figure 3.1 is an atomic-scale diagram of a DLC quantum well formed by a layer of predominantly sp^2 hybridized carbon sandwiched between two layers of predominantly sp^3 hybridized carbon. A schematic of the potential in these regions is shown in yellow. The potential in the $sp^2 - C$ regions is lower than the potential in the $sp^3 - C$ regions so confined eigenstates are expected to form in the $sp^2 - C$ regions. The potential in the sp^2 hybridized region does not vary smoothly from site to site, it follows the Gaussian distribution discussed earlier. The atomic-scale diagram shows the variation in the bond lengths determined by the disorder parameter used in the calculations. Vacancies are also included which are known to be found in $sp^2 - C$ regions. Two graphene layers are shown in Figure 3.1 for clarity however many layers are likely to form during deposition.

The interface between the sp^2 and sp^3 hybridized regions is not smooth as either form of bonding can occur at the interface. sp^2 hybridized carbon regions therefore stretch into the $sp^3 - C$ regions, with both allotropes found simultaneously. We therefore assume that the potential follows a Gaussian form across the interface in order to simulate this disordered interface (see for example [127]). The sp^3 hybridized regions are represented as crystalline diamond as we assume that there are no $sp^2 - C$ inclusions in these regions. A schematic diagram of the measured superlattice structures and the corresponding potential used for the calculations is shown in Figure 3.2 where the bottom lead, formed by the heavily doped silicon injector, is displayed in grey. A potential different shifts the chemical potential across the device as shown in Figure 3.3.

3.3 Diamond-like Carbon Superlattices

3.3.1 Measured Transport Properties

Details of the device preparation and the measurement system can be found in experimental section of this thesis. Figure 3.4 shows the I-V characteristics of a DLC superlattice with 3 wells of width 7 nm and 4 barriers of the same width. There is a small region of

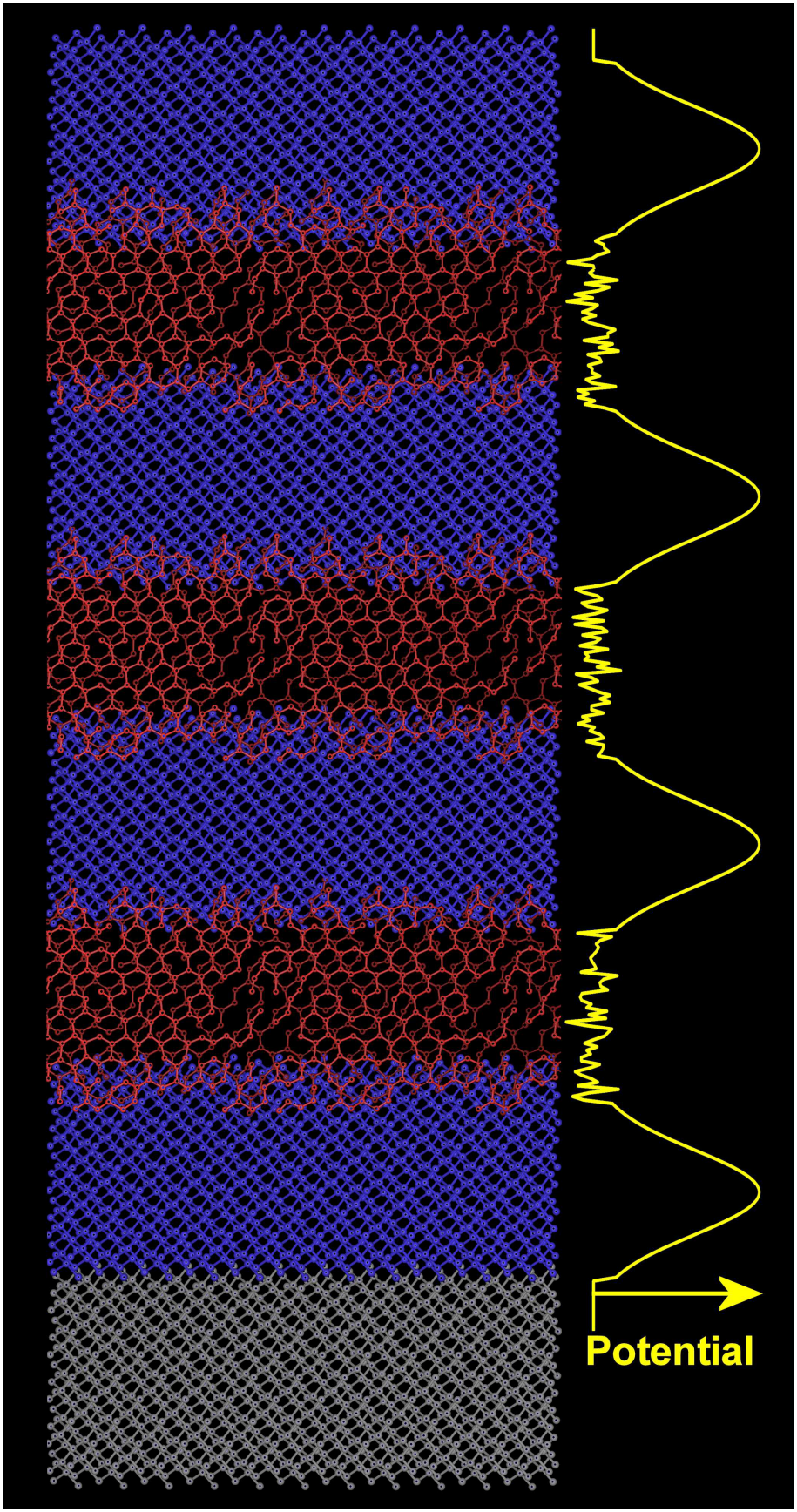


Figure 3.2: An atomic scale schematic diagram of the quantum superlattice formed by alternating layers of predominantly $sp^2 - C$ well (maroon atoms) embedded within two predominantly $sp^3 - C$ barriers (blue atoms). The potential is overlain in yellow.

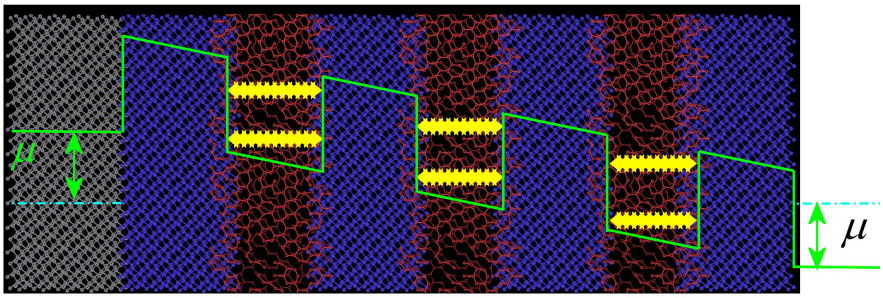


Figure 3.3: An atomic scale schematic diagram of the quantum superlattice formed by alternating layers of predominantly $sp^2 - C$ well (maroon atoms) embedded within two predominantly $sp^3 - C$ barriers (blue atoms). The chemical potential across the device is shown in green.

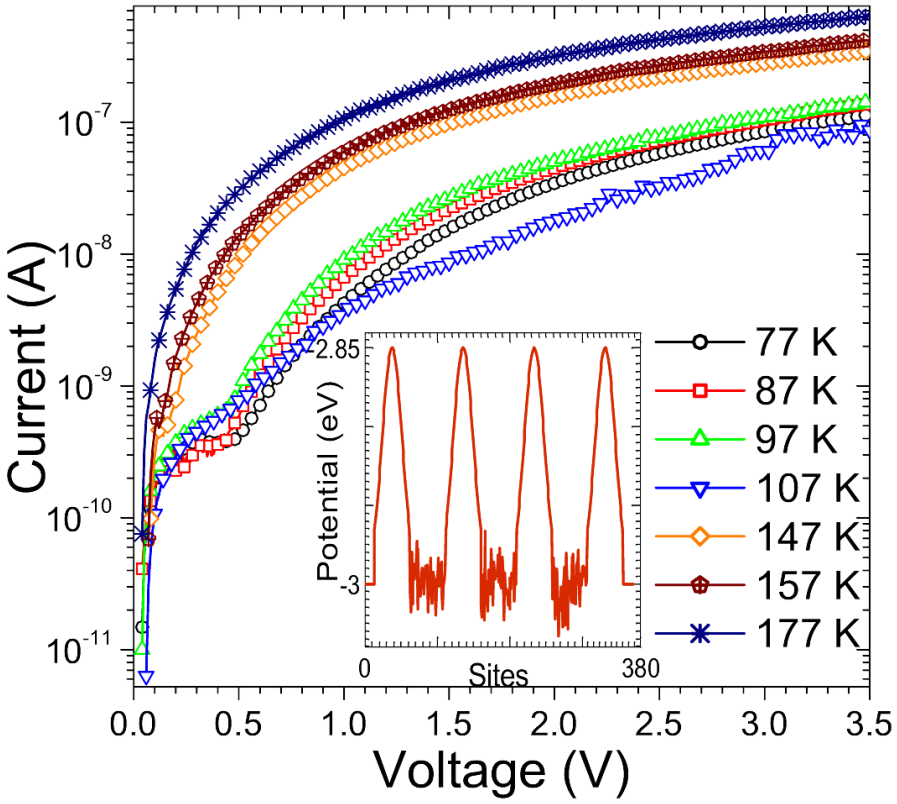


Figure 3.4: Current-voltage characteristics of a DLC superlattice with 4 barriers of 7 nm and 3 wells of 7 nm. Inset is the hopping term at each lattice site.

current suppression at around 0.4 V, indeed showing slight negative differential resistance at low temperatures. The symmetry between the barrier and well width favours resonant transmission (see calculations later on). The temperature dependence is as expected for a quantum superlattice structure, showing no sign of NDR or current suppression when the temperature is increased such that thermionic emission prevents quantum confinement.

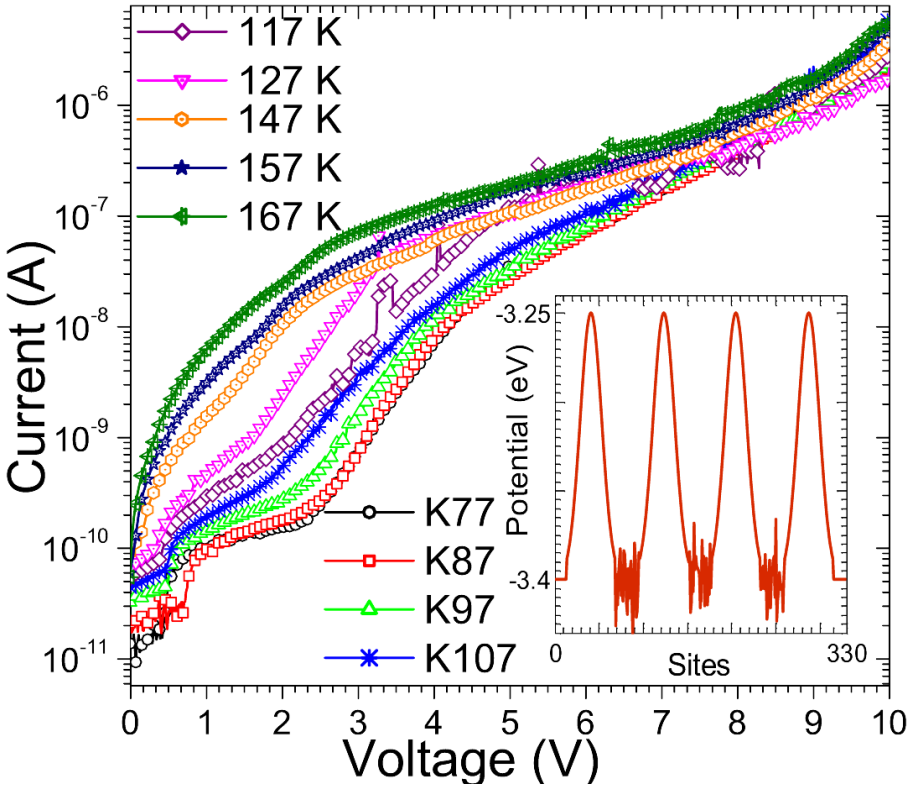


Figure 3.5: Current-voltage characteristics of a DLC superlattice with 4 barriers of 7 nm and 3 wells of 4 nm. Inset is the hopping term at each lattice site.

Figure 3.5 shows the I-V characteristics of an amorphous carbon superlattice structure with 3 wells of width 4 nm and 4 barriers of width 7 nm. At low temperatures, there is strong suppression of the current until a sharp increase in the current at 0.8 V followed by prominent saturation of the current up to approximately 2.4 V. With increasing temperature, this feature shifts to lower potentials due to the increased thermal energy of charge carriers and broadening of the distribution of energies. This is indicative of resonant transmission despite the inherent disorder, pinholes and channels in the material. However there is insufficient confinement to result in negative differential resistance. Instead a wide range of resonant energies form a broad region of current suppression.

The I-V characteristics for a superlattice with 3 wells of width 2 nm and 4 barriers of width 8 nm are shown in Fig. 3.6. At low temperatures, there are two clear step-like features. At 87 K, the first occurs at around 1.5 V while the second is found at around 2 V. There is also an additional step at high potentials (around 5.2 V at 87 K). The first step-like feature shows slight NDR which persists up to 146 K. This feature is less sensitive to temperature than the features in other devices, consistent with the enhanced confinement

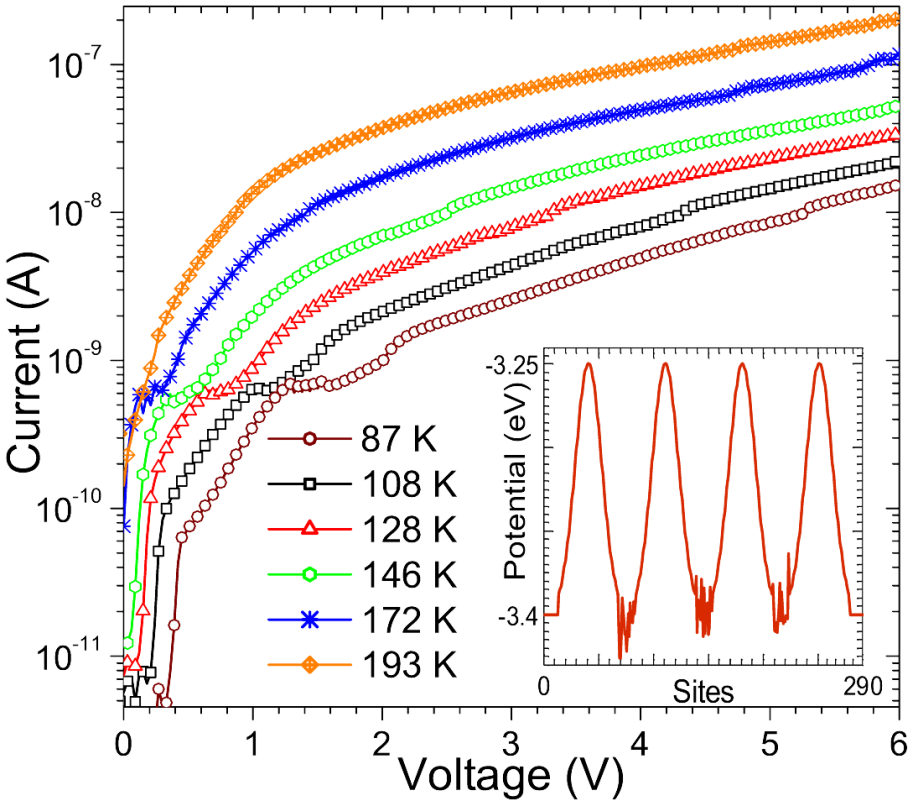


Figure 3.6: Current-voltage characteristics of a DLC superlattice with 4 barriers of 8 nm and 3 wells of width 2 nm. Inset is the hopping term at each lattice site.

which would be expected for a thicker barrier. Despite the large difference between the widths of the quantum wells of this device and the previously discussed device, the resonant transport features are quite similar.

3.3.2 Calculated Current-Voltage characteristics

Figure 3.7 shows the I-V characteristics calculated for an a-C superlattice with four barriers with a width of 7 nm and three wells of the same width, to be compared with the device shown in Figure 3.4 (the profile is shown in the inset of Fig. 3.4). A schematic diagram of the disordered DLC superlattice is shown in Figure 3.2. The relatively ordered sp^3 hybridized regions are represented with blue atoms. The schematic shows the inherent disorder in the $sp^2 - C$ regions (represented with maroon atoms) where there is bond-length disorder as well as the inclusion of sp^3 hybridized impurities and vacancies. The schematic also shows the mixture of sp^2 and sp^3 hybridization at the interface. This mixture is unique to carbon superlattices as carbon tends to form different allotropes easily and in the same regions, resulting in an unusual microstructure.

We assume that the barrier potential in the $sp^3 - C$ regions takes the form of a Gaussian distribution due to the imperfect nature of the interface between the $sp^3 - C$ and $sp^2 - C$ regions [127] (this potential is represented in yellow on the shematic diagram of the super-

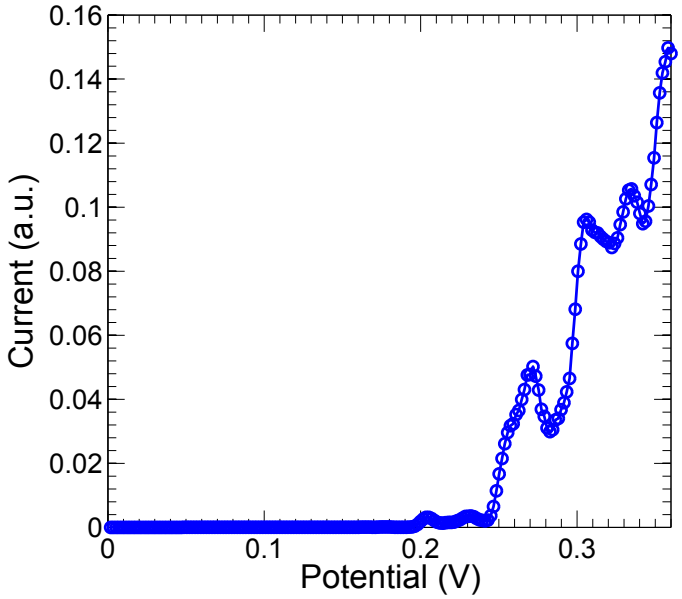


Figure 3.7: Calculated current-voltage characteristics of a DLC superlattice with 4 barriers of 7 nm and 3 well of 7 nm.

lattice). This broad barrier, without a sharp interface, results in a wide range of resonant energies and spreads out the transmission maxima, in turn resulting in wide resonant features in the calculated I-V characteristics. We assume a relatively small difference in the potential energy between the $sp^2 - C$ and $sp^3 - C$ regions (in comparison to our previous work [1]) in an attempt to reproduce the experimental data. We find prominent NDR at potential differences of around 0.25 V and 0.31 V. These low potential differences are consistent with the measured I-V properties.

Figure 3.8 shows the calculated I-V characteristics of a superlattice with 4 barriers of width around 8 nm (also following a Gaussian form) and 3 wells with a width of approximately 2 nm (much narrower than in the previously considered device). We find prominent step-like features related to resonant transmission but no distinct NDR. These regions of current saturation are consistent with the measured I-V characteristics where the devices have smaller well widths. Examination of Figure 3.8 also shows step-like features at higher potentials (around 5 V at 87 K).

These calculations demonstrate that as the well width decreases, the eigenenergies shift to higher potentials however the relatively strong disorder suppresses NDR. Numerous calculations considering different well widths (without changing the barrier height) show that the steps in the I-V characteristics are not very sensitive to the well width while the width of the current steps can be modified by changing the barrier width. The most significant factor by far is the barrier height, with even very slight changes in the barrier height resulting in dramatic suppression of the current in the low bias region. Calculations of the I-V characteristics for the device shown in Figure 3.5 (not shown here) are very similar Figure 3.8 which is consistent with the experimental data as the current suppression is quite similar for both devices.

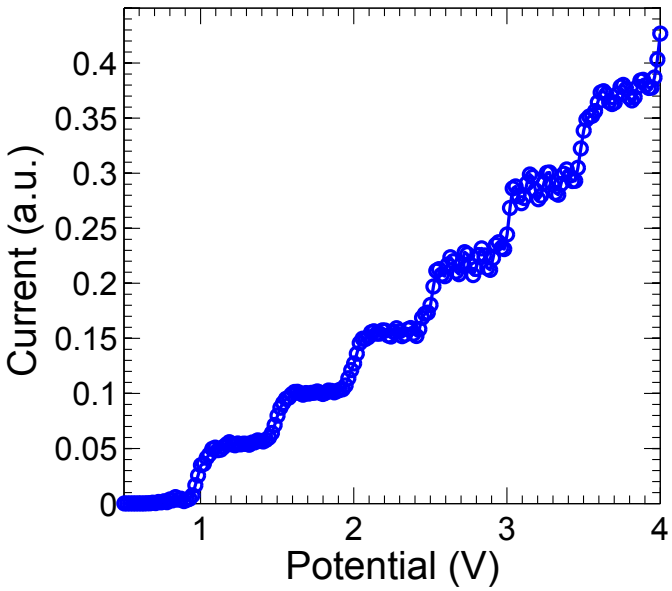


Figure 3.8: Calculated current-voltage characteristics of a DLC superlattice with 4 barriers of 7 nm and 3 wells of 4 nm.

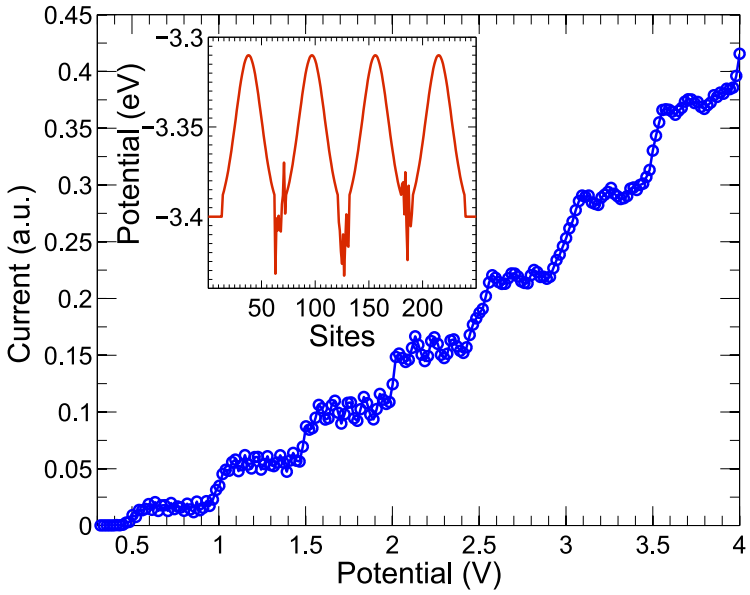


Figure 3.9: Calculated current-voltage characteristics of a DLC superlattice with 4 barriers of 7 nm and 3 wells of 1 nm assuming a Gaussian distribution of around a mean hopping parameter in the $sp^3 - C$ regions and the inclusion of impurity states.

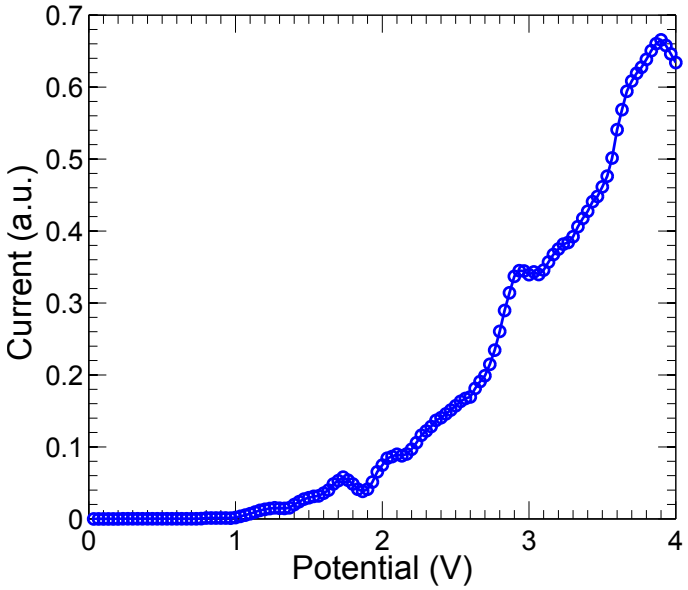


Figure 3.10: Calculated current-voltage characteristics of a DLC superlattice with 4 barriers of 7 nm and 3 wells of 7 nm considering significant bond alternation in the sp^3 hybridized regions.

We now present some calculations on modified superlattices to illustrate further scope for tuning the quantum transport properties. Figure 3.10 shows the calculated current voltage characteristics for a device with the same dimensions as in Figure 3.4 but with significant bond alternation in the $sp^3 - C$ regions (with the same level of disorder in the $sp^2 - C$ regions). Regions of NDR move to higher potential differences as the bond alternation shifts the eigenenergies to the band edges. This also increases the difference in potentials at which NDR occurs. Prominent NDR is found at 1.8 V and close to 4 V while less prominent NDR occurs at around 3 V. Figure 3.21 shows a schematic of the potential in the $sp^3 - C$ regions. Bond-alternation is assumed to occur through polymeric chains (shown in red) which spread through the sp^3 hybridized regions due to the affinity of carbon to form chain-like structures [125].

We have attempted to fit the high-field region of the I-V data using Poole-Frenkel emission, Schottky emission and space charge limited conduction. Considering the microstructure of these devices, these effects can be expected to play a role in the high field regime [128, 129, 130, 131, 132]. Only one device though (device with 3 wells of width 2 nm and 4 barriers of width 8 nm) shows a reasonable fit to Poole-Frenkel emission as shown in Figure 3.11 in the high field regime. It is also possible that this indicates Schottky emission as Schottky emission also shows a linear dependence to voltage squared however the temperature dependence of the current-voltage characteristics is not consistent with Schottky emission. Fits for the other devices are not convincing for either Poole-Frenkel or Shottky emission or space charge limited conduction. This is likely due to a combined contribution from all these effects which can be expected due to the inherent disorder in the material.

The calculated I-V characteristics provide a solid explanation for many of the features of

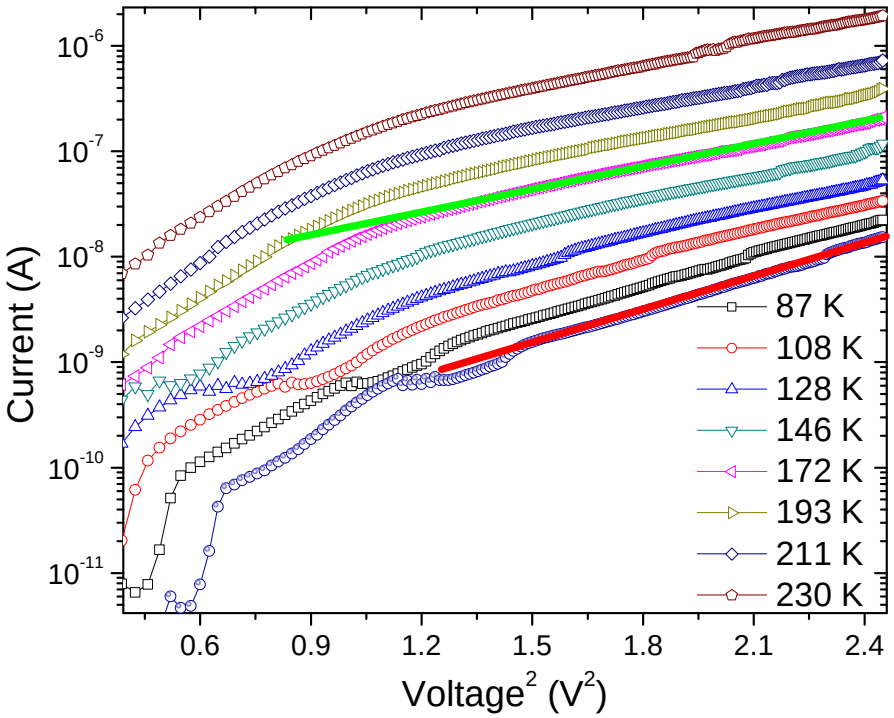


Figure 3.11: Current-voltage characteristics of a DLC superlattice with 4 barriers of 8 nm and 3 wells of width 2 nm as a function of voltage squared to examine Poole-Frenkel and Schottky emission.

the measured I-V characteristics. The differences can generally be ascribed to the relatively high temperatures of the experimental measurements and the resulting thermionic emission which is not taken into account in the calculations. The calculations clearly show that the current steps (and small regions of NDR) in the measurements are a result of resonant transmission in the a-C superlattices. The calculations show that the most prominent effect of disorder is to broaden out features in the I-V characteristics. Calculations considering different parameters for the a-C superlattices clearly show that the barrier height (relative difference between the potential in the sp^2 and sp^3 hybridized regions) has a far greater influence on the features in the I-V characteristics than any other parameter. Thus we can infer that the principle difference between the measured samples is the effect of the extent of the sp^2/sp^3 regions on the barrier at the interface. This is fundamentally different from conventional superlattices and is essential to take into account for future work in band engineering of these a-C devices.

An additional consideration is the effect of significant bond alternation in the sp^3 hybridized regions. This has been successfully applied to nitrogen doped a-C superlattices [2]. In the current experiments, the regions of NDR are found at relatively low potentials. This indicates that bond-alternation is not a prominent feature in the present devices as bond alternation shifts resonant energies close to the band edges, consequently separating out the regions of NDR. The differences between these sets of a-C superlattice devices is likely due to the differences in the synthesis methods (see, for example,[133]) which provides further scope for tuning the device properties.

In addition, prominent current-induced hysteresis was found in these devices. This suggests that conducting channels were formed in the superlattice structures at high bias potentials. Beyond having applications as memory devices, this effect indicates that much of the conduction is through channels within the superlattice.

3.4 Effect of disorder in thin graphitic films

We now apply this model of disorder in the $sp^2 - C$ phase to thin graphitic films grown through laser ablation. The films were grown by Christopher Coleman and Raman studies were performed by Mr. Christopher Coleman and Dr. Rudolph Erasmus of the School of Physics, Wits. In the previous calculations, we considered the role of structural disorder in the sp^2 phase, specifically bond-length distortions, in carbon superlattices. Based on the widely reported saturation of the conductivity of amorphous carbon films with disorder, we developed a model which accounts for the saturation of the disorder in the conjugated phase as a function of the energy gap between bonding and anti-bonding states (similar to a Tauc gap). Here, we employ a model where the sp^2 phase disorder parameter initially increases with the energy gap between π and π^* states and eventually saturates [119].

In the present study, the FWHM of the Raman G peak (Fig. 3.13(a)) indicates the disorder in the sp^2 phase while the energy gap, determined through transport measurements (performed by Chirstopher Coleman and analysed by Ross McIntosh), is related to the energy gap between π and π^* states. Structural disorder in the present graphitic material induces bond-length and bond-angle distortions around grain boundaries and vacancies. We have used the FWHM of the Raman G peak to estimate the disorder parameter and we have calculated the localization length based on a quasi-1D tight-binding model. We have assumed that there is a small concentration of sp^3 hybridized carbon where there is bond-alternation in these regions. After calculating the transmission coefficient, the localization length can be calculated from the relation $L_{loc}(E_{res}) = -2L/lnT(E_{res})$ where L_{loc} is the localization length and $T(E_{res})$ is the transmission coefficient at the resonance energy E_{res}. The calculated localization length is not the same as the experimental localization length due to the computational demands of calculating a system 1 μm in length, however the behavior of the localization length as a function of the disorder parameter is the same in both cases.

Our calculations show that the transmission coefficient at resonant energies decreases with increasing disorder. In addition, the resonant energies shift to higher energies while the FWHM of the transmission peaks increases. The calculated localization length as a function of the disorder parameter (δ_π) is shown in Figure 3.12. The localization length decreases exponentially with increasing disorder parameter as disorder destroys the resonant tunnelling conditions resulting in enhanced backscattering leading to localization. Figure 3.12 (b) shows the experimentally determined activation energy as a function of the Raman

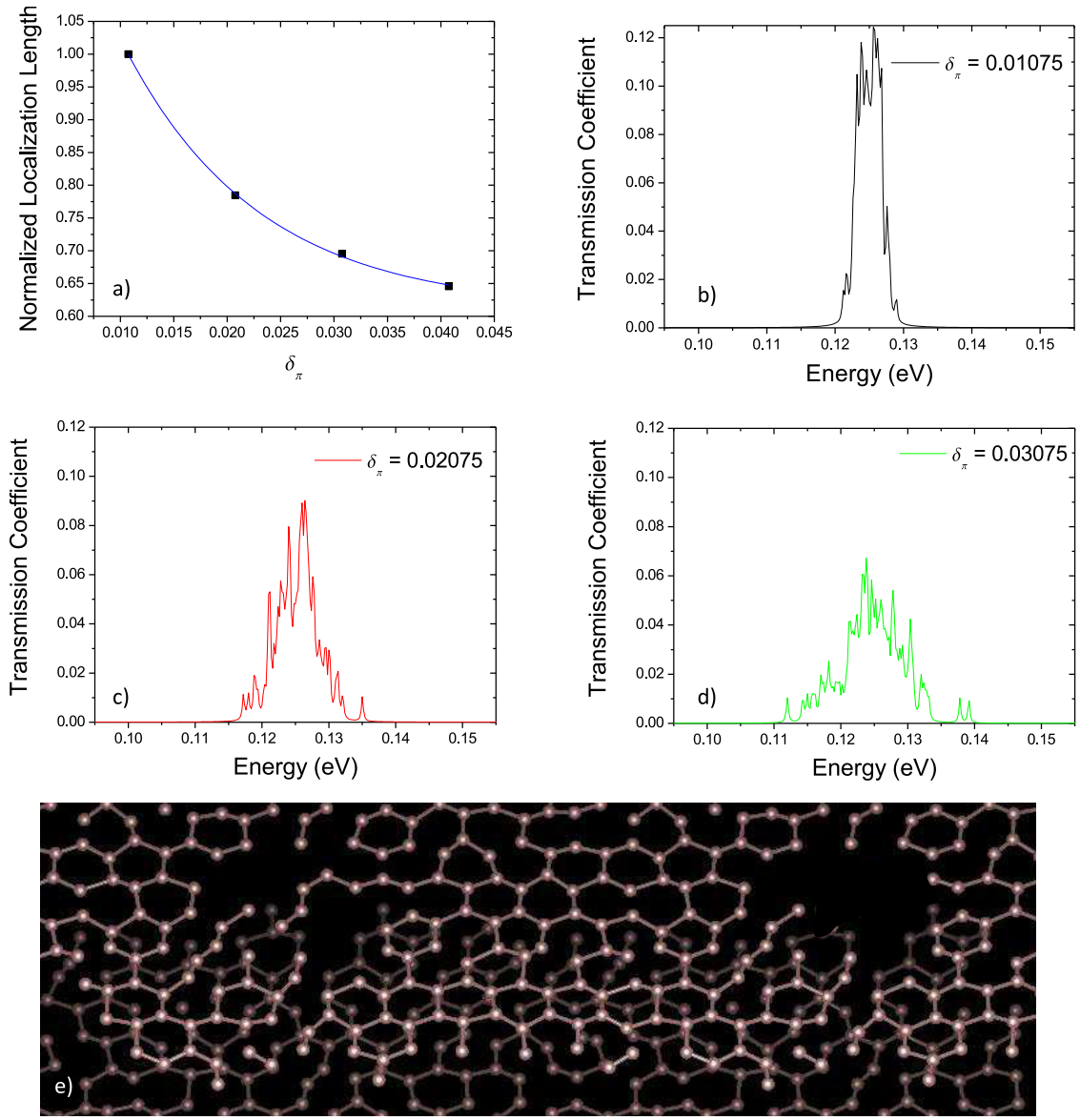


Figure 3.12: (a) Calculated normalized localization length as a function of the disorder parameter δ_π (mean of the Gaussian distribution of π phase hopping terms). (b) to (d) The first transmission peak of the calculated transmission coefficient as a function of energy for different values of δ_π. (e) Schematic diagram of the microstructure of two overlapping disordered graphene layers as a representation of thin graphitic films. The diagram includes bond-length distortions as well as in plane and out of plane bond-angle distortions and vacancies.

G peak FWHM. As the activation energy is directly related to the localization length, this curve indicates that the localization length decreases with increasing disorder in accord with our calculations. This combination of experimental and theoretical studies illustrates how the disorder level influences the bandgap.

We present a schematic diagram of the thin graphitic films in Figure 3.12(e). We propose a microstructure where bond-length and bond angle distortions (in plane and out of plane) are prominent which destroy the symmetry of pristine graphite and result in the formation of non-hexagonal rings. There are vacancies in the material as the ablated material does not grow into a smooth film. In addition, the layers are expected to overlap non-uniformly. Figure 3.12(e) shows two disordered graphene layers which partially overlap. With increasing disorder, the concentration of intact benzene rings decreases and the filamentary current through these regions is prone to enhanced localization, opening up an energy gap.

3.5 Nitrogen Incorporation in a-C Superlattices

We now study the effect of nitrogen doping in the sp^2 hybridized regions of a-C superlattices.

Figure 3.15 is a $3D$ plot of the transmission coefficient as a function of energy for a nitrogen (N) incorporated a-C superlattice with multiple (in this case three) N centres in three of the $sp^2 - C$ wells assuming disorder parameters $\delta t_C = 0.00675\ eV$ (for the carbon regions) and $\delta t_N = 0.0025\ eV$ (for nitrogen impurities). The N hopping term was swept from -0.05 eV to 0.05 eV to determine the effects of the N level relative to E_F. Although there are three N states in some of the $sp^2 - C$ wells, there are still two broad peaks in $T(E)$. Beginning with the N_{up} case with $t_N = -0.05\ eV$ (black line) the N peak is found at higher energy than the C peak as before. As the N potential decreases the N peak shifts to lower energies while the transmission initially increases as the reduction in potential promotes tunnelling. This illustrates the interplay between the N potential and the transmission. If the N barrier is too high, the intensity of the $T(E)$ peak is reduced even though the transparency of the superlattice increases. On the other hand, if the N barrier is too low then although the transmission increases, the transparency decreases along with the overall intensity of the $T(E)$ peak. In addition, as the N potential decreases the overlap between the C and N peaks increases along with the overall amplitude.

However with further decrease of the N potential the eigenenergy of the N incorporated wells begins to decrease along with the intensity of the peak as the transparency of the SL structure decreases. The transmission can therefore be optimized if the N potential can be controlled based on the interplay between the N barrier state and the transmission through the SL structure.

As the N potential decreases, the separation in energy of the peaks decreases. Eventually, as the N potential approaches zero, the C and N peaks merge into a single broad peak (see

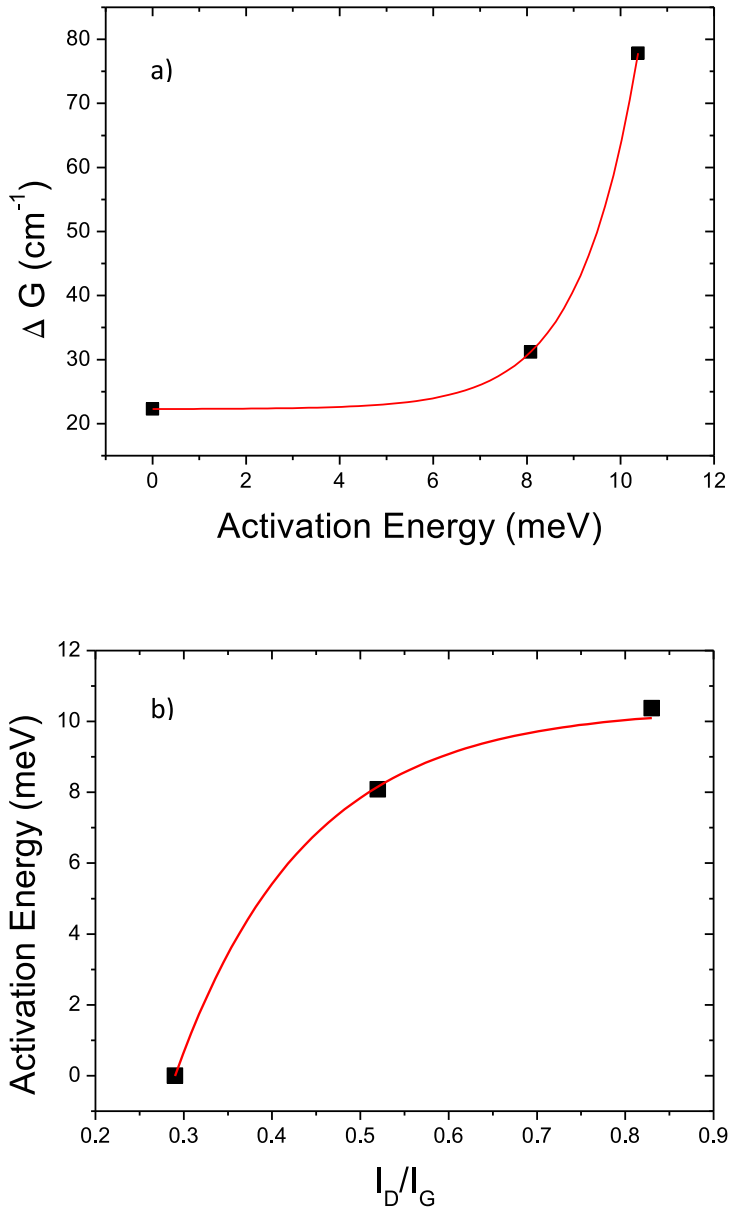


Figure 3.13: (a) The full width at half maximum of the Raman G peak (ΔG) as a function of the activation energy. (b) Activation energy determined through application of Eq. (1) as a function of the I_D/I_G ratio.

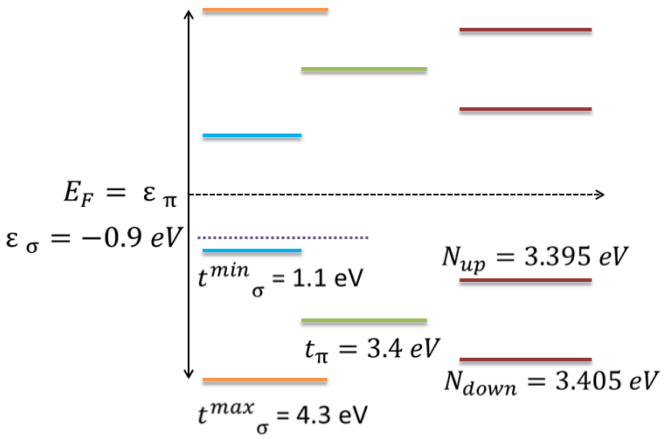


Figure 3.14: Schematic diagram of a range of possible nitrogen induced impurity levels in carbon systems [1].

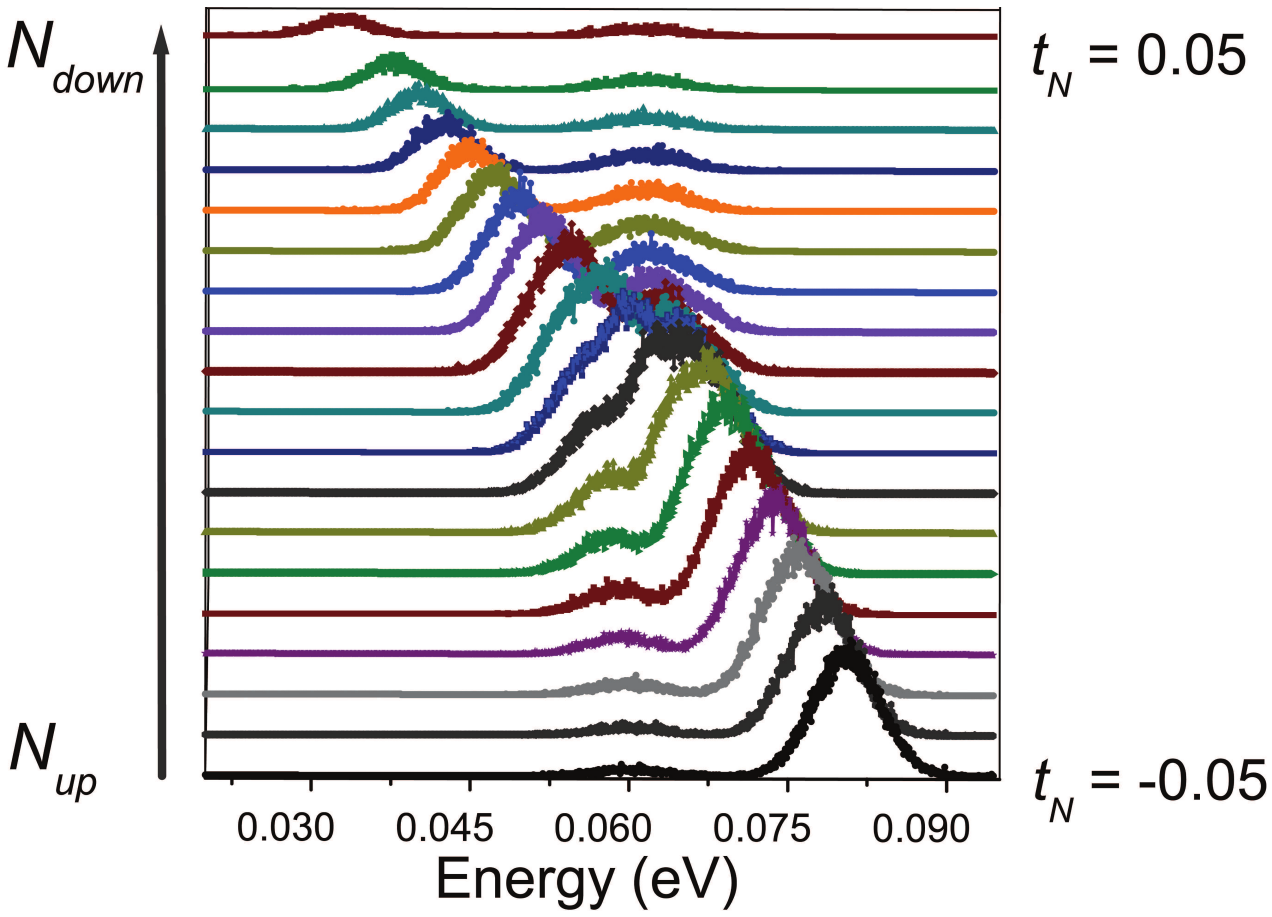


Figure 3.15: Transmission coefficient as a function of incident electron energy as the N potential is varied from N_{up} to N_{down}.

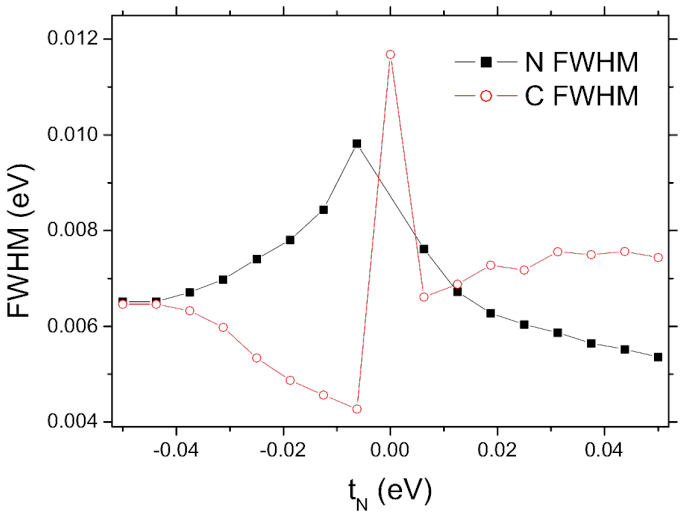


Figure 3.16: Full width at half maximum of the carbon and nitrogen transmission peaks as a function of t_N (the N hopping parameter).

Fig. 3.18 as well). As N decreases further, becoming a trap state, the N peak shifts to still lower energies and the transmission decreases. Thus, as the level of the N changes in relation to E_F, a crossover in the relative energies of the C and N peaks can be induced.

For N_{up} the FWHM of the N peak is always lower than N_{down} peaks. The C peak behaves in the opposite manner. The FWHM depends on the N_{up}/N_{down} which is a major result of this work. The values of the width for C and N peaks can be exchanged by changing the energy position of N atoms from N_{up} to N_{down} position (see Fig. 3.17). In N_{down} structures, the resonant states occur at lower energy and the corresponding width of the N resonant state is smaller than N_{up} resonant states. For N_{up} structures the N peaks are at high energies so the width of N_{up} resonant state is large. Since the position of the C peak changes with N_{up} or N_{down} we find that the width of the C peak varies accordingly. The present results are important to propose new devices based on nitrogen incorporation in carbon where the resonant tunnel spectra can be controlled by the nitrogen energy position instead of applying an external gate bias. More importantly the proposed microscopic model can be used to interpret the long standing issue of identifying the effective nature of nitrogen doping opposed to the effect of disorder.

We have considered a two-channel conduction picture in CN systems associated with C and N atoms. In this case the N channel can be placed higher or lower than E_F of carbon which can offer effectively n- or p-type doping of carbon systems, respectively. Nitrogen can be placed at various energy levels depending on the chemical structures formed in the CN complexes (see Fig. 3.14 and 3.15) and the charge transfer between C and N atoms. Nitrogen contributing free electrons to carbon systems can form levels above E_F close to the conduction band (N_{up}). This shows a small increase of resistance of N channels termed as substitutional doping. However, in many cases N forms defect centres, such as lone-paired

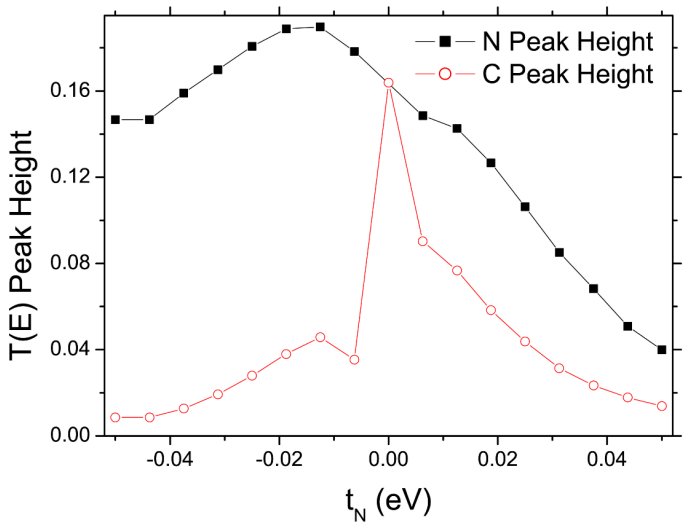


Figure 3.17: The corresponding $T(E)$ peak height as a function of energy.

electrons which absorb electrons from sp^2 carbon atoms (N_{down}) where resistance increases significantly with disorder. In that case both C and N channels have poor conductivity and a slow relaxation process. For N_{up} conduction through the C channel is poor which is affected by disorder. Hence the conduction through the N_{up} channel becomes predominant in the $C-N$ system. The decrease of FWHM shows an enhancement of resonant transmission in these systems. This is a major claim for this work based on the energetic position of nitrogen in carbon matrix.

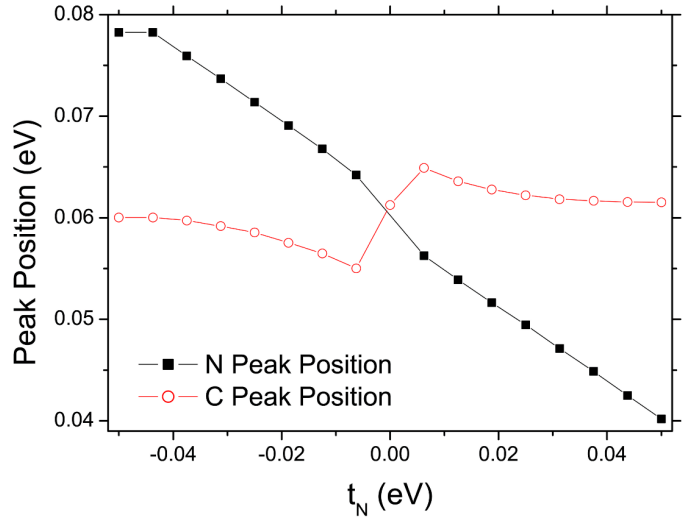


Figure 3.18: The corresponding peak position as a function of t_N.

The full width at half maximum (FWHM) of the transmission peaks as a function of the N hopping potential t_N is shown in Figure 3.16. The FWHM is inversely related to the characteristic lifetime of electrons in quasi-bound states. When t_N is negative (N_{up}) initially there is little difference between the FWHM of the peaks indicating that the characteristic time associated with the C and N states is almost the same. Although the N peak is broader and is more sensitive to disorder-induced broadening, the intensity is also higher and the N disorder parameter is smaller than the C disorder parameter so the FWHM is

almost the same as the C peak. However as t_N approaches zero a substantial difference between the FWHM of the C and N peaks becomes apparent. As the potential of the N barrier decreases, the characteristic time is expected to decrease as transmission increases through N incorporated $sp^2 - C$ wells. The transmission through the $sp^2 - C$ wells without N is therefore reduced so the characteristic time increases. Furthermore as the N potential decreases, the overlap between the C and N peaks increases.

As t_N, now positive (N_{down}), continues to increase, the FWHM of the C peak increases while that of the N peak decreases. As the N trap becomes deeper, the N peak shifts to lower energies where the SL structure is less transparent. Transmission is therefore impeded and the characteristic time associated with transmission through N incorporated wells increases. The FWHM of the C peak changes slightly. When nitrogen acts as a trap state the energy separation of the C and N peaks in the pristine case (no disorder) is larger than when N acts as a potential barrier. Therefore the overlap is smaller and changes in the FWHM of the N peak have a smaller effect on the C peak. When δt_N changes from negative to positive, the sharp crossover of the magnitude of the FWHM of the C and N peaks is directly related to the reduction in transparency through the SL structure at lower energy.

The N peak height initially increases with t_N as the potential of the barrier decreases, reaching a maximum while N acts as a barrier as shown in Fig. 3.17. The overall transmission increases as the N barrier decreases until the resonant energy of the N incorporated wells is so low that the transparency of the SL structure decreases, along with the peak height. The C peak however attains a maximum when N acts as a potential well as a result of the reduction in transmission through the N incorporated wells. With further increase of the N well depth the transmission of both peaks decreases as the resonance associated with the N traps shifts to lower energy. This is illustrated in Fig 3.17. Figure 3.17 also illustrates the repulsion of the C and N bands. As the potential of the N barrier decreases, the energy of the N peak approaches the energy of the C peak and the C peak shifts to lower energy. The C peak also shifts away from the N peak if N acts as a potential well. The next part of the discussion refers to Figures 3.15 to 3.18 to elucidate the interplay between the FWHM, transmission peak height and resonant energy. Considering the N peak, while the FWHM increases, so too does the transmission peak height as the potential of the N barrier decreases and the N peak shifts towards E_F. In contrast, the reduction of FWHM of the C peak is met with an increase in the transmission peak height but mirrors the shift of the C peak position to lower energies. Considering the increase of the N well depth, the FWHM and transmission peak height decrease as the resonant energy of the N wells decreases and the N peak shifts to lower energy.

Figure 3.19(b) shows the I-V characteristics calculated for a superlattice with 4 barriers and 3 wells both 7 nm in length (comparable to Figs. 3.4 and 3.7) with nitrogen impurities incorporated in the $sp^3 - C$ regions. Figure 3.19(a) shows a schematic of the device config-

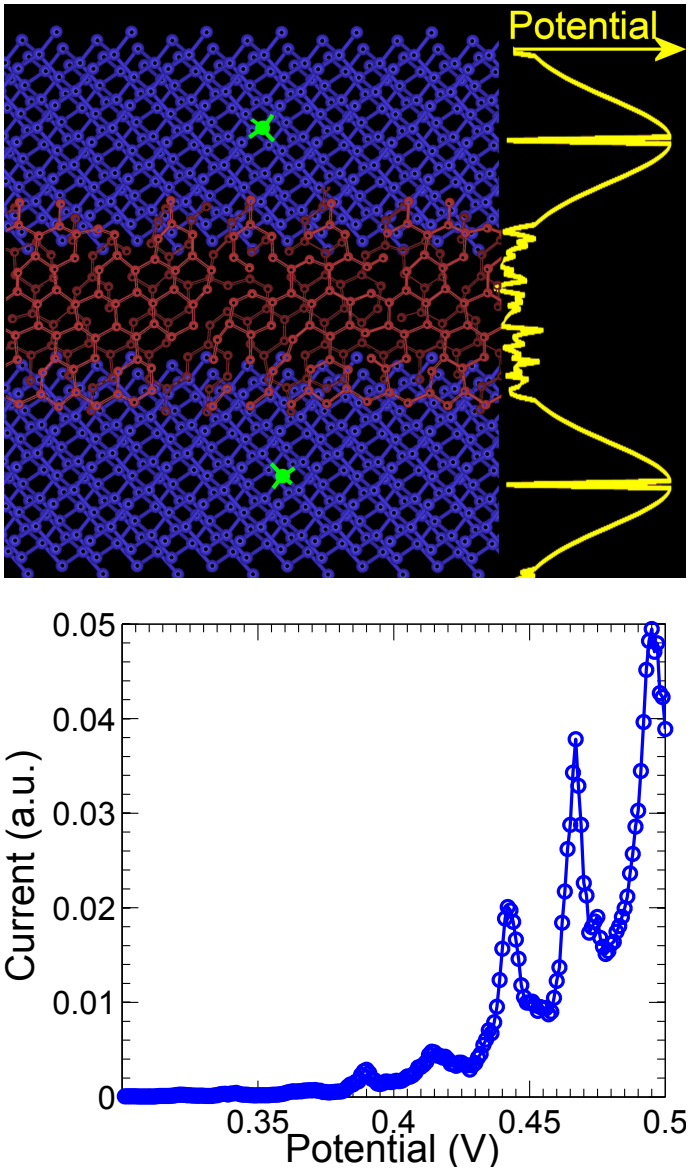


Figure 3.19: a) Schematic diagram of nitrogen incorporated DLC superlattice with nitrogen incorporated in the sp^3 hybridized layers. b) Calculated current-voltage characteristics of a DLC superlattice with 4 barriers of 7 nm and 3 well of 7 nm with nitrogen incorporated in the sp^3 hybridized regions.

uration as well as the potential. These nitrogen impurities create trap states and illustrate how resonant transmission, and consequently the regions of NDR, can be tuned by the inclusion of nitrogen impurities which is of significance for future device applications. The inclusion of nitrogen trap states shifts the eigenenergies to lower energies where the superlattice is less transparent. This results in sharper resonances despite the inherent disorder, resulting in more prominent and sharply defined regions of NDR in comparison to devices with no nitrogen inclusion. The resulting sharp signatures could point the way to quantum devices suitable for quantum information processing.

3.6 Comparison with experiment for nitrogen incorporated a-C superlattices

We now compare calculations of the I-V characteristics with measurements on nitrogen incorporated a-C superlattices which were performed by Neeraj Dwivedi, National University of Singapore. These devices were made through radio-frequency plasma enhanced chemical vapour deposition [2]. By changing the self-bias voltage, the percentage of sp^2 hybridized carbon can be changed during the deposition allowing alternating layers with different percentages of sp^2 hybridized carbon and hence different bandgaps. The bandgap can therefore be modulated to achieve quantum confinement however these a-C superlattices are inherently disordered. N_2 and C_2H_2 were used as precursor gasses and the N_2 partial pressure was changed to change the amount of nitrogen incorporation in the a-C superlattices. Nitrogen incorporation was found to slightly decrease the width of the low bandgap regions (high $sp^2 - C$ %). Details of the growth, microstructure and characterization of the band gap of the different layers can be found in [2]. a-C superlattices with 7 barriers of width 3.5 nm and 6 wells of 2.5 nm were studied.

Measurements of the I-V characteristics (and the fist and second derivatives) are shown in Figure 3.20. These measurements show two prominent regions of NDR. These regions of NDR are separated by a large potential difference which is unlike conventional superlattices. With increasing nitrogen partial pressure, the regions of NDR migrate towards smaller potentials initially however there is little difference between the potential of the onset of the first NDR peak for the devices with 48 % and 65 % nitrogen partial pressure. The second NDR peak however continues to move to lower potentials as the nitrogen partial pressure increases.

In an attempt to understand the effect of the change in microstructure with nitrogen incorporation, we studied two different cases theoretically. Initially, we studied the transmission through disordered superlattices which are similar to conventional superlattice structures i.e. regions of high potential separated by regions of low potential. The eigenenergies are sensitive to the relative difference in potential between the quantum wells and barriers.

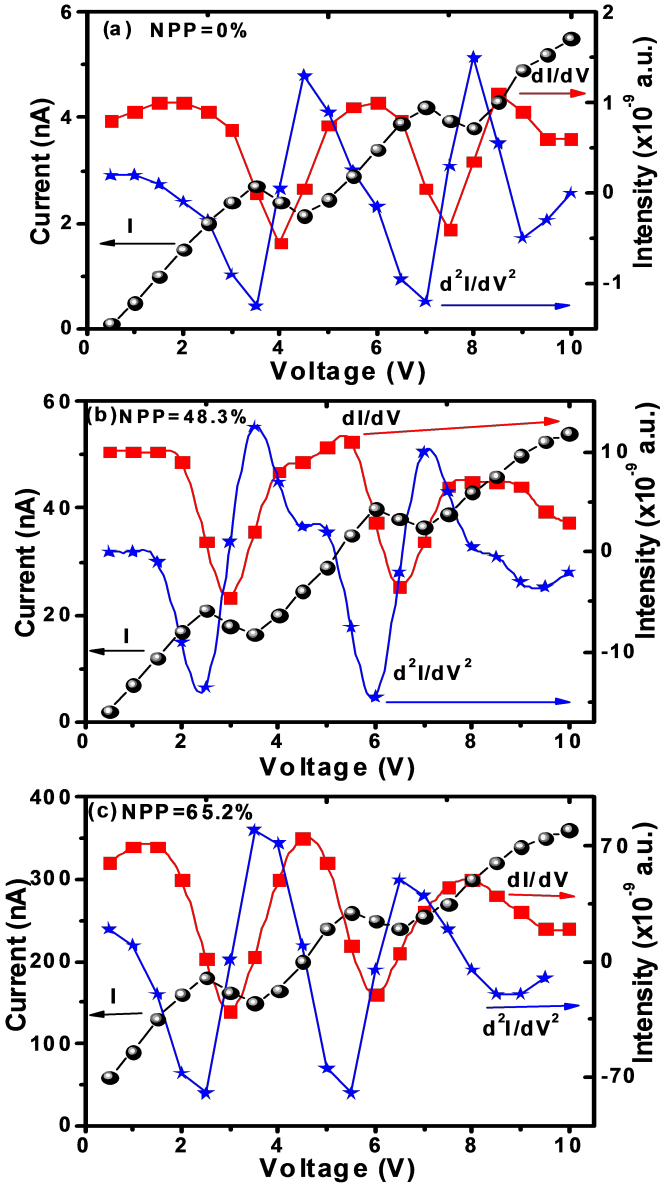


Figure 3.20: Measured I-V characteristics, with first and second derivatives, of DLC superlattices with different amounts of nitrogen incorporation: a) 0 %, b) 48.3 %, c) 65.2 %. Measurements performed by N. Dwivedi [2].

Consequently, the regions where NDR is found in the I-V characteristics can be tuned however the separation of the regions of NDR cannot be tuned to reproduce the experimental data using physical parameters for the potential as the eigenenergies of the superlattice are relatively close together while the experimental data shows a large difference in the potential between the regions of NDR.

This prompted us to study the case of bond alternation in the $sp^3 - C$ regions (shown schematically in Fig. 3.21), which is likely to arise if polymeric chains form within the $sp^3 - C$ hybridized regions. The periodic bond alternation in the $sp^3 - C$ regions results in alternation of the hopping parameter, which varies from one site to the next, from t_σ^{max} to t_σ^{min} which are in the range of 3.3 to 4.3 eV and 1.1 to 2.1 eV respectively with the transfer hopping parameter between the diamond-like and graphitic regions given by $t_{\sigma-\pi}$ which is 1.37 eV. There may also be significant incorporation of $sp^2 - C$ in the $sp^3 - C$ regions as well as incorporation of nitrogen complexes in the $sp^3 - C$ regions however the effects of these inclusions will be similar to bond alternation as they result in a much smaller potential locally in the $sp^3 - C$ regions.

Hence, we neglect to model these defects. There may also be disorder within the bond alternation regions although this has a relatively small effect on the transmission coefficient as the relative change in the potential across the sites due to disorder is quite small in comparison to the change in potential from site to site due to bond alternation. It is difficult to quantitatively reproduce the experimental data as nitrogen can form a number of different C-N complexes (with different potentials) and can modify the microstructure in the region of the nitrogen defect.

Figure 3.22(a) shows the calculated I-V characteristics for a DLC superlattice with the same dimensions as the experimentally studied superlattice, Figure 3.22(b) shows the hopping parameter (inversely related to the potential) at each lattice site in the superlattice. It is assumed that there is structural disorder within the $sp^2 - C$ phase. There are two prominent regions of NDR, where the peaks are at 5 V and 6.7 V as well as additional non-linear features. This is similar to the I-V measurements although the first NDR peak appears at 3.8 V in the measurements. Reflection of the wavefunction from sp^3 hybridized regions results in quantum interference with constructive interference at eigenenergies resulting in resonant transmission when the potential causes alignment of the eigenenergies of the quantum wells with incident electron energies of the leads.

Bond-alternation increases the separation between eigenenergies, shifting eigenenergies closer to the band edges with increasing $sp^3 - C$ percentage. The bond-alternation also increases the transparency of the superlattice and increases the difference between the eigenenergies of the quantum wells as at high incident electron energies, the barriers become more transparent to incident electrons (for a solid barrier) and this effect is enhanced in the case of bond alternation. The disorder in the $sp^2 - C$ phase results in a wide distribution of eigenenergies, resulting in broad transmission maxima and decreasing the peak-to-valley

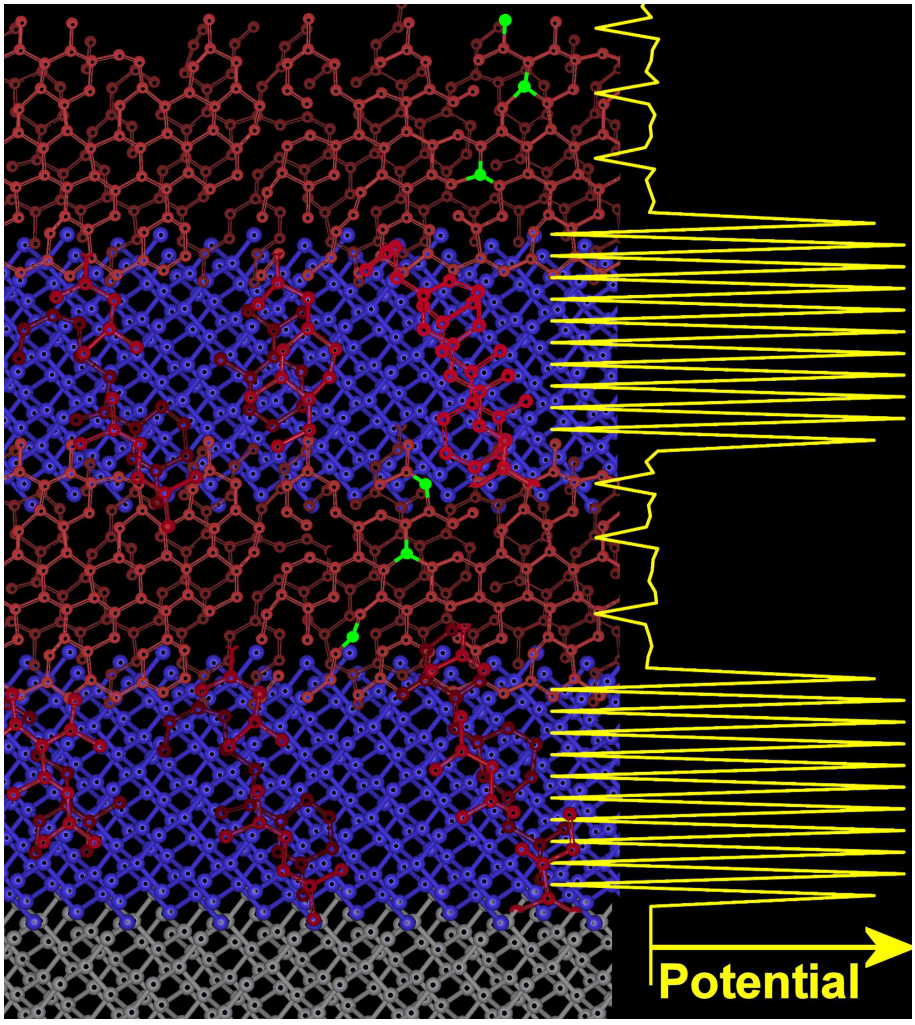


Figure 3.21: An atomic scale schematic diagram of the quantum superlattice formed by alternating layers of predominantly $sp^2 - C$ well (maroon atoms) embedded within two predominantly $sp^3 - C$ barriers (blue atoms) considering significant bond alternation in the $sp^3 - C$ regions. The potential is overlain in yellow.

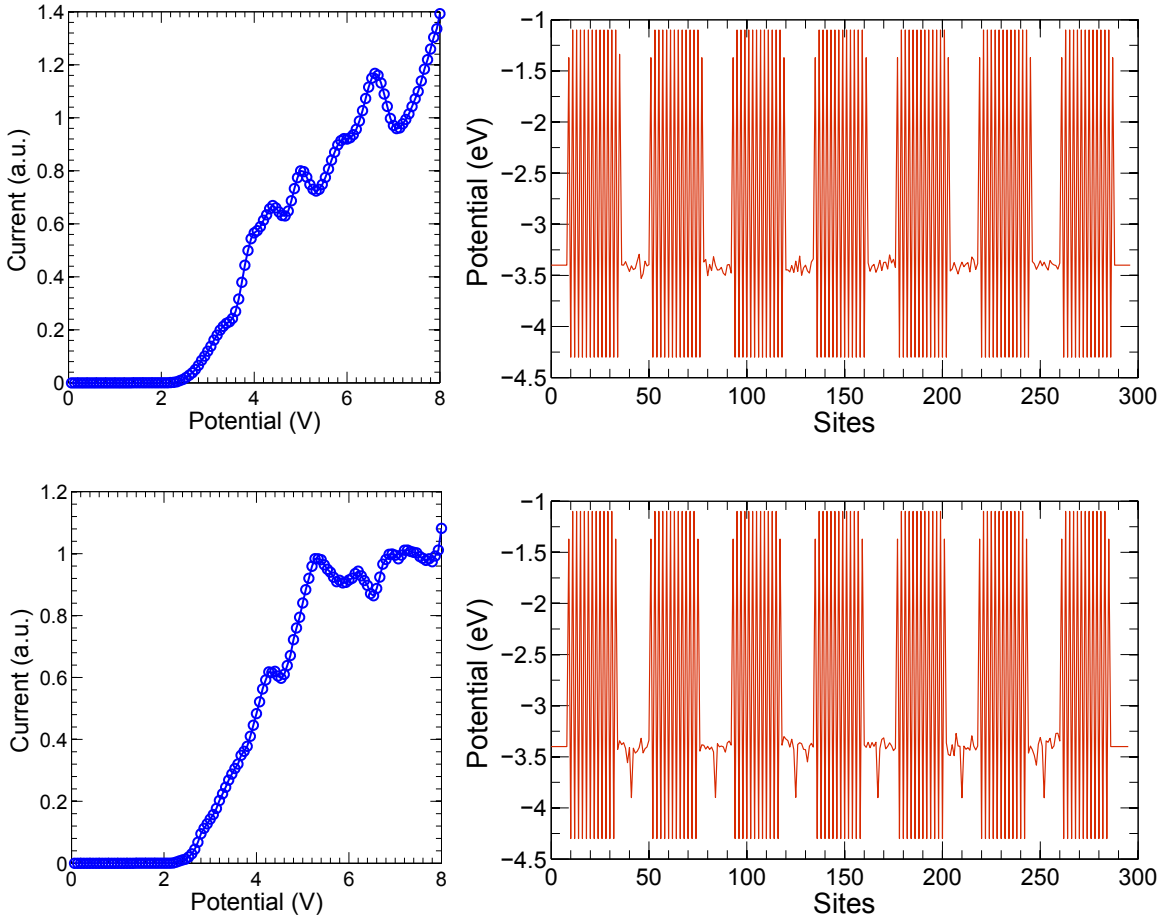


Figure 3.22: a) Calculated current-voltage characteristics of a DLC superlattice with 7 barriers of 3.5 nm and 6 wells of 2.5 nm with no nitrogen incorporated in the sp^2 hybridized regions. b) Schematic diagram of DLC superlattice. c) Calculated current-voltage characteristics of a DLC superlattice with 7 barriers of 3.5 nm and 6 wells of 2.5 nm with nitrogen incorporated in the sp^2 hybridized regions. d) Schematic diagram of nitrogen incorporated DLC superlattice with nitrogen incorporated in the sp^2 hybridized layers.

ratio in the I-V characteristics.

Figure 3.22(c) shows the I-V characteristics with minimal nitrogen inclusion in the sp^2 hybridized layers. Nitrogen incorporation smears out the feature at 3.8 V and shifts the other regions of significant NDR to lower potentials. In addition, it causes saturation of the current at higher potentials. With increasing nitrogen partial pressure during synthesis, the number of nitrogen defects incorporated in the sp^2 hybridized regions increases while the size of the $sp^2 - C$ clusters increases as nitrogen promotes growth of the $sp^2 - C$ phase (as shown by FTIR measurements in this study and found in other studies as well). In modelling the nitrogen incorporated superlattices, we have included these effects however since it is difficult to state with certainty the amount of nitrogen defects incorporated in the $sp^2 - C$ regions, we have included a few nitrogen atoms in these regions to qualitatively interpret the effects of nitrogen defect incorporation.

Figure 3.23(a) shows the calculated current-voltage characteristics of a DLC superlattice with nitrogen defects where the width of the $sp^3 - C$ hybridized regions has been reduced in accordance with the experimentally observed increase in $sp^2 - C$ cluster size. In agreement with the measurements, the regions of NDR shift to lower energies as the superlattice becomes more transparent with decreasing $sp^3 - C$ barrier thickness. The defects decrease the potential at which the first region of NDR occurs while the potential of the second region of NDR shifts to lower potential due to the increased transparency. In addition, higher-order regions of NDR become apparent due to increased quantum well width. These do not appear in the measurements however they may be drowned out by multi-channel effects as many conduction channels form in the DLC sueprlattices. The potential of the Si injector may also play a role in suppressing out these regions.

Figure 3.23(c) shows the calculated I-V characteristics for a nitrogen incorporated DLC superlattice with a still greater defect concentration and further increased $sp^2 - C$ cluster size. The first and second prominent regions of NDR shift to slightly smaller potentials although the shift in potential is not as great as the initial shift when nitrogen is first introduced, coinciding with the measurements. In between these regions additional features are found which indicate broad transmission peaks which are not sufficient to induce NDR. The defect states result in additional eigenenergies forming in the quantum wells. The calculations allow us to interpret with certainty the effects of the nitrogen incorporation in the experimental data.

The experimental results show a marked increase in the conductivity with increasing nitrogen incorporation, almost an order of magnitude with each increase in nitrogen partial pressure. This is likely due to the formation of additional conduction channels (1D chains) in the superlattice. These calculations provide a solid explanation of the experimental data and also yield insight into the possibility of designing DLC superlattices with specified characteristics. Networks, fullerene-like crystallites and polymeric chains readily form in the DLC superlattices. In this work, we have considered uniform nitrogen defects although it is

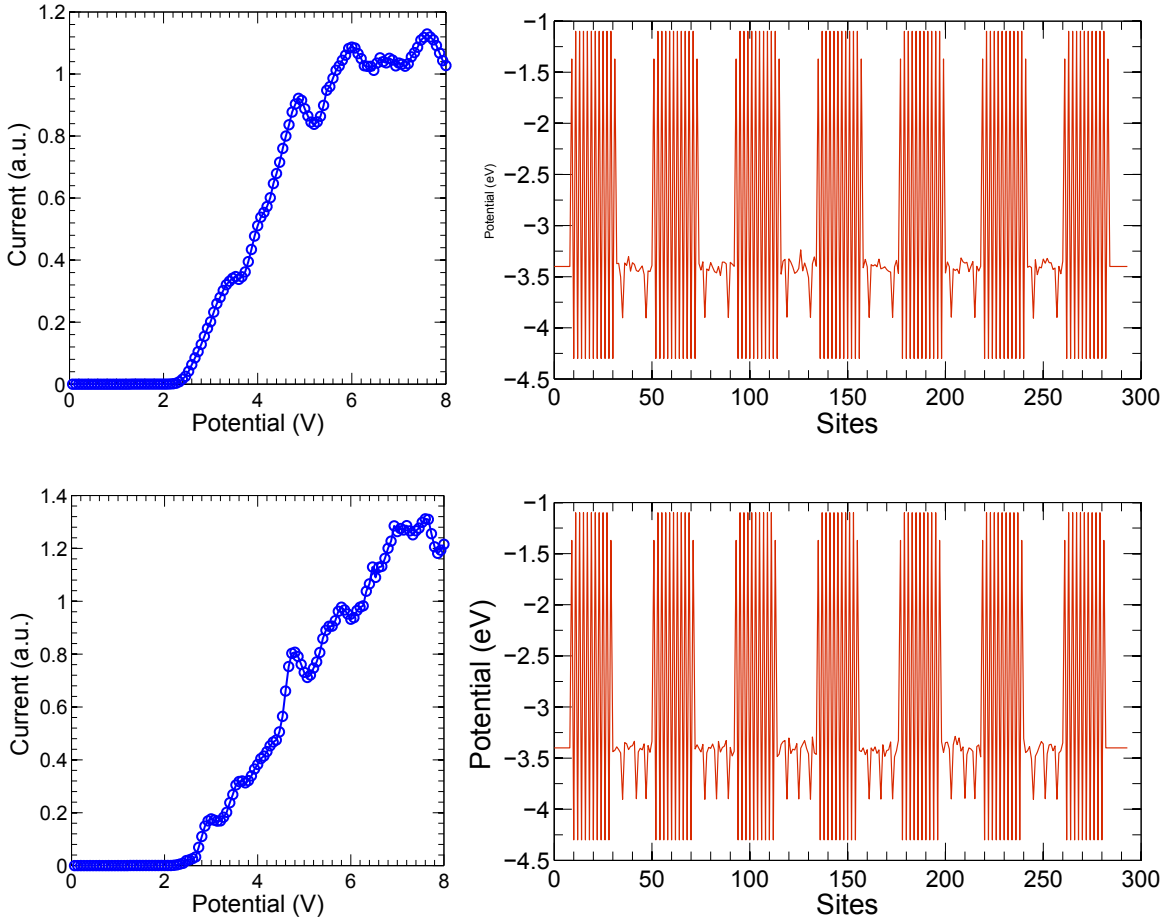


Figure 3.23: a) Calculated current-voltage characteristics of a DLC superlattice with 7 barriers of 3.5 nm and 6 wells of 2.5 nm with nitrogen incorporated in the sp^2 hybridized regions. b) Schematic diagram of nitrogen incorporated DLC superlattice with nitrogen incorporated in the sp^2 hybridized layers. c) Calculated current-voltage characteristics of a DLC superlattice with 7 barriers of 3.5 nm and 6 wells of 2.5 nm with nitrogen incorporated in the sp^2 hybridized regions. d) Schematic diagram of nitrogen incorporated DLC superlattice with nitrogen incorporated in the sp^2 hybridized layers.

possible that different nitrogen-related defects are incorporated in the $sp^2 - C$ regions. This model for structural disorder is applicable to other carbon systems such as nanocrystalline diamond which consist of a heterogeneous mixture of sp^2 and sp^3 hybridized carbon regions.

3.7 Summary

Disorder was shown to broaden features in the I-V characteristics of carbon superlattice structures. A successful model describing disordered carbon superlattices was developed and it was established that the primary influence on resonant transmission in these systems is the effect of the barrier height, which is modified by changing the relative barrier and well widths. The effect of nitrogen incorporation was modelled in the presence of significant bond alternation. This analysis can be used to design carbon superlattices to develop quantum devices with specified resonant energies for a wide range applications.

Chapter 4

Phonons in 1D Chains

This chapter extends the theoretical studies of the previous chapter but is not applied to interpret experimental features of the devices studied in this work. Here we illustrate how phonon interactions influence quantum transport in superlattices and how external AC gate potentials can be used to control resonant states in molecular structures. A nearest neighbour tight-binding approach using a back-propagation technique is employed to study the influence of electron-phonon interactions on resonant transmission. Initially, time-independent transmission through a single molecular site is studied and the effects of the electron-phonon coupling strength, phonon frequency and other parameters are interpreted. Time-dependent electron-phonon interactions are then considered using Floquet theory in conjunction with a matrix recurrence relation. Single quantum dots and double barrier structures are studied.

4.1 Introduction

Electron-phonon interactions, omnipresent in all electronic devices and dominating the transport properties of some materials, become especially prominent in low dimensional systems and molecular systems as a result of electron confinement, particularly in the quantum transport regime. Phonon interactions influence electronic degrees of freedom and vice versa. As a fundamental, unavoidable interaction there is a growing necessity to include electron-phonon interactions in device models. In these systems, resonant tunnelling is the most prominent feature in the transport properties so the influence of electron-phonon interactions on resonant tunnelling is paramount. One one hand, electron phonon scattering can negatively influence device performance by destroying electron phase coherence [68, 134]. On the other hand, electron-phonon interactions can enhance transport through phonon assisted electron tunnelling [135].

The inclusion of phonon interactions in the quantum transport regime is most often treated through the non-equilibrium Green's function technique using Keldysh contours. A different approach, based on a tight binding scheme where the many-body $1D$ interacting

Hamiltonian is replaced by an exact multi-dimensional single body, non-interacting system was developed by Bonca and Trugman [68, 134].

This work was then extended to include the effects of temperature while the current was calculated from the transmission and showed prominent negative differential resistance [135]. This was applied to study the influence of electron-phonon interactions on transport through an Aharonov-Bohm ring where Aharonov-Bohm oscillations were found despite electron-phonon scattering[135]. This conclusively shows that that elastic electron-phonon scattering does not change the phase of the electron.

This method can be extended to include dynamical (time-dependent) variables by using the Floquet theory [75, 136]. Oymak *et al.* studied the influence of the electron-phonon interaction in a single molecular site, including a time-dependent gate potential. By exploiting the Floquet theory and solving the resulting system using a matrix recurrence relation, know as the Ricatti matrix solution, they demonstrated that problems of this form can be solved non-perturbatively [136].

4.2 Model

A tight-binding Hamiltonian is employed to calculate the single electron transmission through a molecular device. The leads are treated as ideal reservoirs free of electron-phonon interactions. The Hamiltonian is modified to include an electron-phonon interaction. In the representation of second quantization, the Hamiltonian is

$$\begin{aligned}\mathcal{H} = \quad & \sum_j \epsilon_j c_j^\dagger c_j - \sum_{\langle j,k\rangle} t_{j,k}(c_j^\dagger c_k + c_k^\dagger c_j) + \sum_m \omega_m a_m^\dagger a_m - \\ & \sum_{j,m} \lambda_{j,m} c_j^\dagger c_j (a_m^\dagger + a_m)\end{aligned} \tag{4.1}$$

with on-site energy ϵ_j, electron creation operator $c_j^\dagger$, hopping parameter $t_{j,k}$, phonon creation operator $a_m^\dagger$, phonon frequency ω_m and electron-phonon coupling parameter λ. Considering nearest neighbour hopping, the many body problem can be treated as a multi-dimensional one body problem as illustrated in Figure 4.1 where the sites can be interpreted as Wannier orbitals. Acting on a wavefunction in the polaron eigenbasis of sites j and phonon quanta n, $\psi_{j,n}$, yields the recurrence relation

$$\begin{aligned}E\psi_{j,n} = \quad & \epsilon_j \psi_{j,n} - t_{j,j-1}\psi_{j-1,n} - t_{j,j+1}\psi_{j+1,n} \\ & + \psi_{j,n} - \lambda \delta_{j,0} \left(\sqrt{n+1}\psi_{j,n+1} + \sqrt{n}\psi_{j,n-1} \right) .\end{aligned} \tag{4.2}$$

The solution to the discretized Schrödinger equation is the sum of incoming and outgoing plane waves in the region before the barrier and consists of only outgoing plane waves in the region after the barrier, assuming ideal leads. This forms the first boundary condition for solving the discretized Schrödinger equation, the transmission is normalized to the final outgoing wave of the uppermost phonon branch. The solution is back-propagated using this condition. In addition, since ideal leads are assumed the coefficients of the incoming and outgoing waves are equal so the coefficient of the initial incoming wave for zero phonon quanta (the branch without phonons) is given by

$$A = \frac{e^{ik}\Psi[-j] - \Psi[-j+1]}{2isin(k)} \tag{4.3}$$

where $\Psi[-j]$ and $\Psi[-j+1]$ represent the wavefunction at the second to last and final sites calculated by back-propagating the solution from the outgoing wave. Here, we consider electron-phonon interactions at the central site only so electrons incident upon the barrier can absorb/emit energy quanta through phonon interactions at the central site only. To solve the Schrödinger equation consider three different wavefunctions which emerge from certain physical constraints: i) The wavefunctions which propagate out from the barrier site, $\psi_{j,n}$. ii) The wavefunction at the barrier site with the phonon interaction included, $\psi_{Cbarrier,n}$. iii) The scaled plane waves which propagate out from the barrier site $s * \psi_{j,m}$ where the scaling factor s is given by

$$s = \frac{\psi_{Cbarrier,n}}{\psi_{barrier,n}} \tag{4.4}$$

where $\psi_{Cbarrier,n}$ is the wavefunction at the central site. Beginning with the outgoing plane wave in the top phonon branch $\psi_{barrier+3,n}$, the solution proceeds through backpropagation using the Schrödinger equation to determine $\psi_{barrier+2,n}$ and $\psi_{barrier+1,n}$. Similarly, solutions are backpropagated from the waves reflected from the barrier. To generate the wavefunctions $\psi_{j-1,n}, \psi_{j,n}, \psi_{j+1,n}$ and $\psi_{j,n+1}$ at the barrier site for the highest two phonon branches, it is assumed that the wavefunctions at the barrier site are the back-propagated plane waves (without any phonon interaction). The wavefunction at the barrier site for the $n-1$ phonon branch ($\psi_{Cbarrier,n-1}$) can then be calculated. The outgoing waves of all subsequent phonon branches are scaled according to 4.4. This preserves the condition

$$s * \psi_{barrier,n} = \frac{\psi_{Cbarrier,n}}{\psi_{barrier,n}} * \psi_{barrier,n} = \psi_{Cbarrier,n} \tag{4.5}$$

where $\psi_{barrier,n}$ is calculated from backpropagation.

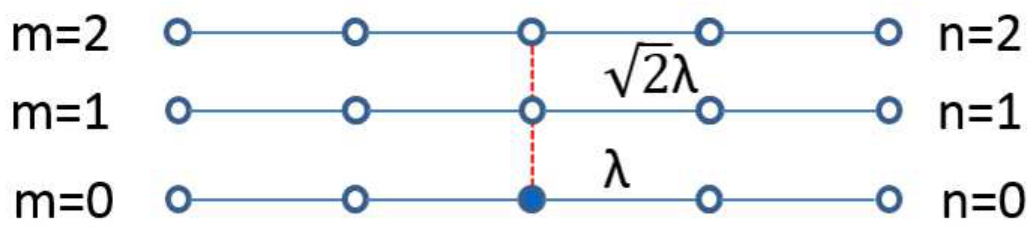


Figure 4.1: Representation of the many-body Hilbert space with each site representing a basis state, sites in the horizontal direction and phonon quanta in the vertical direction.

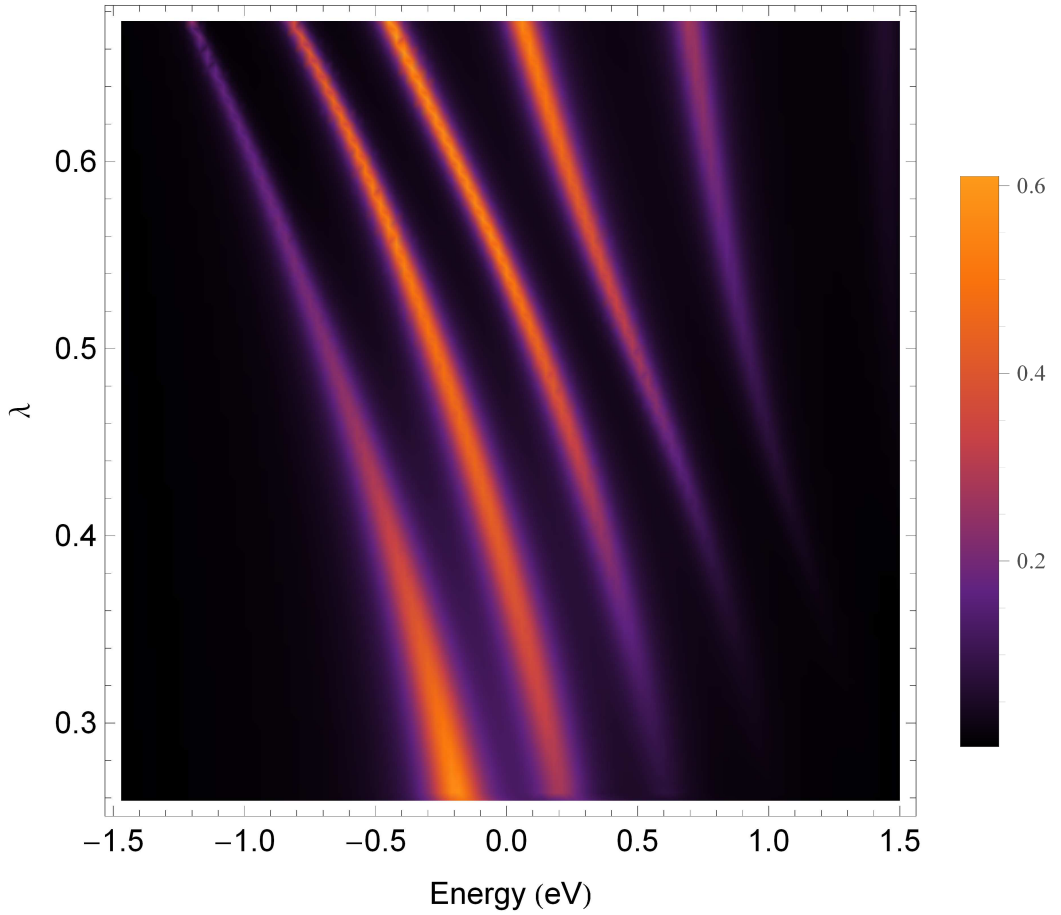


Figure 4.2: Intensity map of the transmission through a single molecular site as a function of the electron energy and the electron-phonon coupling strength.

4.3 Frequency-Independent Results

Figure 4.2 shows the transmission coefficient as a function of the incident electron energy, E, and the electron-phonon coupling strength (λ). The electron-phonon coupling strength is normalized to the hopping parameter. For low electron-phonon coupling strengths there are initially two transmission maxima. In this formalism, the eigenenergies are not calculated directly, instead the tight binding model is solved by back-propagation of the outgoing plane wave. Transmission maxima correspond to resonant energies i.e. the eigenenergies of the system. As the electron-phonon coupling strength increases, more transmission maxima appear which have a smaller full-width at half maximum (FWHM) than at smaller electron-phonon coupling. The transmission maxima also shift to lower (more negative) energies. As the electron phonon-coupling strength increases, more states become available at lower energies due to the exchange of energy between electrons and phonons, hence there are more transmission maxima.

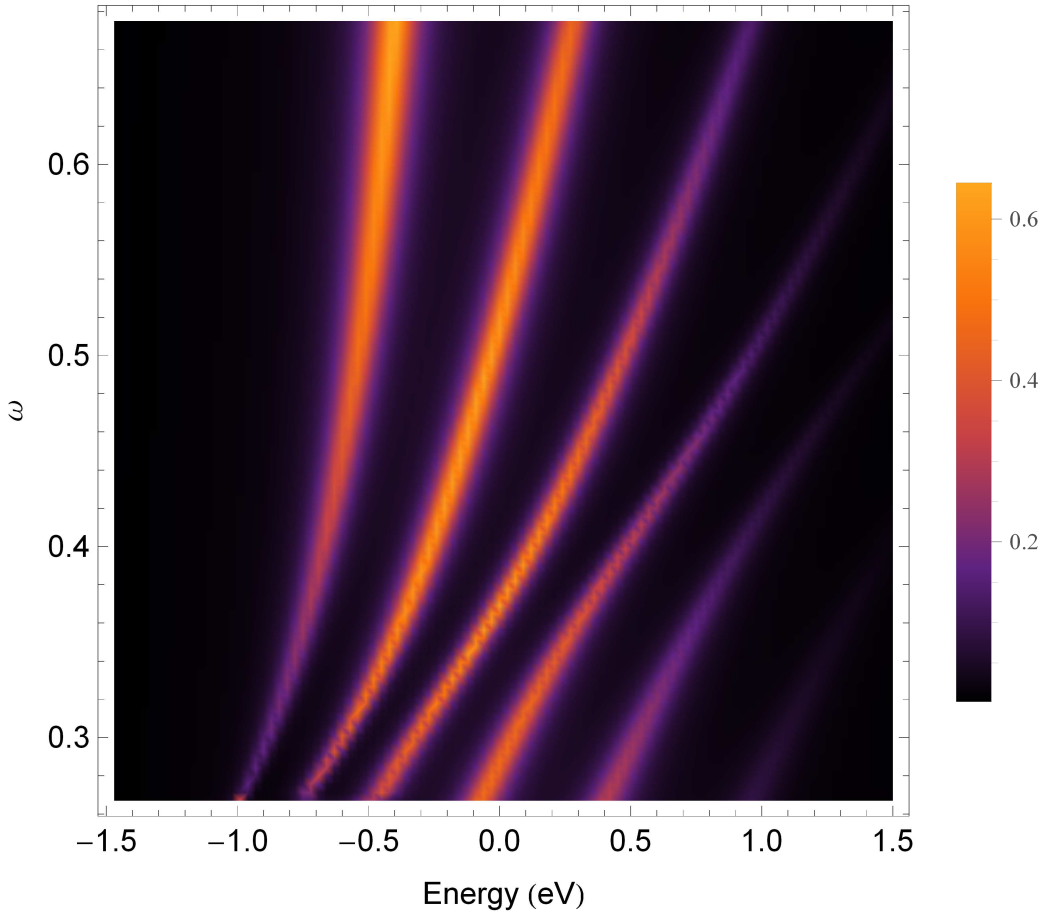


Figure 4.3: Intensity map of the transmission through a single molecular site as a function of the electron energy and the phonon frequency.

Figure 4.3 shows how the transmission changes as the phonon frequency (ω) is varied. As the phonon frequency increases, the eigenenergies shift to higher energy to compensate for the increase in frequency. The number of transmission maxima therefore decreases however the FWHM of the transmission maxima increases.

This method of back-propagation works well for symmetric problems and is well suited to calculations involving a number of phonon modes as it reduces to an exact algebraic problem which can be solved numerically very economically for a large number of phonon modes.

4.4 Time Dependent Electron-phonon Interactions

Time dependent transmission in the presence of electron-phonon interactions can also be studied by extending the variational space using Floquet theory. Here we assume that there is a time-periodic potential acting at the barrier site. The system Hamiltonian remains unchanged (Eq. 4.1) with the inclusion of a time periodic potential in place of the on-site energy with static (v_s) and dynamic potentials (v_d), $v(t) = v_s + v_d\,(e^{iwt} + e^{-iwt})$. This gate potential modifies the on-site energy term. The Hamiltonian for this time dependent problem is therefore the same as the Hamiltonian in Equation 4.1 with the on-site energy term replaced with the time dependent term.

Following Oymak [136], a polaron eigenbasis is employed

$$|j, n\rangle = \frac{1}{\sqrt{n!}} c_j^\dagger (a^\dagger)^n |0\rangle \tag{4.6}$$

and the time-dependent wavefunction is expanded in the polaron eigenbasis

$$\Psi(t) = \sum_{j=-\infty}^{\infty} \sum_{n=-\infty}^{\infty} \psi_{j,n}(t)\,|j, n\rangle \tag{4.7}$$

The Floquet theory is used to treat the time dependence, the wavefunction can be written as $\psi_{j,n}(t) = e^{-iEt}\phi_{j,n}(t)$ where $\phi_{j,n}(t)$ is a time-periodic potential with the same period as the time-periodic potential and E is the Floquet energy. $\phi_{j,n}(t)$ can then be Fourier expanded to yield $|\phi_{j,n}\rangle = \sum_p \phi_{j,n}\,|p\rangle$. This adds an extra dimension to the variational space, which becomes three dimensional and is illustrated in Figure 4.4. If the period is τ, then $\phi_j^n(\tau + t) = \phi_j^n(t)$ which can be Fourier expanded to yield

$$\phi_j^n(t) = \sum_{p=-\infty}^{\infty} \left(\frac{e^{-ip\omega t}}{\sqrt{\tau}}\right) \phi_j^{n,p} \tag{4.8}$$

where p represents Floquet states with $\langle t|p\rangle = \tau^{-1/2} e^{-ip}$. Equation 4.8 can then be expressed in the Floquet basis as

$$|\phi_j^n\rangle = \sum_p \phi_j^{n,p} |p\rangle \tag{4.9}$$

Acting on these states with the Hamiltonian yields

$$(E + p\omega - n\Omega)\phi_j^{n,p} = \quad v_s\phi_j^{n,p} + v_d(\phi_j^{n,p+1} + \phi_j^{n,p-1}) - \lambda(\sqrt{n+1}\phi_j^{n+1,p} + \sqrt{m}\phi_j^{n-1,p}) - t_{j,j+1}\phi_{j+1}^{n,p} - t_{j,j-1}\phi_{j-1}^{n,p} \quad (4.10)$$

This multi-dimensional single-body problem can be expressed compactly as a matrix equation,

$$\mathbf{E}\Phi_j = \mathbf{V}_j\Phi_j - \mathbf{\Delta_{j,j+1}}\Phi_{j+1} - \mathbf{\Delta_{j,j-1}}\Phi_{j-1} \quad (4.11)$$

where $\mathbf{E}$, $\mathbf{V}$ and Δ are matrices and Φ_j is a column vector.

This can then be solved using the following matrix recursion relation (the Ricatti matrix)

$$\Phi_{j+1} = \mathbf{Y}_j\Phi_j \ . \quad (4.12)$$

Further details can be found in [136].

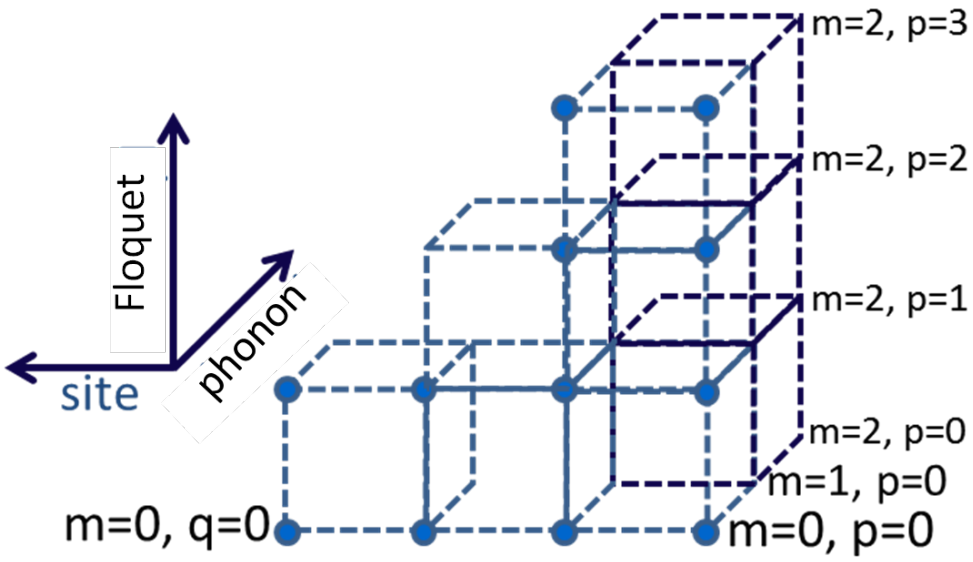


Figure 4.4: Mapping the many-body Hilbert space onto a multi-dimensional single-body problem within the tight-binding scheme using the Floquet theory.

4.5 Results using the Ricatti Matrix Method

Initially, we consider the transmission coefficient for a single barrier with a time-dependent gate potential. Figure 4.5 shows the transmission coefficient as a function of energy for

different strengths of the electron-phonon coupling parameter. When λ is small, there are two satellite transmission maxima which arise symmetrically on either side of the principal transmission maximum. As the electron-phonon coupling strength increases, additional transmission maxima appear asymmetrically about a global transmission maximum. As λ is increased to 0.4 (Fig. 4.5(c)), two transmission maxima of almost the same height occur while the amplitude of some of the other transmission maxima decreases. The energies of the transmission maxima shift as well. The shift in the transmission maxima is consistent with the previous calculations, validating the Ricatti matrix approach. Tuning the strength of the electron-phonon interaction allows the number of maxima as well as the position of the principal transmission maxima to be controlled.

The transmission coefficient for a fixed electron-phonon coupling strength under various phonon frequencies is shown in Figure 4.6. As the phonon frequency increases, the smaller transmission maxima shift however the energy of the principle transmission maximum changes little (while the amplitude increases slightly) and becomes less sensitive to the energy at higher phonon frequencies. This is also consistent with the previous calculations. The transmission coefficient and the position of the transmission maxima on either side of the principle transmission maximum change little.

The transmission coefficient as a function of energy for a fixed electron-phonon coupling strength under different frequencies for the time-dependent gate potential is shown in Figure 4.7. The energy of the principle transmission maximum shifts uniformly to higher energies while there is hardly any change in the amplitude of the transmission coefficient. This is very significant for device applications as it demonstrates that the energy of maximal transmission can be tuned through the frequency of an external gate potential. The relative difference between the amplitude of the largest and second largest maxima can also be tuned by the gate frequency.

4.6 Results from the Double Barrier Case

We now study the case of a double barrier structure which so far has never been studied using this technique. Barriers were created symmetrically about the central lattice site. While the computation becomes considerably more expensive as matrix inverses are calculated, the use of sparse array techniques drastically reduced computing time.

Figure 4.8 shows the transmission coefficient as a function of energy and the electron-phonon coupling strength. There are two prominent transmission maxima. As the coupling strength increases, the transmission maximum at higher energies shifts to lower energies. However the transmission maximum at lower energy does not shift although the amplitude changes slightly. This is significant for device applications. This is also the case for the adjacent smaller transmission maximum.

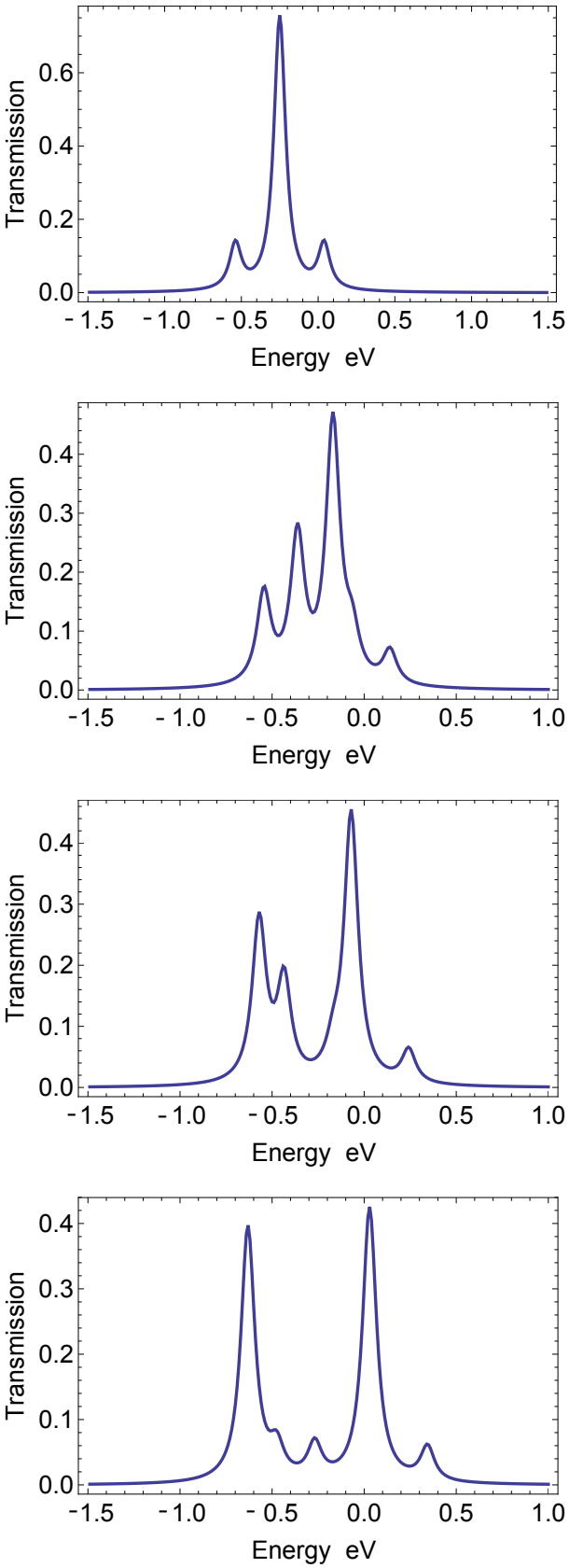


Figure 4.5: Transmission coefficient as a function of energy for a single barrier in the presence of the electron-phonon interaction. The electron-phonon coupling parameter λ is changed from 0 to 0.3 in steps of 0.1 from top to bottom.

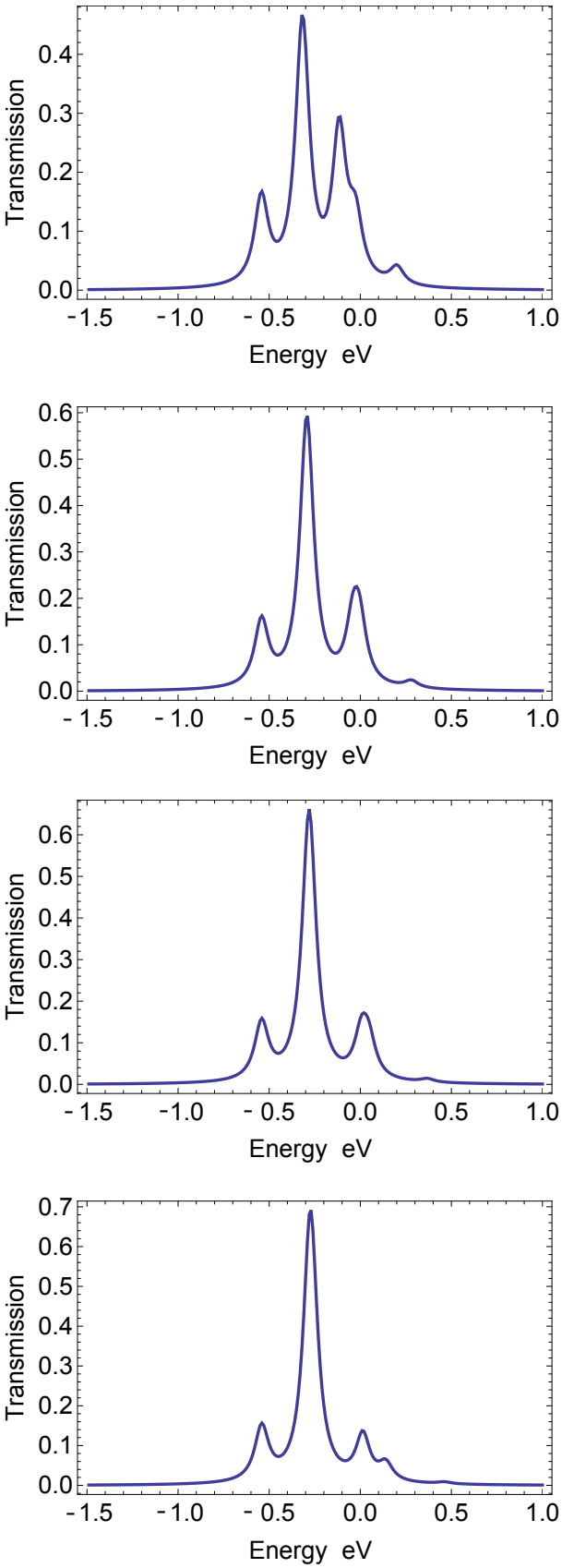


Figure 4.6: Transmission coefficient as a function of energy for a single barrier in the presence of the electron-phonon interaction under the influence of a time-periodic potential. The phonon frequency Ω is changed from 0.1 to 0.4 in steps of 0.1 from top to bottom.

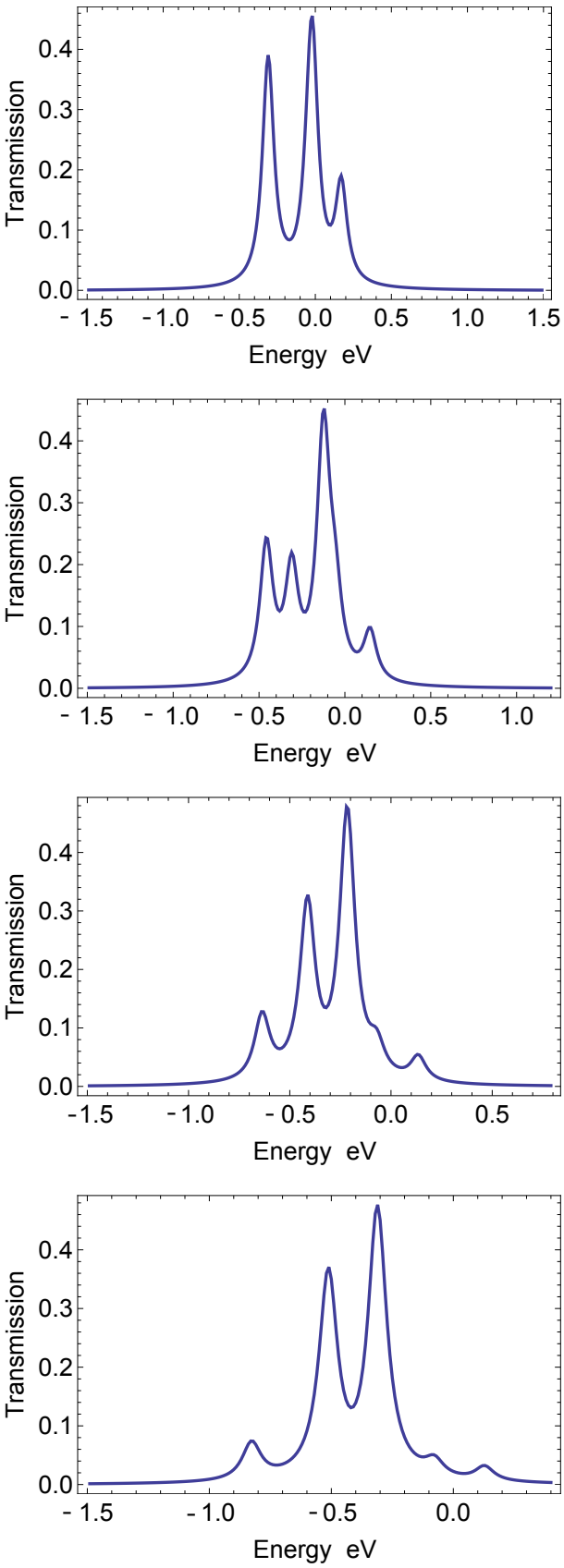


Figure 4.7: Transmission coefficient as a function of energy for a single barrier in the presence of the electron-phonon interaction under the influence of a time-periodic potential. The frequency of the gate potential ω is changed from 0.1 to 0.4 in steps of 0.1 from top to bottom.

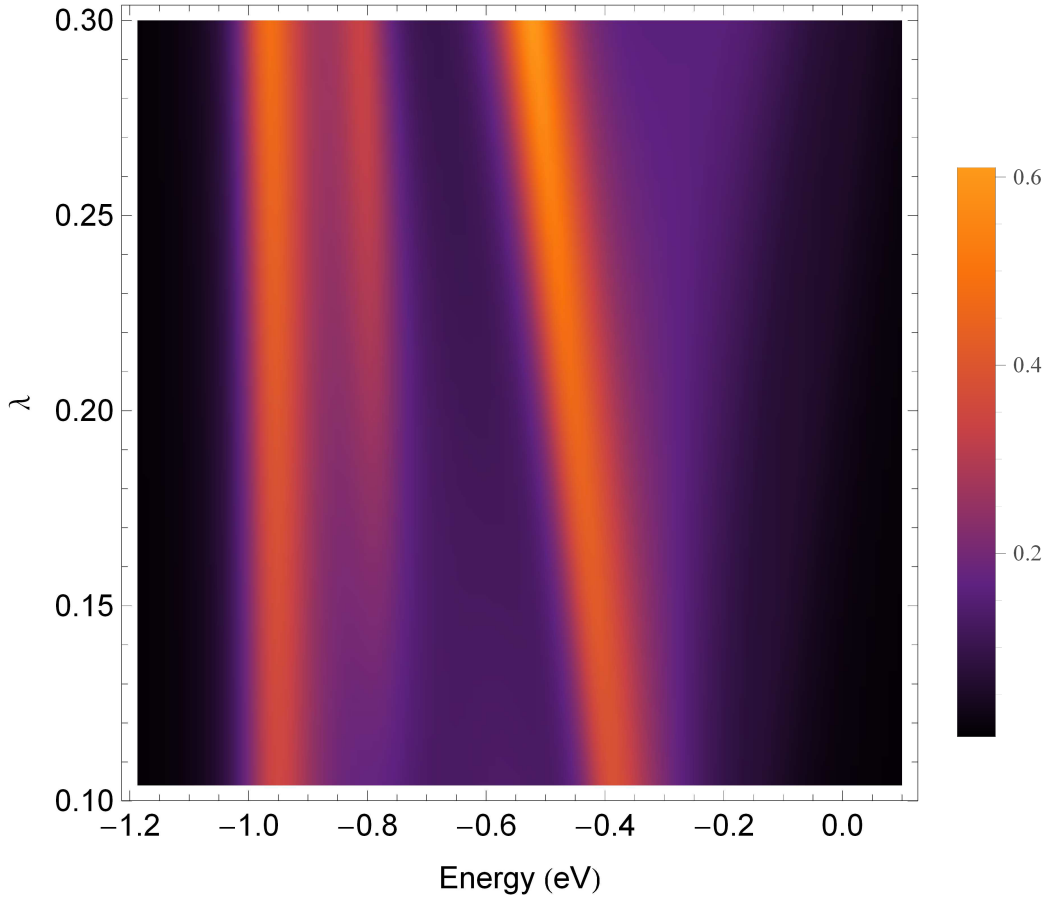


Figure 4.8: Intensity map of the transmission through a double barrier structure in the presence of the electron-phonon interaction and a time-dependent external potential as a function of the electron energy and the electron-phonon coupling parameter with the phonon frequency $\Omega = 0.2$ and $\omega = 0.2$.

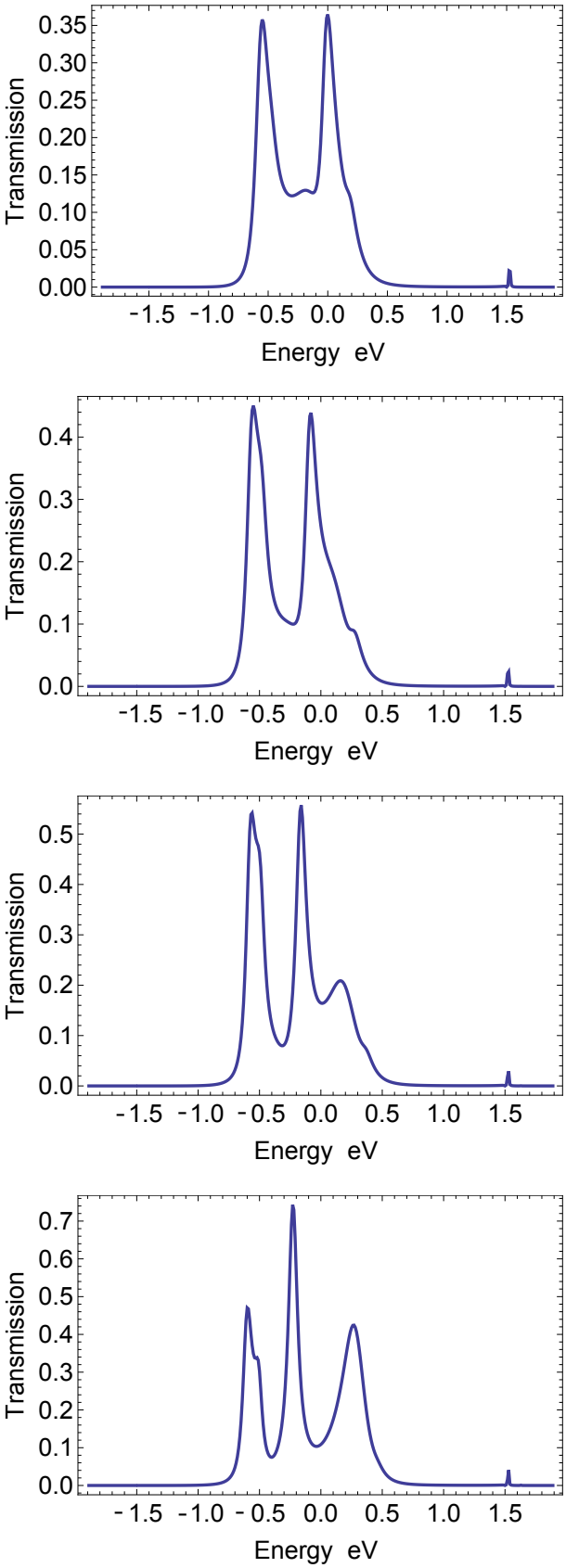


Figure 4.9: Transmission coefficient as a function of energy for a double barrier in the presence of the electron-phonon interaction under the influence of a time-periodic potential. The electron-phonon coupling strength λ is changed from 0.1 to 0.4 in steps of 0.1 from the top figure to the bottom figure.

Figure 4.9 shows the transmission coefficient as a function of energy for different electron-phonon coupling strengths. There are two main transmission maxima with another two transmission maxima merged with these, hence the imperfect Lorentizian shape. This also shows more clearly why the features in the the contour map appear broad (Fig. 4.8).

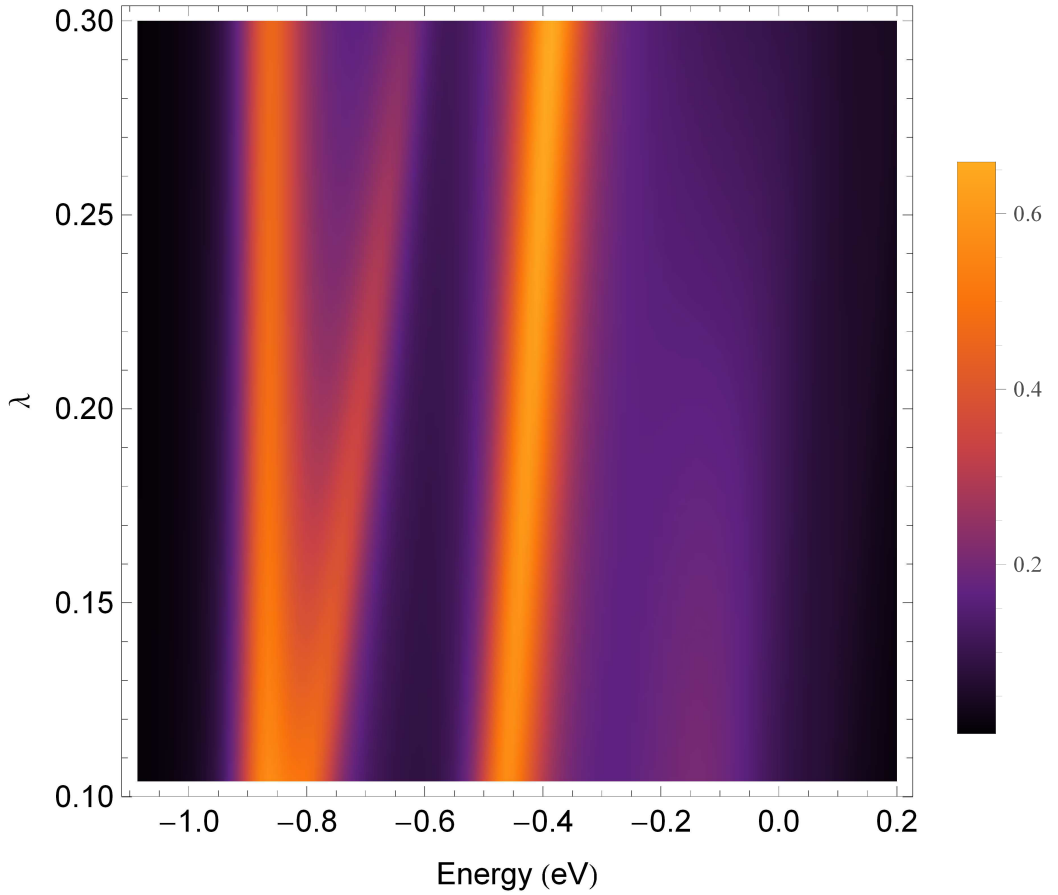


Figure 4.10: Intensity map of the transmission through a double barrier structure in the presence of the electron-phonon interaction and a time-dependent external potential as a function of the electron energy and the phonon frequency with $\lambda = 0.3$ and $\omega = 0.3$.

Figure 4.10 shows the transmission coefficient as a function of energy for different phonon frequencies. In this case there are also two primary transmission maxima. As the phonon frequency increases, the transmission maximum at -0.5 eV moves to lower energies. The second transmission maximum remains at the same energy in this case too while the adjacent transmission maximum shifts to lower energies.

Figure 4.11 shows the transmission coefficient for different frequencies of the gate potential. There are two principle transmission maxima with a very broad tail at higher energies. As the gate potential increases, the energy of the transmission maxima changes however there is hardly any change at all in the profile of the transmission coefficient. This is very significant as it is unlike any of the other cases studied so far. Changing the electron-phonon coupling strength or the phonon frequency has a direct effect on the behaviour of electrons confined in the double barrier structure and influences the transmission coefficient. When

the gate potential is changed though, it is a uniform change to the entire system so while the eigenenergies of the double barrier structure change, the transmission coefficient does not as there is no direct structural change.

The transmission coefficient for different frequencies of the gate potential is shown as an intensity map with $\lambda = 0.2$ and $\Omega = 0.5$ in Figure 4.12. The intensity map clearly shows a linear change in the energy of the transmission maxima with the change in frequency. Figure 4.13 shows the intensity map when the transmission is maximized, with $\lambda = 0.5$ and $\omega = 0.2$. This figure clearly illustrates that maximal transmission can be achieved over a wide range of gate potential frequencies and can easily be tuned very precisely.

4.7 Summary

This chapter provides insight into the control of resonant states in molecular systems using an external gate potential amid the effects of the electron-phonon interaction. Studies of single barrier systems were used to develop intuition and compare with previous works while studies of double barrier systems illustrate the promise of resonant levels which can be precisely tuned over a wide range to further the capabilities of quantum technologies.

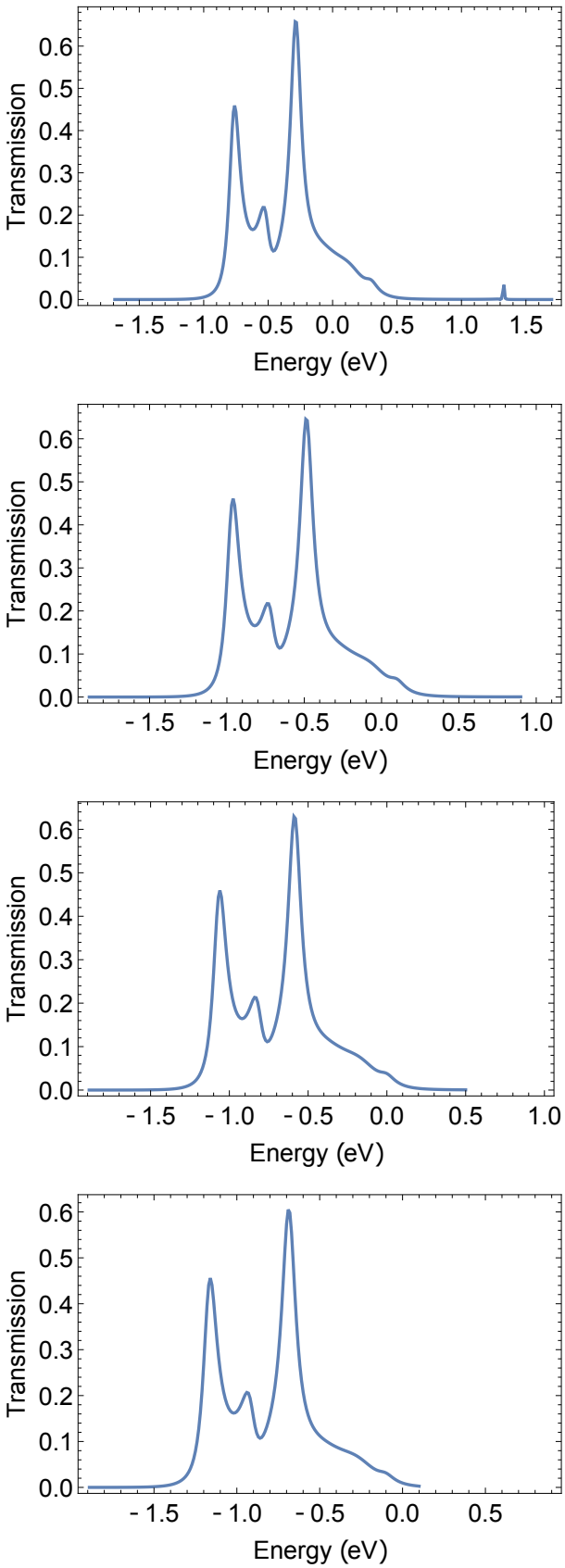


Figure 4.11: Transmission coefficient as a function of energy for a double barrier in the presence of the electron-phonon interaction under the influence of a time-periodic potential. The frequency of the gate potential ω is changed from 0.2 to 0.5 in steps of 0.1 from the top figure to the bottom figure, with $\lambda = 0.3$ and $\omega = 0.3$.

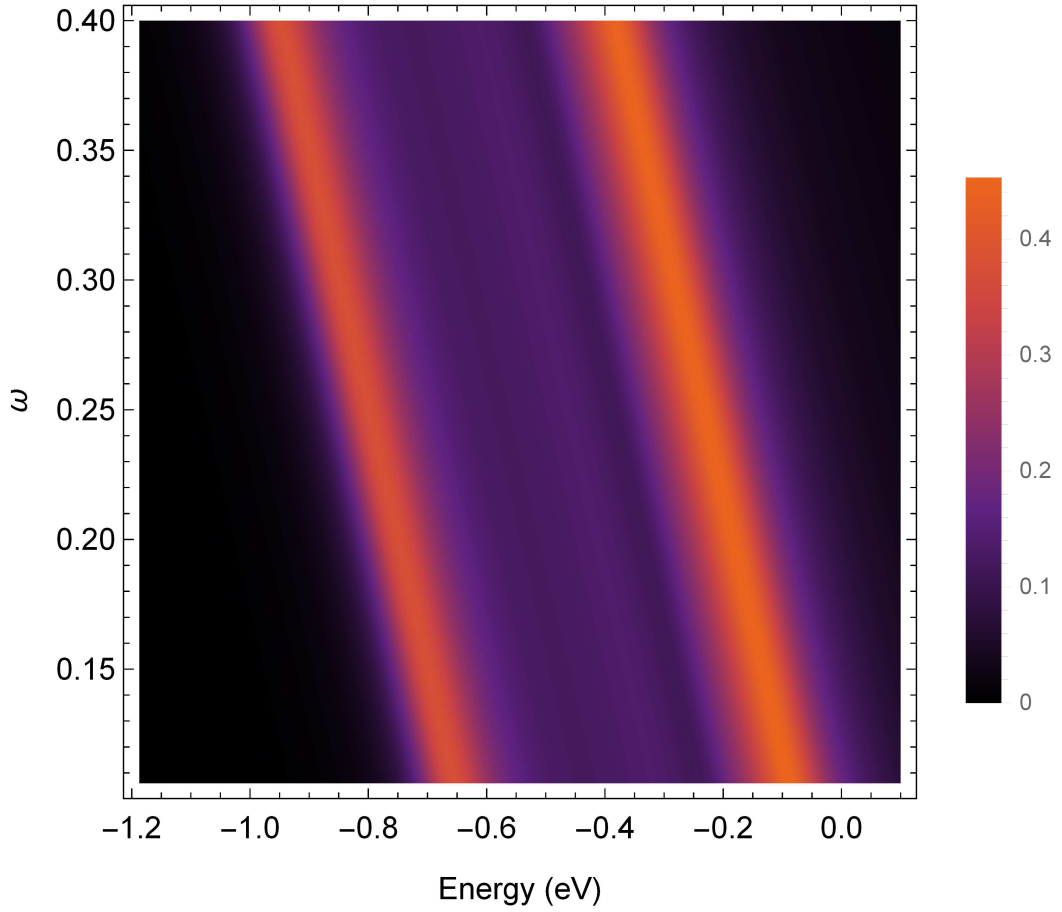


Figure 4.12: Intensity map of the transmission through a double barrier structure in the presence of the electron-phonon interaction and a time-dependent external potential as a function of the electron energy and the frequency of the gate potential with $\lambda = 0.2$ and $\Omega = 0.5$.

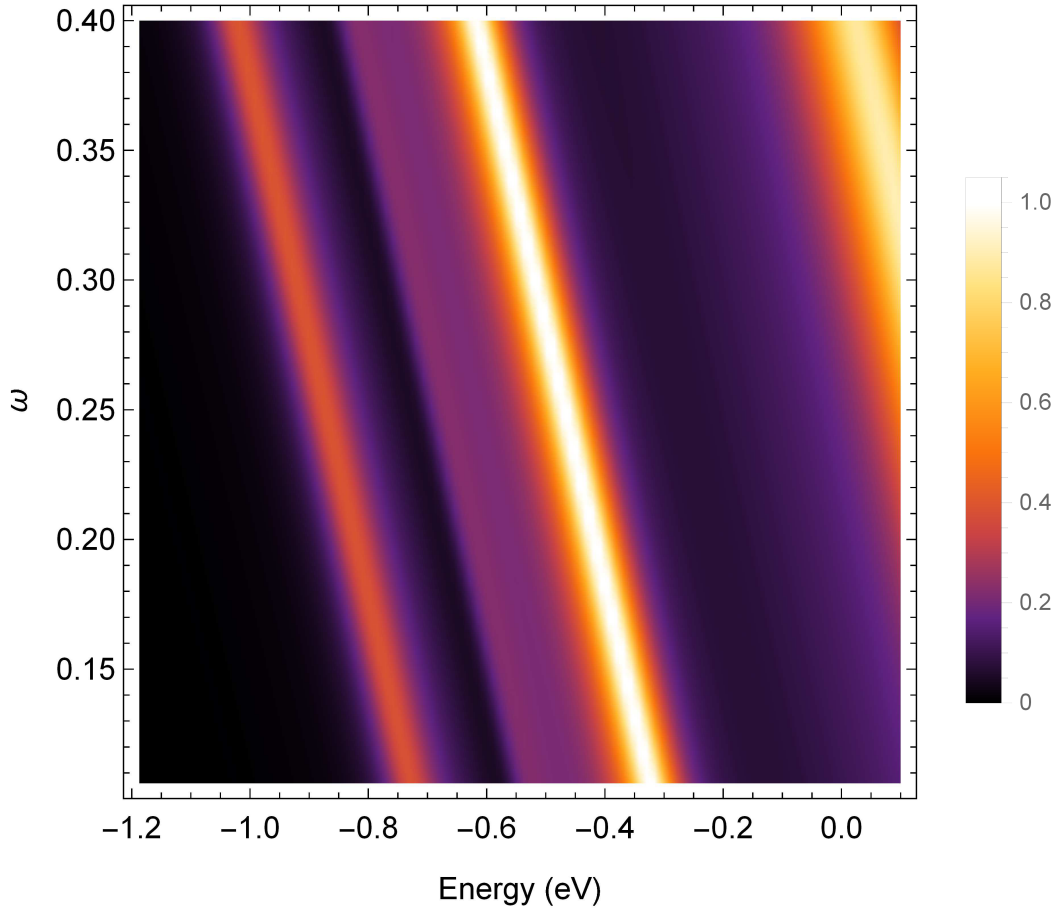


Figure 4.13: Intensity map of the transmission through a double barrier structure in the presence of the electron-phonon interaction and a time-dependent external potential as a function of the electron energy and the frequency of the gate potential with $\lambda = 0.5$ and $\Omega = 0.2$.

Chapter 5

Inhomogeneous BdG Theory Applied to B-NCD

Having explored the influence of structural disorder in nanostructured carbon in detail, the salient features of the model used thus far are adapted and extended to understand superconductivity in BDD and B-NCD. The role of disorder, both on-site and structural, in disordered superconductors was studied through the Bogoliubov-de Gennes theory. We consider a narrow-band, disordered superconductor with strong Coulomb interactions and apply this analysis to understand the role of structural disorder in boron doped diamond and nanodiamond. We illustrate distinct differences between the effects of structural and on-site disorder through calculating the pairing amplitude, density of states, pairing amplitude correlation functions and the superfluid density. Structural disorder is shown to enhance connectivity between adjacent regions, resulting in an overall increase in the mean pairing amplitude while the spectral gap decreases sharply. In addition, states begin to appear within the superconducting gap as structural disorder increases resulting in an pseudo-gap like phase. Calculations of the superfluid density illustrate that structural disorder rapidly destroys global superconductivity.

5.1 Introduction

The interplay of superconductivity and disorder close to the Anderson-Mott transition has long been of significant fundamental interest in understanding quantum phase transitions and emergent phenomena [95, 137, 138]. The pivotal role of disorder in these phase changes has come to the forefront as the influence of different forms of disorder are widely studied [78, 139, 85, 140, 141, 142, 143]. Studies of $2D$ localized superconductors using the Hubbard model with Anderson on-site disorder have shown that the spectral gap remains finite even at very high levels of disorder [83, 144, 84]. The transition from macroscopic superconducting coherence to localized regions with a finite pairing amplitude interspersed by insulating regions has been studied using the BdG theory as well as Monte Carlo analysis [84]. However,

the Coulomb interaction, which is prevalent in many systems close to the Anderson-Mott transition is often neglected [85]. While the role of structural disorder has been examined in the context of localization of electrons, [145] many aspects of the role of structural disorder in the superconductor-insulator transition are yet to be studied.

As a disordered, covalent superconductor with unusual properties, boron doped diamond is of fundamental interest in studying the superconductor-insulator transition. Boron doped diamond is a type II superconductor, with a T_c as high as 10 K [146, 147]. Immediately following the unexpected discovery of superconductivity in BDD came along a proposal that BDD may be a new form of high T_c superconductor, based expectedly on the resonating valence band (RVB) pairing mechanism [148]. However, experimental evidence so far strongly suggests a phonon mediated pairing [149, 150, 147] without any evidence for the involvement of spins.

Diamond is intrinsically a high band-gap insulator with a band-gap of 5.5 eV. Boron can be substitutionally incorporated in diamond, creating a deep, narrow acceptor band 0.37 eV above the valence band [151, 152]. While the acceptor states are three fold degenerate, the small spin-orbit coupling (6 meV) as well as the random distribution of boron impurities is thought to lift this degeneracy [148]. The transition with boron doping from insulator to superconductor has been studied in detail [153], with the critical concentration found to be around 3×10^{20} $carriers/cm^3$. To explain the transition with boron doping, density functional theory studies have indicated a rigid band shift of the Fermi level with doping, however experimental studies suggest impurity states without a rigid band [154]. It has been illustrated that the T_c in boron doped diamond is limited by the low density of states at the Fermi energy [152].

Photoemission studies of polycrystalline boron doped diamond have revealed a superconducting gap in the range expected for a weakly coupled Bardeen-Cooper-Schrieffer (BCS) superconductor while the characteristic broadening of the spectra is attributed to disorder [155]. Scanning transmission spectroscopy studies of B-NCD have indicated regions which exhibit superconductivity consistent with the weak BCS limit interspersed with regions which are non-BCS like [156]. In addition, B-NCD grains have also shown broadening of the gap, believed to be related to disorder, as well as to the distribution of grains with different onset of T_c [157]. The sharp differential conductance peaks (referred to as coherence peaks) associated with s-wave superconductivity have also been observed [147]. Temperature dependent studies of the gap showed that the differential conductance conformed in some regions with BCS theory for weak coupling while the temperature dependence did not follow the conventional BCS dependence in other regions [156].

Theoretical studies employing the coherent potential approximation, with disorder in the form of a random potential at the boron sites, predict an exponentially increasing T_c with boron concentration [158, 154] for disordered boron-doped crystalline diamond while experimental studies show an initially sharp increase in the T_c with boron incorporation

followed by a less prominent increase or even saturation [153, 159, 160, 149] indicating deviations from what would be expected from the standard BCS dependence [161]. The Berlitz theory however has been shown to result in saturation of the T_c which is in good agreement with experimental findings [162]. These studies have indicated that the Coulomb interaction between holes in the acceptor band should be significant (although it has not been included in the calculations) [148, 158, 154]. Density functional theory studies assuming phonon mediated superconductivity with random substitutional boron have suggested that the T_c for BDD could be as high as 55 K [163], providing motivation for understanding the role disorder plays in limiting the T_c. In addition, $ab-initio$ calculations have shown a difference in the bond-length associated with $C-C$ and $C-B$ bonds [163]. These effects, associated with structural disorder, have yet to be studied theoretically and applied to BDD or B-NCD.

In this study, we address the role of structural and on-site disorder within the narrow boron acceptor level. We consider a triangular lattice with a single boron acceptor band employing the inhomogeneous BdG theory. Disorder is treated in the form of random potential fluctuations at the boron sites as well as structural disorder in the form of a non-uniform hopping integral in the tight-binding term between adjacent sites. The level of structural disorder is correlated to the atomic boron concentration as this disorder is expected to increase due to local changes in bond length between $C-B$ bonds and surroungding $C-C$ bonds. We include the Coulomb interaction between holes in the acceptor band as it is a narrow band so the effect of the Coulomb interaction needs to be reckoned with [148]. We study the local pairing amplitude as well as the variation of the mean pairing amplitude, spectral gap and superfluid density as the disorder level increases. Through interpretation of the charge density of states, mean pairing amplitude, spectral gap, local superfluid density and phase stiffness we isolate the differences between structural and on-site disorder. We illustrate some overlap with experimental work, highlighting features of superconducting BDD and B-NCD which can be explained through the inclusion of structural disorder.

5.2 Model

We solve a tight-binding model considering a triangular lattice, incorporating the Coulomb interaction between acceptor states within the attractive Hubbard model. We employ the mean field approximation and generate the Hamiltonian using the BdG theory. The Hamiltonian is given by

$$\begin{aligned}\mathcal{H} = \quad & \sum_{i,\sigma}(\epsilon_i-\mu_i)c^\dagger_{i\sigma}c_{i\sigma}+\sum_i(\Delta(r_i)c^\dagger_{i\uparrow}c^\dagger_{i\downarrow}+\Delta^*(r_i)c_{i\downarrow}c_{i\uparrow}) \\ & -\sum_{\langle i,j\rangle,\sigma}t_{ij}(c^\dagger_{i\sigma}c_{j\sigma}+h.c.)+\sum_{\langle i,j\rangle}W_{ij}(n_in_j),\end{aligned} \tag{5.1}$$

where ϵ_i is the potential at each site, μ_i is the chemical potential at each site with $c^\dagger_{i\sigma}$ ($c_{i\sigma}$) being the fermion operators of creation (annihilation) at each site. The hopping integral between adjacent sites is t_{ij} while the strength of the Coulomb interaction between adjacent sites is W_{ij}, which is also treated within the mean-field approximation. $\Delta(r_i)$ is the local order parameter with co-ordinate r_i at site i and is given by $\Delta(r_i) = -U\langle c_{i\uparrow}c_{i\downarrow}\rangle$ where U is the interaction strength which is held fixed at $U = 4t$.

This Hamiltonian is rendered diagonalizable through the Bogoliubov-Valatin transformations for the fermion operators

$$c_{i\sigma} = \sum_{n,\sigma'} u_{n\sigma\sigma'}(r_i)\gamma_{n\sigma'} + v^*_{n\sigma\sigma'}(r_i)\gamma^\dagger_{n\sigma'} \tag{5.2}$$

The local order parameter can then be expressed as

$$\begin{aligned}\Delta(r_i) = \quad & -U\sum_n u_{n\uparrow}(r_i)v^*_{n\downarrow}(r_i)[1 - f(E_n)] \\ & + u_{n\downarrow}(r_i)v^*_{n\uparrow}(r_i)f(E_n),\end{aligned} \tag{5.3}$$

where $f(E_n)$ is the Fermi-Dirac distribution function. The local occupation number is given by

$$n(r_i) = \sum_n |u_{n\uparrow}(r_i)|^2 f(E_n) + |v_{n\uparrow}(r_i)|^2(1 - f(E_n)) \tag{5.4}$$

The resulting Hamiltonian is of the form

$$\sum_j \begin{pmatrix} \mathcal{H}_{i,j} & \Delta_{i,j} \\ \Delta^*_{i,j} & -\mathcal{H}^*_{i,j} \end{pmatrix} \begin{pmatrix} u_n(r_j) \\ v_n(r_j) \end{pmatrix} = E_n \begin{pmatrix} u_n(r_j) \\ v_n(r_j) \end{pmatrix} \tag{5.5}$$

which is diagonalized self-consistently until sufficient convergence of the order parameter. We work with a triangular lattice of 25×25 sites, having found this to be sufficiently large to overcome finite size effects as shown in the Fig. 5.2. All energy scales were normalized to the hopping integral. The chemical potential of the boron sites (relative to the carbon sites) was determined by calculating self-consistently the chemical potential which would give the correct occupation (for the desired impurity concentration).

The density of charge states is given by

$$\begin{aligned}\rho(E) = \frac{1}{N}\sum_{n,r_i,\sigma} & |u_{n\sigma}(r_i)|^2\delta(E - E_n) \\ & + |v_{n\sigma}(r_i)|^2\delta(E + E_n)\end{aligned} \tag{5.6}$$

where N is the total number of lattice sites.

The superfluid density is calculated to study the rigidity of the superconducting phase [164, 165]. This is achieved through the linear response of the system to an external time-dependent vector potential applied in the x direction, $A_x(r,t) = A(q,\omega)e^{i\mathbf{q}\cdot\mathbf{r}_i - i\omega t}$. The hopping term is then modified by the Peierls phase factor, $c^\dagger_{i+x,\sigma}c_{i\sigma} \to c^\dagger_{i+x,\sigma}c_{i\sigma}e^{ieA_{ij}}$ where $A_{ij} = \int_{\mathbf{r}_j}^{\mathbf{r}_i} \mathbf{A}(\mathbf{r},t)\cdot d\mathbf{r}$ (with units $c = 1 = \hbar$) and $i+x$ represents the next site in the x direction and e is the electron charge . These terms are expanded to second order in A yielding

$$H'(t) = -\sum_i \left(e j^p_x(\mathbf{r}_i)A_x(\mathbf{r}_i,t) + \frac{e^2 k_x(\mathbf{r}_i)}{2} A^2_x(\mathbf{r}_i,t) \right) \tag{5.7}$$

with a kinetic energy density (diamagnetic response)

$$k_x(\mathbf{r}_i) = -\sum_\sigma (t_{i,i+x}c^\dagger_{i\sigma}c_{i+x,\sigma} + H.c.) \tag{5.8}$$

and paramagnetic current density

$$j^p_x(\mathbf{r}_i) = -i\sum_\sigma (t_{i,i+x}c^\dagger_{i\sigma}c_{i+x,\sigma} + H.c.)\,. \tag{5.9}$$

The charge current density operator is given by the functional derivative

$$J^Q_x(\mathbf{r}_i) = -\frac{\delta H'(t)}{\delta A_x(\mathbf{r}_i,t)}\,. \tag{5.10}$$

The superfluid weight ρ_s, defined as the superfluid density divided by mass, is then given by

$$\frac{\rho_s}{m^*} = -\frac{\langle J^Q_x(r_i)\rangle}{e^2 A_x(r_i)}\,. \tag{5.11}$$

The average over the paramagnetic current density can be expressed, in the interaction representation, as

$$\langle j^p_x(r_i)\rangle = -i\int_{-\infty}^{t} \langle [j^p_x(r_i,t), H'(t')]\rangle dt'\,. \tag{5.12}$$

The long-wavelength, zero frequency limit yields the superfluid weight in the direct current regime which is studied here. Using the relation $H' = -\int d^3r\, j^p_x(r_i)A(\mathbf{r},t)$ the thermo-

dynamic average over the paramagnetic current density can be reduced to

$$\langle j_x^p(r_i)\rangle = -\frac{eA_x(r,t)}{N}\Pi_{xx}(\mathbf{q},\omega)\,. \tag{5.13}$$

This is evaluated in the Matsubara formalism as a current-current correlation function

$$\Pi_{xx}(\mathbf{q}, iw_n) = -\int_0^{1/k_BT} d\tau e^{iw_n\tau}\langle T_\tau j_x^p(\mathbf{q},\tau) j_x^p(-\mathbf{q},0)\rangle \tag{5.14}$$

Finally, the superfluid weight can be expressed as

$$\frac{\rho_s}{m^*} = \langle -k_x\rangle + \Pi_{xx}(q_x = 0, q_y \to 0, \omega = 0)\,. \tag{5.15}$$

In real space, the current-current correlation in the Matsubara formalism can be expressed as

$$\Pi_{xx}(\mathbf{r}_1, \mathbf{r}_2; \tau_1 - \tau_1') = -\langle T_\tau j_x^p(\mathbf{r}_1,\tau_1) j_x^p(\mathbf{r}_2,\tau_1')\rangle. \tag{5.16}$$

This is evaluated by performing the Bogoliubov transformations for the Fermion operators, yielding Green's functions taken over 4 operators. These are reduced to products of 2-particle operators using Wick's theorem which states that the Green's functions can be reduced to products of 2-particle Green's functions. So, a Green's function of the form obtained from the Bogoliubov transformations as follows

$$\langle T_\tau \psi_\sigma(\mathbf{r_2},\tau_2)\psi_{\sigma'}(\mathbf{r_2}',\tau_{2'})\psi_{\sigma'}^\dagger(\mathbf{r_1}',\tau_1')\psi_\sigma^\dagger(\mathbf{r_1},\tau_1)\rangle \tag{5.17}$$

can be reduced to

$$\begin{aligned}&\langle T_\tau \psi_\sigma(\mathbf{r_2},\tau_2)\psi_\sigma^\dagger(\mathbf{r_1},\tau_1)\rangle\langle T_\tau \psi_{\sigma'}(\mathbf{r_2}',\tau_{2'})\psi_{\sigma'}^\dagger(\mathbf{r_1}',\tau_1')\rangle \\ -&\langle T_\tau \psi_\sigma(\mathbf{r_2},\tau_2)\psi_{\sigma'}^\dagger(\mathbf{r_1}',\tau_1')\rangle\langle T_\tau \psi_{\sigma'}(\mathbf{r_2}',\tau_{2'})\psi_\sigma^\dagger(\mathbf{r_1},\tau_1)\rangle\end{aligned} \tag{5.18}$$

The final expression for the local kinetic energy (at site i) along lattice sites in the x direction, obtained by substitution of the Bogoliubov-Valatin transformations for the Fermion operators, is given in terms of the eigenvalues of the Bogoliubov quasi-particles as

$$k_x^i = -\sum_{n,\sigma} f(E_n)[u_{i+x,\sigma}^{n*}u_{i\sigma}^n + u_{i+x,\sigma}^n u_{i\sigma}^{n*}] + (1 - f(E_n))[v_{i+x,\sigma}^n v_{i\sigma}^{n*} + v_{i+x,\sigma}^{n*}v_{i\sigma}^n] \tag{5.19}$$

where the summation over n runs over the eigenvalues of the Bogoliubov quasiparticles. The mean kinetic energy is the average over all lattice sites.

The current current correlation function is evaluated using Matsubara formalism for the Green's functions. It is calculated in the long-wavelength, zero frequency limit. The limits must be evaluated in the correct order.

The final expression is given by a double summation over the lattice sites (which is averaged to find the mean paramagnetic response) and the eigenvalues of the Bogoliubov quasi-particles,

$$\Pi_{xx}(q, w \to 0) = \sum_{n_1,n_2} 4\Gamma^i_{n_1,n_2}(\Gamma^{j*}_{n_1,n_2} + \Upsilon^j_{n_1,n_2})\frac{f(E_{n_1}) - f(E_{n_2})}{E_{n_1} - E_{n_2}} \tag{5.20}$$

where

$$\Gamma^i_{n_1,n_2} = u^{n_1*}_{i+x}u^{n_2}_i - u^{n_{1*}i}u^{n_2}_{i+x} \tag{5.21}$$

$$\Upsilon^i_{n_1,n_2} = v^{n_1}_{i+x}v^{n_2*}_i - v^{n_1}_i v^{n_2*}_{i+x} \ . \tag{5.22}$$

Calculations were performed in MATLAB on the Mathematical Sciences cluster, Wits. Calculations of the superfluid density typically took around a day to complete depending on the number of points calculated.

5.2.1 The incorporation of disorder

We study two broad classes of disorder. Initially, we consider disorder in the form of random deviations in the local on-site potential energy at the boron sites only. We assume a normal distribution about some mean value which corresponds to the correct chemical potential to set the correct occupation i.e. we assume ϵ_i takes on values from a normal distribution centered at $\epsilon_i = 0$. The full width at half maximum of the normal distribution is referred to as the disorder parameter, σ. The disorder parameter is quoted in terms of the tight binding hopping parameter, t, as all energies are normalized to this scale. We also study the case of random on-site disorder at each lattice site in order to directly compare the characteristics of on-site disorder to those of structural disorder.

We then study the influence of structural disorder. We assume that bond length disorder results in changes in the tight-binding hopping integral through a deformation potential (which relates the change in distance between atomic sites to a change in the hopping integral (γ) between the sites). A schematic diagram is shown in Figure 5.1. Structural disorder is also incorporated through random nearest neighbour hopping parameters ($t_{i,j}$) following a normal distribution about some mean value with full width at half maximum of σ. We assume structural disorder throughout all lattice sites. In the case of B-NCD grains, structural disorder will likely play a large role due to the inherent structural inhomogeneity.

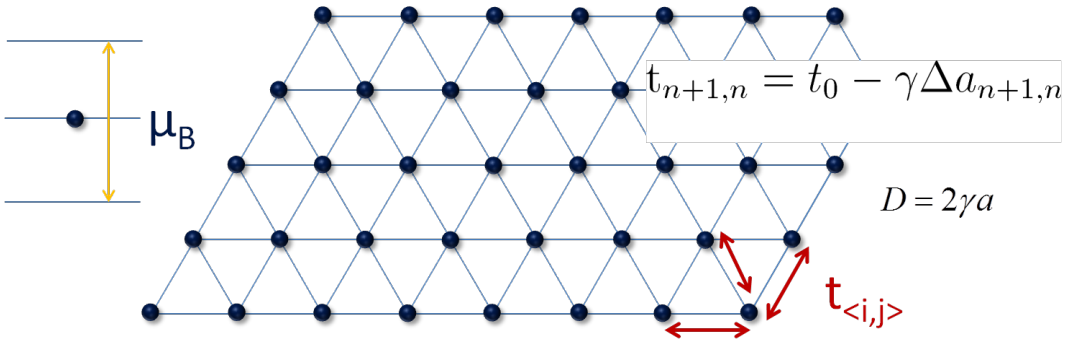


Figure 5.1: Schematic diagram of the structural model we employ.

We also study a form of correlated structural disorder where the structural disorder parameter changes as the boron atomic concentration changes. Experimental studies have shown that boron incorporation in diamond and nanodiamond is accompanied by microstructural changes in the films due to slight modification of the local bonding environment in the region of the boron impurities [153]. At this stage, we assume three different forms of correlated disorder i.e. disorder parameter increasing linearly with the atomic boron concentration, increasing exponentially and inverse exponential increase.

5.2.2 Lattice size

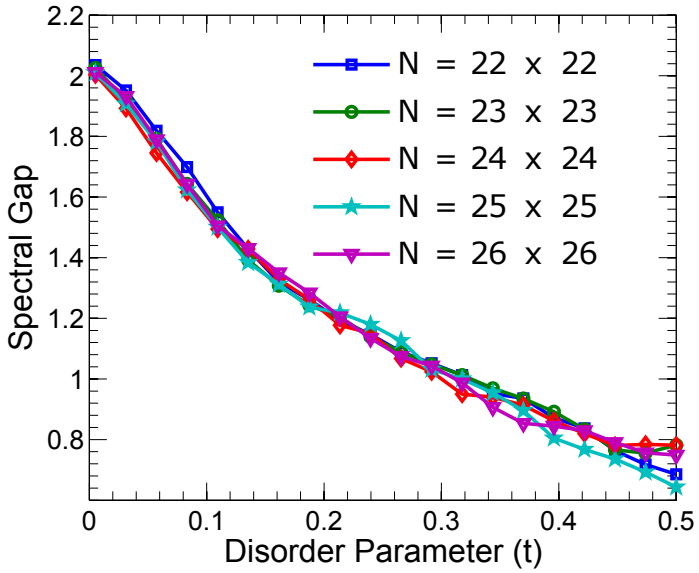


Figure 5.2: Spectral gap as a function of the structural disorder parameter expressed in units of the hopping parameter, t, (in the absence of on-site disorder with W = 0 i.e. no Coulomb interaction) for different lattice sizes.

Figure 5.2 shows the variation of the spectral gap with structural disorder in the absence of on-site disorder and with the Coulomb interaction turned off for lattice sizes ranging from 22×22 to 26×26. There is hardly any difference in the spectral gap indicating that a lattice size of 25×25 is sufficient to yield consistent results.

5.3 Results

5.3.1 On-site potential disorder

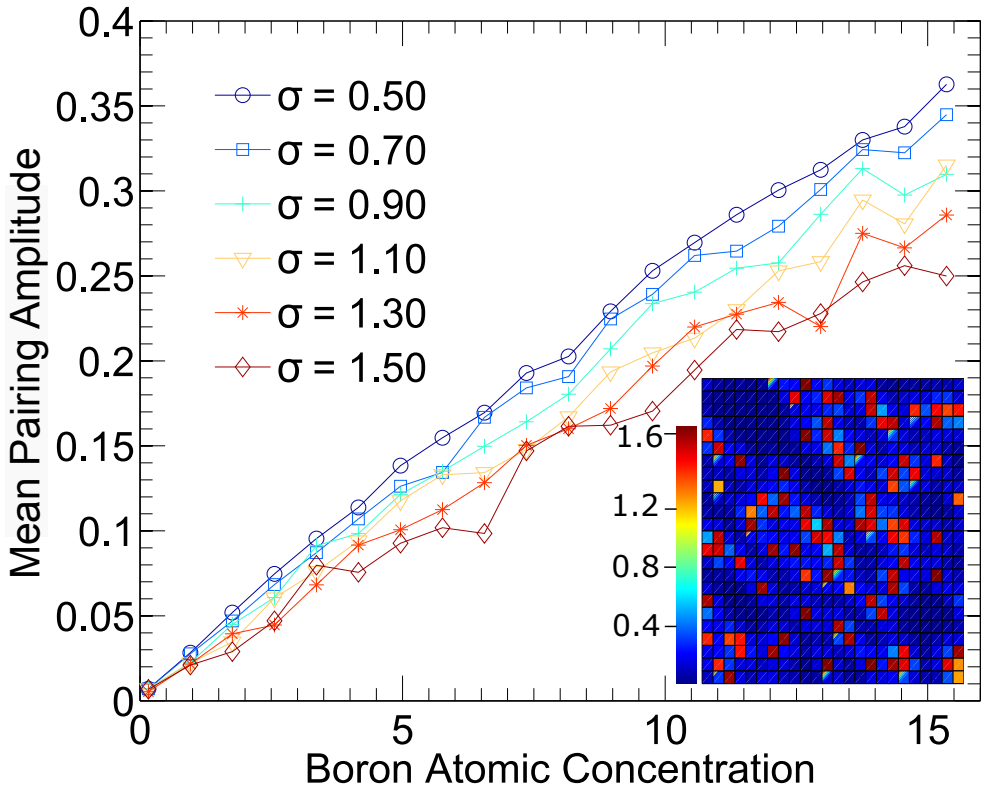


Figure 5.3: Mean pairing amplitude as a function of the boron concentration considering only on-site disorder where the disorder parameter is varied from 0.5 to 1.5. Inset is the local pairing amplitude considering a small on-site disorder parameter $\sigma = 0.05$

Although the upper limit of the boron doping concentration in diamond is relatively low (up to around 5 %), we focus on doping concentrations from 0 % up to 15 % to highlight the effects of disorder. The inset in Fig. 5.3 shows the local pairing amplitude at each lattice site where there is only on-site disorder considering a small disorder parameter (0.05). The local pairing amplitude is finite only at or close to the boron sites and correlates well with the local occupation in the low disorder regime (not shown here).

Figure 5.3 shows the mean pairing amplitude as a function of the atomic boron concentration for various on-site disorder parameters from 0.5 to 1.5 considering on-site disorder only at the boron sites. The mean pairing amplitude varies non-smoothly with increasing disorder parameter. Figure 5.3 shows that while on-site disorder can suppress the mean pairing amplitude to some extent, this is only possible if the potential fluctuations are very large, on the order of the hopping parameter. This indicates that disorder in the form of on-site energy of the boron impurities alone is not sufficient to reproduce the experimentally reported suppression (at relatively low doping concentrations) of the pairing amplitude

with increasing boron concentration. Comparison of the local on-site energy with the local pairing amplitude (not shown here) indicates that where the on-site energy is reduced, the pairing amplitude increases.

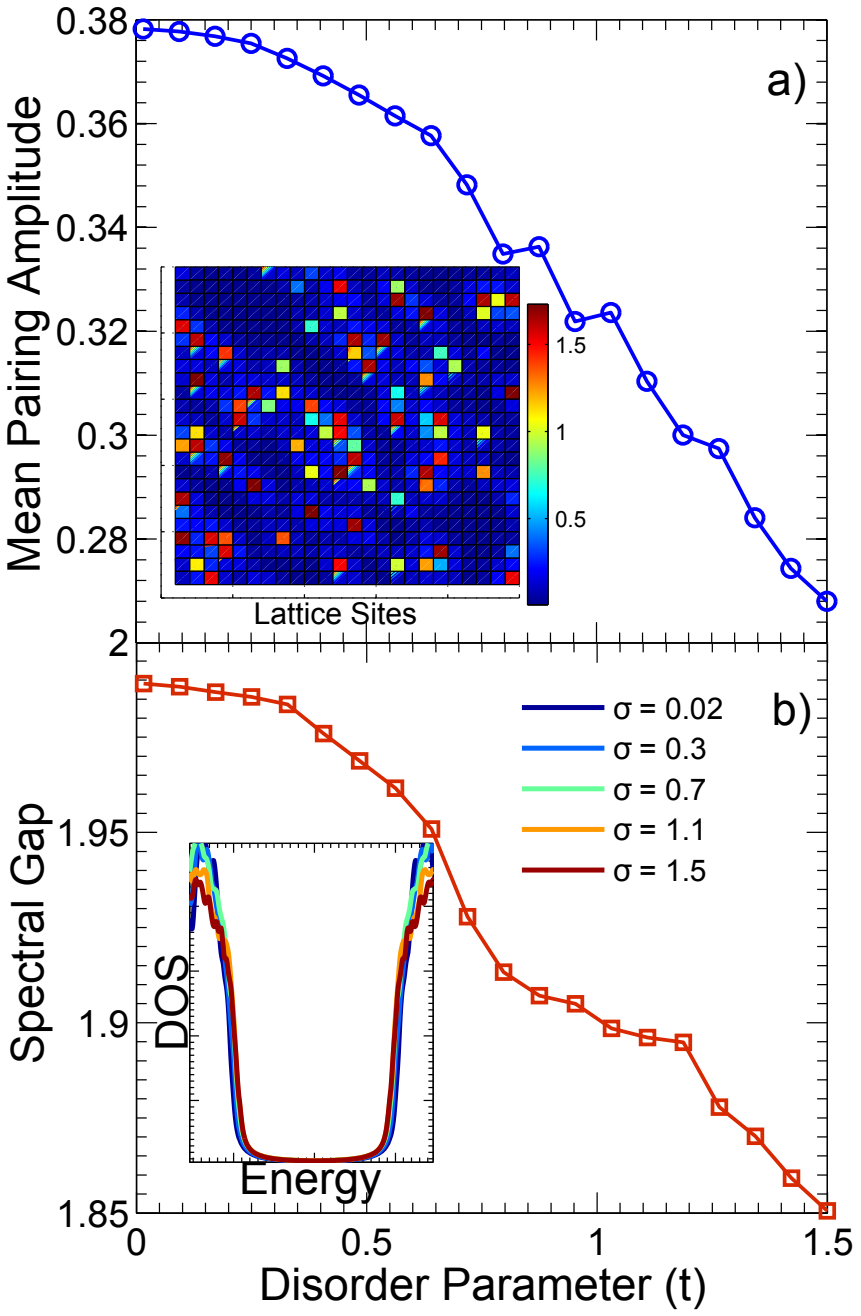


Figure 5.4: a) Mean pairing amplitude as a fucntion of the on-site disorder paramater (considering only on-site potential disorder at the boron sites only) where the atomic boron concentration is held fixed at 15 %. Inset is the local pairing amplitude at each lattice site with a relatively large on-site disorder parameter of $\sigma = 1.5$. b) The corresponding spectral gap as a function of the on-site disorder paramater. Inset is the density of the states in the vicinity of the gap.

To determine the effects of on-site disorder we study the mean pairing amplitude, spec-

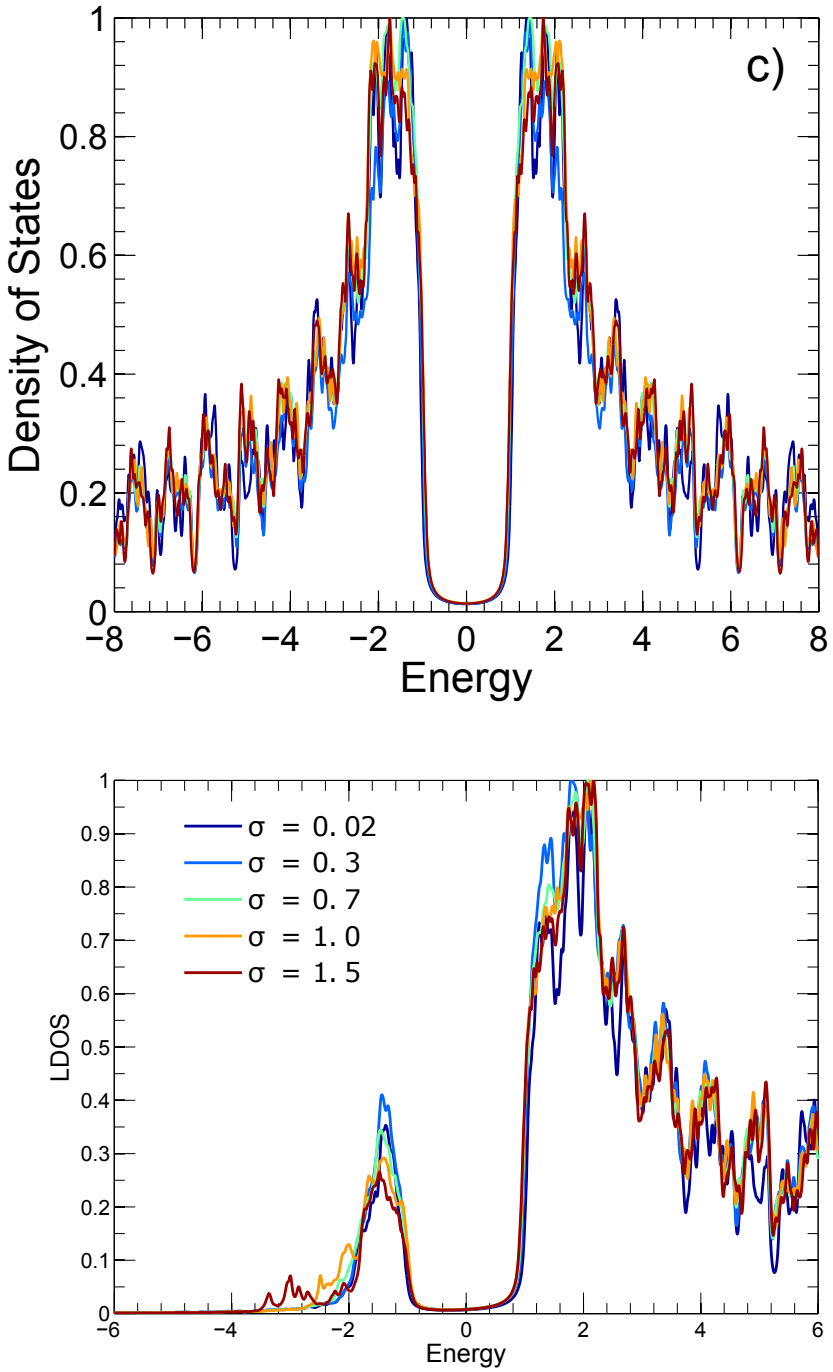


Figure 5.5: a) Density of states where the boron concentration is held fixed and the on-site disorder parameter is varied. b) Corresponding local density of states

tral gap, density of states and the distribution of pairing amplitudes for different disorder parameters while the boron concentration is held fixed, initially assuming on-site potential fluctuations at the boron sites only. The on-site disorder parameter (σ) is varied from 0.5 to 1.5. Figure 5.4(a) shows the variation of the mean pairing amplitude as the on-site disorder parameter is varied. The mean pairing amplitude decreases with increasing disorder. In the high disorder regime there is a wider distribution of local pairing amplitudes (inset of Fig. 5.4(a)).

The spectral gap decreases with increasing disorder however the overall change is not very large, as illustrated in Fig. 5.4(b). The spectral gap follows a similar trend to the mean pairing amplitude. The variation is inherently noisy as we have assumed a very small smearing factor (to approximate the delta function, see Eq. 5.6) when calculating the DOS so calculations of the spectral gap are very sensitive to the very small changes in the disorder parameter which arise due to on-site disorder).

The density of states (Fig. 5.5(a)) shows very little change, despite the on-site disorder parameter varying largely. The spectral gap remains intact and does not transition to a pseudo-gap however there is a small decrease in the density of states in the region close to the gap (corresponding to a decrease in the sharpness of the coherence peaks). The noise in the DOS is due to the small smearing factor we have used in approximating the delta function in Eq. 5.6 which is necessary to reveal the small changes which take place in the vicinity of the gap.

The local density of states (density of states at a specific lattice site), shown in Figure 5.5(b), highlights the effects of structural disorder in the region of the gap. While no states become available within the gap region, there is a clear shift in the coherence peaks. Initially, the amplitude of the coherence peaks increases slightly although they do broaden as well. With increasing on-site disorder, the amplitude of the coherence peaks begins to decrease as they continue to broaden out. The coherence peaks are an important feature of conventional superconductors.

Figure 5.6 shows the distribution of the local pairing amplitudes considering only on-site disorder at the boron sites. When the disorder parameter is low the number of lattice sites with an almost uniform pairing amplitude of around $1.6t$ is relatively large while most lattice sites have zero pairing amplitude. With increasing on-site disorder, the number of lattice sites with pairing amplitude around $1.6t$ decreases while the number of lattice sites with pairing amplitude around zero increases. Except for relatively high disorder (disorder parameter 1.5) there are few lattice sites with pairing amplitude between $0.6t$ and $1.2t$. We study the correlation functions of the local pairing amplitude, $D(|r_i - r_j|) = \langle \Delta(r_i)\Delta(r_j) \rangle$ to glean insight into the range of the order parameter. The inset in Fig. 5.6 shows the pairing amplitude correlation function considering only on-site disorder with a small disorder parameter ($0.02t$, blue curve) while the red curve shows the corresponding correlation function where the structural disorder parameter is larger ($1.5t$). The change in

the correlation functions is not large however there is a crossover in the correlation functions as the distance increases.

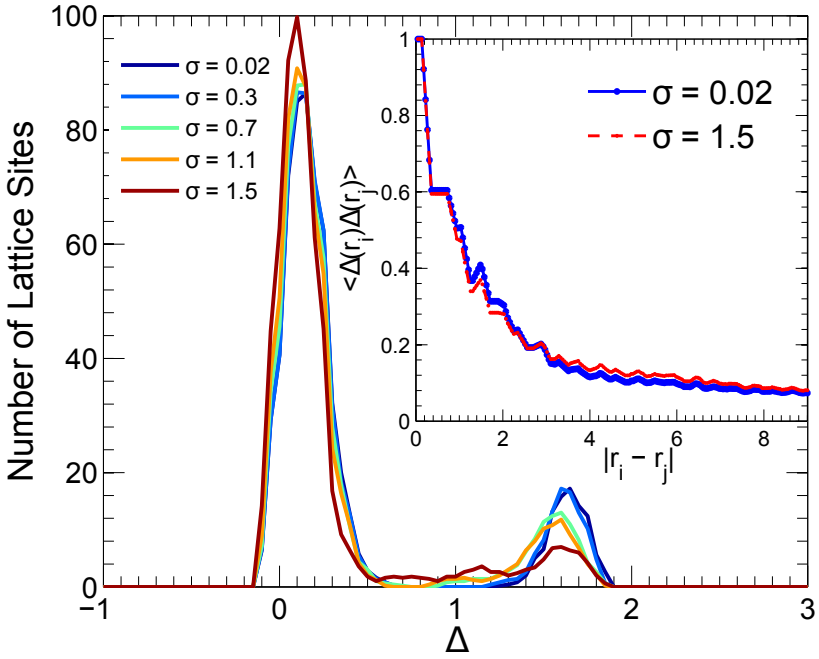


Figure 5.6: Distribution of the local pairing amplitude for different realizations of the on-site disorder parameter considering only on-site disorder at the boron sites. Inset is the pairing amplitude correlation function considering only on-site disorder with a disorder parameter of $\sigma = 0.02$ (blue) and $\sigma = 1.5$ (red).

We then assume that there are on-site potential fluctuations at all sites in the lattice, as opposed to only where boron is incorporated. Figure 5.7(a) shows the variation of the mean pairing amplitude with on-site disorder while the atomic boron concentration held at 15 %. In this case, the mean pairing amplitude increases slightly as the disorder parameter increases, in contrast to the case where on-site potential fluctuations are assumed only at the boron sites. The spectral gap however decreases slightly as the disorder parameter increases as shown in Fig. 5.7(b). Figure 5.8 shows the distribution of local pairing amplitudes where on-site disorder is assumed at all lattice sites (to be compared with the case where on-site disorder is assumed only at the boron sites, Fig. 5.6). In this case, the number of sites with local pairing amplitude around zero decreases with increasing disorder (in contrast to the case where there is on-site disorder only at the boron sites) hence the mean pairing amplitude increases. The number of lattice sites with local pairing amplitude around 1.6 decreases slightly. The inset in Fig. 5.8 shows the pairing amplitude correlation function for a small disorder parameter (blue dots) and a large disorder parameter (red dashed line). There is hardly any change at all in the correlation functions.

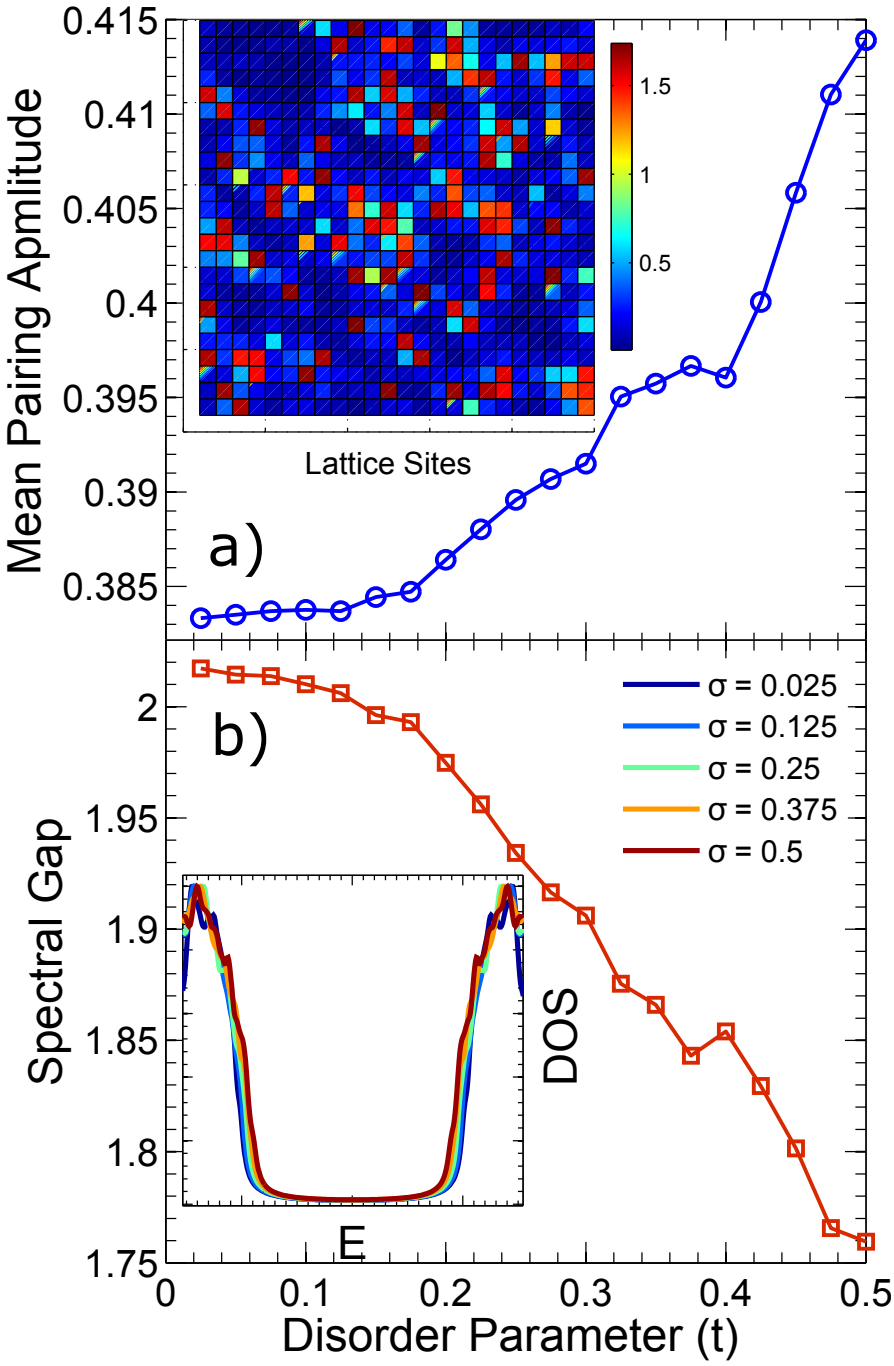


Figure 5.7: a) Mean pairing amplitude as a function of the on-site disorder parameter considering on-site disorder at all sites in the lattice at a constant atomic boron concentration of 15 %. Inset is the local pairing amplitude considering an on-site disorder parameter of $\sigma = 1.5$. b) The corresponding spectral gap. Inset is the density of states around the gap region.

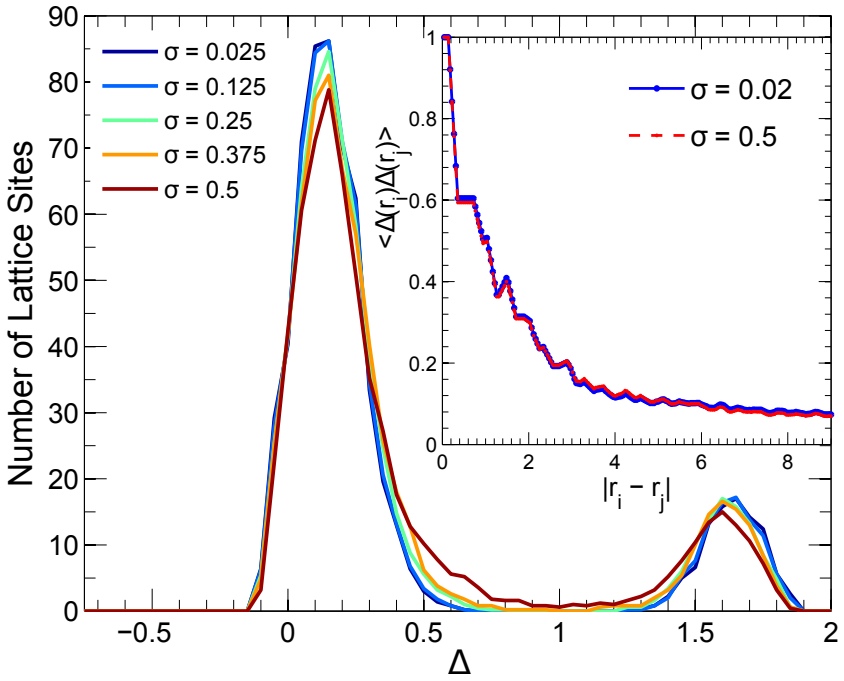


Figure 5.8: Distribution of the local pairing amplitude as a function of the boron concentration for different realizations of the on-site disorder parameter considering on-site disorder at all sites. Inset is the pairing amplitude correlation function considering a small on-site disorder parameter (blue dots) and a larger diosrder parameter (red dashed line).

5.3.2 Correlated Structural disorder

We now study the effects of structural disorder in the form of a random distribution of the tight-binding hopping parameter (non-diagonal disorder) about a constant mean value for all lattice sites in the absence of on-site disorder. We assume that the structural disorder parameter (σ) can increase either linearly, exponentially or inverse exponentially as shown in Fig. 5.9(a) which shows the variation of the disorder parameter as a function of the boron concentration. We assume these three variations as there is as yet insufficient experimental data directly relating the change in the microstructure of BDD or B-NCD to the atomic boron concentration. In the case of nitrogen incorporation in nano-diamond and amorphous carbon films, the variation of the structural disorder with nitrogen incorporation is non-linear [52] showing an initially rapid increase in disorder and tending towards saturation with increasing nitrogen incorporation. To isolate the effects of structural disorder, we first assume that the on-site energy at all sites is uniform.

Figure 5.9(b) shows the variation of the mean pairing amplitude as a function of the boron concentration for the three different variations of correlated disorder. It is evident that structural disorder has a much larger effect than disorder in the form of on-site potential fluctuations (Fig. 5.3). Of particular interest is the case of the disorder parameter increasing inverse exponentially with the boron concentration. The mean pairing amplitude shows significant saturation with the boron concentration, especially in the region of 5 - 6 % atomic boron concentration (this is more significant than in the case of on-site disorder only) and is similar to experimental results [153].

To illuminate the influence of structural disorder, we study the mean pairing amplitude, the distribution of pairing amplitudes, the spectral gap and the density of states while the boron concentration is fixed at 15 % and the structural disorder parameter is varied (assuming no on-site disorder). Figure 5.10(a) shows the variation of the mean pairing amplitude as a function of the structural disorder parameter. The mean pairing amplitude shows an unexpected significant increase with increasing structural disorder. This is in contrast to the case of on-site disorder with random fluctuations at the boron sites only (refer to Fig. 5.4(a)) where the mean pairing amplitude decreases with disorder. The spectral gap as a function of the disorder parameter is shown in Fig. 5.10(b). The spectral gap decreases with increasing disorder and the decrease is far more significant than in the case of on-site disorder (whether it be on-site disorder at the boron sites only or throughout the lattice).

Figure 5.11(a) shows the density of states for different structural disorder parameters, from 0 (blue) to 0.5 (red). The significant effect of structural disorder on the spectral gap is evident as the gap rapidly reduces however up to a structural disorder parameter of 0.5 it does not transition to a pseudo-gap. States become available within the former gap region as the gap narrows.

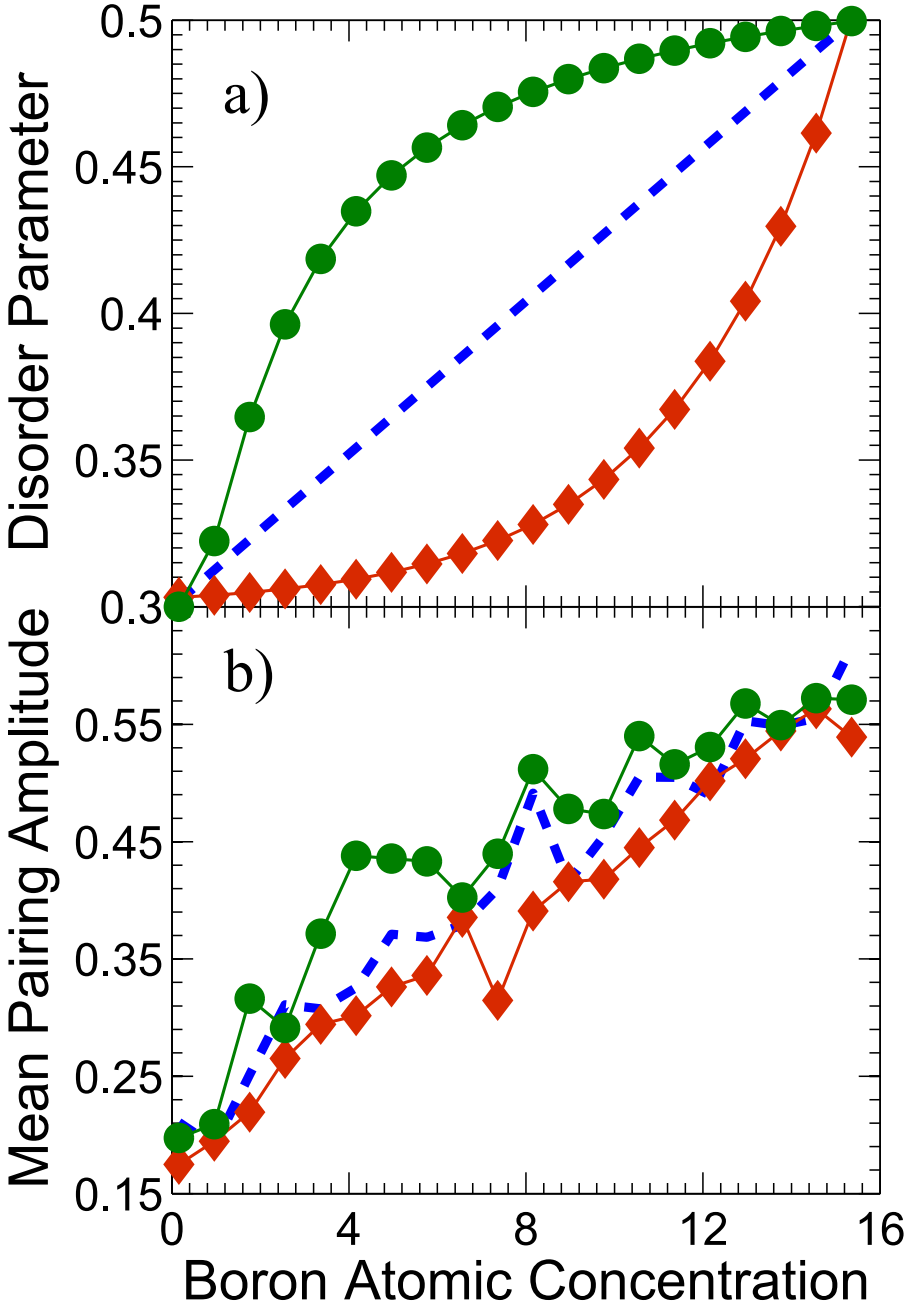


Figure 5.9: a) Variation of the structural disorder parameter as a function of the atomic boron concentration for three different cases. b) The mean pairing amplitude as a function of the atomic boron concentration for three different cases. The case of linear correlated disorder corresponds to the blue dashed line while the exponential variation of disorder corresponds to the red diamonds and inverse exponential variation corresponds to the green dots.

The local density of states considering structural disorder is shown in Figure 5.11(b). Even for low structural disorder parameters, the coherence peaks broaden rapidly while states become available in the gap. This behaviour is entirely distinct from the case of on-site disorder alone. With increasing structural disorder, the coherence peaks continue to broaden although they do not continue to broaden out at the same rate. The amplitude of the coherence peaks increases, then decreases however the width of the gap decreases monotonically as states become available within the gap.

The Coulomb interaction further promotes the introduction of states in the gap, as shown in Figure 5.12(a). With such a large Coulomb interaction, superconductivity is unstable so even slight disorder disrupts the superconducting phase. The local density of states (shown in Fig. 5.12(b)) does not show coherence peaks indicating that the repulsive Coulomb interaction competes against superconductivity. While states do appear with coherence peaks absent, the density of states for higher values of structural disorder shows a very interesting pseudo-gap like feature with a deep minimum in the density of states at zero energy and states piling up on either side.

The distribution of local pairing amplitudes (Fig. 5.13) shows that the the number of sites with pairing amplitude in the region of 1.6 diminishes rapidly, in stark contrast to the case of on-site disorder only. On the other hand, the number of sites with zero local pairing amplitude decreases, with the number of sites with non-zero pairing increasing. This shows why the mean pairing amplitude increases overall. In addition, structural disorder promotes connectivity between regions with non-zero pairing. The inset in Fig. 5.13 shows the pairing amplitude correlation functions for different structural disorder parameters. Correlation persists in the high disorder regime due to the enhanced connectivity of the local pairing amplitude which structural disorder induces.

5.3.3 Combined Structural and On-site Disorder

In this section structural disorder is combined with on-site disorder while the Coulomb interaction parameter is finite ($W = 3t$). The variation of the mean pairing amplitude as a function of the boron concentration for different cases of linear, exponential and inverse exponential disorder with boron concentration is shown in Fig. 5.14. The Coulomb interaction parameter decreases the mean pairing amplitude. Small Coulomb interaction parameters do not have a significant influence on the overall mean pairing amplitude. The Coulomb interaction serves to suppress the pairing amplitude as it acts in competition to superconductivity, hence the mean pairing amplitude is reduced. In addition, the overall trend of the mean pairing amplitude as a function of the boron concentration also changes slightly, showing an initial exponential-like increase followed by regions of local maxima.

Figure 5.15 shows a comparison of the calculated variation of the mean pairing amplitude along with experimental data from various studies. When the structural disorder parameter

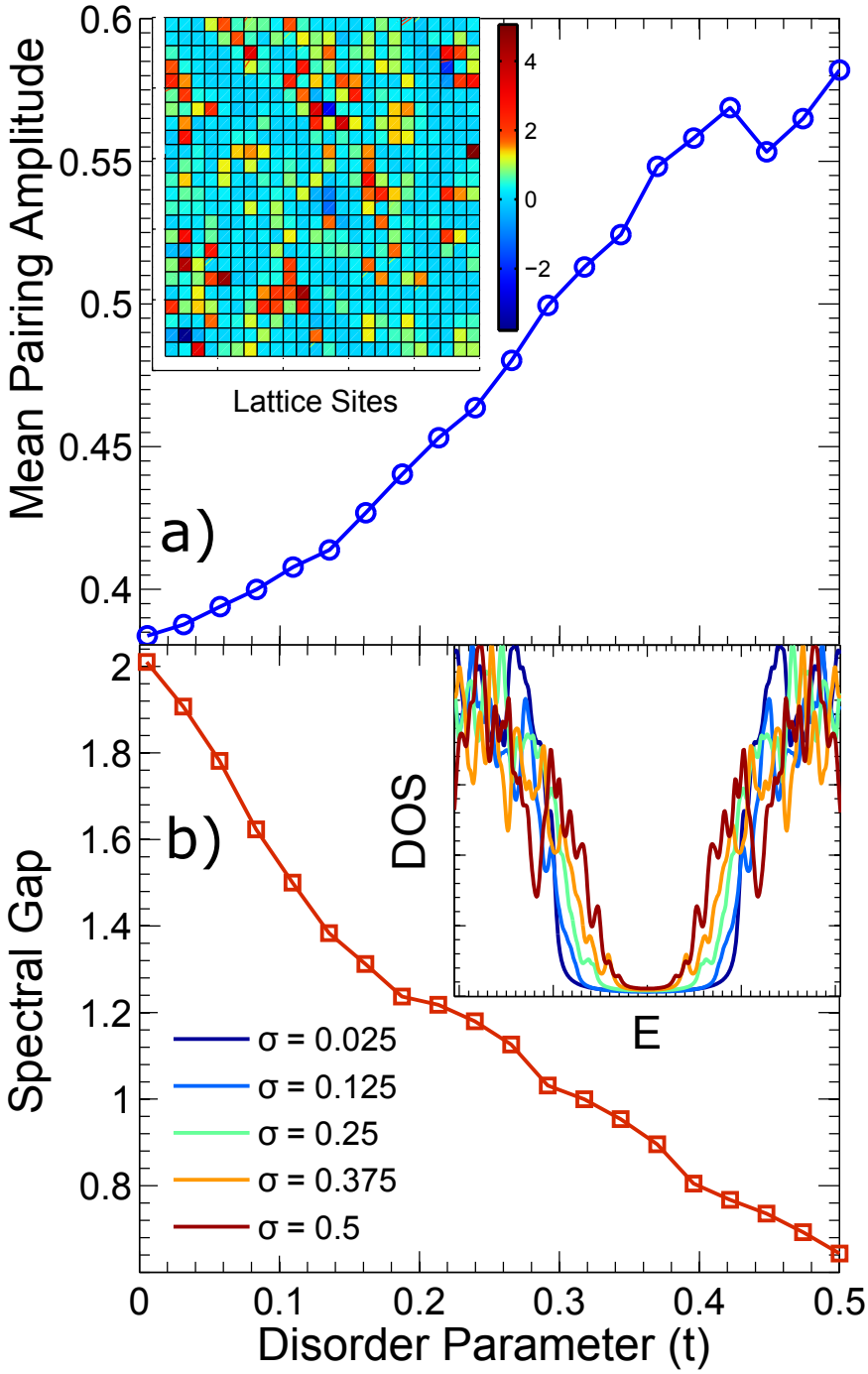


Figure 5.10: a) Mean pairing amplitude at a constant boron concentration of 15.4 % while the structural disorder parameter varies from 0 to 0.5 in the absence of on-site disorder. Inset is the local pairing amplitude where the structural disorder patameter is 0.5. b) The corresponding spectral gap as a function of the disorder paramater. Inset is the density of states in the region around the gap.

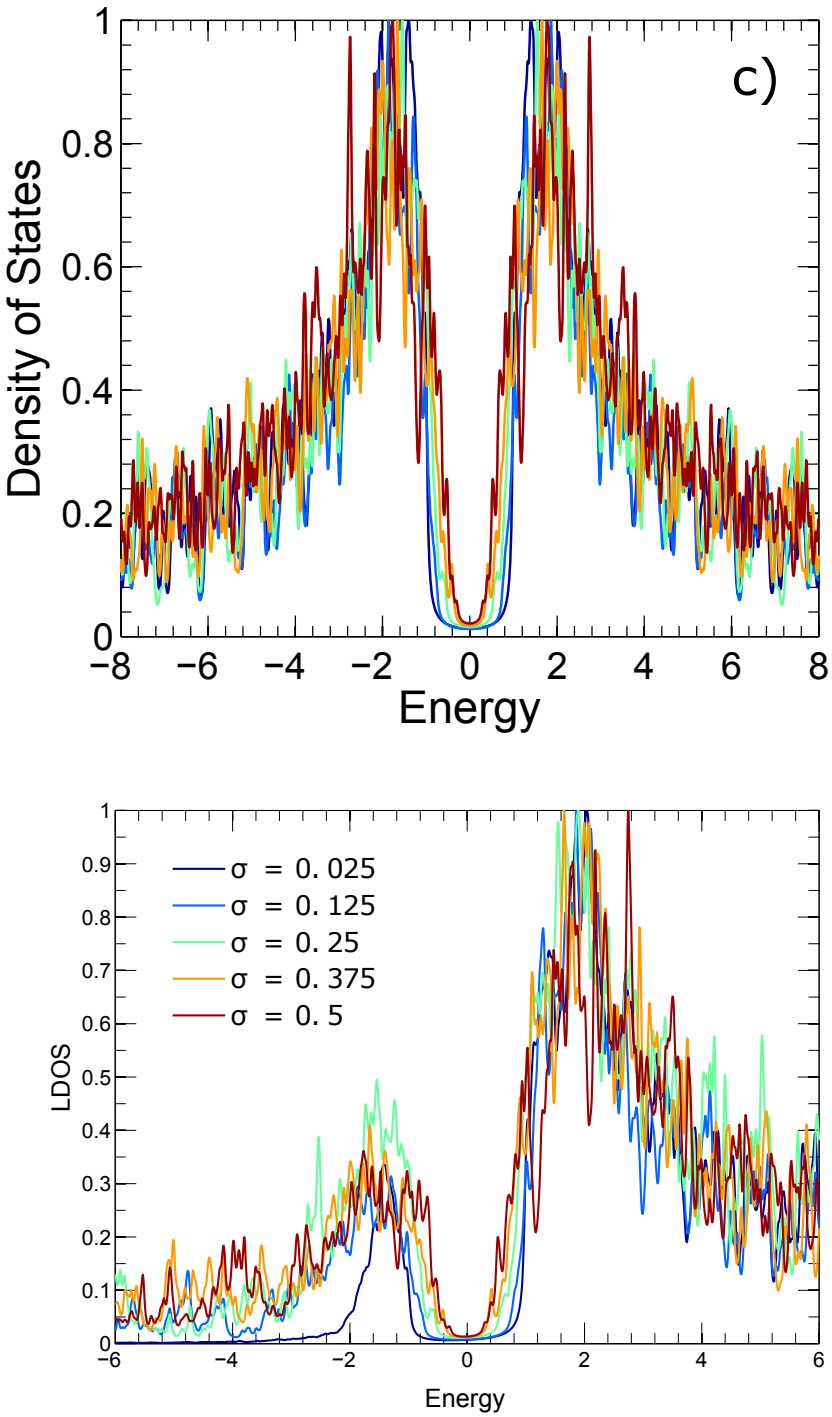


Figure 5.11: a) The density of states considering different structural disorder parameters. b) The corresponding local density of states.

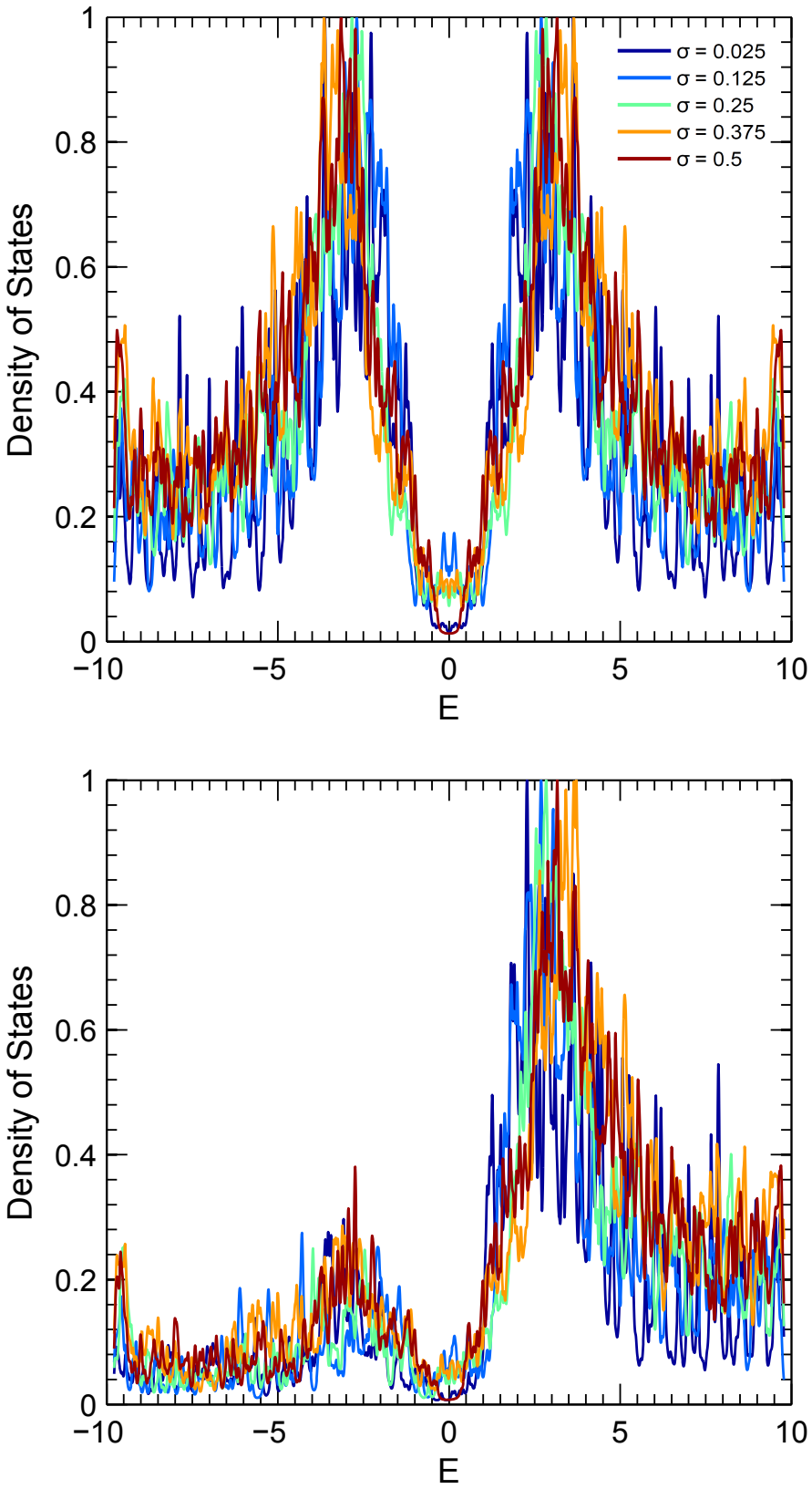


Figure 5.12: a) The density of states considering different structural disorder parameters with a large Coulomb interaction ($W = 3t$). b) The corresponding local density of states.

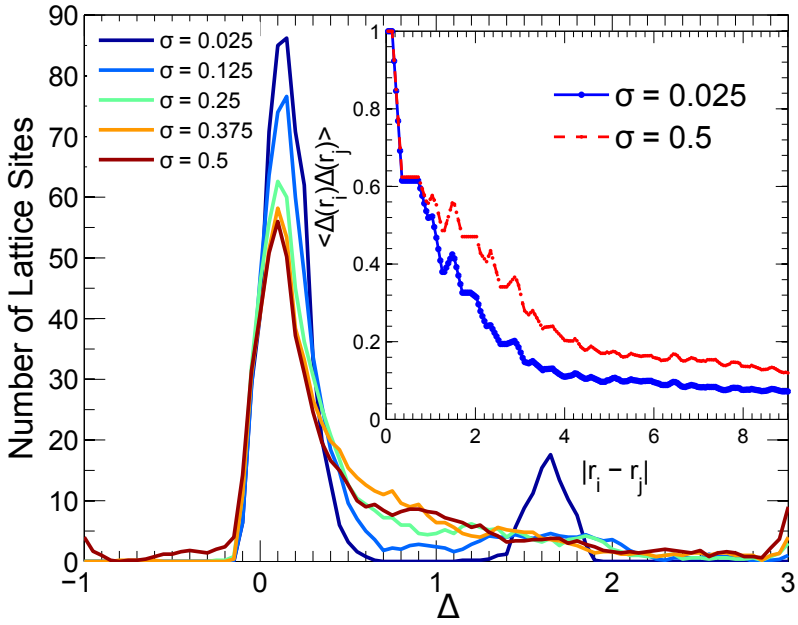


Figure 5.13: Distribution of the local pairing amplitude as a function of the boron concentration for different realizations of structural disorder in the absence of on-site disorder. Inset is the pairing amplitude correlation function for a relatively low disorder parameter (0.025, blue dots) and a higher disorder parameter (0.5, red dashed line).

varies inverse-exponentially with the boron concentration, the mean pairing amplitude shows clear signs of saturation as reported experimentally [153]. Given the energy scales needed to observe saturation of the mean pairing amplitude with boron concentration, this analysis shows that the combination of structural disorder as well as on-site disorder is necessary to reproduce the tendency towards saturation of the mean pairing amplitude found experimentally. Although the mean pairing amplitude cannot be directly compared to the transition temperature, the variation of the mean pairing amplitude is indicative of the variation of the superconducting transition temperature. In this study we find reasonable qualitative agreement with experiment, finding an initially rapid increase in the mean pairing amplitude followed by a more gradual increase. Assuming that the hopping integral varies in an inverse-exponential manner with increasing boron concentration shows the most prominent change in the gradient with the mean pairing amplitude coming close to saturating as the boron concentration increases. As an extreme case, when the structural disorder parameter is large enough, the spectral gap finally disappears (not shown here) through the combination of structural disorder, on-site disorder and the Coulomb interaction.

5.3.4 Finite Temperature Analysis

We study some cases of the mean field phase diagram to compare with the experimental phase diagrams. The temperature dependence of the mean pairing amplitude is shown for

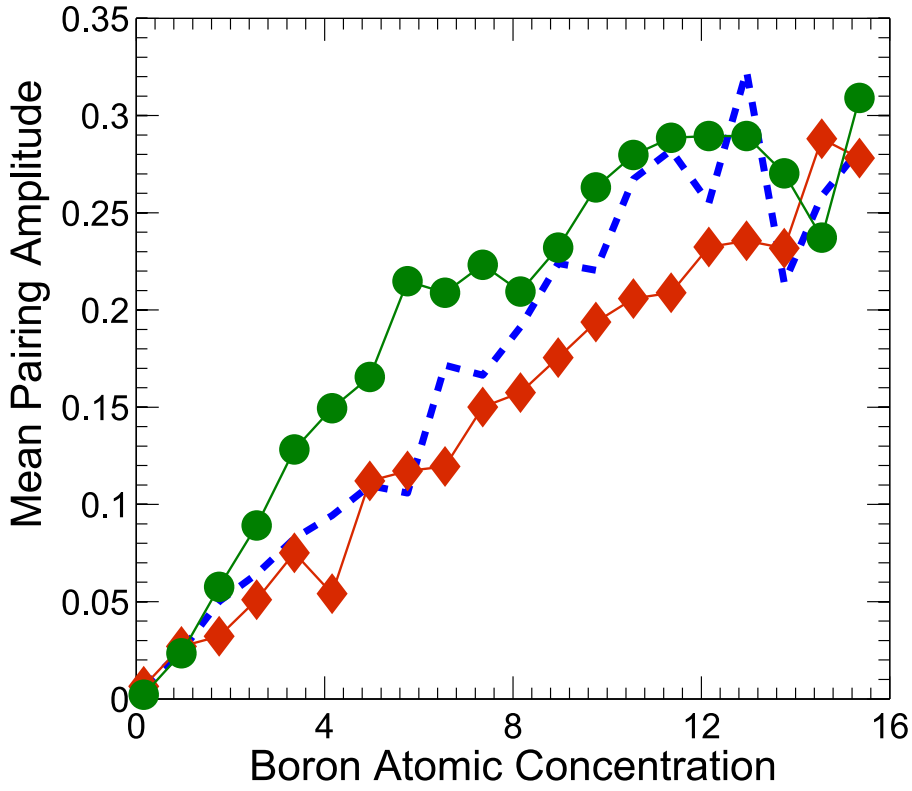


Figure 5.14: Mean pairing amplitude as a function of the atomic boron concentration where the on-site disorder parameter is 0.8, the Coulomb interaction parameter is turned on (W = 3) and the structural disorder parameter varies with the atomic boron concentration. The case of linear correlated disorder corresponds to the dashed blue line while exponentially varying disorder corresponds to the red diamonds and inverse exponentially varying disorder corresponds to the green dots.

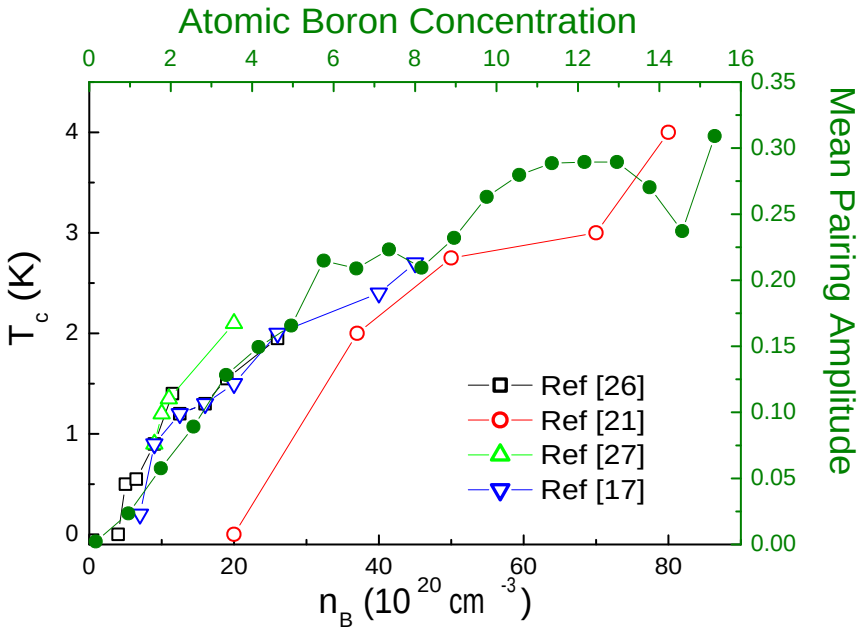


Figure 5.15: Comparison between measured T_c as a function of the boron concentration (open symbols) from various references and the calculated variation of the mean pairing amplitude as a function of the atomic boron concentration (filled green circles).

different cases of both on-site and structural disorder in Fig. 5.16(a). In the case of on-site disorder (whether at the boron sites only (black circles) or at all lattice sites (green squares) with a constant boron concentration of 15 %) the mean pairing amplitude follows quite closely the behaviour expected for a BCS superconductor even for a relatively large on-site disorder parameter. Considering structural disorder (blue dots represent a high boron concentration, red diamonds a lower boron concentration), the variation of the mean pairing amplitude with temperature is less reminiscent of a standard BCS superconductor. The mean pairing amplitude does not fall to zero within the same temperature range as for on-site disorder (although it does fall to zero at higher temperatures) although the spectral gap (Fig. 5.16(b)) is considerably smaller in the case of structural disorder.

To illustrate the fundamental difference between the nature of on-site and structural disorder, we show the DOS at different temperatures from $T = 0$ to $T = t$ considering structural disorder only (Fig. 5.17(a)) and considering only on-site disorder at all sites (Fig. 5.17(b)) for a boron concentration of 15 % and with the same disorder parameter in both cases. The pseudo-gap which forms with increasing temperature is different for both cases. While the DOS transitions to a deep V pseudo-gap in the case of on-site disorder only, there is an intermediate flat region in the case of structural disorder, which eventually transitions to a deep V with the pseudo-gap persisting to higher temperatures in the case of structural disorder.

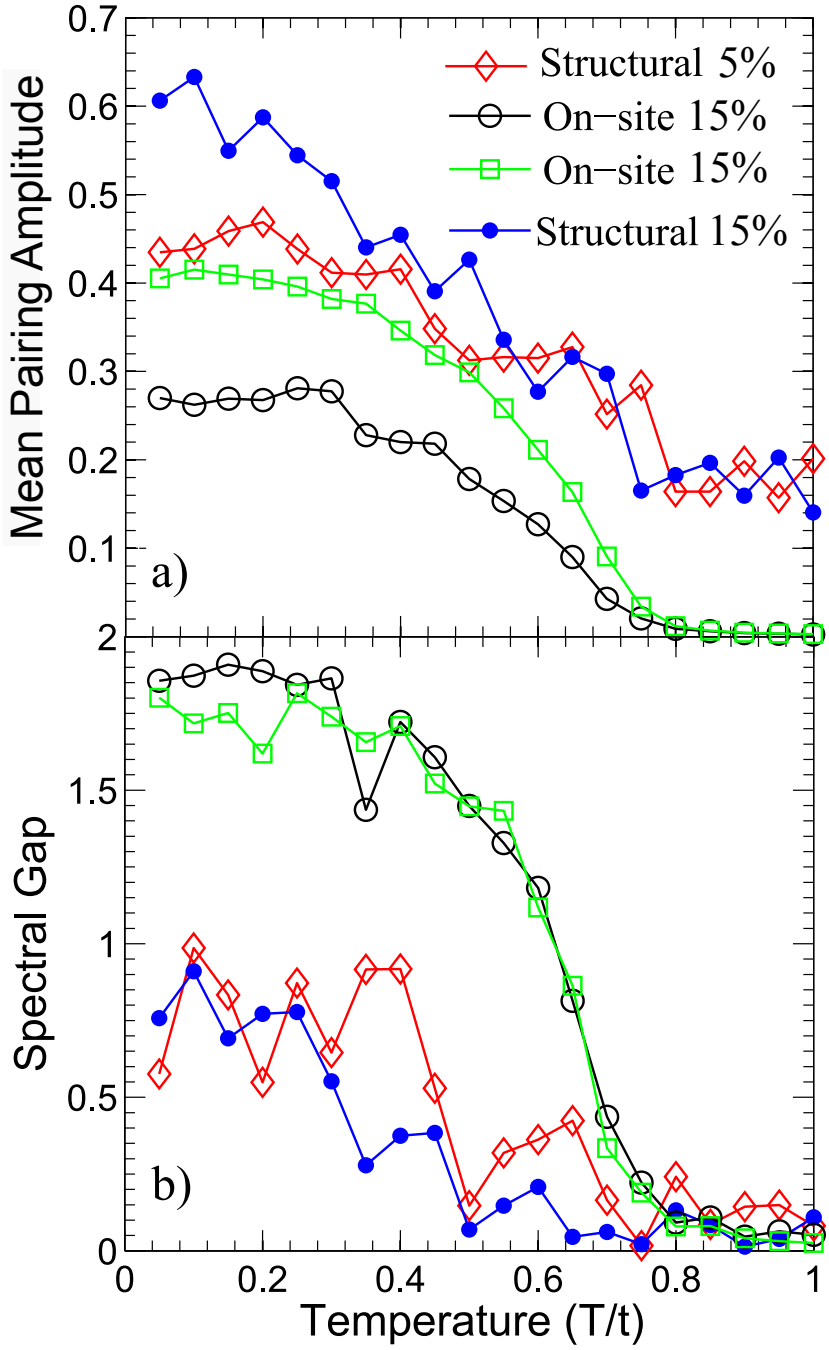


Figure 5.16: The mean pairing amplitude (a) and the spectral gap (b) as a function of temperature for different realizations of disorder. The black open circles represent a high boron atomic concentration (15%) considering only on-site disorder at the boron sites with a disorder parameter of 1.5 while the green squares represent on-site disorder at all lattice sites with a disorder parameter of 0.5. The red diamonds represent structural disorder with a relatively low boron concentration (5%) while the blue dots represent structural disorder with a high boron concentration (15%) while the structural disorder parameter is 0.5.

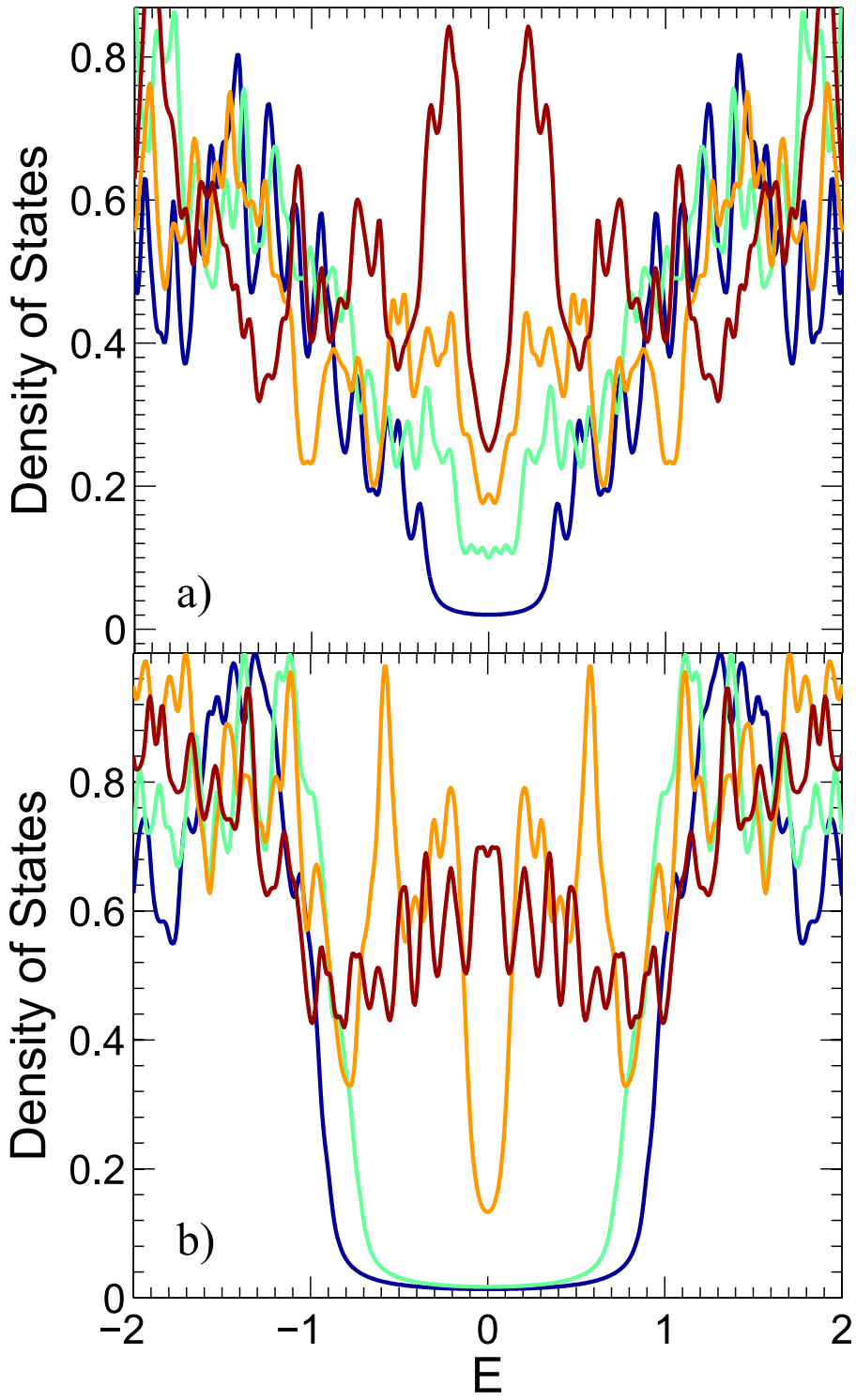


Figure 5.17: Density of states for different temperatures considering only structural disorder (a) and only on-site disorder at all lattice sites (b). The blue curve represents $T = 0$, the green curve $T = 0.5t$, the orange curve $T = 0.75t$ and the maroon curve $T = 1.0t$.

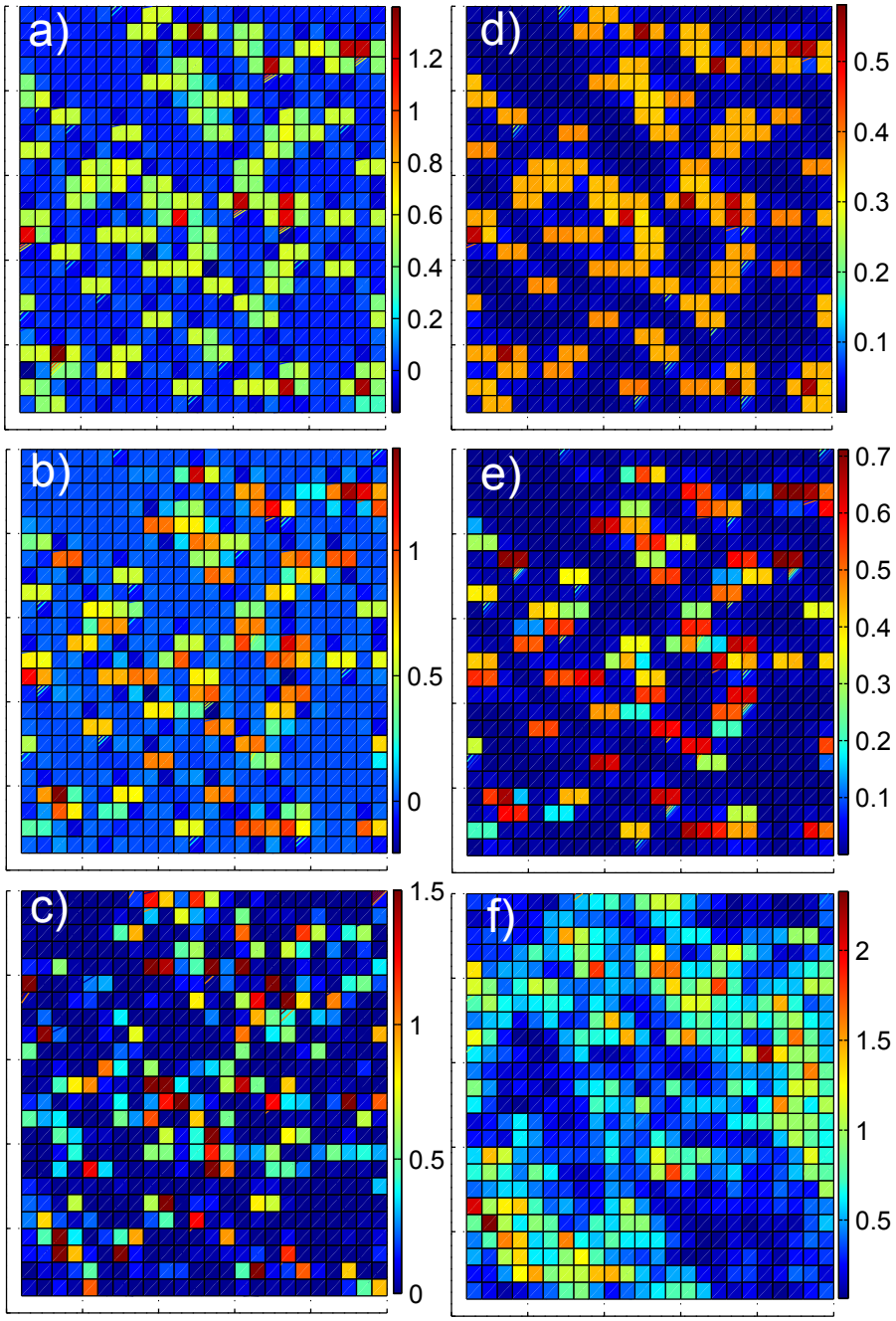


Figure 5.18: a) Local kinetic energy where the on-site disorder parameter is 0.05 considering on-site disorder at the boron sites only. b) Corresponding figure considering on-site disorder at all lattice sites when the disorder parameter is 0.5. c) Local kinetic energy considering only structural disorder where the disorder parameter is 0.5. d) Local paramagnetic response where the on-site disorder parameter is 0.05 considering on-site disorder at the boron sites only. e) Corresponding figure considering on-site disorder at all lattice sites when the disorder parameter is 0.5. f) Local kinetic energy considering only structural disorder where the disorder parameter is 0.5.

5.3.5 Superfluid phase stiffness

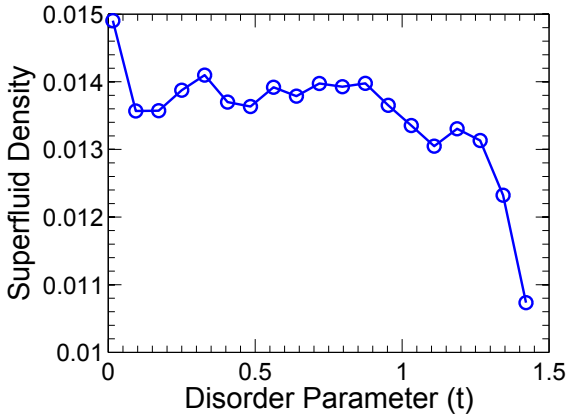
Figure 5.18 (a) shows the local kinetic energy considering low on-site disorder ($\sigma = 0.05$) at the boron sites only while Fig. 5.18 (b) shows the corresponding figure considering on-site disorder at all lattice sites (with $\sigma = 0.5$). The relative uniformity of the kinetic energy specifically in the superconducting regions illustrates the robustness of the local kinetic energy to on-site disorder. However considering only structural disorder with a disorder parameter of 0.5 (Fig. 5.18 (c)) we find that there is a large variation in the local kinetic energy, so much so that the energy scale is very different to the case of on-site disorder at all sites. This reflects the more drastic changes in the kinetic energy which accompany changes in the hopping parameter and the concurrent overall increase in the kinetic energy with increasing structural disorder.

Figure 5.18 (d) shows the paramagnetic response considering low on-site disorder ($\sigma = 0.05$) at the boron sites only and illustrates uniformity within the superconducting regions. Considering on-site disorder at all lattice sites (Fig. 5.18 (e) with $\sigma = 0.5$) we find a relatively small change in the paramagnetic response of superconducting regions. However considering structural disorder only (Fig. 5.18 (f) with $\sigma = 0.5$) shows a marked difference to on-site disorder. The paramagnetic response clearly shows an overall increase with enhanced connectivity between superconducting regions.

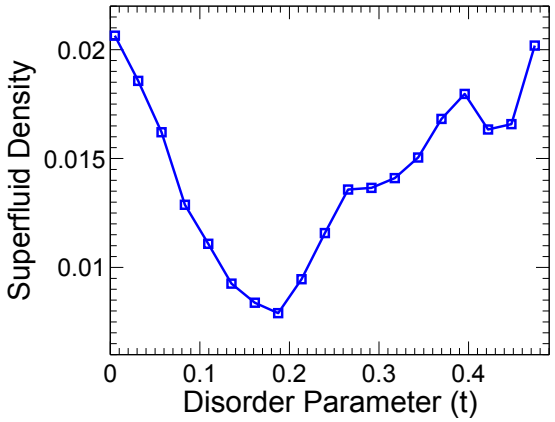
These inherent differences between on-site and structural disorder are further highlighted considering the total superfluid density as a function of on-site disorder only (Fig. 5.19 (a)) and structural disorder only (Fig. 5.19 (b)). While on-site disorder results in a monotonic decrease in the superfluid density, structural disorder shows an initially rapid decrease followed by an increase however the superfluid density is quite small. In Figure 5.19 (c), the total superfluid density for varying structural disorder *with a strong Coulomb interaction* ($W = 3t$) is presented. Initially, there is a rapid decrease to a negative value of superfluid density, followed by a marked increase back to a positive superfluid density as the structural disorder increases.

The kinetic energy and paramagnetic contribution both decrease monotonically with increasing on-site disorder (Fig 5.20 (a) and (b)). However this is not the case for structural disorder. Initially, the kinetic energy changes little with structural disorder (Fig. 5.21 (a)) however at higher structural disorder, the kinetic energy begins to increase, as does the paramagnetic response resulting in the initial drop followed by an increase.

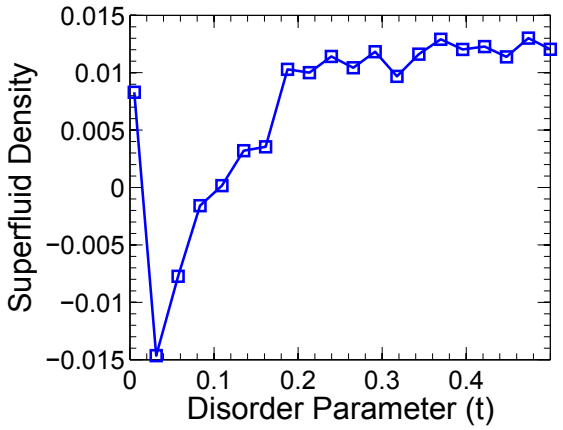
Figure 5.22 shows the local kinetic energy and paramagnetic response where the *Coulomb interaction parameter is turned on* ($W = 3t$). This should be compared with Figure 5.18 and each sub-figure follows the same scenarios as in Figure 5.18. The Coulomb interaction prevents the persistence of superconductivity with disorder, consequently Figure 5.22 does not show the same connectivity which is a hallmark of Figure 5.18.



(a)

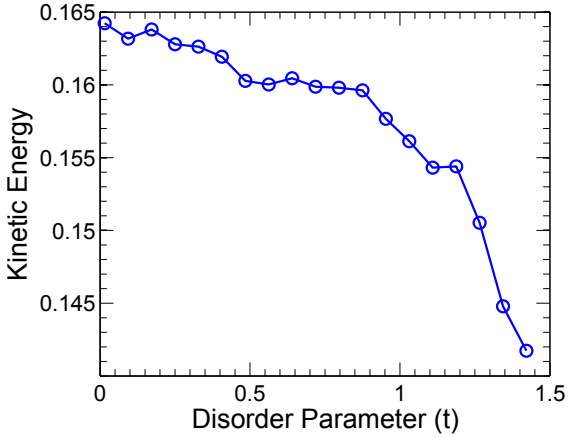


(b)

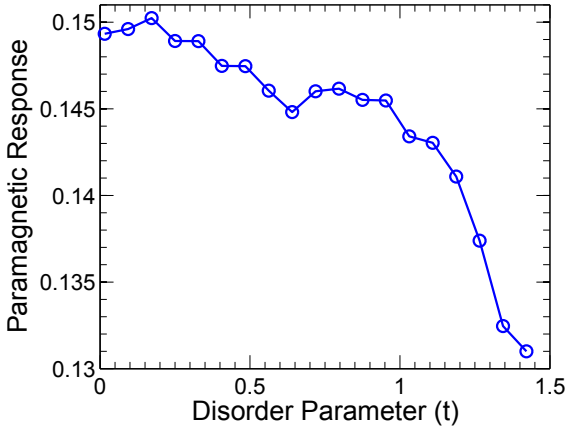


(c)

Figure 5.19: a) Total superfluid density as a function of the on-site disorder parameter (at a fixed boron concentration). b) Corresponding figure considering structural disorder only. c) Corresponding figure considering structural disorder only with the Coulomb interaction turned on.



(a)

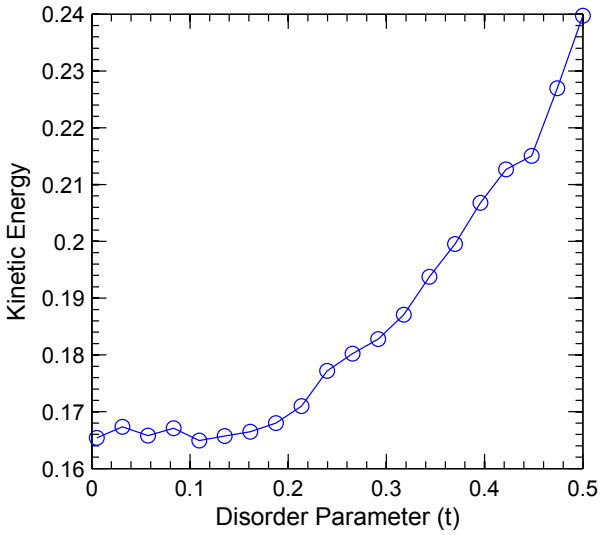


(b)

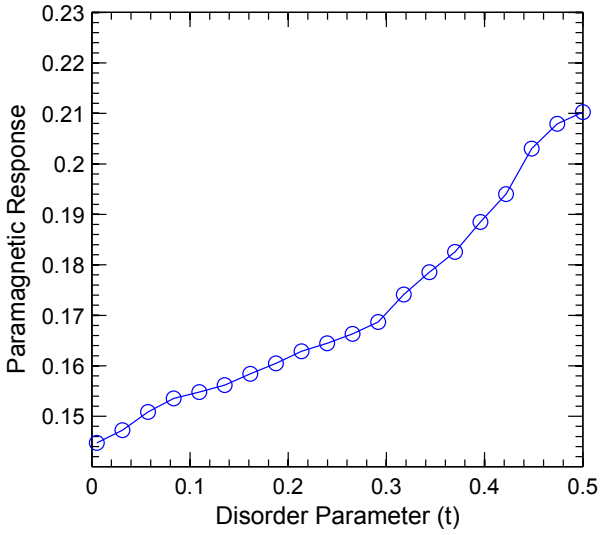
Figure 5.20: a) Kinetic energy with changing on-site disorder (in the absence of structural disorder). b) Paramagnetic response with changing on-site disorder (in the absence of structural disorder).

5.4 Discussion

The variation of the structural disorder parameter with boron concentration was motivated by examining Raman studies of B-NCD which show a change in the D and G peaks as the boron concentration is changed [166] although the significance of the structural change has not yet been established [167]. A greater change in the Raman spectra has been found in nitrogen doped carbon films and nitrogen doped nano-crystalline diamond films where nitrogen incorporation significantly modifies the microstructure of these films. The incorporation of boron modifies the diamond lattice in the regions where the boron is substitutionally incorporated. We assume that the disorder parameter may vary linearly, exponentially or inverse exponentially along with the boron concentration as there is yet insufficient Raman analysis available to specify the change in the level of structural disorder with the boron concentration. The three different cases can however be compared to experimental data of the variation of the T_c with the boron concentration which is also comparable to the be-



(a)



(b)

Figure 5.21: a) Kinetic energy with changing structural disorder (in the absence of on-site disorder). b) Paramagnetic response with changing structural disorder (in the absence of on-site disorder).

haviour found theoretically using the Berlitz theory (which is an application of the McMillan formula for disordered systems) [162].

The significance of structural disorder can be determined by comparing the distribution of local pairing amplitudes for the different cases of on-site potential disorder and structural disorder. In the case of on-site disorder, there is a decrease in the number of sites with pairing amplitude around $1.6t$ while the number of sites with a local pairing amplitude of zero increases only slightly. Conversely, in the case of structural disorder the number of sites with local pairing amplitude close to $1.6t$ decreases rapidly while the number of sites with non-zero pairing amplitude increases dramatically, with the number of sites with zero pairing amplitude decreasing. This complete difference in behaviour highlights the

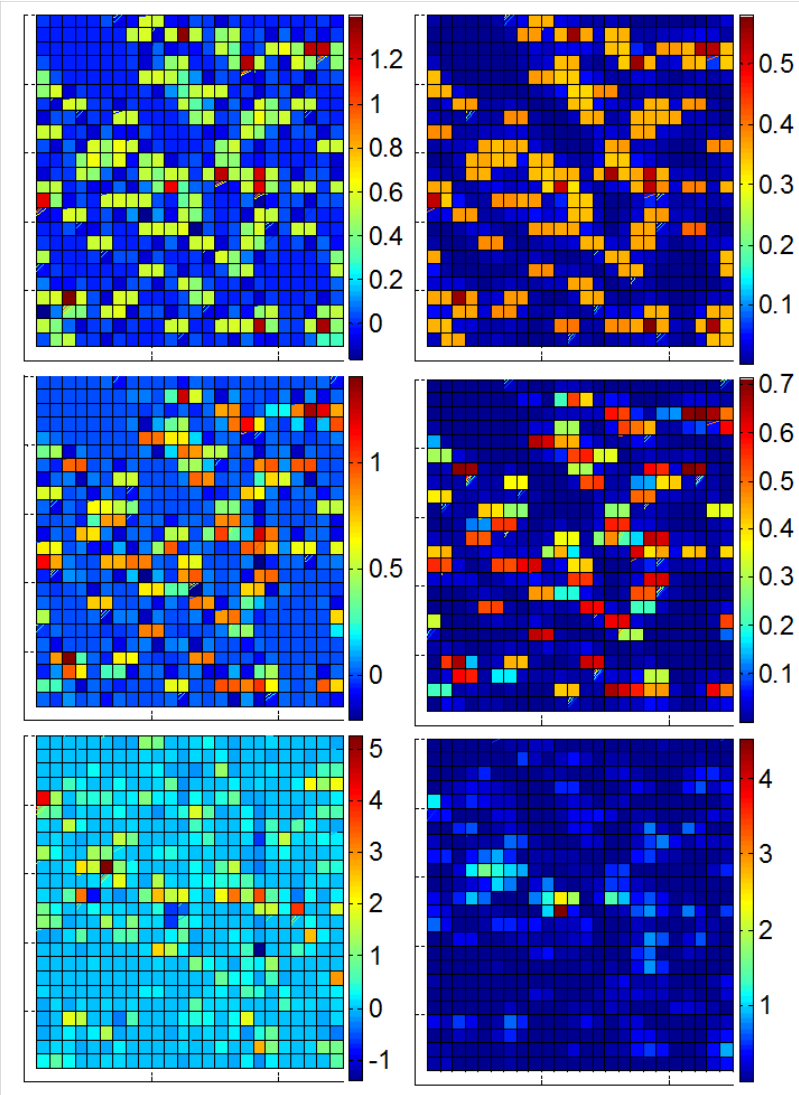


Figure 5.22: a) (Top left)Local kinetic energy where the on-site disorder parameter is 0.05 considering on-site disorder at the boron sites only *with a large Coulomb interaction parameter* $W = 3t$. b) (Middle left) Corresponding figure considering on-site disorder at all lattice sites when the disorder parameter is 0.5. c) (Lower left) Local kinetic energy considering only structural disorder where the disorder parameter is 0.5. d) (Top right)Local paramagnetic response where the on-site disorder parameter is 0.05 considering on-site disorder at the boron sites only. e (Middle right)) Corresponding figure considering on-site disorder at all lattice sites when the disorder parameter is 0.5. f) (Bottom right) Local kinetic energy considering only structural disorder where the disorder parameter is 0.5.

different natures of structural and on-site disorder. On-site disorder results in shifts of the eigenenergies at boron sites resulting in little spread of the pairing amplitude while structural disorder can promote connectivity between regions with non-zero pairing amplitude due to the distribution of eigenenergies it creates. Opposite trends in the behaviour of the average kinetic energy have been noted for structural and on-site disorder [90] where it was found that the average kinetic energy increases for on-site disorder and decreases for structural disorder.

On-site potential disorder results in enhanced localization of Cooper pairs. On the other hand, structural disorder results in a change in the coupling between different sites, resulting in a greater number of sites with non-zero pairing amplitude due to enhanced connectivity. While the mean pairing amplitude increases with increasing disorder in the case of structural disorder as well as considering on-site disorder at all sites the increase in the case of structural disorder is far greater, as is the decrease in the spectral gap with disorder. In addition, the distribution of local pairing amplitudes is very different for on-site and structural disorder even for the same values of disorder parameter. On-site disorder largely preserves the local pairing amplitude while structural disorder rapidly decreases the number of sites with relatively large pairing amplitude. This highlights the fundamental difference in the effects of structural and on-site disorder.

It is significant that in the case of on-site potential disorder the spectral gap in the density of states does not close (this has been found in other studies as well [84]). It has been shown that in the half-filled Hubbard Hamiltonian the different changes in symmetry introduced by structural and on-site disorder have different effects on the conductivity [78]. Examination of the density of states shows that on-site disorder does not induce available states close to the gap. As the coupling between lattice sites varies, a significant number of eigenstates become available in competition to the energy gained through gap formation. In the extreme case of high structural and on-site disorder, the gap eventually vanishes resulting in a pseudo-gapped ground state.

Considering the temperature dependence, experimental scanning transmission spectroscopy studies of B-NCD have shown different temperature dependences of the local energy gap for BCS-like and non-BCS like regions [156]. In addition, the superconducting gap has been found to vary within nano-diamond grains themselves [168]. The different temperature dependences of the calculated spectral gap and mean pairing amplitudes for structural as opposed to on-site disorder suggest that in regions where structural disorder is dominant, the temperature dependence will not follow the conventional BCS temperature dependence while in regions where structural disorder is less influential than on-site disorder (or where disorder of both kinds is minimal) the temperature dependence will follow the conventional BCS dependence. While the pairing mechanism does not change in these different regions, structurally disordered systems show a significant deviation from the variation in the temperature dependence of the spectral gap which may explain the deviations from the con-

ventionally expected BCS dependence found in B-NCD grains experimentally. This would manifest as variations in the gap within the grains, particularly close to grain boundaries and within grain boundaries as found experimentally [156] due to the increased structural disorder and decreased boron concentration in these regions. The differences in the temperature evolution of structural as opposed to on-site disorder shows further deviation from the conventional BCS theory. This is also reflected in the substantial difference between the changes induced in the superfluid density by on-site and structural disorder.

The initial decrease followed by an increase in the superfluid density with structural disorder is counter-intuitive although it can be understood as follows. Initially, the increase in structural disorder rapidly decreases the number of lattice sites with relatively high local pairing amplitudes so the mean superfluid density rapidly decreases. With further increase in the structural disorder, the number of sites with non-zero pairing continues to increase with the random variation of the pairing amplitudes resulting in increased isotropy as local superconducting islands begin to spread out. This is borne out by the increase in the range of the pairing amplitude correlation function when considering high structural disorder (inset in Fig. 5.13). The local paramagnetic response (Fig. 5.18 (f)) shows an overall increase with enhanced connectivity between regions with a high paramagnetic response. The average superfluid density, being sensitive to the uniformity of the pairing amplitude across adjacent regions, therefore begins to increase with increasing structural disorder. The double summations in calculating the superfluid density are computationally intense, as such small numerical errors will creep in however averaging over different disorder configurations minimizes these errors and the calculations are quantitatively reliable within the limits of the mean field approximation.

Figure 5.19 (c) shows the variation of the superfluid density with structural disorder when the Coulomb interaction is turned on. The superfluid density rapidly becomes negative indicating an instability. Its recovery to a positive value is also highly counter-intuitive. The explanation given above is still largely applicable. The repulsive Coulomb interaction acts in opposition to superconductivity so superconductivity is destroyed by structural disorder however as the structural disorder increases, it promotes connectivity between superconducting islands until eventually a positive superfluid density is regained. This has implications for superconductors close to the Anderson-Mott transition with significant electron-electron interactions. In the case of B-NCD, some highly disordered samples have shown that the T_c is surprisingly high and this may provide an explanation. This is also reflected in the DOS considering a large Coulomb interaction parameter.

Burmistrov *et al.* [169] found that Anderson localization can enhance the T_c of disordered superconductors considering a short range electron-electron interaction. This enhancement was shown to be a result of the multifractality of the wavefunction near the Anderson localization threshold [169, 170]. Anderson localization is believed to enhance the strength of correlations between multifractal wavefunctions which increases the matrix elements of

the interaction [169, 171].

The current study employing a Hubbard model for a structurally disordered system also shows enhancement of the T_c by disorder although it is not monotonic. The inhomogeneity in parameters such as the local pairing amplitude and the local superfluid density is in many ways reminiscent of a multifractal system. In particular, off diagonal disorder has a substantial influence on the matrix elements and we find that the pairing amplitude correlation function is enhanced by structural disorder. In addition, our analysis highlights the persistence of a pseudogap well into the normal regime in the case of significant structural disorder (Fig. 5.17 (a)). Other studies have also demonstrated a similar feature, either a hard-gap insulating phase or pseudo-gap phase depending on the level of disorder [171].

Chapter 6

Measured Transport Properties of B-NCD

The superconductor-insulator transition in boron incorporated nanodiamond films (B-NCD) is studied through low temperature transport measurements. Two different sets of B-NCD films, grown with different percentages of CH_4/H_2 in plasma were studied. The sets of samples had different microstructures (average grain sizes of 70 nm and 45-50 nm) and different doping concentrations (3.3×10^{21} cm^{-3} and 5.3×10^{21} cm^{-3}) for the samples grown with 1% and 5% CH_4 in the chamber respectively. Magnetoresistance was measured at different temperatures in the region of the transition and the current-voltage characteristics were studied at different temperatures and fields as a means to probe the transition from the superconducting phase to the non-superconducting phase which reveals competing quantum phases in this disordered, granular superconductor.

6.1 Introduction

Studies of the superconductor-insulator transition are spurned by the need to understand the onset of global phase coherence in disordered and granular superconductors. Boron doped nanocrystalline diamond, (B-NCD) has recently generated interest as a disordered superconductor in which the superconducting diamond grains are embedded in an $sp2$-C grain-boundary network [172, 173, 174]. Potential disorder at the randomly distributed boron centres within the individual grains [167], may yield insight as an extreme case in the study of vortex dynamics and flux pinning. The influence of boron doping on B-NCD films has been widely studied across the metal-insulator transition into the superconducting regime [166, 146, 172, 175].

It is widely accepted that superconductivity arises within the narrow boron acceptor band attributed to substitutional boron doping *within the diamond grains* while the narrow graphitic grain boundaries do not contribute to the superconducting transition [156].

However the grain boundaries can act as weak links coupling neighbouring superconducting grains forming a non-uniform array of Josephson junctions [173]. The role of vortices in such systems is still widely studied. Unlocking the relationship between flux pinning and disorder, arising from the local potential fluctuations, is of fundamental importance in understanding the onset of superconductivity in unconventional superconductors towards the eventual realization of ever higher T_c superconductors [93, 176]. While the initial surge in interest in boron doped diamond was driven by the possibility of a new form of high T_c superconductor, strong evidence, in particular the isotope effect, suggests that pairing is phonon mediated [149, 150, 177]. As superconductivity arises within the grains in B-NCD, there is almost no doubt that pairing in B-NCD is also phonon mediated.

While separate studies of magnetoresistance and magnetic field dependent differential resistance have been carried out, combined studies of both of these effects are required to understand the quantum phase transitions in more detail. Although vortex behaviour in crystalline boron doped diamond has been investigated, the phase change from vortex anti-vortex pairs through to unbound vortices in B-NCD has not yet been discussed [178]. Transitions of this kind which occur in $2D$ materials, known as BKT transitions, have been established in networks of 1D single walled carbon nanotubes and 2D graphene-metal hybrids [179, 180, 176] however BKT transitions in B-NCD films have not yet been reported.

As discussed earlier, extensive structural characterization of superconducting BDD has shown that boron incorporation induces structural disorder [181, 163]. Given the predictions of our theoretical analysis of BDD, we interpret some of the features found experimentally in measured B-NCD devices with different microstructures and boron concentrations.

6.2 Results

6.2.1 B-NCD device grown with 1 % CH_4 in the chamber

Figure 6.1 shows resistance as a function of temperature for a B-NCD device grown with 1% CH_4 in the chamber. The resistance increases with decreasing temperature, showing insulating characteristics, until the onset temperature (T_{ons}) of 3 K. The decrease in resistance towards the superconducting state then occurs rapidly. The resistance increases logarithmically as the temperature decreases over a wide range in the higher temperature regime as shown in Figure 6.2. This dependence persists virtually right up to the onset temperature.

The temperature dependence of the resistivity for a B-NCD device grown with 1% CH_4 in the chamber at different magnetic fields is shown in Figure 6.3. At zero field, the onset of the phase transition towards superconductivity is 3.2 K. At 1 T, the transition broadens out as superconductivity sets in at 0.5 K. At a magnetic field of 2 T, the device does not

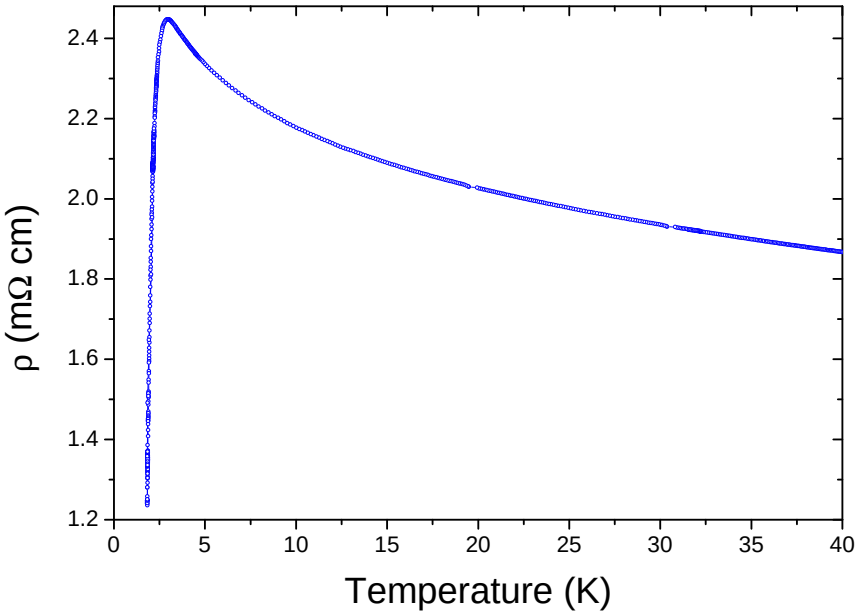


Figure 6.1: Resistivity as a function of temperature for a B-NCD device grown with 1% CH_4 in the chamber.

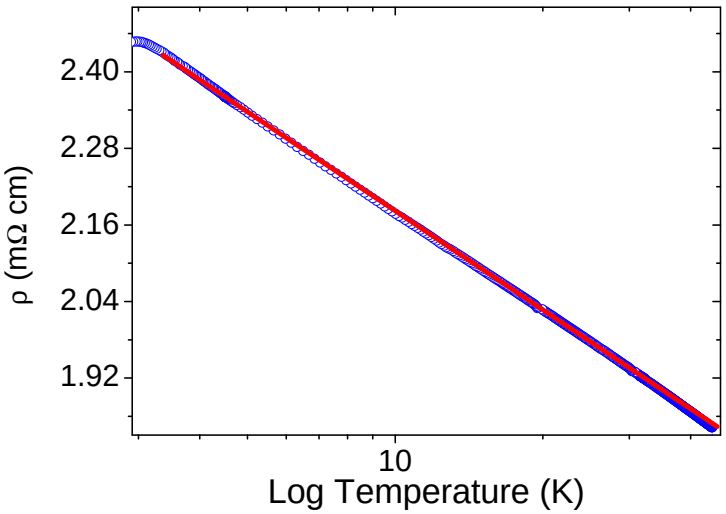


Figure 6.2: Semi-logarithmic plot of the resistivity as a function of temperature for a B-NCD sample grown with 1% CH_4 in the chamber. The red line is a straight line showing the logarithmic trend.

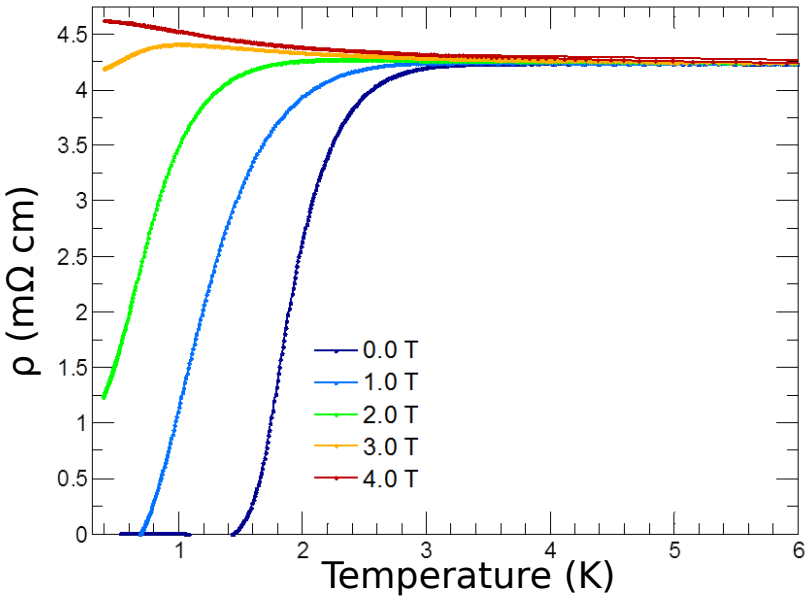


Figure 6.3: Resistivity as a function of temperature at different magnetic fields for a B-NCD device grown with 1% CH_4 in the chamber.

reach the superconducting phase at 300 mK although the onset temperature does not show as large a change. The resistivity still shows a transition at 1 K for a magnetic field of 3 T however at 4 T there is no sign of the transition, only saturation of the resistance at low temperatures. At temperatures greater than 3 K all the curves tend to collapse onto a single curve in the normal state.

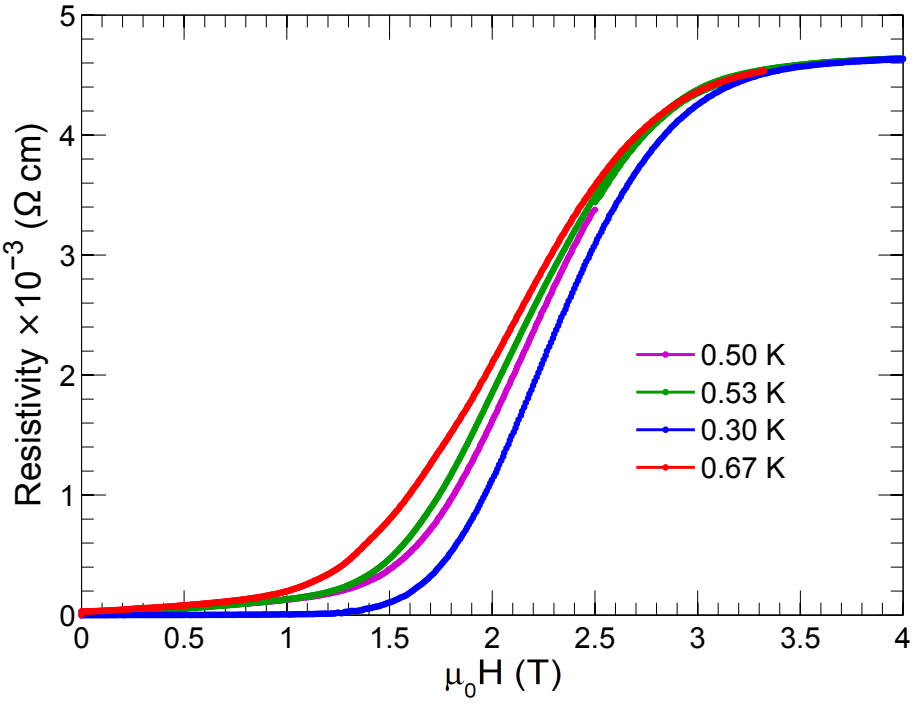


Figure 6.4: Magnetoresistivity for a B-NCD device grown with 1% CH_4 in the chamber at different temperatures, from 0.3 K to 0.67 K.

The magnetoresistance at different temperatures (from 0.3 K) for a B-NCD device grown with 1% CH_4 in the chamber is shown in Figure 6.4. At 0.3 K, superconductivity begins to break down at 1.3 T. With increasing temperature, the critical fields decrease however above 3 T all the curves collapse to a single trend.

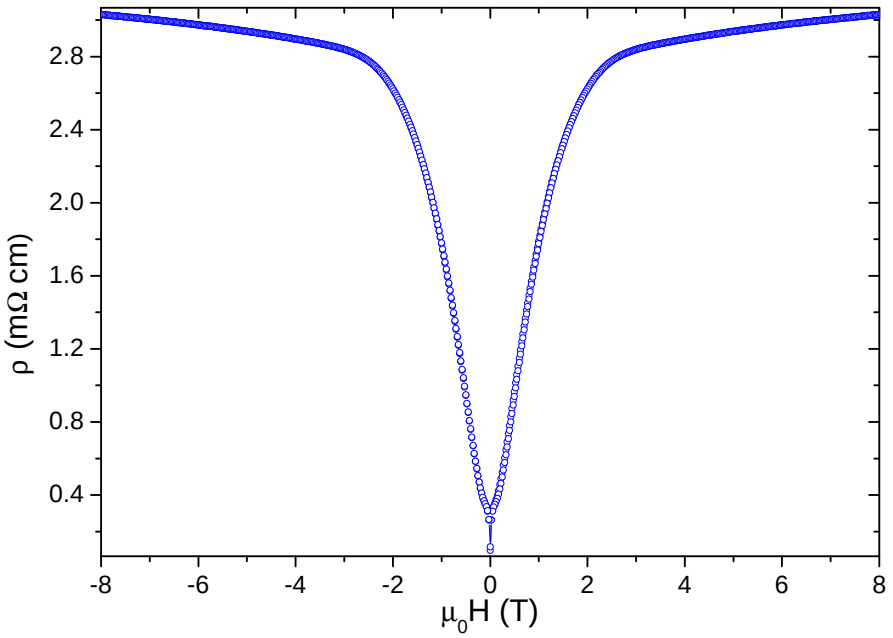


Figure 6.5: Magnetoresistivity of a B-NCD device grown with 1 % CH_4 at 1.4 K.

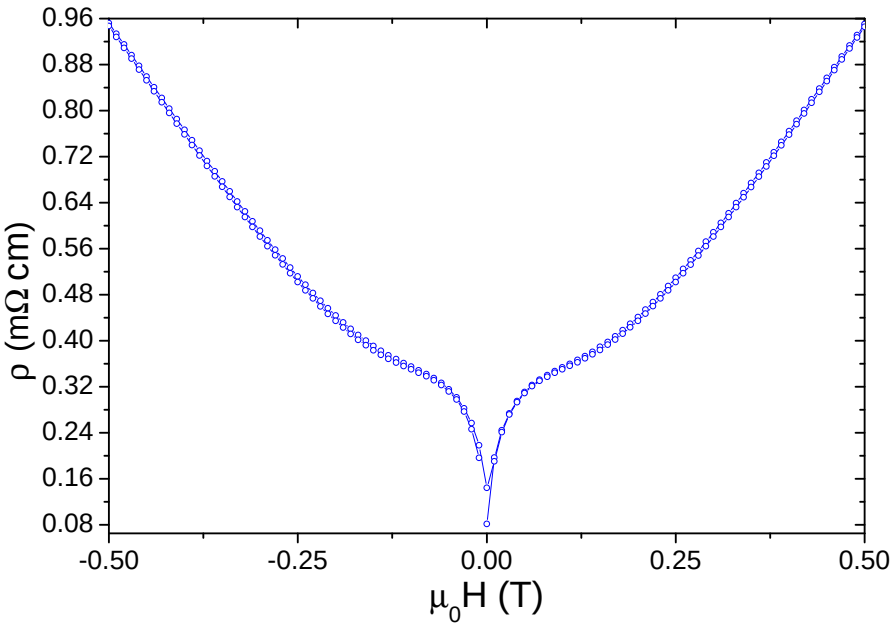


Figure 6.6: Low field magnetoresistivity of a B-NCD device grown with 1 % CH_4 at 1.4 K.

Figure 6.5 shows the magnetoresistance at 1.4 K. At this temperature, the device is just outside the superconducting phase with the resistance at zero field almost dropping to zero. The is the ideal region to study the phase transition as it is in a regime where quantum phase fluctuations have a strong influence on the transport properties. As the magnetic field

increases, the resistance increases sharply. At fields of around 0.1 T, this increase becomes less rapid, flattening out locally. This robust, repeatable feature is extremely significant as it demonstrates two distinct phases. This is highlighted in Figure 6.6. At around 2 T, the magnetoresistance levels off as the entire device makes the transition out of the vortex phase into the normal phase.

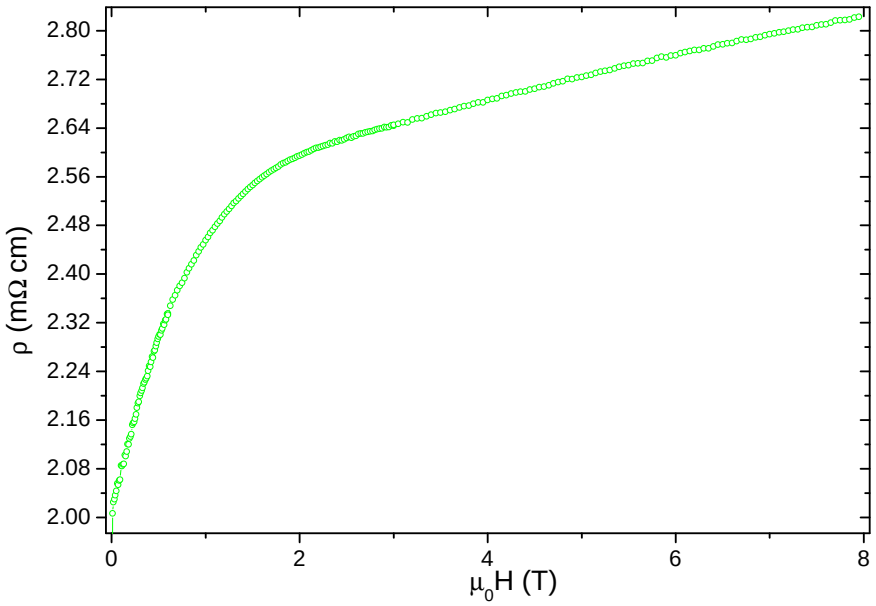


Figure 6.7: Magnetoresistivity of a B-NCD device grown with 1 % CH_4 at 1.8 K.

At 1.8 K, there is no indication of the sharp drop in resistance around zero field followed by saturation of the resistance (shown in Fig. 6.7). Instead, there is a uniformly increasing gradient until about 1.4 T. The resistance at zero field is far higher than at 1.4 K however the steep change in gradient associated with the transition to the normal phase remains at around 2 T, indicating some persistence of superconductivity.

The magnetoresistivity at 2.1 K (Fig. 6.8) also shows a rapid increase as a function of field however there is a small region from 0 T to 0.025 T where the magnetoresistivity shows hardly any field dependence, as illustrated in Figure 6.9. This is proceeded by a steep increase in the magnetoresistivity.

Figure 6.10 shows the magnetoresistivity at 2.8 K. This is close to the onset temperature at zero field. There is still a region of very small magnetoresistivity around zero field as was the case at 2.1 K however it is slightly broader. The increase from zero field is much less rapid than at lower temperatures however there still remains a decrease in the gradient at around 1 T. The change occurs at lower fields in this case due to the higher temperature which breaks down superconducting regions. At higher fields, there is an almost linear increase in the magnetoresistivity.

At 3.4 K (shown in Fig. 6.11), the magnetoresistivity shows no sign of a transition to a less steep gradient, indicating the total breakdown of superconductivity. The magnetoresistivity

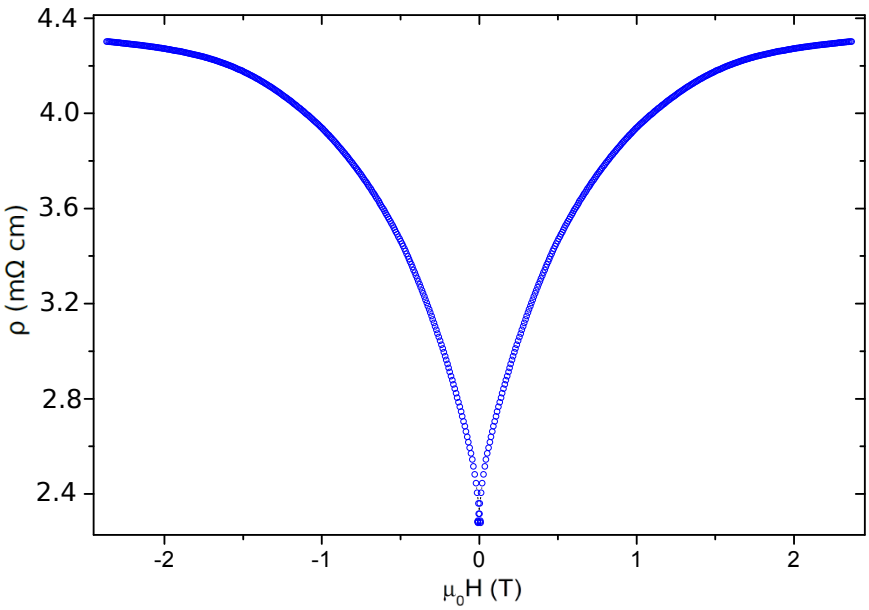


Figure 6.8: Magnetoresistivity for B-NCD sample grown with 1% CH_4 in the chamber at 2.1 K.

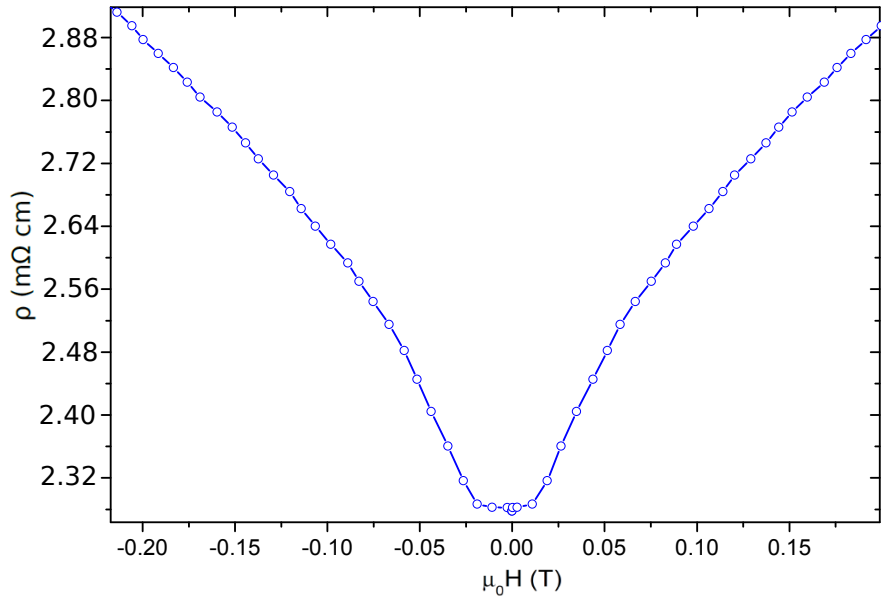


Figure 6.9: Magnified magnetoresistivity for B-NCD sample grown with 1% CH_4 in the chamber at 2.1 K.

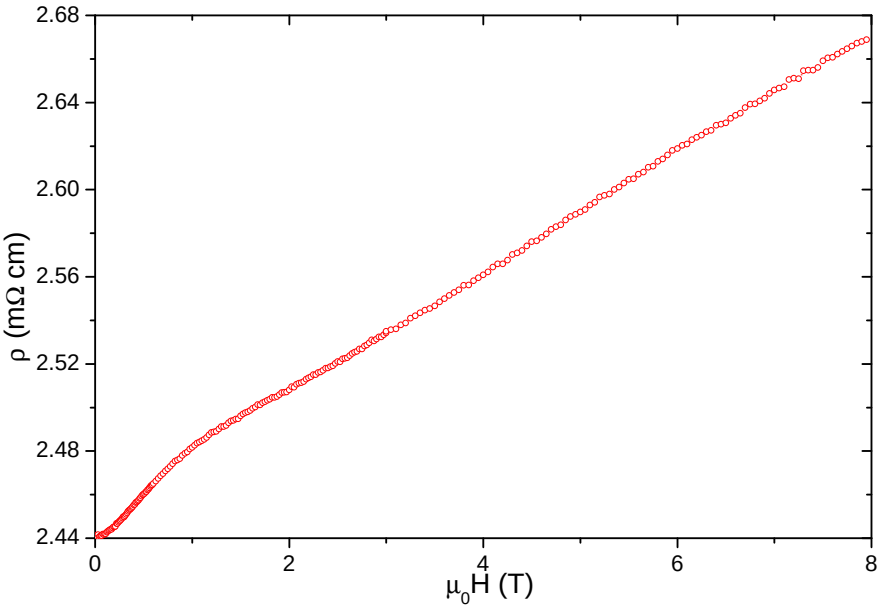


Figure 6.10: Magnetoresistivity for B-NCD sample grown with 1% CH_4 in the chamber at 2.8 K.

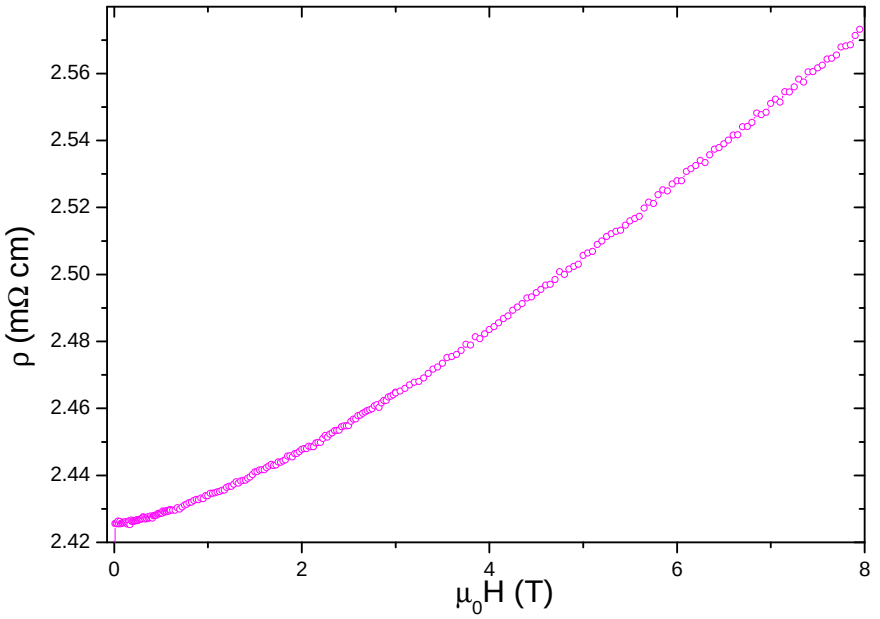


Figure 6.11: Magnetoresistivity of a B-NCD device grown with 1 % CH_4 at 3.4 K.

is strictly positive although the change in resistivity is quite small, 4 Ω over a change of 8 T. In this case, the increase is greater than linear (up to 4 T). Figure 6.12 shows the magnetoresistivity at 10.1 K. The trend is similar to that at 3.4 K indicating no change in the transport mechanism however the change in magnetoresistivity is extremely small. At 14 K, there is possibly a very small region of negative magnetoresistivity as shown in Figure 6.13 however as the change in resistivity is very small, this is not entirely reliable.

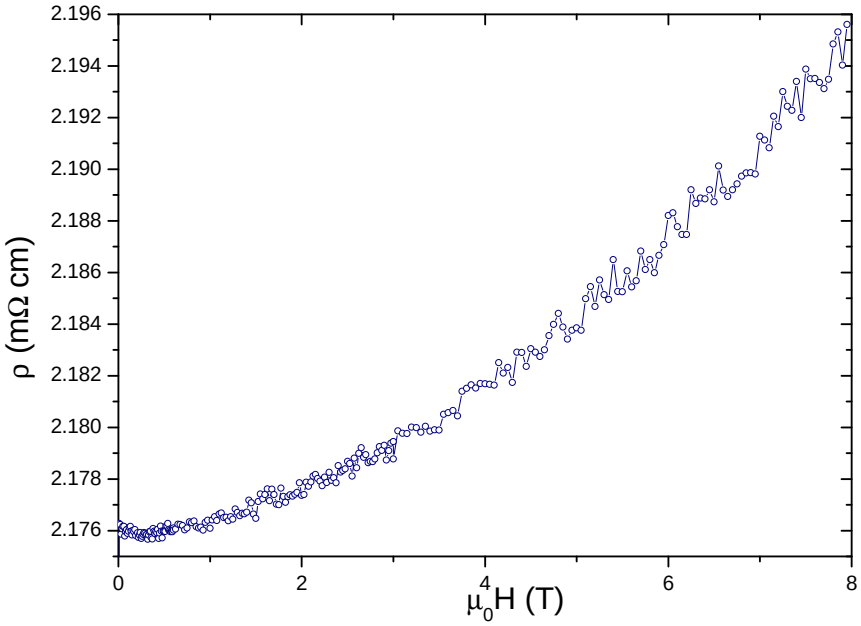


Figure 6.12: Magnetoresistivity of a B-NCD device grown with 1 % CH_4 at 10.1 K.

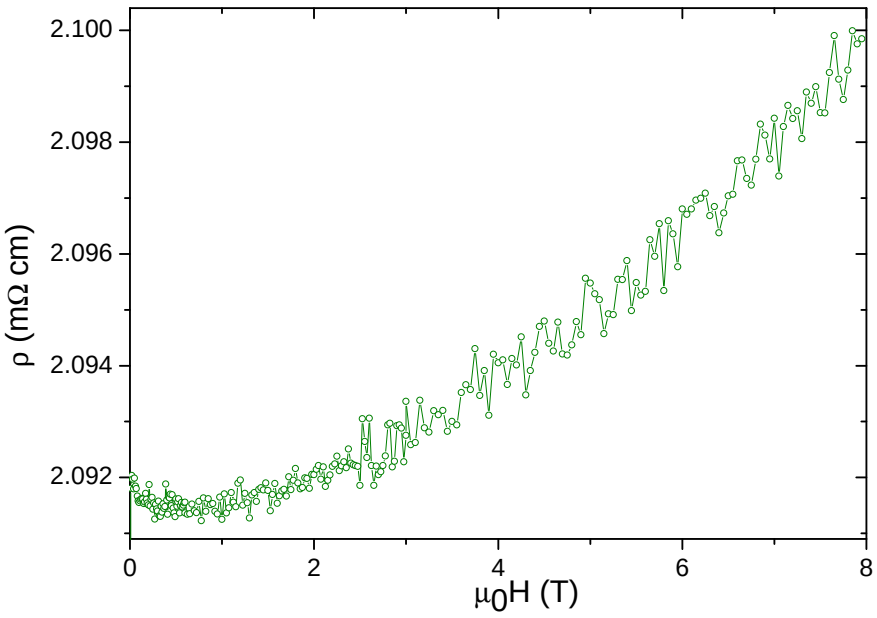


Figure 6.13: Magnetoresistivity of a B-NCD device grown with 1 % CH_4 at 14.9 K.

We now present analysis of the current-voltage dependence of a B-NCD sample grown with 1% CH_4 in the chamber at different temperatures and at different magnetic fields in the region of the superconductor-insulator transition. Figure 6.14 shows the measured voltage

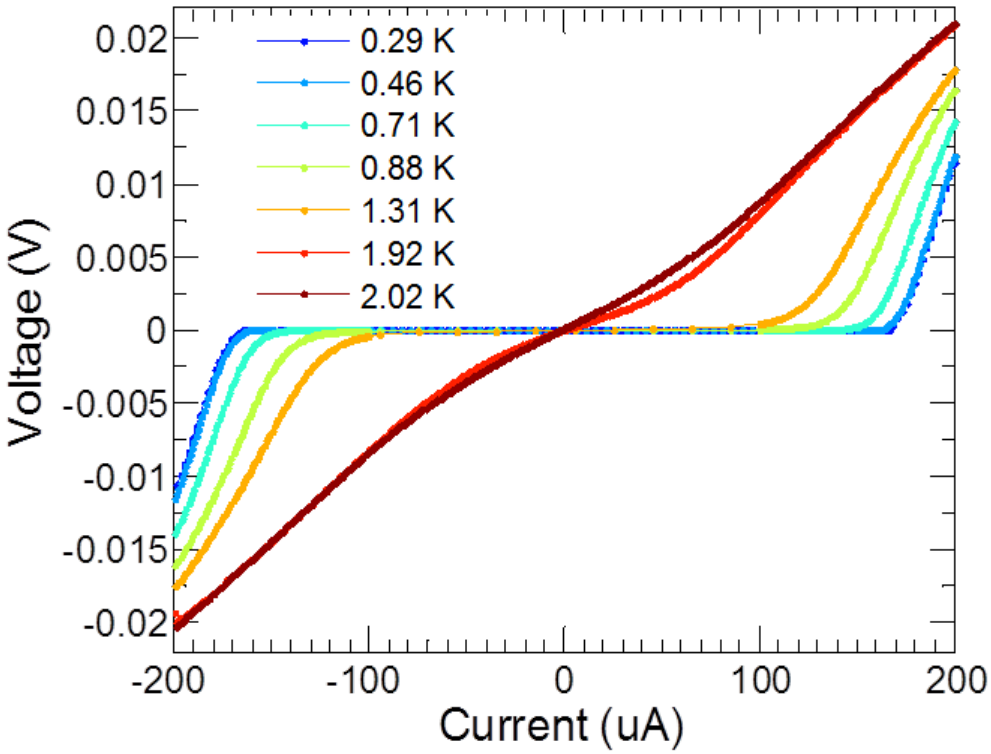


Figure 6.14: Voltage-current characteristics of a B-NCD device grown with 1% CH_4 at different temperatures.

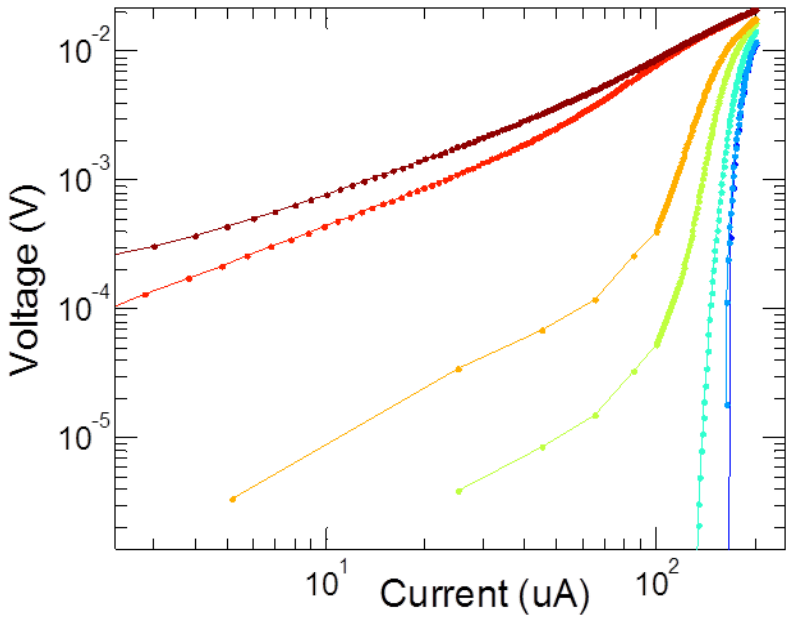


Figure 6.15: Voltage-current characteristics plotted logarithmically at different temperatures for a B-NCD device grown with 1% CH_4 in the chamber at different temperatures.

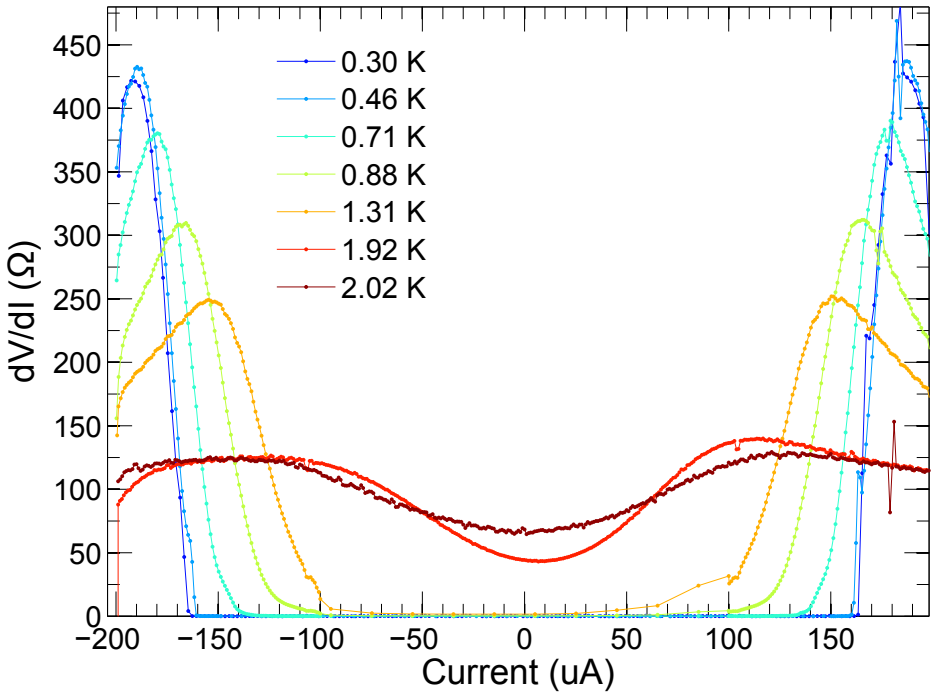


Figure 6.16: Differential resistivity as a function of current for a B-NCD device grown with 1% CH_4 in the chamber at different temperatures.

as a function of applied current at different temperatures. At 0.3 K, the critical current is 175 μA. At 0.46 K, the critical current is only very slightly reduced. At 0.71 K, the transition out of the superconducting phase begins to broaden out. At higher temperatures, distinct variations in the gradient become apparent. At 1.3 K, the device still clearly shows a distinct transition out of the superconducting phase. At 1.9 K and at 2 K there is no sign of a superconducting phase however there are discernible changes in gradient. At higher currents, the curves at 1.9 K and 2 K collapse onto a single curve in the normal phase. The current-voltage characteristics remain non-linear up to 2.02 K.

The current-voltage dependence at different temperatures is shown on a logarithmic scale in Figure 6.15. There is a region of linear dependence at 0.88 K with a steep gradient (implying a power law dependence over some region of current). There are also distinct regions of linear dependence at low currents at 1.9 K and 2 K with a less steep gradient.

The temperature dependence of the differential resistivity, shown in Figure 6.16 has interesting features. At 1.3 K, there is a marked change in gradient at around 100 (-100) μA. At higher temperatures, a local minimum around zero bias persists. The slight asymmetry is due to very slight temperature changes of the order of 10 mK during the course of the current voltage sweep.

Figure 6.17 shows the current-voltage characteristics of a B-NCD device grown with 1% CH_4 in the chamber at 0.3 K at different magnetic fields, from 0 T to 4.5 T. At 0.25 T, the critical current is 130 μA. Above 1.75 T the critical current becomes negligible. There is

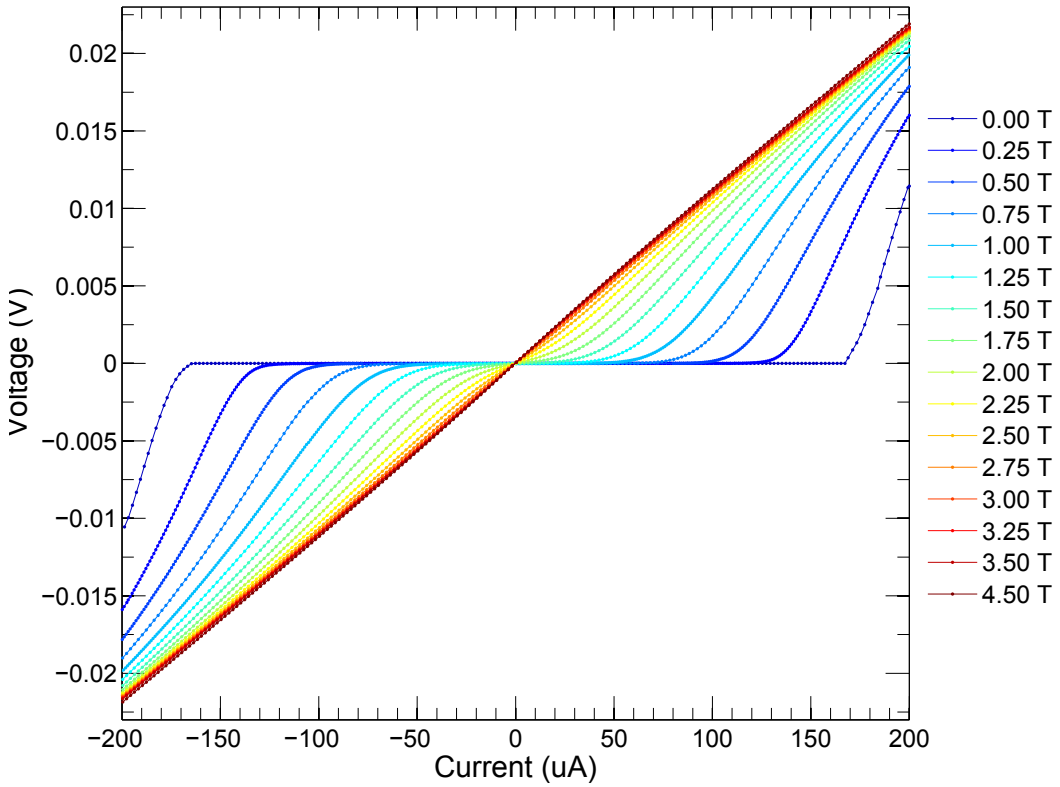


Figure 6.17: Voltage-current characteristics for a B-NCD sample grown with 1% CH_4 in the chamber at 0.3 K at different magnetic fields.

a gradual trend towards almost linear current-voltage characteristics. The current-voltage characteristics plotted on a logarithmic scale (Fig. 6.18) show regions of linearity with a gradual transition from a steep gradient to a less steep gradient as the device transitions out of the superconducting phase with increasing magnetic field.

The differential resistance at different magnetic fields at 0.3 K (Fig. 6.19) also shows interesting features. As the magnetic field increases, the amplitude of the symmetric differential resistance peaks on either side of zero bias decreases indicating a more gradual transition. The differential resistance at 0.75 T shows an interesting, repeatable feature at 105 (-105) μA. This local saturation of the differential resistance is comparable to a similar local saturation in the differential resistance at 0.31 K (Fig. 6.16) which is also found at around 100 μA. This is also similar to the local saturation of the magnetoresistivity at 1.4 K shown in Figure 6.5.

Figure 6.20, a logarithmic scale plot of the differential resistance as a function of current, shows that as the magnetic field increases, a distinct local minimum in the differential resistance persists up to 3 T while the maxima in the differential resistance on either side of zero bias also vanish at 3 T. At yet higher fields, the local minimum transforms into a global maximum in the differential resistance with the zero bias differential resistance increasing along with the field.

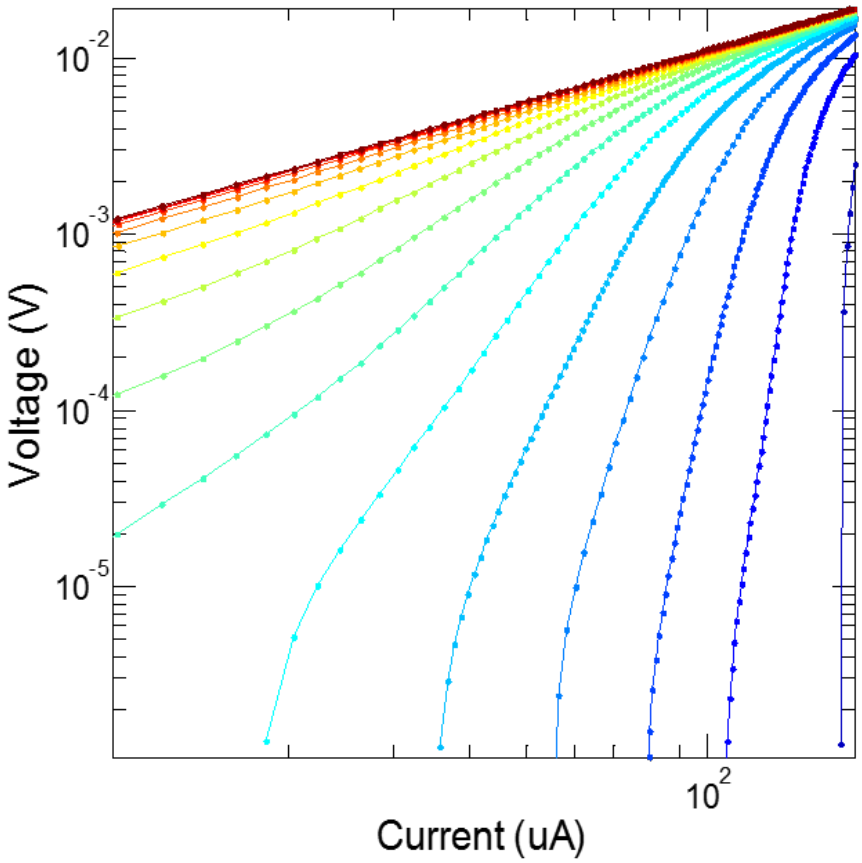


Figure 6.18: Voltage-current characteristics on a logarithmic scale for a B-NCD sample grown with 1% CH_4 in the chamber at 0.3 K at different magnetic fields.

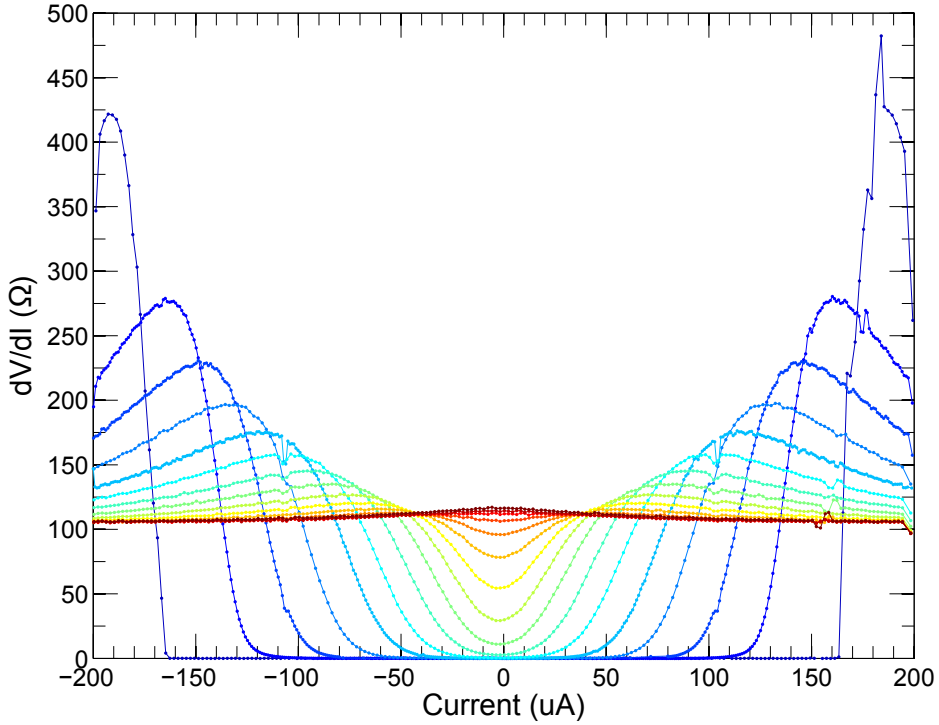


Figure 6.19: Differential resistance as a function of current for a B-NCD sample grown with 1% CH_4 in the chamber at 0.3 K at different magnetic fields.

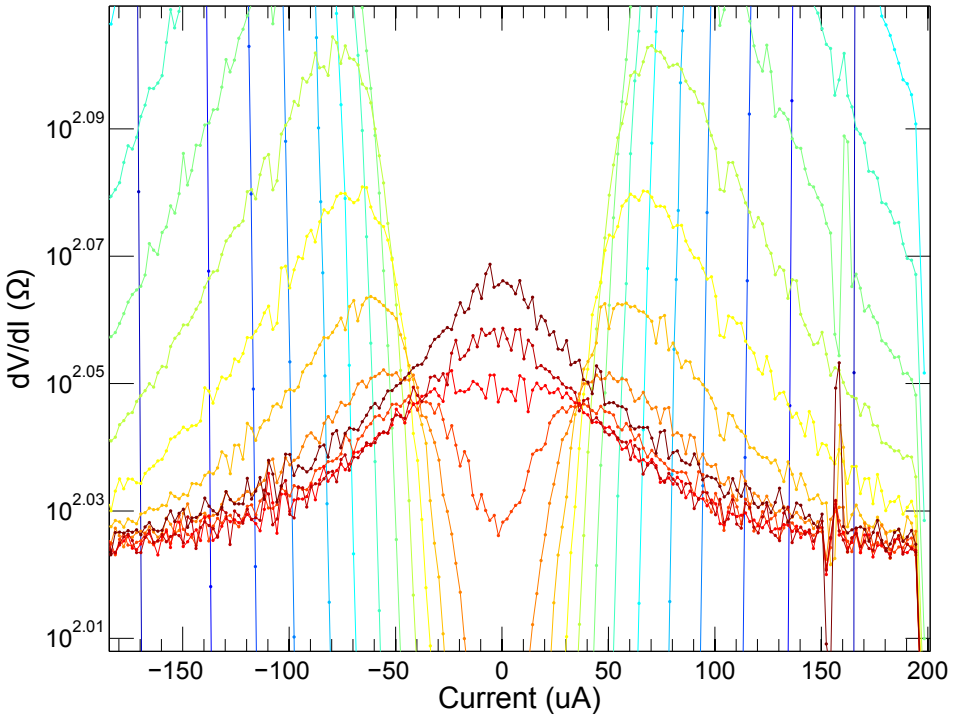


Figure 6.20: Differential resistance plotted logarithmically as a function of current for a B-NCD sample grown with 1% CH_4 in the chamber at 0.3 K at different magnetic fields.

6.2.2 B-NCD device grown with 5 % CH_4 in the chamber

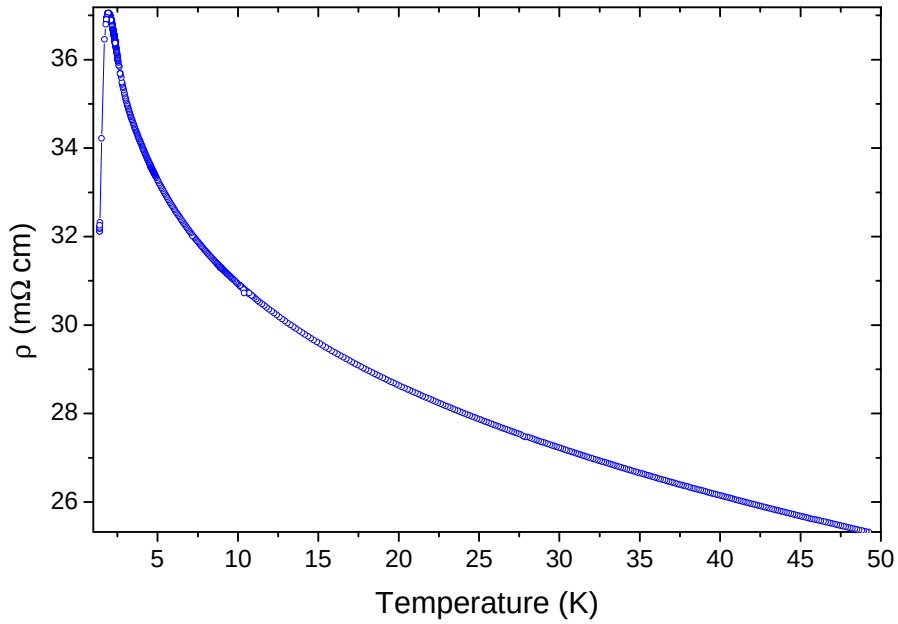


Figure 6.21: Resistance as a function of temperature for B-NCD device grown with 5 % CH_4.

Figure 6.21 shows resistivity as a function of temperature for a B-NCD device grown with 5% CH_4 in the chamber. The resistivity of this device is more than an order of magnitude greater than the device grown with 1% CH_4 in the chamber (both samples have the same dimensions). The resistivity increases rapidly as the temperature decreases until the onset of the superconductor-insulator transition at around 2 K. An Efros-Shklovskii variable range hopping fit to the data is shown in Figure 6.22. While there is some region which scales as $T^{-1/2}$ the fit is not entirely convincing although there is significant overlap at low temperatures, around the region of the onset of the superconducting transition. Resistivity is shown as a function of the logarithm of the temperature in Figure 6.23. At higher temperatures, there is a clear tendency towards a logarithmic dependence however at low temperatures, there is a marked divergence from the logarithmic trend as shown by the green line. This region is better described by the Efros-Shklovskii fit.

The magntoresistivity of a B-NCD device grown with 5% CH_4 in the chamber at 1.4 K is shown in Figure 6.24. At 1.4 K, the device is outside the regime of global superconductivity. The resistivity initially increases rapidly indicating superconductivity in local regions. At 1.8 T, there is a maximum in the resistivity which then decreases until 3.8 T, subsequently increasing monotonically. A fit to the data describing the region after the local maximum in the resistivity is shown as a red line.

The contribution to the conductivity from the density of states term as a function of

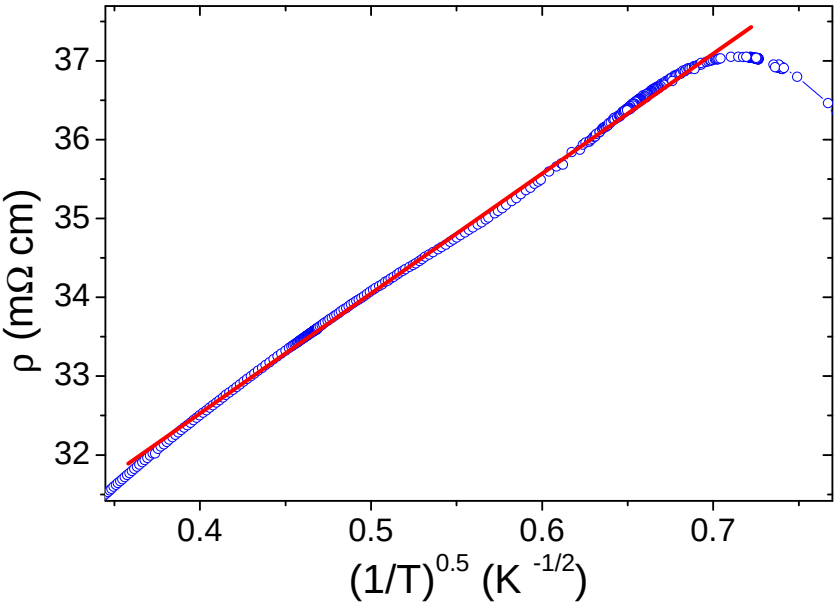


Figure 6.22: Resistivity as a function of $T^{-1/2}$ for a B-NCD device grown with 5% CH_4 in the chamber.

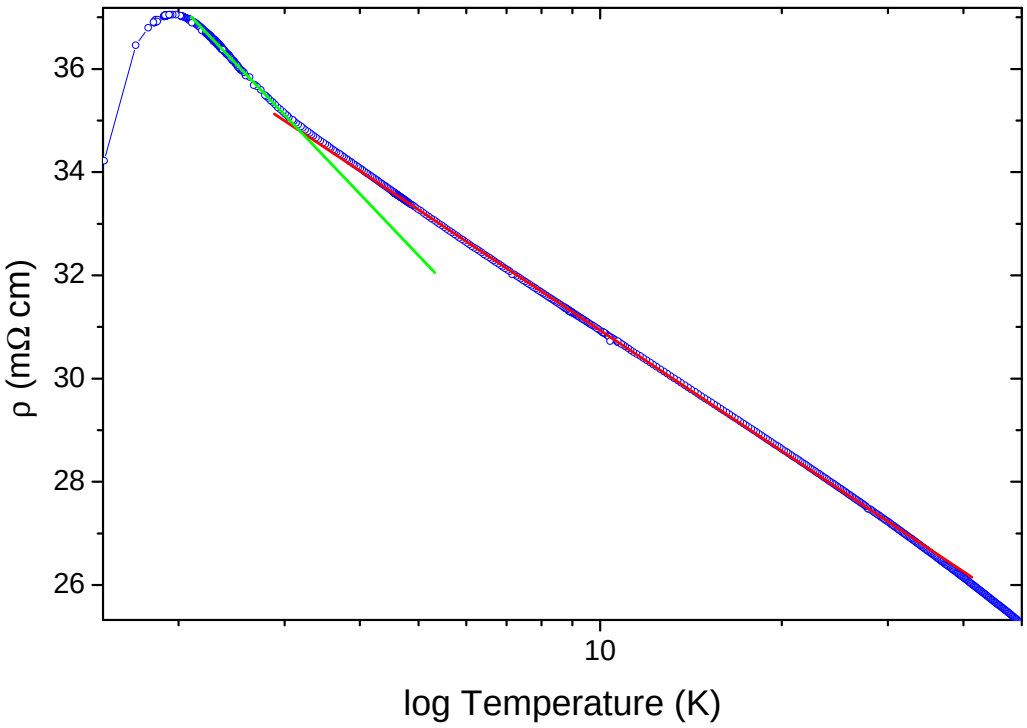


Figure 6.23: Resistivity as a function of temperature plotted logarithmically for a B-NCD device grown with 5% CH_4 in the chamber. The red line shows the fit to a logarithmic dependence in the high temperature regime, the green line shows a significant change in gradient in the low temperature regime

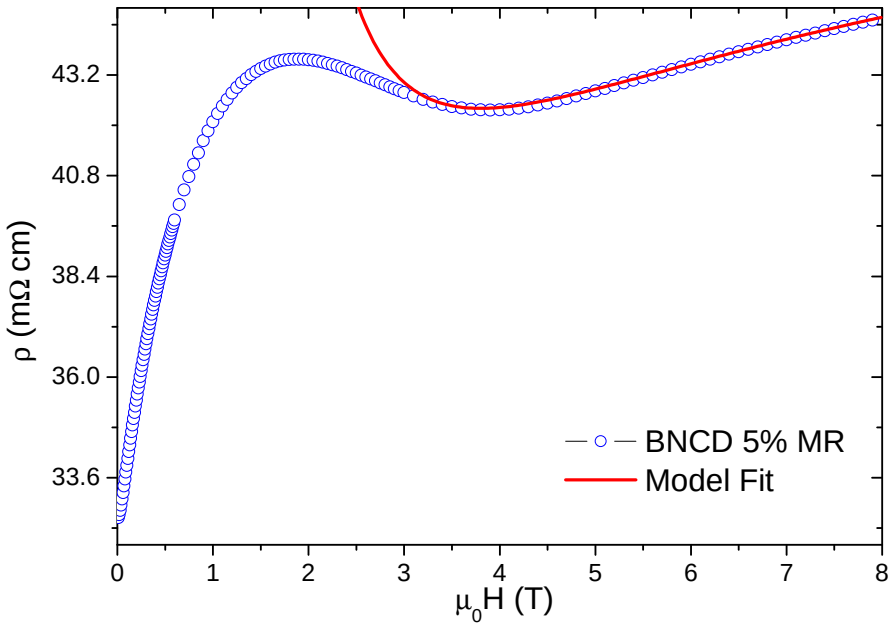


Figure 6.24: Magnetoresistivity at 1.4 K for a B-NCD device grown with 5% CH_4 in the chamber. The red line is a fit to the data based on the model discussed in the text.

applied magnetic field is given by [182, 100, 183]

$$\frac{\delta\sigma_{dos}}{\sigma_0} = \frac{-1}{3g}\frac{\Gamma}{E_0(H)} ln^{-1}\left(\frac{E_0(H)}{\Delta_0}\right) \tag{6.1}$$

where δ is the mean level spacing within the granules, g is the inter-granule tunnelling conductance, $\Gamma = g\delta$ is a characteristic energy scale defined similarly to the Thouless energy and Δ_0 is the average order parameter on the grains. $E_0(H) = 2D(eHR)^2/5c^2$ where D is the intra-granular diffusion coefficient and R is an average measure of the radius of the grains. A fit to the data was obtained by assuming appropriate parameters for the current samples and treating the other parameters as free variables. To a achieve a satisfactory fit, a mean level spacing of 6 meV was used with the pairing amplitude on each grain being 2.5 eV. These parameters are consistent with what would be expected for B-NCD.

The contribution from the Aslamazov-Larkin process to the conductivity can be expressed as [182, 100, 183]

$$\frac{\delta\sigma_{AL}}{\sigma_0} \propto \frac{1}{g}\frac{T^2}{\Delta_0^{3/2}\Gamma^{1/2}}\left(\frac{H_c}{H-H_c}\right)^{3/2} \tag{6.2}$$

where H_c is the critical field. The contribution from Maki-Thompson processes is given by

$$\frac{\delta\sigma_{MT}}{\sigma_0} \propto \frac{1}{g}\frac{\Gamma}{\Delta_0}\frac{T^2}{\Delta_0^2} \tag{6.3}$$

The fit in Figure 6.24 is the sum of the contributions to the conductivity from the density of states, Maki-Thompson and Azlamazov-Larkin contributions.

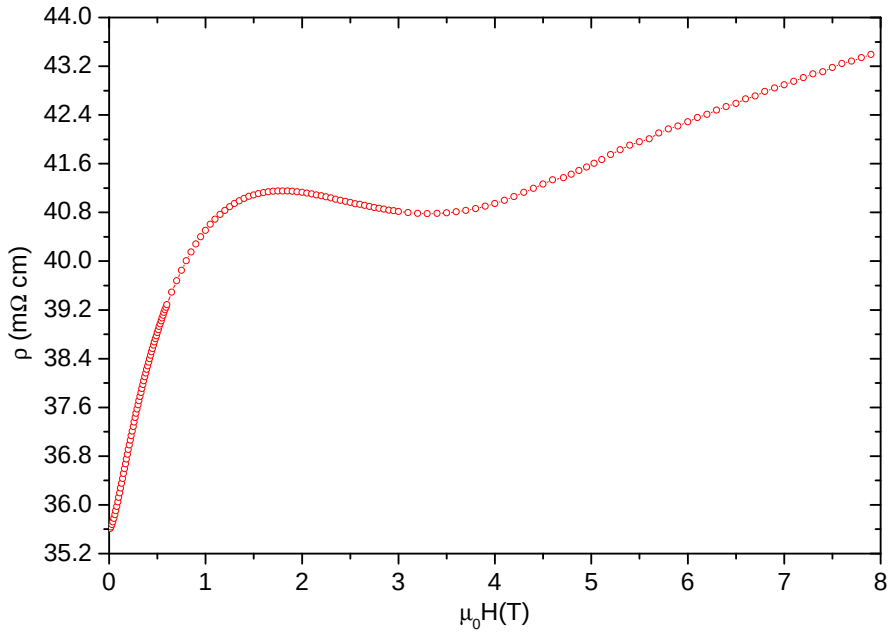


Figure 6.25: Magnetoresistivity of a B-NCD device grown with 5 % CH_4 at 1.6 K.

Figure 6.25 shows the magnetoresistivity at 1.6 K. A distinct local maximum at 1.75 T persists although the relative difference in the resistivity between the local maximum and the subsequent minimum is not as large as at 1.4 K. In addition, the peak broadens out slightly. The transition to increasing magnetoresistivity at 3.3 T is also not as sharp at was the case at 1.4 K.

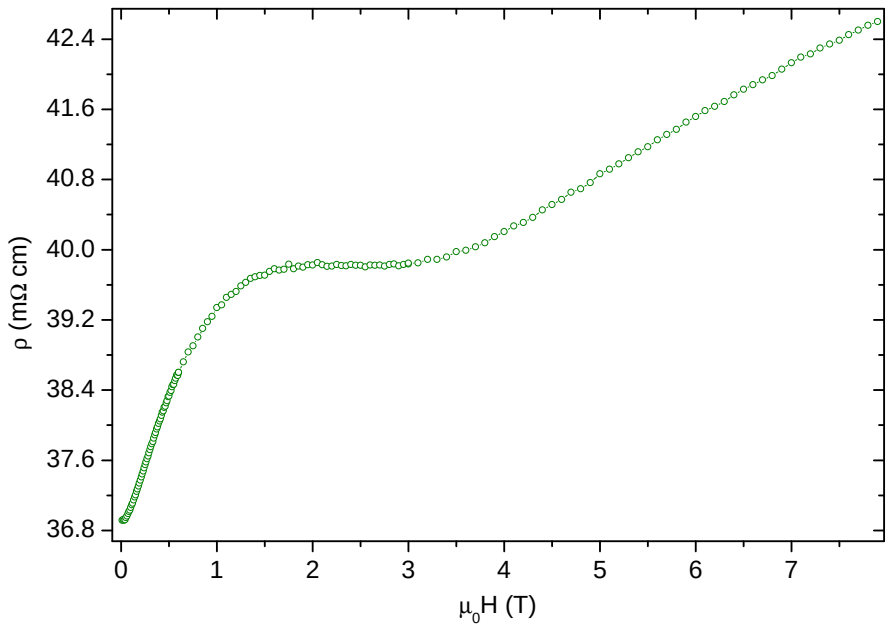


Figure 6.26: Magnetoresistivity of a B-NCD device grown with 5 % CH_4 at 1.8 K.

At 1.8 K, a distinct step-like feature remains in the magnetoresistivity beginning at around 1.5 T with the magnetoresistivity then increasing monotonically from 3 T, as shown

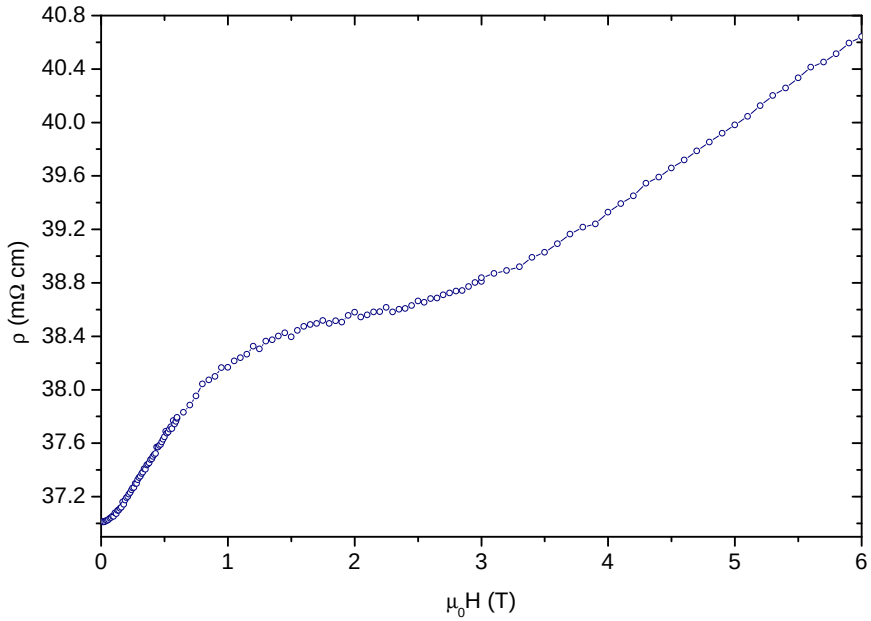


Figure 6.27: Magnetoresistivity of a B-NCD device grown with 5 % CH_4 at 2.0 K.

in Figure 6.26. Initially, there is a rapid increase in the magnetoresistivity while above 3 T the increase is not as sharp. The step-like feature is still discernible at 2 K (Fig. 6.27) however the resistivity no longer levels off. The initial increase in the magnetoresistivity from 0 T is considerably less steep than at lower temperatures while the resistivity at 6 T is much less than the resistivity at at 6 T at 1.8 K.

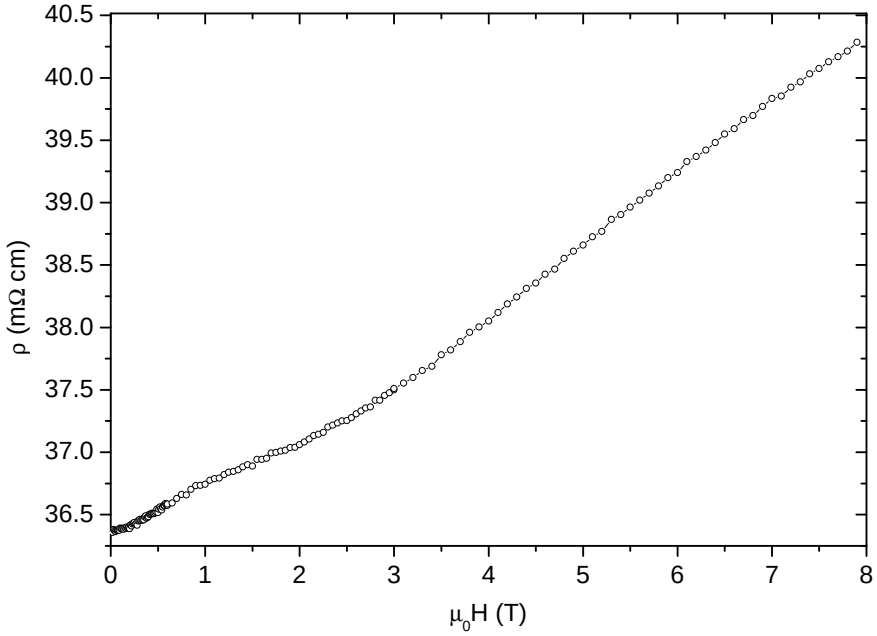


Figure 6.28: Magnetoresistivity of a B-NCD device grown with 5 % CH_4 at 2.4 K.

Even at 2.4 K (Fig. 6.28), the magnetoresistivity shows a change in gradient, beginning at 0.9 T, however the local maximum is no longer a distinct feature. At 3 K, no trace of the step-like feature remains and the resistivity increases monotonically through the region of the magnetic field sweep, as shown in Figure 6.29. Figure 6.30 shows the magnetoresistivity

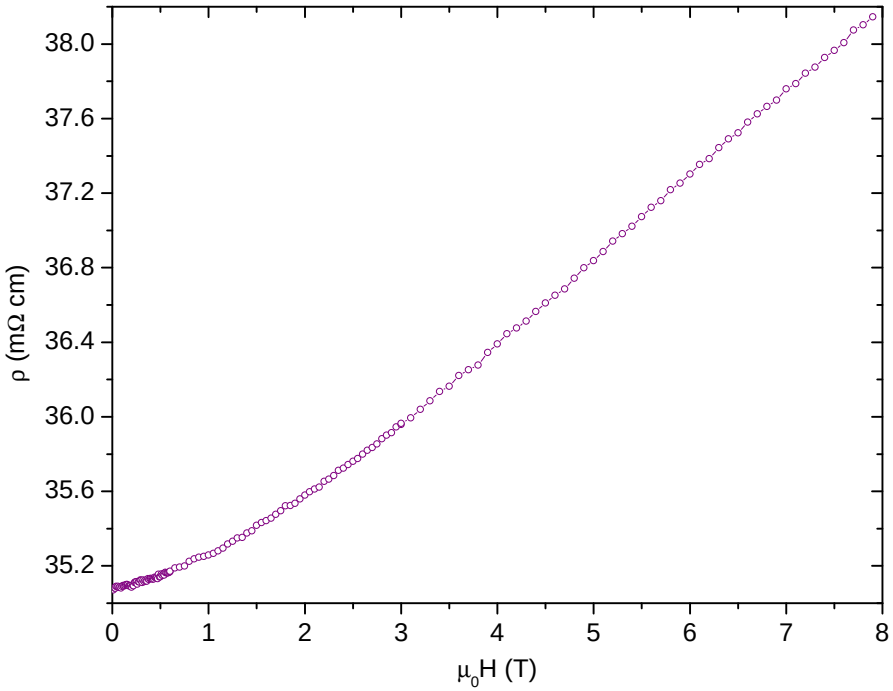


Figure 6.29: Magnetoresistivity of a B-NCD device grown with 5 % CH_4 at 3.0 K.

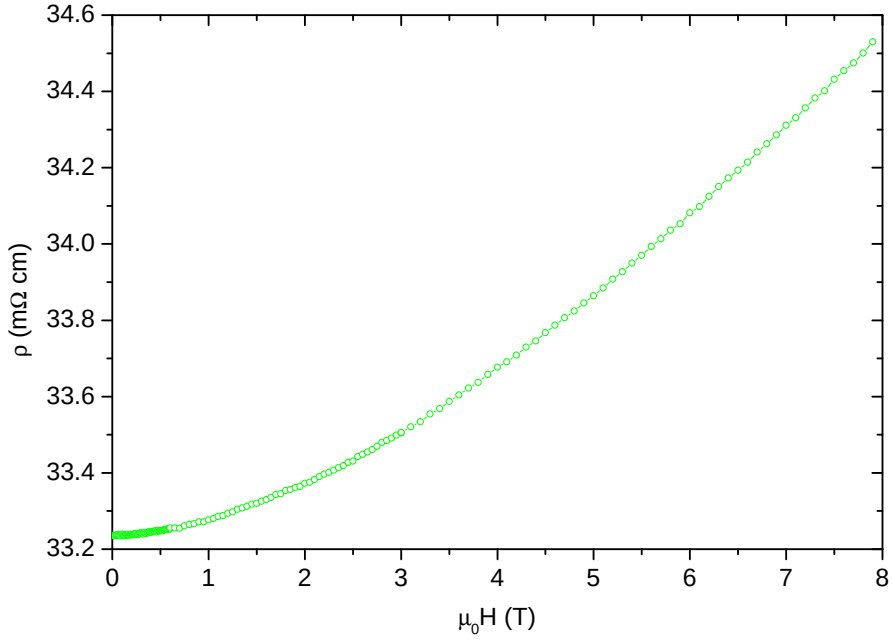


Figure 6.30: Magnetoresistivity of a B-NCD device grown with 5 % CH_4 at 5.1 K.

at 5.1 K. This shows a similar trend to the magnetoresistivity at 3 K however the change in magnetoresistivity from 0 T to 8 T is much smaller. The magnetoresistivity remains distinctly positive throughout.

6.3 Discussion

Detailed Hall effect measurements have been carried out on a number of devices made in the same lab, under the same conditions as the devices studied here [106]. These studies showed that as the concentration of CH_4 in the plasma during growth was increased, the grain sizes decreased while the amount of boron incorporated in the B-NCD films increased. Concurrently, the T_c of these films was found to decrease. The increase in boron concentration was borne out by Hall effect measurements which showed an increase in the carrier concentration [106]. While the mobility decreased as expected, the carrier activation energy increased. This is indicative of the increase in structural disorder. Previous sections in this work show that structural disorder has a detrimental effect on the T_c so the decrease in the T_c in these B-NCD films can be conclusively ascribed to the increase in structural disorder which accompanies the decreasing grain sizes, despite the increasing boron concentration which should enhance the T_c.

The local saturation of the magnetoresistivity at around 0.1 T of the device grown with 1% CH_4 in the chamber at 1.4 K is related to the coexistence of two quantum phases corresponding to the breakdown of superconductivity across the grain boundaries first, followed by the breakdown of superconductivity within the grains resulting in two distinct phases. This feature is absent in the magnetoresistivity at 1.8 K. At 2.1 K, there is saturation of the magnetoresistivity around zero applied field however this feature cannot have the same origin as the feature at 1.4 K as it is absent in the magnetoresistivity at 1.8 K.

The features in the magnetoresistivity of a device grown with 1% CH_4 in the chamber, coupled with features in the differential resistance at 1.3 K and at 0.3 K under an applied field of 0.75 T provide convincing evidence of distinct quantum phases in the region of the superconducting transition. As superconductivity breaks down, there is a corresponding change in the magnetoresistivity or differential resistance. Phase fluctuations play an important role in granular superconductors such as B-NCD. The tunnelling across the grain boundaries allows weak links to be formed between the grains. The charging energy of the grains has to be overcome by Josephson coupling for global superconductivity to occur [184].

The logarithmic temperature dependence of the resistivity found in this device is also consistent with that of a granular superconductor. There is still ongoing debate surrounding the origins of this logarithmic dependence. A number of theoretical studies suggest that the conductance rather than the resistivity should show a logarithmic dependence [182]. A

number of experimental studies though have shown this logarithmic temperature dependence and it has been shown that a logarithmic dependence can be expected when there is strong coupling between the grains [185, 98, 186]. Where the inter-granular coupling is not as strong, the temperature dependence has been found to be of the form $R \propto exp(-a/T^{1/2})$ [186]. This suggests that as the coupling strength increases, the effect of the Coulomb interaction between the islands becomes less significant. In the case of B-NCD, the coupling strength is directly related to the size of the grains.

The magnetoresistivity is uniformly positive below 10 K, ruling out the dominance of weak localization although it will likely have some contribution to the transport above the superconducting transition temperature. Weak localization is expected to contribute to the transport mechanism within the grains where there is a random distribution of boron dopants.

At 14 K, there is a small region of slightly negative magnetoresistivity however the change in resistivity is extremely small and in the region of 0 to 1 T the variable temperature insert temperature of any cryostat will invariably increase slightly as the magnetic field is ramped up in this range so the region of negative magnetoresistivity is most likely due to a slight increase in temperature. Although this effect is prominent at low temperatures as well, in this device the change in marnetoresistivity from zero field to high field is very large so at lower temperatures the resistivity of the device is less sensitive to changes in temperature than at higher temperatures.

The temperature dependence of the resistivity of the device grown with 5% CH_4 in the chamber shows a logarithmic dependence at higher temperatures however there is a distinct shift from the logarithmic dependence as the device approaches the transition. In fact this region is quite well fitted by an Efros-Schlovskii fit. This is consistent with other studies of granular superconductors [184] and indicates the enhancement of the influence of the Coulomb interaction as the grain size decreases and charging effects between grains become more significant.

Considering the magnetoresistivity of the device grown with 5% CH_4 in the chamber at 1.4 K (Fig. 6.24), the magnetoresistivity as a function of field increases rapidly as global superconducting coherence begins to break down across the grain boundaries initially until eventually even the superconducting coherence within the grains breaks down. The resistivity shows a distinct local maximum in the magnetoresistivity at around 1.6 T which is of significance in determining the influence of superconducting fluctuations. Such local maxima have been reported in other studies of B-NCD close to the superconductor -insulator transition [184, 187, 188].

Similar features have also long been studied in various granular superconductors [91]. It has been suggested that a necessary condition is some form of natural uniformity in the grain size and coupling between the grains, based on the assumption that there is a critical normal state resistivity which controls the global phase coherence that is related to the resistivity

of the grains and a characteristic length scale [183]. The local maximum in the magnetoresistivity is related to the reduction of tunnelling across grain boundaries and concurrent suppression of the density of states (DOS) under the influence of a magnetic field due to the persistence of virtual Cooper pairs, even above the field where superconductivity within the grains breaks down [182, 100]. B-NCD shows features of a granular superconductor and we interpret the behaviour of the magnetoresistivity using a model developed for disordered arrays of Josephson junctions.

A fit to the magnetoresistivity is shown in Figure 6.24. In the model used, it is assumed that the superconducting gap is less than the Thouless energy [182, 100, 183]. The condition stipulated for large tunnelling is valid in B-NCD since the grain boundaries are graphitic so the grains are strongly coupled and do not pose a significant tunnel barrier resulting in a strong proximity effect. This is borne out by STM studies which show strong coupling between the grains [156]. The contribution to the resistivity from the suppression of the density of states is maximal at the magnetic field corresponding to the breakdown of superconducting coherence within the grains [182]. This contribution then falls sharply with increasing magnetic field resulting in the region of negative magnetoresistivity (as tunnelling is no longer actively suppressed) and eventually levels off at higher fields.

However we also observe a crossover to an increase and eventual tendency towards saturation of the magnetoresistivity with increasing field in B-NCD which is an unusual feature which is not common to all granular superconductors. The positive magnetoresistivity at higher fields shows that there is a contribution to the magnetoresistivity which is in competition with the DOS contribution. This behaviour can be explained by a combination of the Aslamazov-Larkin and Maki-Thompson processes, which also originate with superconducting fluctuations, resulting also in positive magnetoresistivity [182]. We found the fit to the data to be closest with minimal contribution from the Maki-Thompson process, which suggests that the formation of charge channels by non-equilibrium Cooper pairs is more prominent than the Maki-Thompson contribution.

It has been suggested that local regions of negative magnetoresistivity can be attributed to weak localization [189] however the authors of this work caution that this interpretation is strictly limited to a specific case of their study. In B-NCD there is most likely a contribution from weak localization although it is not the predominant contribution to the resistivity, as also shown in detailed experimental studies on disordered, granular TiN thin films where contributions as a result of quantum fluctuations with weak localization as an additive term to the resistivity were used to interpret experimental data [190].

The differential resistance (Figs. 6.19 and 6.20) at 0 T shows a broad superconducting region with a rapid change to the non-superconducting state with increasing current. With increasing magnetic field, the prominent minimum in the differential resistance remains. This suggests a mixture of superconducting and non-superconducting regions as superconductivity breaks down across the grain boundaries but persists within the grains. This is

also the case at 1.9 and 2 K where there is a local minimum in the differential resistance (Fig. 6.16).

As the magnetic field increases, these local resistance maxima decrease in amplitude and move towards zero current while the sharp local minimum remains at zero current. At 3 T, the local minimum transitions to a global maximum. Significantly, this is consistent with the MR which shows that the magnetoresistivity at different temperatures of a few hundred mK collapse onto a single curve at around 3 T indicating the total breakdown of superconductivity within the grains. This strongly indicates that the minimum in the differential resistance is due to the persistence of superconductivity in the grains up to 3.2 T. The current flows preferentially through channels with maximal Josephson coupling so local superconductivity still influences the conductivity, hence there is a local minimum at zero current although global phase coherence is lost. The differential resistance then shows a maximum at zero current at above 3 T. With further increasing field the resistance of this maximum increases.

The voltage versus current characteristics at different temperatures show a power law dependence, $V(I) = I^{\alpha}$, in some regions of the current-voltage characteristics (Fig. 6.15). This is especially evident in the current-voltage characteristics at under different magnetic fields (Fig. 6.18). At 1.25 T the voltage as a function of the current (over the linear region in the logarithmic plot) can be fitted with $\alpha = 3$. At 2.75 T, the voltage as a function of current can be fitted with $\alpha = 1$. At higher magnetic fields, the gradient of the voltage-current curves changes little. This is consistent with a magnetic field induced Berezinski-Kosterlitz-Thouless (BKT) transition [190]. The BKT transition describes the onset of global superconductivity in two dimensional or thin film type II superconductors. Below the BKT transition temperature, vortices are bound to anti-vortices and vortex anti-vortex pairs within the Abrikosov lattice preserving the superconducting coherence and allowing dissipation-less current to flow. With increasing magnetic field, these pairs become unstable and unbind resulting in free vortices which drift through the material leading to finite resistance. A well established signature of the BKT transition is the power law dependence of the voltage-current characteristics where the exponent changes from 3 or below before the BKT transition to 1 at or above the BKT transition.

The origin of the differential resistance peak is an interesting feature to be still deconvoluted. It does however indicate a process that is in a competition with superconductivity and merits further investigation. It has been suggested in studies of 4-angstrom carbon nanotubes [180] which show a similar peak that the peak is related to either the Peierls transition, Luttinger liquid or granular contacts but all of these are unlikely in B-NCD (unless conduction is predominantly through quasi 1D channels, where a Peierls transition would be possible). Given the nature of the narrow boron acceptor level in B-NCD, the Coulomb interaction is expected to make a significant contribution to the transport properties. As such, another possible explanation for the maximum in the differential resistance would be

some form of charge density wave behaviour [191] however this cannot be confirmed at this point.

B-NCD shows some features in both MR measurements and V-I characteristics which are similar to features found in superconducting thin films of TiN which from superconducting islands and interact through Josephson coupling, which have exhibited a BKT transition [190, 192]. Specifically, the vortex lattice of superconducting boron doped diamond has been studied through STM measurements. Although the pairing gap was found to be nearly uniform over the whole sample (a strongly disordered triangular lattice was found), some unexpected resonances were found in the gap across vortex lines, their origin remains unexplained [147]. STM studies in B-NCD revealed that some grains show a BCS gap while some are not BCS-like [156]. Both 1D and 2D carbon systems have shown BKT transitions [176, 180].

Networks of superconducting nanotubes have also shown features of a BKT transition as evidenced by the power law dependence of V-I measurements and the temperature dependence of the resistivity [180]. It was shown that the nanotube network behaves like Josephson arrays as there is sufficient coupling between the individual nanotubes in the network. Supercurrents in graphene have also been widely studied [176]. It has been demonstrated that in thin layers of tin decorated graphene, where the tin forms isolated superconducting islands, that the system behaves as 2D Josephson coupled arrays [193]. BKT transitions have also been established in these devices [176].

These previous studies and the similar power law dependence of the IV characteristics lend weight to the claim of a BKT transition in B-NCD films. The diamond grains in B-NCD form superconducting regions while the graphitic grain boundaries are unlikely to contribute to the onset of superconductivity although they can effectively carry a supercurrent. The Josephson coupling is strongest where diamond grains are closest together. B-NCD may therefore be interpreted as a disordered network of Josephson arrays. While the formation of vortices in crystalline doped diamond has been clearly shown, the influence of the grain boundaries on vortex dynamics, which form a network through the entire material, is not yet understood.

Chapter 7

Conclusion

Quantum confinement effects were demonstrated in amorphous carbon superlattices through prominent current suppression in a-C superlattice devices. These temperature dependent features in the measured I-V characteristics are interpreted through calculations of the I-V characteristics using a $1D$ model for a disordered superlattice within the Landauer-Büttiker formalism. The calculations indicate that the extent of the sp^2/sp^3 hybridized regions results in changes of the *potential barrier at the interface*. This effect, far less prominent in crystalline superlattices, has a strong influence on features in the current-voltage characteristics and can be used to inform the design of future quantum devices. The low power requirements of these devices opens the possibility of in-vivo spectral imaging.

The role of disorder on the transport properties of thin graphitic films was addressed. Films with various degrees of structural disorder were studied through a combination of Raman spectroscopy and transport studies. Using a tight-binding model, we calculated the localization length as a function of the disorder parameter for the sp^2 phase while sp^3 hybridized defects were treated as potential barriers. The overlap with experiments shows that this model accurately captures the role of structural disorder in graphitic carbon films. In future studies, graphene layers may be grown and the effects of disorder studied systematically using this method.

The effect of the incorporation of different nitrogen complexes in DLC superlattices was studied. The satellite nitrogen peak in transmission appears due to the introduction of nitrogen centres, which breaks the tunnelling conditions. In this model, carbon and nitrogen peaks can be separated throughout the range of energy. Disorder reduces transmission maxima and has a more drastic effect on the carbon peak than on the nitrogen peak. By adjusting the energy position of nitrogen centres relative to the Fermi energy, we can tune the transport in CN structures through the relative intensity of the carbon and nitrogen peaks. Indeed, nitrogen atoms forming energy levels lower or higher than that of sp^2 carbon act as scattering centres by forming a thin barrier to 1D transport and by breaking the symmetry of the quantum wells. Most importantly, a crossover of the carbon and nitrogen transmission peaks can be achieved by adjusting the position of nitrogen potential in relation

to E_F.

We thoroughly explained the quantum size effects observed in nitrogen doped diamon-like carbon superlattices in the form of resonant tunnelling. The electrical properties revealed enhanced resonant transmission with increasing nitrogen partial pressure in the synthesis phase, in agreement with the theoretical calculations conducted using a 1D tight-binding model which included significant bond alternation in the sp^3 hybridized regions. The NDR voltage consecutively shifted toward smaller potentials while the total current increased with increasing nitrogen partial pressure. The generation of nitrogen-induced additional 1D channels and networks, which arise as the number of sp^2 clusters increases, is the origin of the enhanced tunnel transport in N-DLC QSL structures. This discovery can be extremely important toward the development of cost-effective and mechanically robust fast quantum electronic devices.

Time dependent studies of the influence of the electron-phonon interaction in quantum dots and double barrier quantum wells showed that the frequency of an external gate potential can be used to tune the resonant energy very precisely. In addition, the transmission coefficient at resonance changes little. This is significant for device applications and could be used to develop oscillators in the THz regime. This could also be exploited to develop opto-electronic devices which can operate over a wide frequency range with unprecedented resolution.

Having firmly established the nature of structural disorder in nano-structured carbon materials, the influence of structural disorder on superconductivity was studied. The contrasting nature of on-site random potential disorder and structural disorder in the form of non-uniform random tight-binding hopping parameters has been illustrated and the results were applied to understanding the superconductor-insulator transition in BDD and B-NCD. While on-site potential disorder at the boron sites alone decreases the mean pairing amplitude and spectral gap, structural disorder can increase the mean pairing amplitude although the spectral gap still decreases as the disorder parameter increases. This significant difference in behaviour stems from the introduction of states within the gap region in the case of structural disorder, resulting in a wide distribution of mean pairing amplitudes. The calculated temperature dependence also highlights the different natures of structural and on-site disorder as structurally disordered systems show a marked deviation from the temperature dependence expected for a conventional BCS superconductor. This work is of particular interest when applied to B-NCD due to the high level of structural disorder inherent in this unconventional superconductor. Through the combination of structural disorder, random on-site potential fluctuations and the Coulomb interaction in the narrow acceptor band, the experimentally found saturation of the T_C in BDD as a function of the boron concentration can be understood. This study illustrates a minimal Hamiltonian which captures some of the features found in experimental studies of BDD and B-NCD and lays a foundation for further work where grain boundaries in B-NCD (which act as weak links) can be built into

the theory through Josephson junctions to more closely reflect B-NCD and be more directly comparable to transport measurements.

Recently, the highest T_c ever reached with crystalline boron doped diamond has been achieved [194]. The reduction in disorder was conclusively shown to be the dominant factor in increasing the T_c. This result is borne out by the work in this thesis which clearly demonstrates the stark differences between structural and on-site disorder and categorically shows how detrimental the effects of structural disorder on superconductivity are.

In experimental work on B-NCD films, we find evidence of a BKT transition in highly-boron doped nanodiamond films through a power law dependence of the voltage-current characteristics. We find a distinct local maximum in magnetoresistance measurements leading to a region of negative magnetoresistance which is often associated with arrays of Josephson junctions. We interpret this feature through suppression of the density of states and together with the the Aslamazov-Larkin and and Maki Thopmson contributions. In devices with large grain sizes, we demonstrate distinct evidence of competing quantum phases through a combination of features in the voltage-current characteristics and magnetoresistance measurements.

Chapter 8

Publications

Ross McIntosh and Somnath Bhattacharyya, Phys. Status Solidi, Rapid Research Letters 6, 56 (2012).
"The Kondo Effect in Reduced Graphene Oxide Films".

Ross McIntosh, Messai A. Mamo, Brice Jamieson, Saibal Roy, and Somnath Bhattacharyya, Europhys. Lett. 97, 38001 (2012).
"Improved Electronic and Magnetic properties of Reduced Graphene Oxide Layers".

R. McIntosh, N. Mohanta, A. Taraphder, and S. Bhattacharyya, arXiv:1358553, (2016) under review for Phys. Rev. B.
"Influence of structural disorder and Coulomb interactions in the superconductor-insulator transition applied to boron doped diamond".

R. McIntosh, S. J. Henley, S. R. P. Silva and S. Bhattacharyya, Scientific Reports 6, 35526 (2016).
"Coherent quantum transport features in carbon superlattice structures".

Dmitry Churochkin*, Ross McIntosh* and Somnath Bhattacharyya, J. Appl. Phys. 113, 044305 (2013).
"Tuning resonant transmission through geometrical configurations of impurity clusters".

Mikhail V. Katkov, Ross McIntosh and Somnath Bhattacharyya, J. Appl. Phys. 113, 093701 (2013).
"Tunnel transport model in nitrogen doped disordered carbon superstructures".

Christopher Coleman, Ross McIntosh and Somnath Bhattacharyya, J. Appl. Phys. 114,

043716 (2013).
"Controlling the activation energy of graphene-like thin films through disorder induced localization".

Neeraj Dwivedi, Ross McIntosh, Chetna Dhand, Sushil Kumar, Hitendra K. Malik, and Somnath Bhattacharyya, ACS Appl. Mater. Interfaces, 7, 20726 (2015).
"Structurally Driven Enhancement of Resonant Tunnelling and Nanomechanical Properties in Diamond-like Carbon Superlattices".

Chapter 9

Appendix

9.1 Triplet Superconductivity in Superconducting spin valves

Finally, we include some results which are related to the central themes of this thesis but fall outside its scope. We stress that although these results are not related to carbon nanostructures, some of the work in this thesis (for example, the inhomogeneous Bogoliubov de Gennes theory) can be extended to interpret these results. We present results of transport measurements, coupled with measurements of the magnetic properties, of superconducting spin valves. The study of controllable triplet superconductivity has driven the recent surge in interest in superconducting spin valves. The exchange interaction, which promotes the alignment of electron spins, is in direct competition with Cooper pairing in ferromagnetic materials [195]. The superconducting state therefore decays rapidly in superconductor-ferromagnet junctions.

However under the right experimental conditions the proximity effect in conjunction with the exchange interaction can result in triplet superconducting states which can exist close to the junction. The triplet state with net spin zero (which has an oscillating wavefunction and usually decays rapidly) can decay into triplet states with non-zero spin (which have longer lifetimes) [196]. As the spins are aligned, there is no difference in the Lorentz force experienced by the fermions making up the pairs (the orbital effect) and the Zeeman effect does not contribute to pair breaking hence the lifetime is longer than the spin zero triplet state [195]. Since these triplet pairs carry a net spin, this effect has stimulated marked interest towards spintronic applications.

Spin valves allow the spin polarization of the different ferromagnetic layers to be changed independently and provide the control necessary for fundamental studies of triplet superconductivity [197, 198]. Generally, when the ferromagnetic layers are anti-parallel, the superconducting transition temperature should be higher than in the parallel configuration due to the decreased exchange interaction [197]. However theoretical and experimental work

has shown that the reverse situation may arise when interference effects of the pair wavefunction arise in the spin valve, which depends on the thickness of the layers [199]. Recently, the role of film coverage in Pb superconducting spin valves has been studied [200] where it was found that although smoother films show a more conventional spin-valve effect, the smoothness (connectivity) of the Pb film has little effect on the superconducting transition temperature.

Here we study different configurations of superconducting spin valves.

9.1.1 Experimental Methods

Superconducting spin valves were grown by the author at the University of Leeds by DC magnetron sputtering in a high vacuum chamber. The magenetic layers were grown in a strong forming field to set the anisotropy. Spin valves with different configurations (and hence different switching fields) were studied.

The first configuration consisted of the following layers: Ta, Pb, permalloy, Cu, Co, IrMn, Co, Ta on a SiO_2 wafer. The first layer of tantalum provides a smooth seeding layer. The next layer, Co is pinned using IrMn followed by another layer of Co. These three layers result in a strong exchange bias which shifts the hysteresis of the spin valve, effectively forming a single magnetic layer. This is followed by a Cu spacer layer which prevents the exchange interaction penetrating into the next layer. The second magnetic layer is permalloy which has a much smaller coercivity than the strongly exchange-biased layer. A layer of superconducting Pb was grown on top of this permalloy layer. Finally, the entire superconducting spin valve was capped in a layer of Ta to shield the Pb layer from oxidation.

A second set of superconducting spin valves was grown without a layer with a strong exchange bias and consisted of the following layers: Ta, Co, Cu, Py, Pb, Ta. In this case, the difference between the conductivity of the of the two magnetic layers is much smaller as it relies only on the difference between the natural coerciviteis of Co and permalloy.

The magnetic properties were characterized in a helium cooled Oxford Instruments vibrating sample magnetometer (VSM) and a Quantum Design superconducting quantum interference device (SQUID-VSM). Transport measurements were performed in an Oxford Instruments cryostat using a Keithly 2600 source meter and a 2182 voltmeter. A rotating sample platform was used to change the orientation of superconducting spin valves relative to the magnetic field of the cryostat.

9.1.2 Magnetic Properties

The hysteresis of the first configuration of superconducting spin valves (with a large exchange

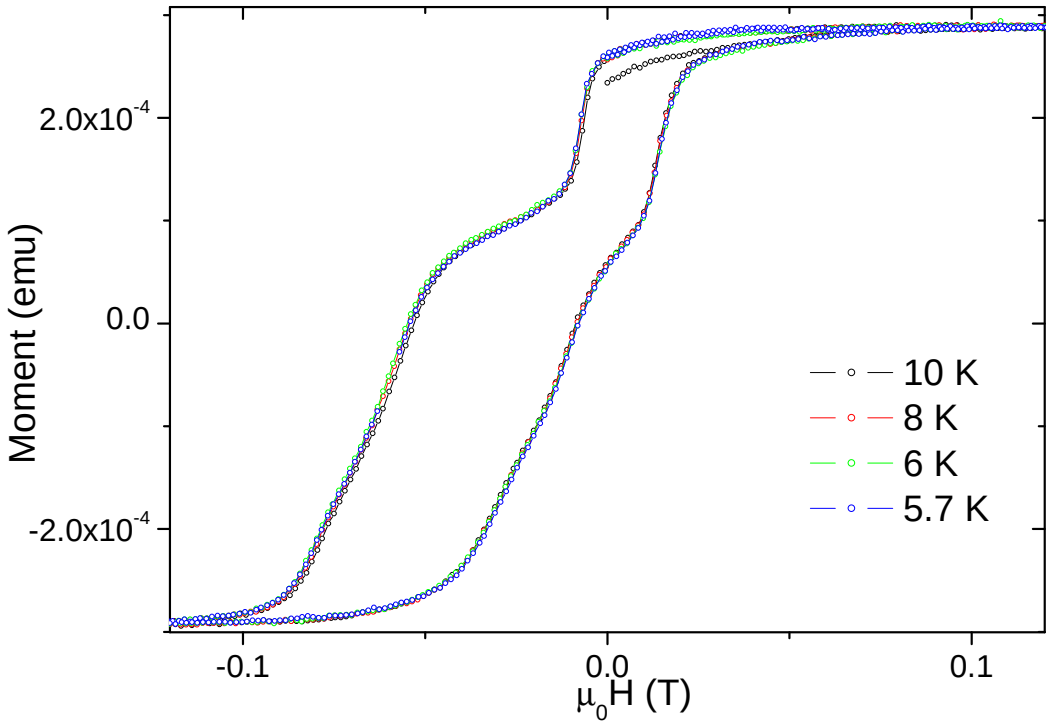


Figure 9.1: Hysteresis of a Pb superconducting spin valve above the T_c.

bias due to the Co, IrMn, Co layers) at temperatures from 10 K down to 5.7 K is shown in Figure 9.1. The superdoncucting spin valves were placed in the VSM with the with the direction of the anisotropy in the same direction as the positive magnetic field generated by the magnet in the VSM. Initially, as the field is swept to 0.1 T both magnetic layers saturate. As the field is decreased below 0 T, the anisotropy of the permalloy layer (free layer) reorients in the direction of the negative magnetic field at -0.005 T. The anisotropy of the pinned layer aligns with the field at -0.05 T until saturation at -0.12 T.

The hysteresis at 5.6 K shows very interesting features. Close to zero field on the sweep up to high positive fields, there is initially a drop in the moment. Close to zero field on the sweep back to negative fields there is an *increase* in the moment. The change in the moment due to the switching of the permalloy layer still occurs at the same field and the rest of the hysteresis loop is similar to the that at 5.7 K (Fig. 9.1).

At 5.5 K the hysteresis shows a dramatic change. The moment increases along with the field of reaching a maximum of 9.5×10^{-4} emu at about 0.2 T, it then decreases until 0.4 T where it saturates at around 9.5×10^{-4} emu. This is the same saturation moment is the same as it was at higher temperatures. In the negative field region, some remnant of the hysteresis observed at higher temperatures remains as the strong exchange bias shifts the hysteresis to more negative fields. The hysteresis curves do not change at lower temperatures (not shown here) indicating that the transition to the superconducting state occurs between 5.5 and 5.6 K.

The hysteresis is very different to what would normally be expected for a superconductor

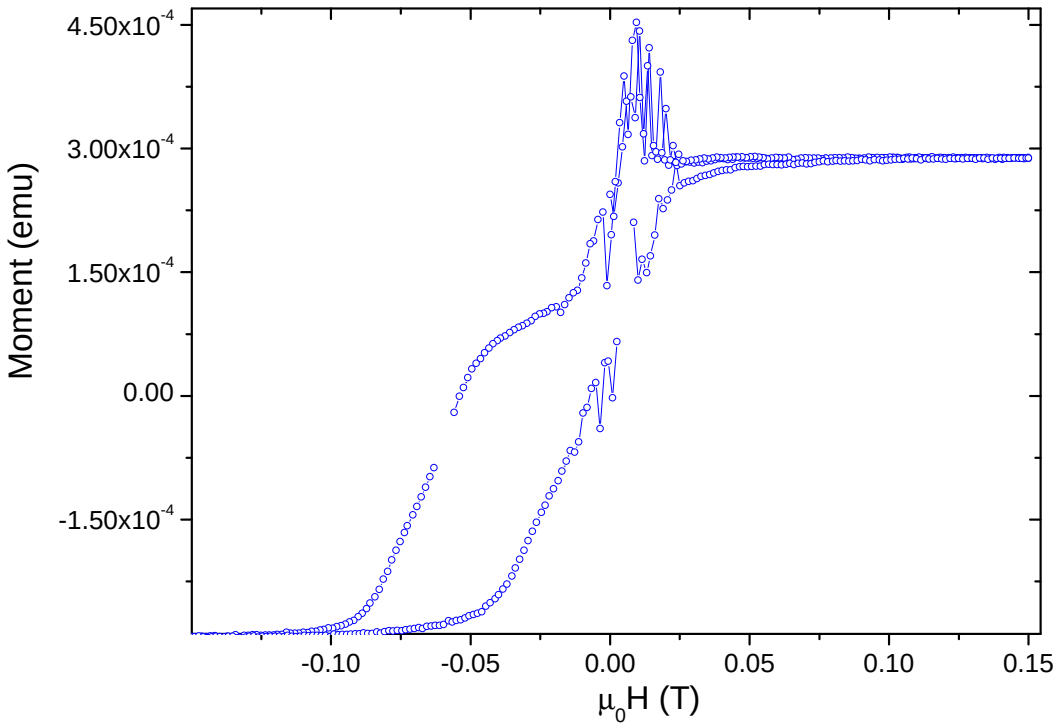


Figure 9.2: Hysteresis of a Pb superconducting spin valve at 5.6 K, in the region of the T_c.

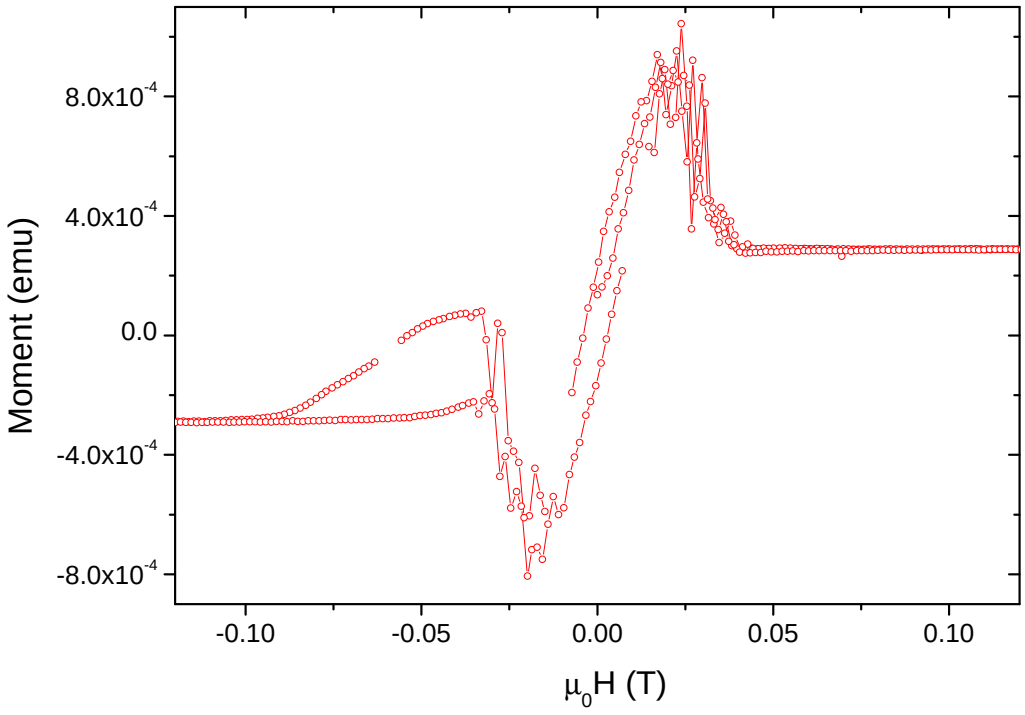


Figure 9.3: Hysteresis of a Pb superconducting spin valve at 5.5 K, just below the T_c.

in the superconducting state. There is no signature of diamagnetism (the Mesissner effect) in the hysteresis curves however there is a significant enhancement of what seems to be a strong paramagnetic response which then breaks down. This behaviour is exactly opposite to the diamagnetic response that would be expected for a superconductor in the superconducting state.

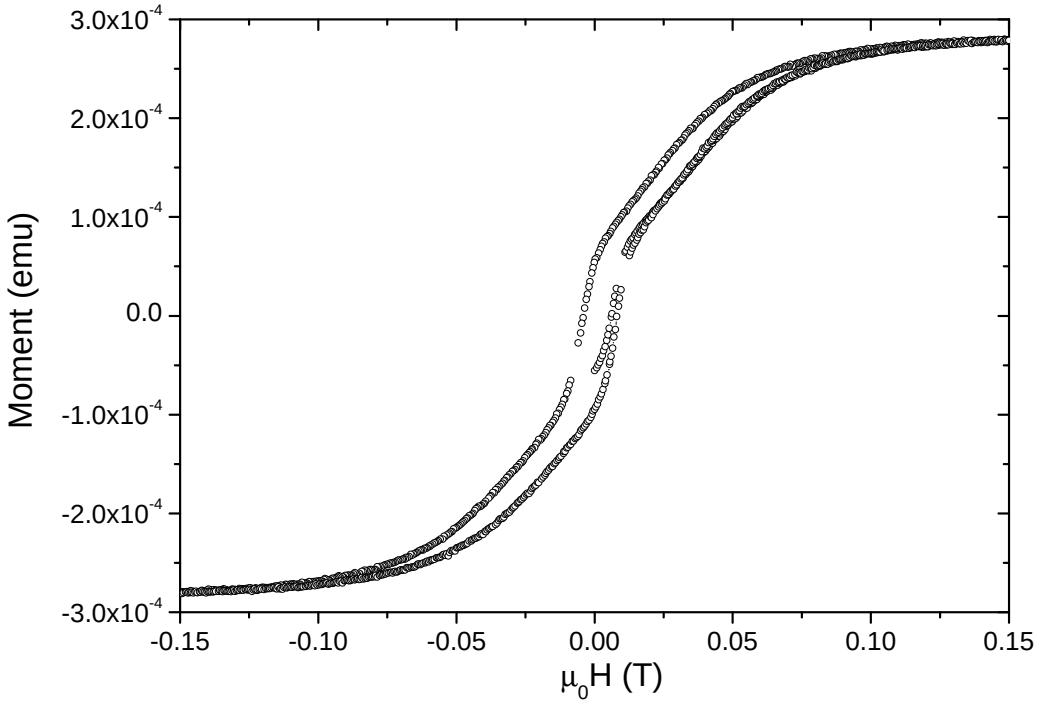


Figure 9.4: Hysteresis of a Pb superconducting spin valve at 6 K with the device rotated at 90 degrees (in the plane of the substrate) to the previous measurements.

The hysteresis at 6 K with the superconducting spin valve (and therefore the anisotropy) oriented perpendicularly to the magnetic field of the VSM is shown in Figure 9.4. The minor and major hysteresis loops (due to the permally and strongly pinned layers respectively) are not as clear as when the anisotropy is aligned in the direction of the field.

The magnetization as a function of temperature, shown in Figure 9.5, reveals a more or less constant magnetization until a drastic increase in magnetization at 5.6 K which is entirely consistent with the hysteresis loops.

9.1.3 Transport Measurements

The magnetoresistance of the same device, with the anisotropy aligned with the magnetic field of the cryostat, at 7 K is shown in Figure 9.6. The magnetoresistance is positive throughout with no indication of hysteresis. There is slight anisotropy in the magnetoresistance, which may be related to the exchange bias of the pinned layer.

The magnetoresistance at 5.69 K at different orientations is shown in Figure 9.7. The

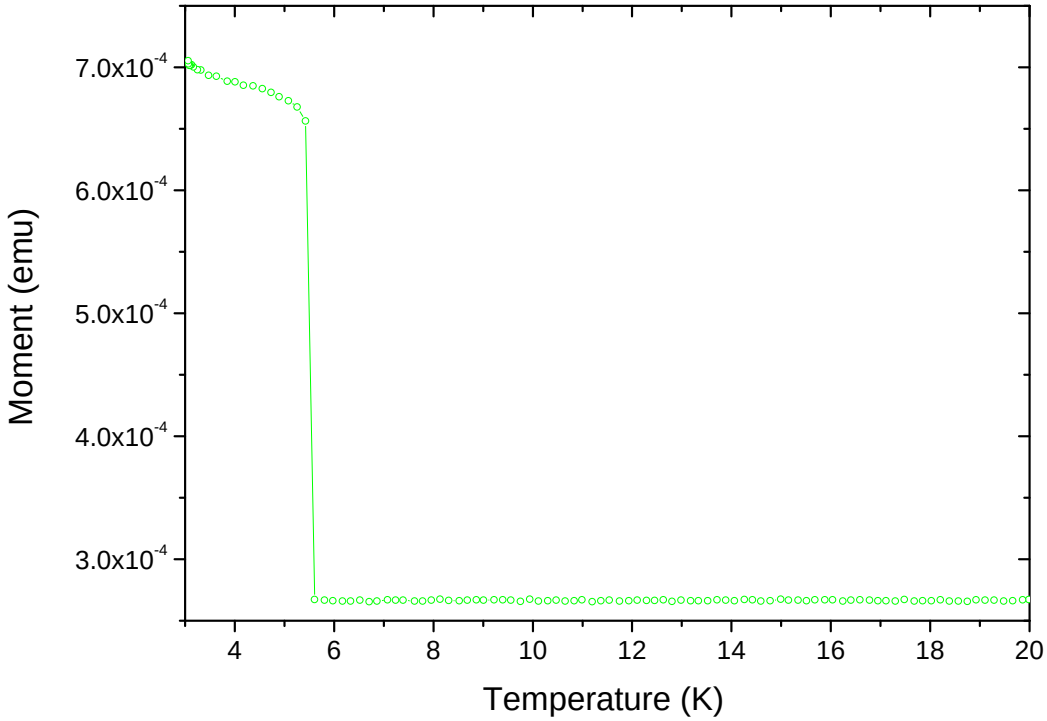


Figure 9.5: Magnetization as a function of temperature for a Pb superconducting spin valve. The transition begins at 5.6 K.

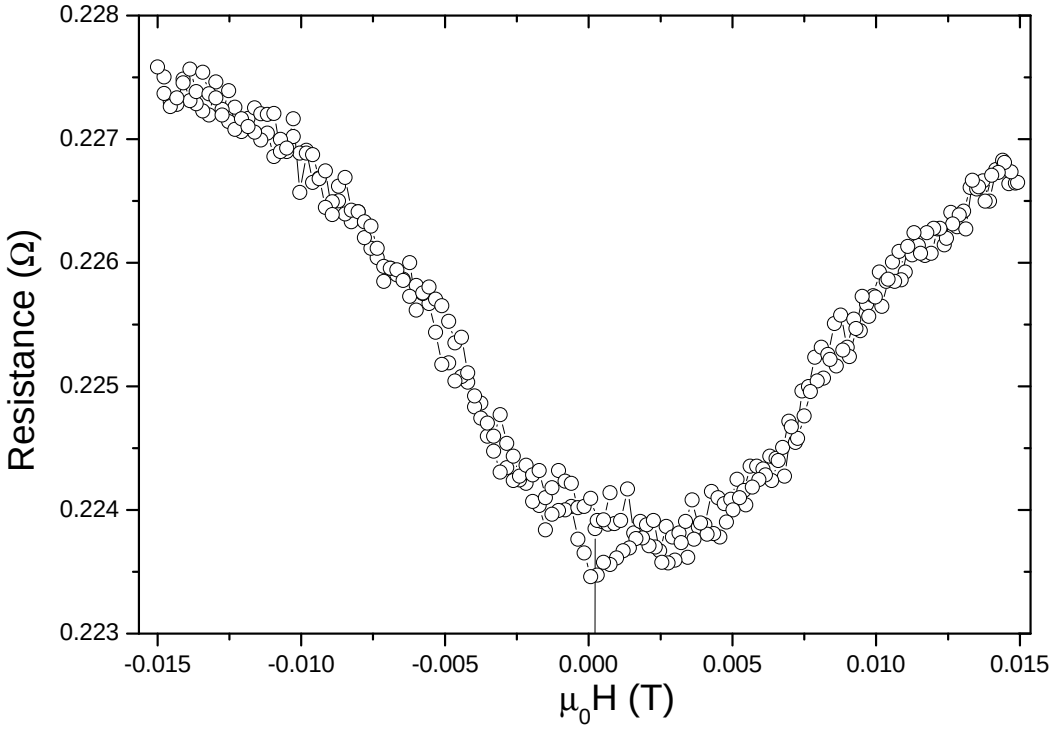


Figure 9.6: Magnetoresistance of a Pb superconducting spin valve at 7 K. Magnetization measurements show a transition at 5.6 K.

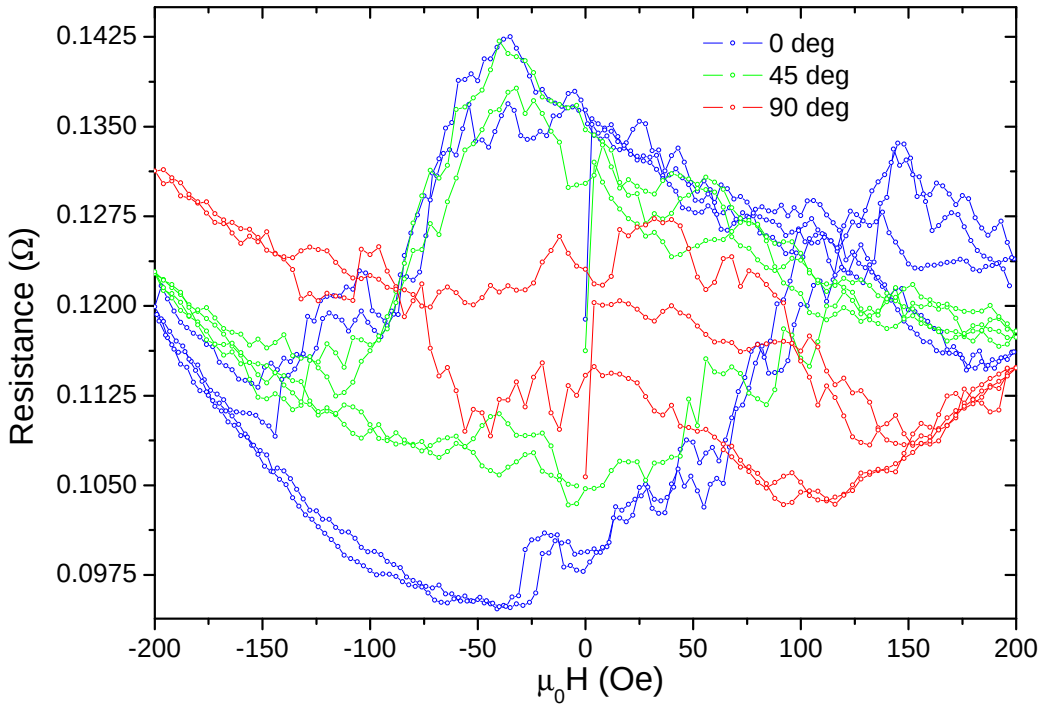


Figure 9.7: Magnetoresistance of a Pb superconducting spin valve at 5.69 K. Magnetization measurements show a transition at 5.6 K.

magnetic field was ramped up from 0 T to 200 Oe then ramped down to -200 Oe and the cycle was repeated to ensure consistency. There is significant hysteresis in the magnetoresistance when the anisotropy of the superconducting spin valve is aligned with the magnetic field of the cryostat. The magnetoresistance is not symmetric about zero field, there is a region above 100 Oe at O^o where there is a cross over of the magnetoresistance from the two different sweeps. This is related to the exchange bias as when the device is rotated to 45^o this feature is diminished and it is absent at 90^o. The degree of hysteresis is also related to the separation of the major and minor hysteresis loops. As the superconducting spin valve is rotated, the separation between the major and minor loops decreases (illustrated in Fig. 9.4).

At 5.6 K, the magnetoresistance (Fig. 9.8) is quite similar to the magnetoresistance at 5.6 K. The difference between the maximum and minimum resistance decreases, as does the asymmetry between the resistance at 200 Oe and -200 Oe. The changes in the hysteresis as the device is rotated are consistent.

The magnetoresistance at 5.5 K, with the anisotropy of the device oriented in the direction of the magnetic field, is shown in Figure 9.9. There is still significant asymmetry in the hysteresis. The hysteresis in the negative field region is smaller than at 5.6 or 5.69 K making the relative difference between the hysteresis in the positive and negative regions smaller. This trend continues at 5.53 K (Fig. 9.10) where the hysteresis begins to look more symmetric. The feature in the positive field region seems to shift to ever smaller fields while the amplitude of the change in the hysteresis in the negative field region decreases. In

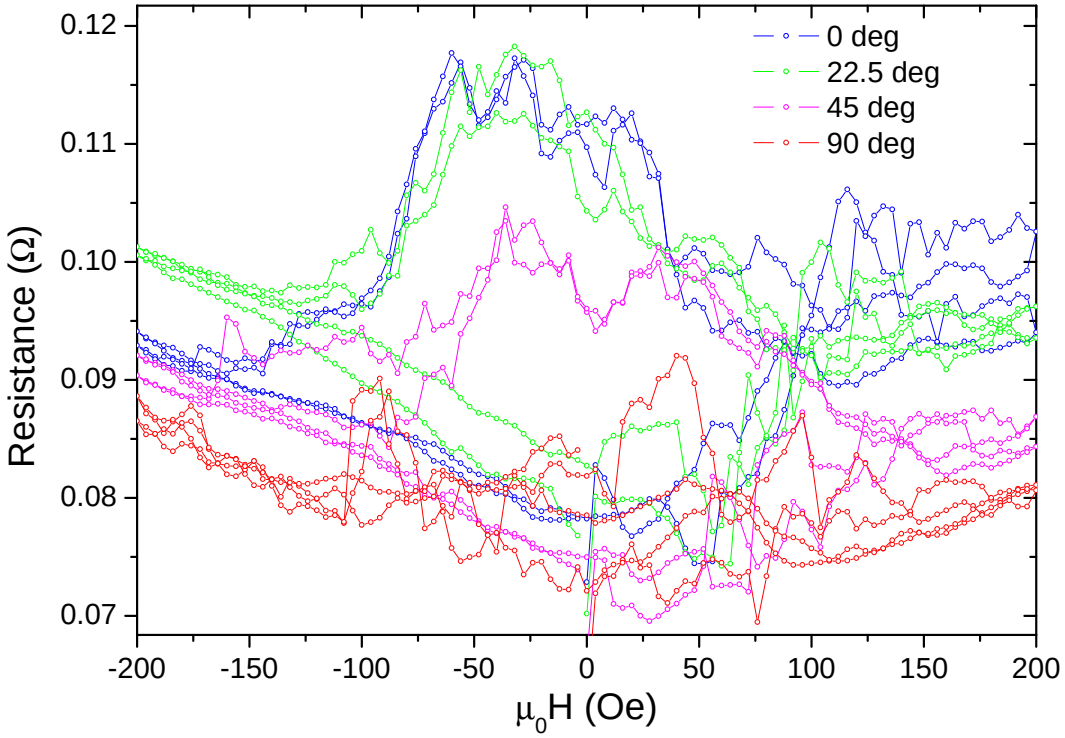


Figure 9.8: Magnetoresistance of a Pb superconducting spin valve at 5.6 K. Magnetization measurements show a transition at 5.6 K.

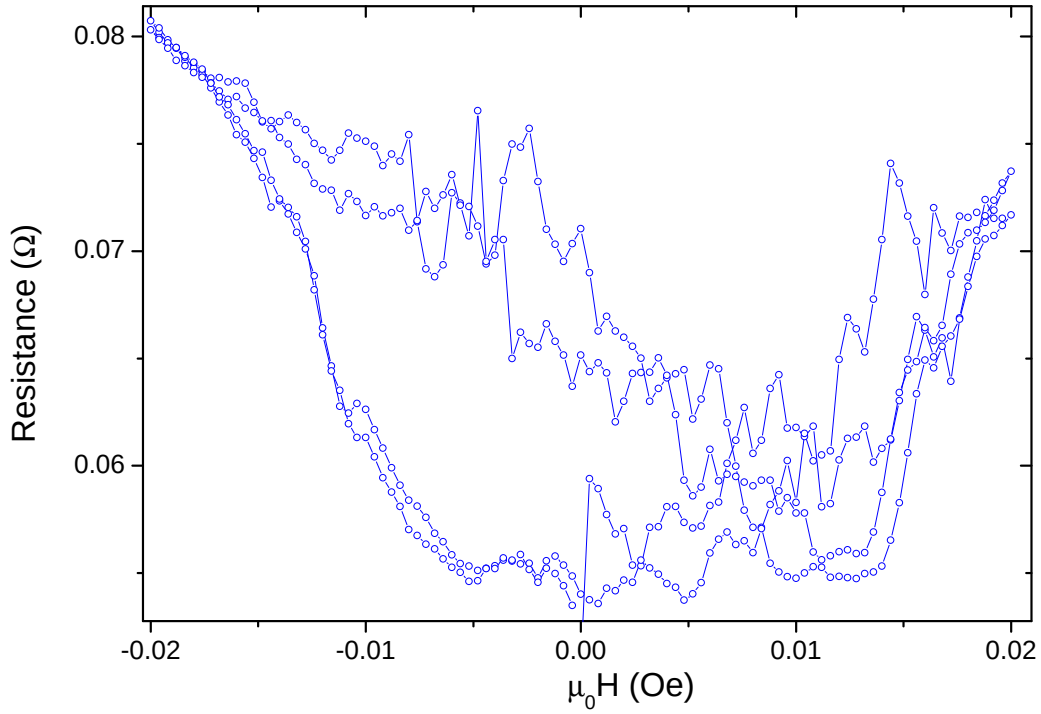


Figure 9.9: Magnetoresistance of a Pb superconducting spin valve at 5.55 K. Magnetization measurements show a transition at 5.6 K.

addition, a plateau in the magnetoresistance appears at -150 Oe.

At 5.50 K the magnetoresistance shows a strong indication of the superconducting regime where the resistance falls below the lower limit of the voltmeter and remains that way until 120 Oe. The hysteresis at positive and negative fields is now much more symmetric and the hysteresis is more reminiscent of a spin valve. There are local maxima at around (+/-) 100 Oe and plateaus in the resistance above those fields.

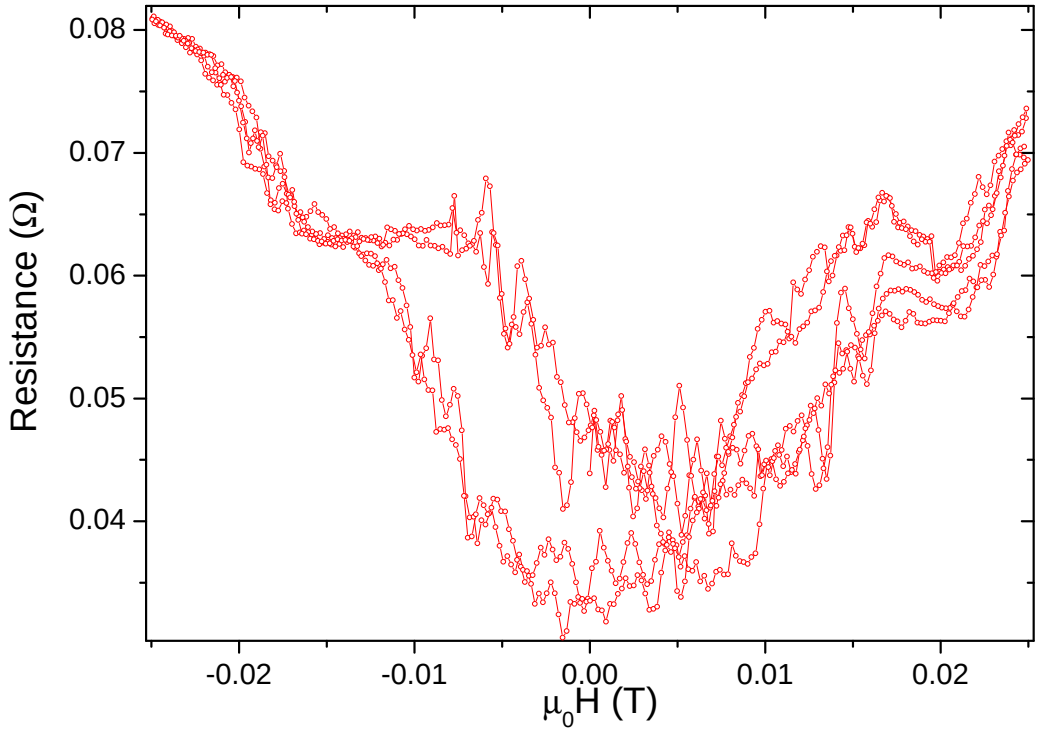


Figure 9.10: Magnetoresistance of a Pb superconducting spin valve at 5.53 K. Magnetization measurements show a transition at 5.6 K.

The resistance as a function of temperature where the superconducting spin valve was saturated under magnetic field of 100 Oe at different orientations is shown in Figure 9.12. The blue squares represent a configuration where the free and pinned layers are anti-parrallel, the green circles represent a configuration where the free and pinned layers are parallel, the light blue circles are a repeat of the same configuration. The dark green circles filled with crosses represent a configuration where both layers are parallel saturated at 100 Oe oriented at 45^o while the purple triangles represent a parallel configuration oriented at 90^o.

The resistance as a function of temperature shows interesting features. There is marked step in the resistance at 6.45 K and the transition into the superconducting state is not smooth.There are noticeable changes in gradient at 5.8 K and 5.65 K. These features are likely related to the disorder in the Pb film as well as disorder at the interface of the layers in the heterostructure where multiple quantum phases are expected to exist in the region of the transition.

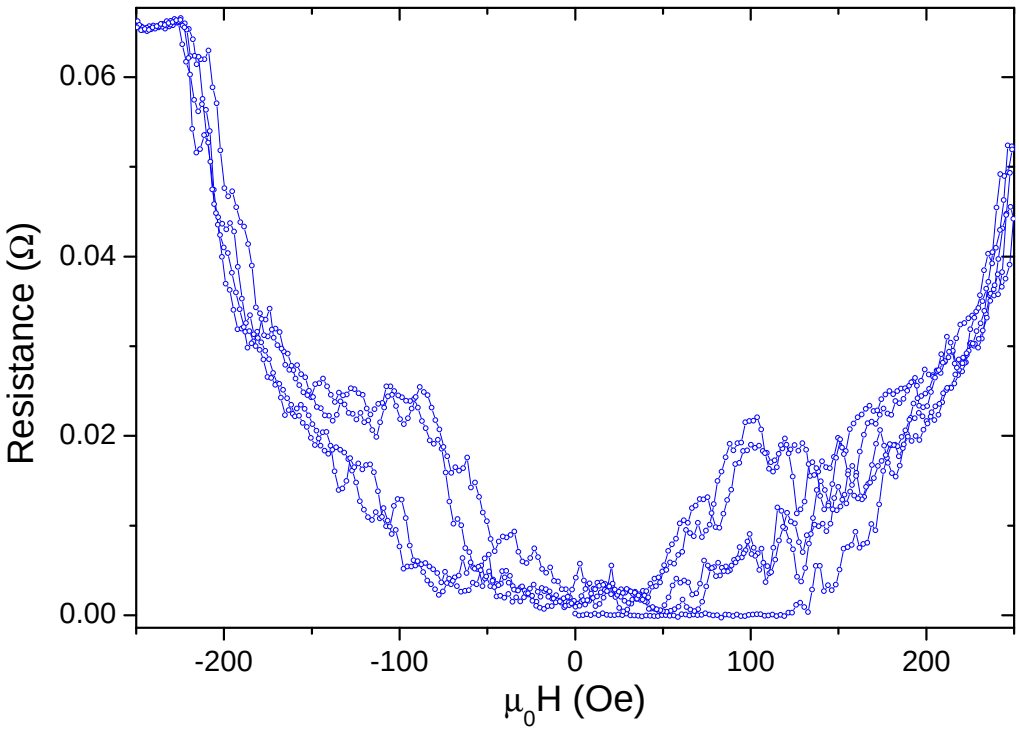


Figure 9.11: Magnetoresistance of a Pb superconducting spin valve at 5.50 K. Magnetization measurements show a transition at 5.6 K.

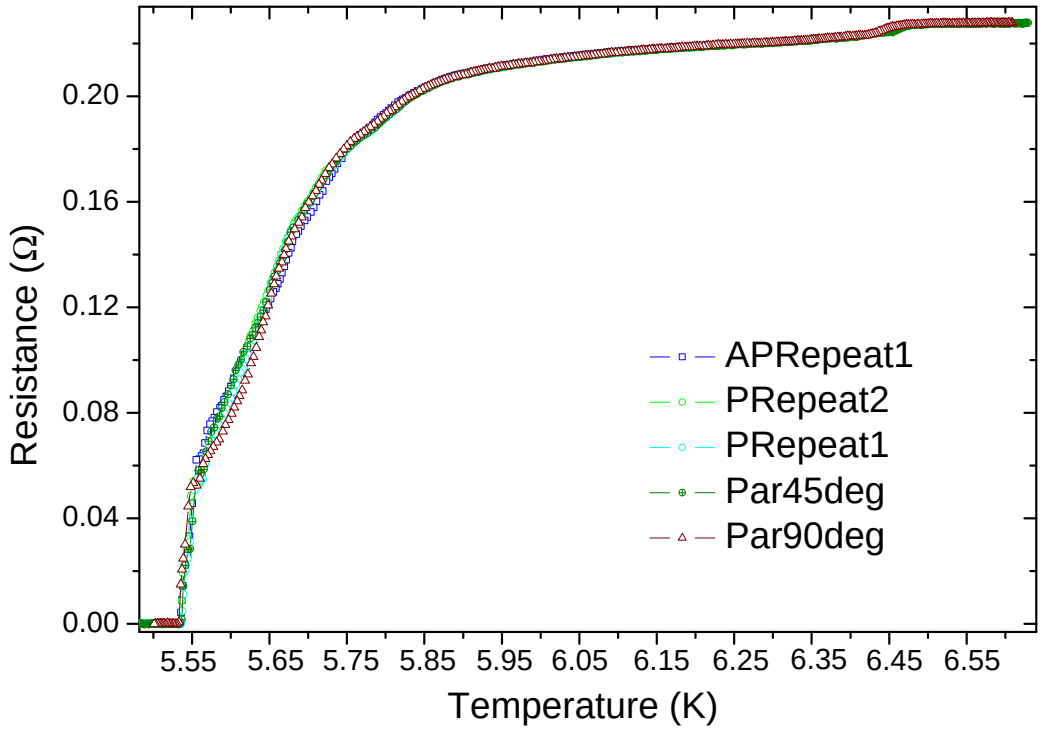


Figure 9.12: Resistance as a function of temperature for a Pb superconducting spin valve saturated under a magnetic field of 0.01 T at different orientations. Magnetization measurements show a transition at 5.6 K.

9.2 Superconducting Spin Valve Without Large Exchange Bias

9.2.1 Magnetic Measurements

We now study the second configuration of superconducting spin valve which has Co and permalloy layers which are not pinned.

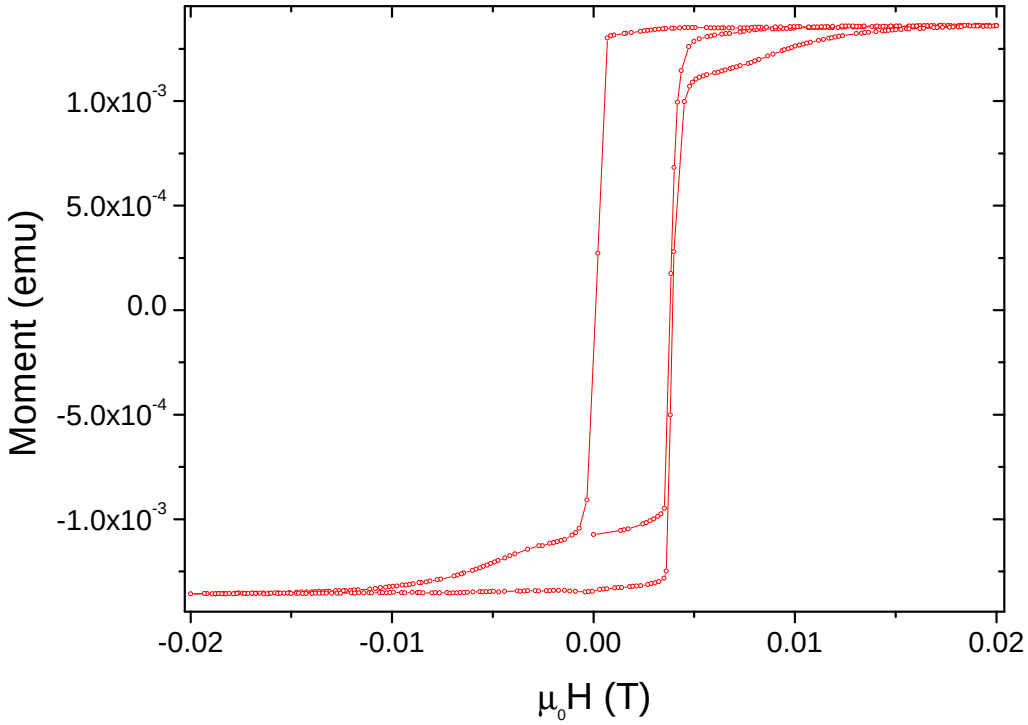


Figure 9.13: Hysteresis of a Pb superconducting spin valve at 5.7 K (above the T_c).

Figure 9.13 shows the hysteresis of a superconducting spin valve without a strong exchange bias at 5.7 K. The major and minor loops are distinguishable but not as well separated as was the case with a strongly pinned layer. In the positive field direction, the moment saturates at aroun 0.016 T while saturation occurs at around -0.014 T at negative fields.

At 5.2 K, the hysteresis does not saturate up to 0.03 T (Fig. 9.14). There is still some remnant of the major and minor loops superimposed on a strongly paramagnetic background.

At 4.5 K, the hysteresis shows a strong paramagnetic response, with the major and minor loop still discernible, followed by a diamagnetic response 0.075 to 0.125 until the moment eventually saturates at 0.13 T (Fig. 9.15). This is similar to the hysteresis of the superconducting spin valve with large exchange bias below the transition temperature (Fig. 9.3).

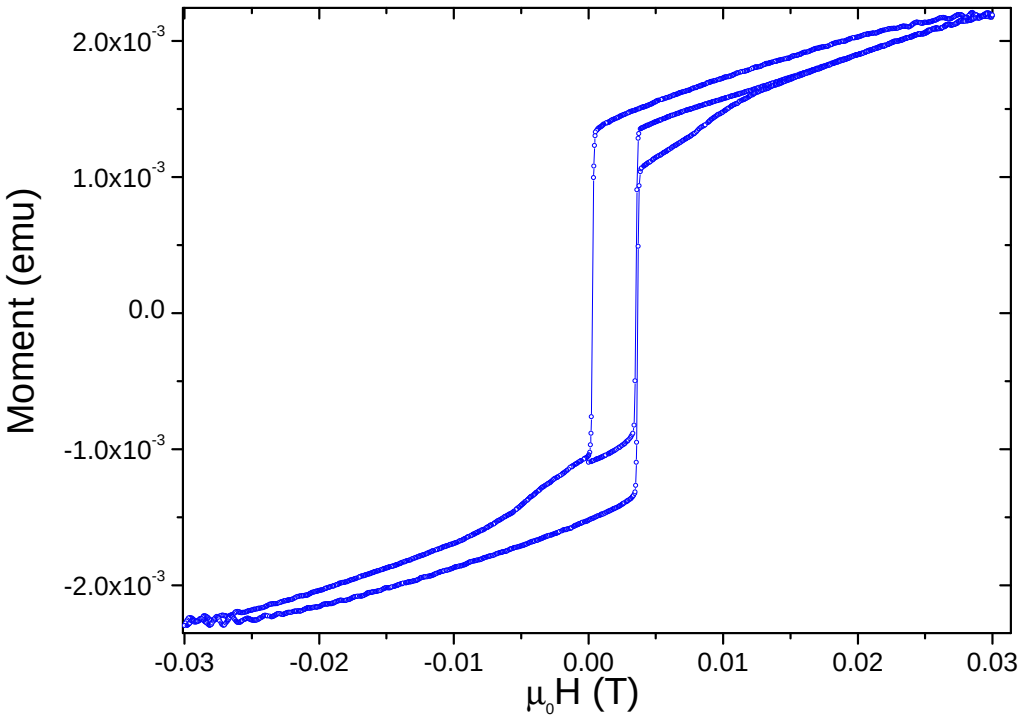


Figure 9.14: Hysteresis of a Pb superconducting spin valve at 5.2 K.

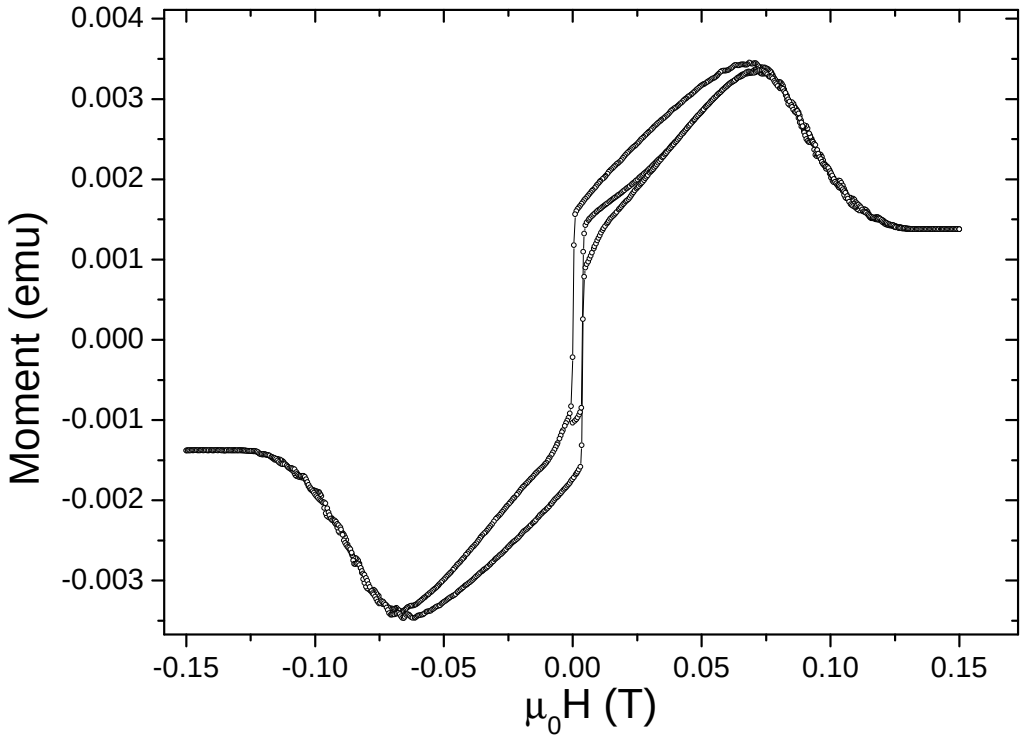


Figure 9.15: Hysteresis of a Pb superconducting spin valve at 4.5 K.

9.2.2 Transport Measurements

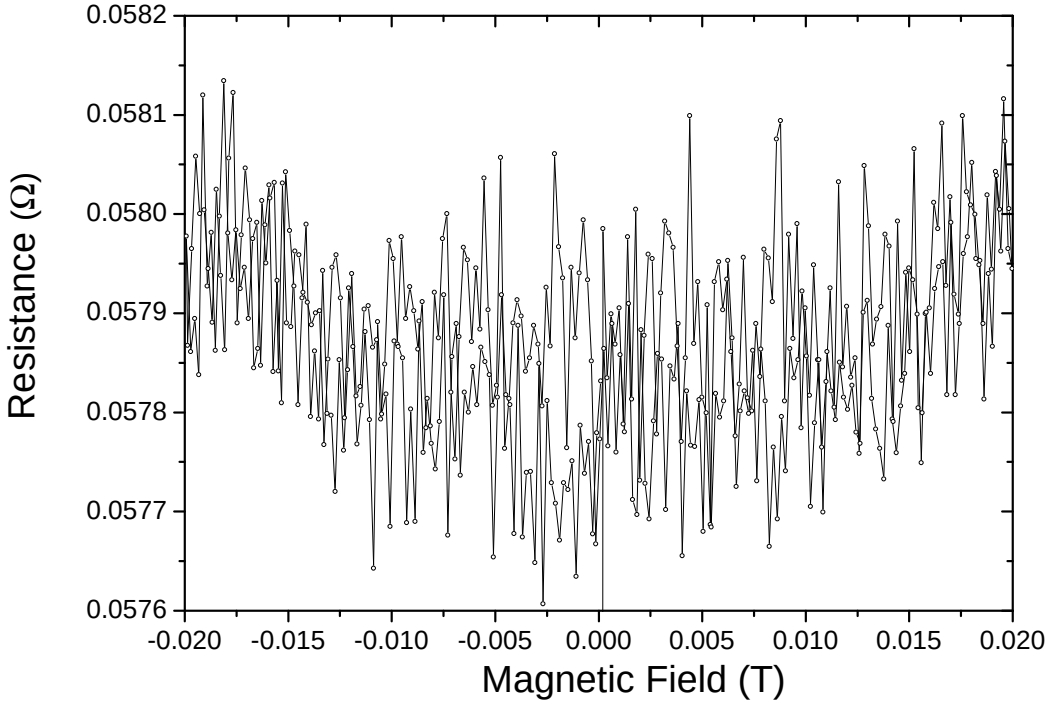


Figure 9.16: Magnetoresistance of a Pb superconducting spin valve at 5.8 K.

The magnetoresistance at 5.8 K is shown in Figure 9.16. The are no discernible features and the magnetoresistance is very small although it remains positive throughout. At 5.2 K there is noticeable, reproducible hystersis as shown in Figure 9.18. At 5.0 K, the hysteresis is enhanced as shown in Figure 9.18. At very low fields, in the region of 0.0025 T in the positive field direction and -0.0015 T in the negative field region there are sharp, repeatable minima in the magnetoresistance.

Resistance as function of temperature with the magnetic layers saturated at a field of 100 Oe in different orientations is shown in Figure 9.19. At 6.45 K there is a step in the magnetoresistance, similar to the case for a strongly exchange biased superconducting spin valve (Fig. 9.12). This is followed by a significant reduction in the gradient of the resistance at 5.80 K. This is reminiscent of re-entrant behaviour. Measurements of the magnetic properties do show a significant change in the moment in this temperature region. In this region the resistance for the different orientations also splits up. At 5.60 K, where the sharp decrease in resistance begins, the split of the different orientations is consistent with 0^o sequentially followed up until 90^o.

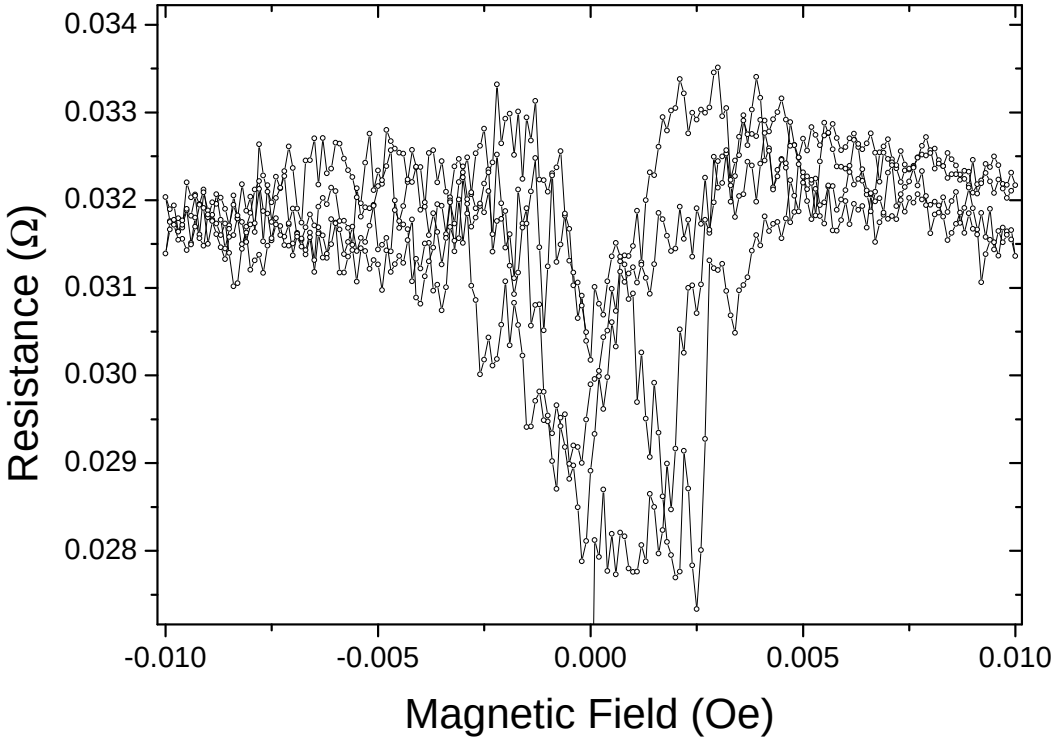


Figure 9.17: Magnetoresistance of a Pb superconducting spin valve at 5.2 K.

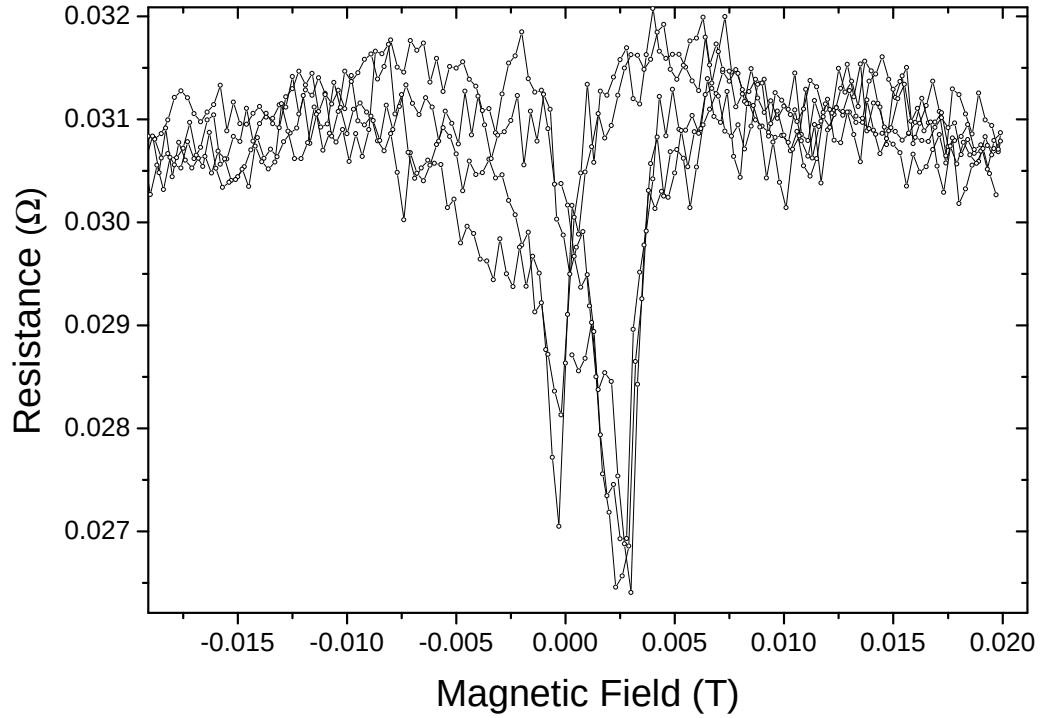


Figure 9.18: Magnetoresistance of a Pb superconducting spin valve at 5.0 K.

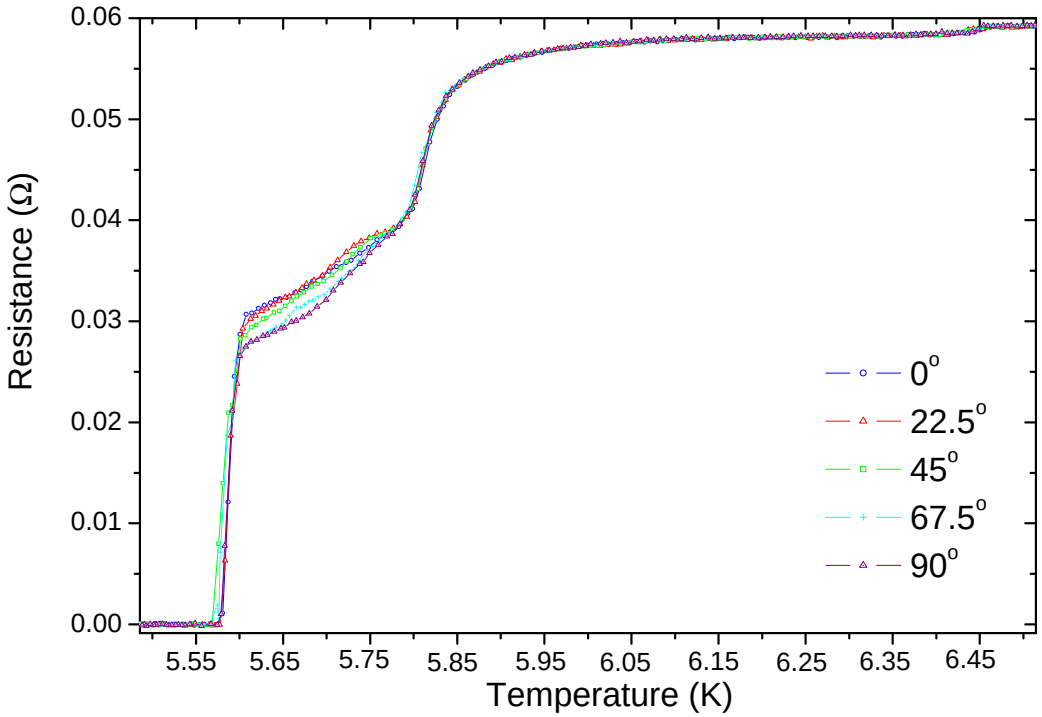


Figure 9.19: Resistance as a function of temperature for a superconducting spin valve where the field was saturated at 100 *Oe* in different orientations.

Bibliography

[1] M. V. Katkov, R. McIntosh, and S. Bhattacharyya, J. Appl. Phys. **113**, 093701 (2013). 13, 28, 42, 43, 50, 58

[2] N. Dwivedi *et al.*, ACS Applied Materials & Interfaces **7**, 20726 (2015), PMID: 26343275. 13, 42, 43, 53, 63, 64

[3] R. E. Miles, P. Harrison, and D. Lippens, *Terahertz sources and systems*, Springer, 2001. 21, 22, 25

[4] D. K. Ferry and S. M. Goodnick, *Transport in Nanostructures*, Cambridge University Press, 2009. 21

[5] S. Datta, *Electronic transport in mesoscopic systems*, Cambridge University Press, 1997. 21

[6] V. M. Mitin, D. I. Sementsov, and N. Z. Vagidov, *Quantum mechanics for Nanostructures*, Cambridge University Press, 2006. 21

[7] R. Miles, X.-C. Zhang, H. Eisele, and A. Krotkus, *Terahertz Frequency Detection and Identification of Materials and Objects*, Springer, 2007. 21, 22, 23, 25

[8] l. Esaki and R. L. Tsu, IBM J. Res. Dev **14**, 61 (1970). 22

[9] C. Waschke *et al.*, Phys. Rev. Lett. **70**, 3319 (1993). 22

[10] R. L. Tsu, *Superlattice to Nanoelectronics*, Elsevier, 2007. 23

[11] R. Tsu, Nanoscale Research Letters **6**, 1 (2011). 23

[12] Y. Fu and S. C. Dudley, Phys. Rev. Lett. **70**, 65 (1993). 23

[13] P. Dean *et al.*, Journal of Physics D: Applied Physics **47**, 374008 (2014). 23, 24

[14] A. Spott *et al.*, Opt. Lett. **40**, 1480 (2015). 24

[15] M. J. Pilling *et al.*, Faraday Discuss. **187**, 135 (2016). 25

[16] H. Amrania *et al.*, Faraday Discuss. **187**, 539 (2016). 25

[17] B. Bird and M. J. Baker, Trends in Biotechnology **33**, 557 (2015). 25

[18] E. van Mastrigt *et al.*, Journal of Breath Research **10**, 026003 (2016). 25

[19] K. Haase, N. Kroger-Lui, A. Pucci, A. Schonhals, and W. Petrich, Faraday Discuss. **187**, 119 (2016). 25

[20] A. Reyes-Reyes, R. C. Horsten, H. P. Urbach, and N. Bhattacharya, Analytical Chemistry **87**, 507 (2015), PMID: 25506743. 25

[21] S. Liakat *et al.*, Biomed. Opt. Express **5**, 2397 (2014). 25

[22] C. Vrani *et al.*, Analytical Chemistry **86**, 10511 (2014), PMID: 25329042. 25

[23] M. Rocha *et al.*, Sensors **10**, 9359 (2010). 25

[24] L. Consolino *et al.*, Sensors **13**, 3331 (2013). 25

[25] P. Geiser, V. Avetisov, L. Espinoza-Nava, N. Menegazzo, and P. Kaspersen, Photonics **3**, 16 (2016). 25

[26] S. Welzel *et al.*, Sensors **10**, 6861 (2010). 25

[27] G. Fanchini and A. Tagliaferro, Appl.Phys. Lett. **85**, 730 (2004). 26, 28, 44

[28] M. A. Green, K. Emery, Y. Hishikawa, W. Warta, and E. D. Dunlop, Progress in Photovoltaics: Research and Applications **23**, 1 (2015), PIP-14-274. 26

[29] E. Smirnov *et al.*, Microelectronic Engineering **167**, 6 (2017), Materials for Advanced Metallization 2016 (MAM 2016). 26

[30] S. Roche *et al.*, Solid State Commun. **152**, 1404 (2012). 27

[31] M. V. Katkov and S. Bhattacharyya, EPL **99**, 37005 (2012). 27, 28

[32] L. L. Zhang, R. Zhou, and X. S. Zhao, J. Mater. Chem. **20**, 5983 (2010). 27

[33] M. D. Stoller, S. Park, Y. Zhu, J. An, and R. S. Ruoff, Nano Lett. **8**, 3498 (2008). 27

[34] D. Chen, L. Tang, and J. Li, Chem. Soc. Rev. **39**, 3157 (2010). 27

[35] E. V. Castro *et al.*, Phys. Rev. Lett. **99**, 216802 (2007). 27

[36] H. Min, B. Sahu, S. K. Banerjee, and A. H. MacDonald, Phys. Rev. B **75**, 155115 (2007). 27

[37] A. C. Ferrari *et al.*, Phys. Rev. Lett. **97**, 187401 (2006). 27

[38] L. Malard, M. A. Pimenta, G. Dresselhaus, and M. S. Dresselhaus, Physics Reports **473**, 51 (2009). 27

[39] Z. Ni, Y. Wang, T. Yu, and Z. Shen, Nano Res. **1**, 273 (2010). 27

[40] I. Childres, L. A. Jauregui, J. Tian, and Y. P. Chen, New J. Phys. **13**, 025008 (2011). 27

[41] M. Y. Han, J. C. Brant, and P. Kim, Phys. Rev. Lett. **104**, 056801 (2010). 27

[42] F. Mohammed and S. Bhattacharyya, EPL **100**, 26009 (2012). 27

[43] R. McIntosh, M. A. Mamo, B. Jamieson, S. Roy, and S. Bhattacharyya, EPL (Europhysics Letters) **97**, 38001 (2012). 27

[44] A. Ferrari and J. Robertson, Phil. Trans. R. Soc. A **362**, 2477 (2004). 28

[45] M. V. Katkov and S. Bhattacharyya, EPL **99**, 37005 (2012). 28, 42

[46] U. Stephan, T. Frauenheim, P. Blaudeck, and G. Jungnickel, Phys. Rev. B **50**, 1489 (1994). 28

[47] A. R. Merchant, McKenzie, and D. G. McCulloch, Phys. Rev. B **65**, 024208 (2001). 28

[48] J. Robertson, Semicond. Sci. Technol. **18**, S12 (2003). 28, 44

[49] S. R. P. Silva *et al.*, J. Appl. Phys. **81**, 2626 (1997). 28

[50] L. Cheah, X. Shi, J. Shi, E. Liu, and S. Silva, J. Non-Cryst. Solids **242**, 40 (1998). 28

[51] Y. Miyajima, A. A. D. Adikaari, S. J. Henley, J. M. Shannon, and S. R. P. Silva, Appl. Phys. Lett. **92**, 152104 (2008). 28, 36, 42

[52] F. Alibart, M. Lejeune, O. Durand Drouhin, K. Zellama, and M. Benlahsen, Journal of Applied Physics **108**, 053504 (2010). 28, 43, 44, 104

[53] V. S. Veerasamy *et al.*, Phys. Rev. B **48**, 17954 (1993). 28

[54] B. S. Satyanarayana, A. Hart, W. I. Milne, and J. Robertson, Appl. Phys. Lett. **71**, 1430 (1997). 28

[55] A. A. Valladares and F. Álvarez Ramírez, Phys. Rev. B **73**, 024206 (2006). 28

[56] S. Bhattacharyya, Phys. Rev. B **70**, 125412 (2004). 28

[57] R. Gago *et al.*, Phys. Rev. B **72**, 014120 (2005). 28

[58] S. Souto, M. Pickholz, M. C. dos Santos, and F. Alvarez, Phys. Rev. B **57**, 2536 (1998). 28, 29

[59] M. C. dos Santos and F. Alvarez, Phys. Rev. B **58**, 13918 (1998). 28, 29

[60] C. Bhattacharyya, S.and Cardinaud and G. Turban, J. Appl. Phy. **83**, 4491 (1998). 28, 29

[61] I. Jiménez, R. Gago, J. M. Albella, D. Cáceres, and I. Vergara, Phys. Rev. B **62**, 4261 (2000). 28

[62] S. Bhattacharyya and S. R. P. Silva, Appl. Phys. Lett. **90**, 082105 (2007). 28

[63] E. B. Halac, E. Burgos, and M. Reinoso, Phys. Rev. B **77**, 224101 (2008). 28, 29

[64] S. Bhattacharyya and S. Silva, Thin Solid Films **482**, 94 (2005), {EMRS} 2004, Symposium {JProceedings} of Symposium J on Synthesis, Characterisation and Advanced Applications of Amorphous Carbon Films, {EMRS} 2004 Conference. 28

[65] M. V. Katkov and S. Bhattacharyya, J. Appl. Phys. **111**, 123711 (2012). 28

[66] H. Hsu and L. E. Reichl, Phys. Rev. B **72**, 155413 (2005). 29

[67] H. M. Pastawski, L. F. Torres, and E. Medina, Chemical Physics **281**, 257 (2002). 29, 30

[68] J. Bonca and S. A. Trugman, Phys. Rev. Lett. **75**, 2566 (1995). 29, 71, 72

[69] L. E. F. Foa Torres, H. M. Pastawski, and S. S. Makler, Phys. Rev. B **64**, 193304 (2001). 29

[70] L. F. Torres, H. Pastawski, and S. S. Makler, Brazilian Journal of Physics **32**, 300 (2002). 29

[71] L. Foa Torres and S. Roche, Applied Physics A **86**, 283 (2007). 30

[72] L. E. F. Foa Torres, R. Avriller, and S. Roche, Phys. Rev. B **78**, 035412 (2008). 30

[73] H. R. Vanaie, M. Yaghobi, and Z. Sedaghat, Molecular Physics **113**, 3606 (2015). 30

[74] L. E. F. Foa Torres, Phys. Rev. B **72**, 245339 (2005). 30

[75] L. F. Torres and G. Cuniberti, Comptes Rendus Physique **10**, 297 (2009). 30, 72

[76] C. G. Rocha, L. E. F. F. Torres, and G. Cuniberti, Phys. Rev. B **81**, 115435 (2010). 30

[77] L. E. F. F. Torres and G. Cuniberti, Applied Physics Letters **94**, 222103 (2009). 30

[78] P. J. H. Denteneer, R. T. Scalettar, and N. Trivedi, Phys. Rev. Lett. **87**, 146401 (2001). 30, 32, 89, 121

[79] M. Feigel'man, L. Ioffe, V. Kravtsov, and E. Cuevas, Annals of Physics **325**, 1390 (2010), July 2010 Special Issue. 30, 31

[80] M. V. Feigel'man, L. B. Ioffe, V. E. Kravtsov, and E. A. Yuzbashyan, Phys. Rev. Lett. **98**, 027001 (2007). 30, 31

[81] D. J. Scalapino, S. R. White, and S. C. Zhang, Phys. Rev. Lett. **68**, 2830 (1992). 31, 32

[82] D. J. Scalapino, S. R. White, and S. Zhang, Phys. Rev. B **47**, 7995 (1993). 31, 32

[83] A. Ghosal, M. Randeria, and N. Trivedi, Phys. Rev. Lett. **81**, 3940 (1998). 32, 89

[84] A. Ghosal, M. Randeria, and N. Trivedi, Phys. Rev. B **65**, 014501 (2001). 32, 89, 121

[85] N. Trivedi, R. T. Scalettar, and M. Randeria, Phys. Rev. B **54**, R3756 (1996). 32, 89, 90

[86] N. Trivedi and M. Randeria, Phys. Rev. Lett. **75**, 312 (1995). 32

[87] I. S. Burmistrov, I. V. Gornyi, and A. D. Mirlin, Phys. Rev. Lett. **108**, 017002 (2012). 32

[88] A. Paramekanti, N. Trivedi, and M. Randeria, Phys. Rev. B **57**, 11639 (1998). 32

[89] M. R. K. Bouadim, Y. L. Loh and N. Trivedi, Nat. Phys. **7**, 884 (2011). 32, 33

[90] P. Dey and S. Basu, J. Phys. Condens. Matter **20**, 485205 (2008). 33, 121

[91] V. F. Gantmakher and V. T. Dolgopolov, Physics-Uspekhi **53**, 1 (2010). 33, 34, 145

[92] P. A. Lee and T. V. Ramakrishnan, Rev. Mod. Phys. **57**, 287 (1985). 33

[93] B. Sacépé *et al.*, Nat. Phys. **7**, 239 (2011). 33, 34, 125

[94] V. F. Gantmakher, Low Temperature Physics **37**, 59 (2011). 33

[95] D. Belitz and T. R. Kirkpatrick, Rev. Mod. Phys. **66**, 261 (1994). 33, 89

[96] Y.-H. Lin, J. Nelson, and A. Goldman, Physica C: Superconductivity and its Applications **514**, 130 (2015). 33

[97] Y. Zou, I. Klich, and G. Refael, Phys. Rev. B **77**, 144523 (2008). 33

[98] A. Gerber, A. Milner, G. Deutscher, M. Karpovsky, and A. Gladkikh, Phys. Rev. Lett. **78**, 4277 (1997). 33, 145

[99] I. S. Beloborodov, A. V. Lopatin, V. M. Vinokur, and K. B. Efetov, Rev. Mod. Phys. **79**, 469 (2007). 33

[100] I. S. Beloborodov and K. B. Efetov, Phys. Rev. Lett. **82**, 3332 (1999). 33, 140, 146

[101] T. I. Baturina and V. M. Vinokur, Annals of Physics **331**, 236 (2013). 34

[102] M. R. Beasley, J. E. Mooij, and T. P. Orlando, Phys. Rev. Lett. **42**, 1165 (1979). 34

[103] A. Erez and Y. Meir, Phys. Rev. B **88**, 184510 (2013). 34

[104] S. Bhattacharyya *et al.*, Nature Mater. **5** (2005). 36, 42

[105] W. M. Tsang, S. J. Henley, V. Stolojan, and S. R. P. Silva, App.Phys. Lett. **89**, 193103 (2006). 36, 42

[106] S. D. Janssens *et al.*, New Journal of Physics **13**, 083008 (2011). 36, 37, 144

[107] J. Mare, P. Hubk, M. Nesldek, D. Kindl, and J. Kritofik, Diamond and Related Materials **15**, 1863 (2006), Proceedings of the joint 11th International Conference on New Diamond Science and Technology and the 9th Applied Diamond Conference 2006. 36

[108] J. Mare, P. Hubk, J. Kritofik, D. Kindl, and M. Nesldek, Chemical Vapor Deposition **14**, 161 (2008). 36

[109] B. Abeles and T. Tiedje, Phys. Rev. Lett. **51**, 2003 (1983). 41

[110] B. Xu and Y. Dubi, J. Phys.: Condens. Matter **27**, 263202 (2015). 41

[111] T. Zheng, W. C. H. Choy, and Y. Sun, Adv. Funct. Mater. **19**, 2648 (2009). 41

[112] R. Pati, M. McClain, and A. Bandyopadhyay, Phys. Rev. Lett. **100**, 246801 (2008). 41

[113] L. Chen *et al.*, Phys. Rev. Lett. **99**, 146803 (2007). 41

[114] L. Ravagnan *et al.*, Phys. Rev. Lett. **98**, 216103 (2007). 42

[115] V. Stolojan, P. Moreau, M. J. Goringe, and S. R. P. Silva, Appl. Phys. Lett. **88**, 122109 (2006). 42

[116] S. Silva, G. Amaratunga, Rusli, S. Haq, and E. Salje, Thin Solid Films **253**, 20 (1994). 42

[117] S. R. P. Silva, G. A. J. Amaratunga, C. N. Woodburn, M. E. Welland, and S. Haq, Jpn. J. Appl. Phys. **33**, 6458 (1994). 42

[118] S. Silva, Rusli, K. Homewood, and G. Amaratunga, Journal of Non-Crystalline Solids **227230, Part 2**, 1137 (1998). 42

[119] C. Coleman, R. McIntosh, and S. Bhattacharyya, J. Appl. Phys. **114**, 043716 (2013). 42, 54

[120] F. Alibart, O. D. Drouhin, C. Debiemme-Chouvy, and M. Benlahsen, Solid State Communications **145**, 392 (2008). 43

[121] F. Alibart *et al.*, Diamond and Related Materials **17**, 925 (2008). 43

[122] F. Alibart, M. Lejeune, K. Zellama, and M. Benlahsen, Diamond and Related Materials **20**, 409 (2011). 43

[123] K.-M. Roh, S.-J. You, S.-K. Choi, J.-H. Kim, and D.-J. Seong, Journal of Physics D: Applied Physics **42**, 175405 (2009). 43

[124] Y. Kikuchi *et al.*, Carbon **93**, 207 (2015). 43

[125] A. Onipko, Phys. Rev. B **59**, 9995 (1999). 43, 44, 52

[126] J. Robertson, Materials Science and Engineering: R: Reports **37**, 129 (2002). 44

[127] D. Churochkin, R. McIntosh, and S. Bhattacharyya, Journal of Applied Physics **113**, 044305 (2013). 45, 49

[128] Y. Miyajima *et al.*, Thin Solid Films **516**, 257 (2007). 52

[129] S. D. Ganichev *et al.*, Phys. Rev. B **61**, 10361 (2000). 52

[130] O. Mitrofanov and M. Manfra, Journal of Applied Physics **95**, 6414 (2004). 52

[131] M. Vila, C. Prieto, and R. Ramrez, Thin Solid Films **459**, 195 (2004), Proceedings of the 8th European Vacuum Congress Berlin 2003, 23-26 June 2003, featuring the 8th European Vacuum Conference and 2nd Annual Conference of the German Vaccum Society. 52

[132] M. E. S.P. Murarka and A. Sinha, *Interlayer Dielectrics for Semiconductor Technologies*, Elsevier, 2007. 52

[133] E. Cappelli *et al.*, Appl. Phys. A **93**, 751 (2008). 53

[134] J. Bonca and S. A. Trugman, Phys. Rev. Lett. **79**, 4874 (1997). 71, 72

[135] K. Haule and J. Bonca, Phys. Rev. B **59**, 13087 (1999). 71, 72

[136] H. Oymak, D. Shin, and J. Hong, EPL (Europhysics Letters) **77**, 37005 (2007). 72, 76, 77

[137] F. Evers and A. D. Mirlin, Rev. Mod. Phys. **80**, 1355 (2008). 89

[138] V. F. Gantmakher and V. T. Dolgopolov, Phys. Usp. **53**, 1 (2010). 89

[139] M. Jiang, R. Nanguneri, N. Trivedi, G. G. Batrouni, and R. T. Scalettar, New J. Phys. **15**, 023023 (2013). 89

[140] B. Sacépé *et al.*, Phys. Rev. Lett. **101**, 157006 (2008). 89

[141] I.-D. Potirniche, J. Maciejko, R. Nandkishore, and S. L. Sondhi, Phys. Rev. B **90**, 094516 (2014). 89

[142] N. Mohanta and A. Taraphder, Journal of Physics: Condensed Matter **26**, 025705 (2014). 89

[143] N. Mohanta and A. Taraphder, Phys. Rev. B **92**, 174531 (2015). 89

[144] B. Chatterjee and A. Taraphder, Solid State Commun. **148**, 582 (2008). 89

[145] V. Z. Cerovski, S. D. Mahanti, T. A. Kaplan, and A. Taraphder, Phys. Rev. B **59**, 13977 (1999). 90

[146] Y. Takano *et al.*, Appl. Phys. Lett. **85** (2004). 90, 124

[147] B. Sacépé *et al.*, Phys. Rev. Lett. **96**, 097006 (2006). 90, 148

[148] G. Baskaran, J. Supercond. Nov. Magn. **21**, 45 (2008). 90, 91

[149] P. Achatz *et al.*, Diamond Relat. Mater. **19**, 814 (2010). 90, 91, 125

[150] N. Dubrovinskaia *et al.*, Appl. Phys. Lett. **92**, 132506 (2008). 90, 125

[151] E. Ekimov *et al.*, Nature **428**, 542 (2004). 90

[152] X. Blase, C. Adessi, and D. Connétable, Phys. Rev. Lett. **93**, 237004 (2004). 90

[153] A. Kawano *et al.*, Phys. Rev. B **82**, 085318 (2010). 90, 91, 96, 104, 110

[154] T. Shirakawa, S. Horiuchi, Y. Ohta, and H. Fukuyama, J. Phys. Soc. Jpn **76**, 014711 (2007). 90, 91

[155] H. Okazaki *et al.*, J. Phys. Chem. Solids **72**, 582 (2011). 90

[156] F. Dahlem *et al.*, phys. status solidi (a) **207**, 2064 (2010). 90, 121, 122, 124, 146, 148

[157] F. Dahlem *et al.*, Phys. Rev. B **82**, 033306 (2010). 90

[158] Y. Ohta, T. Shirakawa, S. Horiuchi, and H. Fukuyama, Physica C: Supercond. **460462**, 121 (2007). 90, 91

[159] T. Klein *et al.*, Phys. Rev. B **75**, 165313 (2007). 91

[160] E. Bustarret *et al.*, Phys. Rev. Lett. **93**, 237005 (2004). 91

[161] K. Winzer, D. Bogdanov, and C. Wild, Physica C **432**, 65 (2005). 91

[162] B. **S**opik, New J. Phys. **11**, 103026 (2009). 91, 119

[163] J. E. Moussa and M. L. Cohen, Phys. Rev. B **77**, 064518 (2008). 91, 125

[164] T. Das, J.-X. Zhu, and M. J. Graf, Phys. Rev. B **84**, 134510 (2011). 93

[165] H. Huang, Y. Gao, J.-X. Zhu, and C. S. Ting, Phys. Rev. Lett. **109**, 187007 (2012). 93

[166] W. Gajewski *et al.*, Phys. Rev. B **79**, 045206 (2009). 118, 124

[167] G. Zhang *et al.*, Adv. Mater. **26**, 2034 (2014). 118, 124

[168] B. L. Willems *et al.*, Phys. Rev. B **80**, 224518 (2009). 121

[169] I. S. Burmistrov, I. V. Gornyi, and A. D. Mirlin, Phys. Rev. Lett. **108**, 017002 (2012). 122, 123

[170] E. J. König *et al.*, Phys. Rev. B **92**, 214503 (2015). 122

[171] M. V. Feigel'man, L. B. Ioffe, V. E. Kravtsov, and E. A. Yuzbashyan, Phys. Rev. Lett. **98**, 027001 (2007). 123

[172] N. Dubrovinskaia *et al.*, Proc. Natl. Acad. Sci. U.S.A **105**, 11619 (2008). 124

[173] J. Mare, P. Hubk, M. Nesldek, D. Kindl, and J. Kritofik, Diamond and Related Materials **15**, 1863 (2006), Proceedings of the joint 11th International Conference on New Diamond Science and Technology and the 9th Applied Diamond Conference 2006 ICNDST-ADC 2006. 124, 125

[174] G. Zhang *et al.*, Phys. Rev. B **84**, 214517 (2011). 124

[175] K. Ishizaka *et al.*, Phys. Rev. Lett. **100**, 166402 (2008). 124

[176] A. Allain, Z. Han, and V. Bouchiat, Nat. Mater. **11**, 590 (2012). 125, 148

[177] E. Ekimov *et al.*, Sci.Technol. Adv. Materials **9**, 044210 (2008). 125

[178] B. Sacépé *et al.*, Phys. Rev. Lett. **96**, 097006 (2006). 125

[179] S. Bhattacharyya, Phys. Rev. B **77**, 233407 (2008). 125

[180] Z. Wang *et al.*, Phys. Rev. B **81**, 174530 (2010). 125, 147, 148

[181] Y.-G. Lu *et al.*, Applied Physics Letters **101**, 041907 (2012). 125

[182] I. S. Beloborodov, A. V. Lopatin, V. M. Vinokur, and K. B. Efetov, Rev. Mod. Phys. **79**, 469 (2007). 140, 144, 146

[183] I. S. Beloborodov, K. B. Efetov, and A. I. Larkin, Phys. Rev. B **61**, 9145 (2000). 140, 146

[184] P. Achatz *et al.*, physica status solidi (a) **206**, 1978 (2009). 144, 145

[185] A. Gerber, Journal of Physics: Condensed Matter **2**, 8161 (1990). 145

[186] R. W. Simon, B. J. Dalrymple, D. Van Vechten, W. W. Fuller, and S. A. Wolf, Phys. Rev. B **36**, 1962 (1987). 145

[187] P. Achatz *et al.*, Phys. Rev. B **79**, 201203 (2009). 145

[188] B. L. Willems *et al.*, Journal of Physics D: Applied Physics **43**, 374019 (2010). 145

[189] A. P. Stephenson, A. P. Micolich, U. Divakar, P. Meredith, and B. J. Powell, Phys. Rev. B **81**, 144520 (2010). 146

[190] T. I. Baturina *et al.*, EPL **97**, 17012 (2012). 146, 147, 148

[191] E. Slot, M. A. Holst, H. S. J. van der Zant, and S. V. Zaitsev-Zotov, Phys. Rev. Lett. **93**, 176602 (2004). 148

[192] A. Mironov *et al.*, Physica C **470, Supplement 1**, S808 (2010), Proceedings of the 9th International Conference on Materials and Mechanisms of Superconductivity. 148

[193] B. M. Kessler, i. m. c. O. Girit, A. Zettl, and V. Bouchiat, Phys. Rev. Lett. **104**, 047001 (2010). 148

[194] H. Okazaki *et al.*, Applied Physics Letters **106**, 052601 (2015). 151

[195] F. S. Bergeret, A. F. Volkov, and K. B. Efetov, Rev. Mod. Phys. **77**, 1321 (2005). 154

[196] F. S. Bergeret, A. F. Volkov, and K. B. Efetov, Phys. Rev. Lett. **86**, 4096 (2001). 154

[197] P. V. Leksin *et al.*, Phys. Rev. Lett. **106**, 067005 (2011). 154

[198] P. V. Leksin *et al.*, Physics of the Solid State **58**, 2165 (2016). 154

[199] Y. V. Fominov *et al.*, JETP Letters **91**, 308 (2010). 155

[200] P. V. Leksin *et al.*, Nano Research **9**, 1005 (2016). 155